



**EFFLORESCENCE AND LEACHING BEHAVIOUR OF FLY
ASH-SLAG BASED ALKALI-ACTIVATED MATERIALS**

A Thesis submitted by

Lakshmikanth Srinivasamurthy, M.S.

For the award of

Doctor of Philosophy

2021

ABSTRACT

Over the past few decades, alkali-activated materials (AAMs) have shown the potential as alternative construction materials because of their high mechanical performance, low CO₂ emissions, and the utilisation of industrial wastes as raw material such as fly ashn(FA). However, the curing conditions, reaction mechanisms, and durability or long-term performance of AAMs over ordinary Portland cement materials (OPC) are still under exploration. In addition, AAMs are required to exhibit adequate/superior durability to match OPCs. A wide range of precursor materials, different chemical compositions, lack of standard code of practices, complex reaction mechanisms, and variable experimental methodologies in the AAM field, have led to complexities in engineering and application and assessing durability.

This body of work aims at understanding efflorescence, leaching properties and the mechanical properties of low, intermediate, and high-calcium-based AAMs. AAMs with different calcium contents in the FA precursor, with sodium silicate, sodium hydroxide, and sodium carbonate were used as activators. Representative molecular models of geopolymer were developed and molecular dynamics (MD) simulations were performed on AAMs with alkaline solvents, aimed to understand the underlying atomistic interactions.

The primary objective was to understand the FA-slag based AAMs phases deterioration under efflorescence and leaching exposure, with a detailed physical and chemical analysis of the process. The research conducted was multidisciplinary and broadly classified into three parts. The first part of the work was to understand the effect of mixed activators on phase deterioration of AAMs. The second part of the work was to understand the effect of FA-slag ratio and Na₂O content on reaction products. Specifically focused to understand the changes in ²⁷Al and ²³Na environment before and after efflorescence exposure. The third part of the research work discusses the effect of FA-slag ratio and Na₂O content on the reaction products under leaching exposure.

The outcomes of this research have contributed to the knowledge of efflorescence and leaching behaviour of alkali-activated materials. The parametric formulations of

precursors and activators discussed in this work can be optimised to develop stable AAMs under various conditions.

KEYWORDS

Alkali-activated materials, ordinary Portland cement, geopolymer, durability, leaching, reaction kinetics, carbonation, molecular dynamics, fly ash

CERTIFICATION OF THESIS

This Thesis is the work of Lakshmikanth Srinivasamurthy except where otherwise acknowledged, with the majority of the authorship of the papers presented as a Thesis by Publication undertaken by the Student. The work is original and has not previously been submitted for any other award, except where acknowledged.

Principal Supervisor: Prof. Hao Wang

Associate Supervisor: Prof. Zuhua Zhang

Student and supervisors' signatures of endorsement are held at the University.

ACKNOWLEDGEMENTS

First, I would like to thank the University of Southern Queensland (USQ) and the Centre for Future Materials for providing an opportunity to conduct research. I would like to take this opportunity to express my regards and gratitude to my principal supervisor, Prof. Hao Wang, for providing this opportunity, financial support, and unwavering support throughout my PhD candidature. I would like to seize this opportunity to express my gratitude to my associate supervisor Dr Zuhua Zhang for his patience, constant support, financial support, and technical input during the last four years.

I take this opportunity to thank the staff of USQ, specifically Mr Wayne Crowell, Mr Martin Geach, Mr Mohan Trada, Dr Susette Eberhard, Dr Marlon A Longhi and Dr Buddhi Wahalathantri for their support while conducting experiments. I would like to thank Mrs Mary Johnson, Associate Operational Support Officer for the pep talks during tough times and for providing coffee and tea. I would also like to thank Mr Christopher Droney, Graduate Research Student Officer (GRS) for providing constant support throughout my studies. I would take this opportunity to thank Mrs Sneha Koduru for the proof reading, fixing grammar, syntax, and language in the thesis and journal papers.

I would like to thank my parents Mrs Nagarathna and Mr Srinivasamurthy for their constant support during my PhD. In addition to this, I would like to thank my in-laws Mrs Tripura Sheshadri and Mr Sheshadri for their support. I would like to take this opportunity to express my gratitude to my beloved wife Mrs Ambika, for the sacrifice, moral support, love, and encouragement throughout my PhD candidature. I would like to thank Master Akshaj Sankriti and baby Chiku for their support. In addition to this, I would like to thank my family members Mrs Roopashri, Mr Ranganath, Prof K R Prabhu, and Mrs Jyothi Prabhu, for their constant support and encouragement throughout my studies.

I am extremely thankful to my friends, Dr Venkata Chevali and Mrs Chevali for the support, discussion, and tasty food. I also take this opportunity to convey my gratitude to Mr Steven McKerlie, Mrs Sue McKerlie and Ms Yen Pham for their support, long technical discussions during lunch and dinner. I would also like to thank my friends

Dr Pradeep Raja, Mr Kumar Srinivasan and Mrs Shambhavi Dileep for the encouragement and support.

I would also like to thank Prof J M Chandra Kishen for his support. Prof N Suryaprakash and Mr Chunchesh for providing access and technical assistance to NMR services at IISc, Bangalore, India. I would like to thank Prof Micheal Rajamathi and Mr Bhojraj for providing access and technical assistance to XRD services at St. Joseph's College, Bangalore, India.

Finally, yet importantly, I take this opportunity to thank the Australian Research Council for funding this research. I would also like to thank USQ shuttle bus drivers for driving back-and-forth from Springfield to the Toowoomba campus.

LIST OF PUBLICATIONS BY CANDIDATE AND CONTRIBUTION STATEMENT

Paper 1: Phase changes under efflorescence in alkali-activated materials with mixed activators, Lakshmikanth Srinivasamurthy, Venkata S. Chevali, Zuhua Zhang, and Hao Wang, *Construction and Building Materials*, IF – 6.141 (Published)

LS was responsible for 75% of the conceptualization, formal analysis, investigation, methodology, project administration, writing - original draft. HW and ZZ are responsible for funding acquisition, supervision, and writing - review & editing. VSC is responsible for analysis - interpretation of data and editing and proofreading.

Paper 2: The effect of fly ash/slag ratio and activator concentration on efflorescence of fly ash/slag-based alkali-activated materials, Lakshmikanth Srinivasamurthy, Zuhua Zhang, Venkata Chevali, Márton A. Longhi, Thomas Loh, Hao Wang, *Construction and Building Materials*, IF-6.141 (Under review)

LS was responsible for 75% of the conceptualization, formal analysis, investigation, methodology, project administration, writing - original draft. HW and ZZ are responsible for funding acquisition, supervision, and writing - review & editing. VSC is responsible for analysis - interpretation of data and editing and proofreading. ML is responsible for the investigation and providing technical inputs. TL is responsible for characterization and providing technical inputs.

Paper 3: Effect of fly ash/Slag ratio and sodium content on AAMs under leaching, Lakshmikanth Srinivasamurthy, Venkata S. Chevali, Zuhua Zhang, and Hao Wang, *Journal of Building Engineering*, IF-5.1 (In submission)

LS was responsible for 75% of the conceptualization, formal analysis, investigation, methodology, project administration, writing - original draft. HW and ZZ are responsible for funding acquisition, supervision, and writing - review & editing. VSC is responsible for analysis - interpretation of data and editing and proofreading.

Paper 4: Durability behaviour of alkali-activated materials, Lakshmikanth Srinivasamurthy, Zuhua Zhang, Venkata Chevali, Hao Wang, *Construction and Building Materials*, IF: 6.141 (In Submission)

LS was responsible for 75% of the literature review, 75% of analysis and interpretation of the data and 100% of drafting the initial draft and final submission. HW and ZZ is responsible for the literature review and editing the draft and providing necessary technical inputs. VSC is responsible for literature review and editing drafts and providing inputs.

THESIS ORGANISATION

This thesis consists of eight chapters. The thesis chapters are presented in a coherent manner that supports the main findings of the research, described as follows:

Chapter 1: This chapter discusses the research theme and the main objectives of the research.

Chapter 2: This chapter discusses the literature, and the chapter has been divided into three sections. The first part of the literature review discusses the distinct types of phases present in the alkali-activated material systems and the effect of these phases on the material properties. The second part of the thesis discusses several durability aspects of alkali-activated materials. The third part of this chapter discusses molecular dynamics simulation related to alkali-activated materials.

The literature review is being submitted for publication as a review titled “Durability behaviour of alkali-activated materials,” authored by Lakshmikanth Srinivasamurthy, Zuhua Zhang, Venkata Chevali, Hao Wang

Chapter 3: This chapter discusses motivation, conceptual framework, research gaps and objectives of the thesis.

Chapter 4: This chapter discusses the material selection and methods involved in the research. Specifically, experimental and characterization methods, techniques and specifications while experimenting.

Chapter 5: This chapter discusses the effect of mixed activators on the efflorescence behaviour of alkali-activated materials, including the analysis of the formation and changes in phases under efflorescence. This work is published as a journal article as follows “Phase changes under efflorescence in alkali-activated materials with mixed activators, Lakshmikanth Srinivasamurthy, Venkata S. Chevali, Zuhua Zhang, and Hao Wang.

Chapter 6: This chapter discusses the effect of low slag and activator concentration on phase changes of alkali-activated materials under efflorescence. This chapter is currently under review as “The effect of fly ash/slag ratio and activator concentration on efflorescence of fly ash/slag-based alkali-activated materials,” Lakshmikanth

Srinivasamurthy, Zuhua Zhang, Venkata Chevali, Márton A. Longhi, Thomas Loh, Hao Wang,

Chapter 7: This chapter discusses the effect of slag and activator concentration on alkali-activated materials exposed to leaching conditions. Specifically focused to understand the effect of leaching on phase and mechanical properties changes. This chapter is in submission as “Effect of fly ash/Slag ratio and sodium content on AAMs under leaching, Lakshmikanth Srinivasamurthy, Venkata S. Chevali, Zuhua Zhang, and Hao Wang,

Chapter 8: This chapter has been divided into two sections. The first part of the chapter discusses the overall conclusions of the research. The second part discusses the future directions of the research related to alkali-activated materials.

TABLE OF CONTENTS

ABSTRACT	I
KEYWORDS	II
CERTIFICATION OF THESIS	III
ACKNOWLEDGEMENTS	IV
LIST OF PUBLICATIONS BY CANDIDATE AND CONTRIBUTION STATEMENT	VI
THESIS ORGANISATION	VIII
TABLE OF CONTENTS	X
LIST OF FIGURES	I
LIST OF TABLES.....	IX
CHAPTER 1 INTRODUCTION.....	1
CHAPTER 2 LITERATURE REVIEW	4
2.1 Type of precursors and their alkali-activation products.....	6
2.2 Durability.....	32
2.3 Molecular dynamics simulations	68
2.4 Literature summary and conclusions	73
CHAPTER 3 OBJECTIVES AND CONCEPTUAL FRAMEWORK.....	77
3.1 Objectives.....	77
3.2 Conceptual framework	79
CHAPTER 4 METHODOLOGY	81
4.1 Materials and methods	81
4.2 Property testing.....	82

4.3	Microstructural characterization.....	83
CHAPTER 5 PHASE CHANGES UNDER EFFLORESCENCE IN ALKALI-ACTIVATED MATERIALS WITH MIXED ACTIVATORS		
		87
5.1	Introduction	87
5.2	Materials and methods.....	90
5.4	Results and discussion	93
5.5	Conclusions	109
CHAPTER 6 EFFECT OF FLY ASH/SLAG RATIO AND ACTIVATOR CONCENTRATION ON EFFLORESCENCE OF FLY ASH/SLAG-BASED ALKALI-ACTIVATED MATERIALS.....		
		111
6.1	Introduction	111
6.2	Materials and Methods.....	113
6.3	AAM synthesis and efflorescence conditioning.....	114
6.4	Testing and characterization	114
6.5	Results and Discussion	116
6.6	Conclusions	141
CHAPTER 7 EFFECT OF FLY ASH/SLAG RATIO AND Na_2O CONTENT ON THE LEACHING BEHAVIOUR OF ALKALI-ACTIVATED MATERIALS		
		143
7.1	Introduction	143
7.2	Materials and Methods.....	146
7.3	Results and discussion	152
7.4	Conclusions	177
CHAPTER 8 CONCLUSION AND FUTURE DIRECTIONS		
		180
8.1	Conclusions	180
8.2	Future directions	181
8.3	Contributions.....	183
APPENDIX A STATEMENTS OF CONTRIBUTIONS OF CO-AUTHORS		
		184

APPENDIX B SUPPLEMENTARY INFORMATION	187
REFERENCES	199

LIST OF FIGURES

Fig. 2-1 A schematic of the cement manufacturing process showing the major raw materials and steps.	4
Fig. 2-2 A schematic of alkali-activated cement or geopolymerization process showing the main phases and intermediate steps.	5
Fig. 2-3 X-ray diffractograms of (a) unreacted slag, and unexposed alkali-activated slag after (b) 8 days, (c) 14 days, and (d) 3 years of curing [55].	8
Fig. 2-4 Compressive strength development in the different alkali-activated systems [56]....	9
Fig. 2-5 Microstructure of NaOH activated slag at early ages of curing showing the C-S-H layer around the slag particles as well as platelets of hydrotalcite. (a) Low alumina slag with NaOH, and (b) High alumina slag with NaOH [56].....	10
Fig. 2-6 SEM images of AAS activated with NaOH and Na ₂ SiO ₃ at later stages [57].....	10
Fig. 2-7 Compressive strength of the pastes vs. (a) degree of hydration and (b) coarse porosity of AAS activated with NaOH and Na ₂ SiO ₃ [60].....	12
Fig. 2-8 SEM-image of NaOH and Na ₂ SiO ₃ activated slag with 13wt.% of MgO after 1 year [58].	12
Fig. 2-9 XRD of alkali-activated fly ash with various SiO ₂ content Q: quartz (SiO ₂), M: mullite (Al _{4.8} O _{9.54} Si _{1.2}), H: hydroxysodalite (Na ₄ Al ₃ Si ₃ O ₁₂ (OH)), F: faujasite (Na _{1.84} Al ₂ Si ₄ O _{11.92} H ₂ O) [62]	14
Fig. 2-10 XRD of alkali-activated fly ash with various Na ₂ O contents, Q: quartz (SiO ₂), M: mullite (Al _{4.8} O _{9.54} Si _{1.2}), F: faujasite (Na _{1.84} Al ₂ Si ₄ O _{11.92} •7H ₂ O) [62].....	14
Fig. 2-11 SEM pictures: (a) raw FA, (b) FA activated with 8 M NaOH for 5 h at 85 °C [64]..	15
Fig. 2-12 SEM pictures. FA activated with 8 M NaOH for 20 h at 85 °C; (a) reaction process of a large sphere, (b) singular details of the reaction of some small spheres [64].	15
Fig. 2-13 Evolution of the reaction degree of FA activated with an 8 M NaOH dissolution. Curing temperature: 85 °C [64].	16
Fig. 2-14 (a) Evolution of the mechanical strength of the activated FA mortars as a function of time; (b) rate of mechanical strength gaining. Mortars were cured in the stove for (2, 5, 12, and 24 h) at 45°, 65°, and 85°C, and then were kept at 23 ± 1°C and 95% relative humidity for 1, 2, 3, 7, and 15 d [61].	17
Fig. 2-15 ²⁹ Si NMR spectrum of (A) original FA, and (B) FA attacked with HF, and (C) ²⁷ Al NMR spectrum of original FA [61].	17
Fig. 2-16 ²⁹ Si MAS-NMR spectra of (A) the original FA; (B) alkali-activated FA 5 h at 85°C; (C) 24 h at 85°C; and (D) 1 week at 85°C [61].	18
Fig. 2-17 ²⁹ Si NMR MAS spectra of the alkali-activated FA at (A) 24 h at 65°C, (B) 1 week at 65°C, and (C) 1 week at 45°C [61].	18

Fig. 2-18 XRD patterns of AAMK after activation with NaOH solution of 6–12 mol/L at 30 °C for 72 h (kaolinite, $\text{Al}_2 \text{Si}_2 \text{O}_5 (\text{OH})_4$; halloysite, $\text{Al}_2 \text{Si}_2 \text{O}_5 (\text{OH})_4 \cdot 2\text{H}_2 \text{O}$; quartz; hydroxysodalite, $\text{Na}_8 \text{Al}_6 \text{Si}_6 \text{O}_{24} (\text{OH})_2 \cdot 2\text{H}_2 \text{O}$; sodium carbonate, Na_2CO_3) [73].	21
Fig. 2-19 XRD patterns AAMK activated with NaOH solution 10 mol/L at 40 °C (zeolite A, $\text{Na}_{96} \text{Al}_{96} \text{Si}_{96} \text{O}_{384} \cdot 216\text{H}_2\text{O}$) [73].	21
Fig. 2-20 FTIR spectra of MK and the geopolymerization products after activation with NaOH solution at 30 °C for 72 h. [73].	22
Fig. 2-21 SEM micrographs of the fracture surfaces of geopolymerization products of MK activated with NaOH solution: (a) 6 mol/L, (b) 8 mol/L, (c) 10 mol/L and (d) 12 mol/L. [74].	23
Fig. 2-22 Compressive strengths of hardened binders synthesized with liquid/solid ratio of 0.65 mL/g at 25 °C [74].	23
Fig. 2-23 High-resolution synchrotron X-ray diffraction patterns ($k = 0.458 \text{ 879 \AA}$) of 28-d cured alkali-activated pastes with GBFS/(GBFS + MK) ratios of (A) 1.0, (B) 0.9 and (C) 0.8 [59].	25
Fig. 2-24 Compressive strength of mortars based on silicate activated GBFS/MK blends [80].	26
Fig. 2-25 (a) Compressive strength development; (b) porosity values [76].	28
Fig. 2-26 X-ray diffraction patterns of FA metakaolin blends [76].	28
Fig. 2-27 Effect of ageing time on compressive strength and effects of blast furnace slag content on the rates of compressive strength development of airtight ambient cured geopolymer mortars [83].	29
Fig. 2-28 X-ray diffractograms of alkali-activated slag/fly ash binders, as a function of the slag/fly ash ratio and the time of curing: (A) 100 wt.% slag, (B) 75 wt.% slag/25 wt.% fly ash, (C) 50 wt.% slag/50 wt.% fly ash, (D) 25 wt.% slag/75 wt.% fly ash and (E) 100 wt.% fly ash [19].	31
Fig. 2-29 Physical condition of samples: A w/b 0.40; B w/b 0.50; and C w/b 0.60, after immersion in Na_2SO_4 and MgSO_4 for 90 days [99].	34
Fig. 2-30 Compressive strength of AAS concrete subjected to 5 wt.% Na_2SO_4 solution and compressive strength reduction of AAS and OPC samples subjected to sulphate attack in 5 wt.% Na_2SO_4 solution [100].	34
Fig. 2-31 Compressive strength of AAS concrete subjected to 5 wt.% MgSO_4 solution and compressive strength reduction of AAS and OPC samples subjected to sulphate attack in 5 wt.% MgSO_4 solution [100].	34
Fig. 2-32 The compressive strengths of specimens before and after the sulphate exposure for 3, 7, 28, and 120 days: (a) A3 of PVA and PP fibre reinforced geopolymers, (b) B9 of PVA and WS fibre reinforced geopolymers (Pure geopolymer-Geo & Control group with fibres-CG) [101].	35

Fig. 2-33 The XRD pattern of samples exposed to sulphate for 28 days: (a) A3 of PVA and PP fibre reinforced geopolymers, (b) B9 of PVA and WS fibre reinforced geopolymers [101].	35
Fig. 2-34 BSE image and elemental maps of alkali-activated 75 wt.% slag/25 wt.% fly ash concrete with 28 d curing after 6 months of magnesium sulphate exposure [102].	36
Fig. 2-35 The relationship between the number of freezing-thawing cycles and the mass-loss rate of (a) uncalcined and (b) calcined [103].	37
Fig. 2-36 The relationship between cycle times of salt freeze-thaw and mass-loss rate of (a) uncalcined and (b) calcined [103].	37
Fig. 2-37 The relationship between the salt-frost and the relative dynamic modulus of elasticity of (a) uncalcined and (b) calcined [103].	38
Fig. 2-38 SEM image of ACSC freeze-thaw cycles of (a) W100 and (b) S100 [103].	38
Fig. 2-39 Results of application of AgNO ₃ to concretes at the end of the ponding test for concretes with 28 days of curing, as a function of slag/FA proportion: (A) 100 wt.% slag, (B) 75 wt.% slag/25 wt.% FA, (C) 50 wt.% slag/50 wt.% FA, and (D) OPC [104].	40
Fig. 2-40 XRD diffractograms of 100% FA geopolymer and PC samples before or after the ponding test. Mullite (Al _{4.56} Si _{1.44} O _{9.72}); Quartz (SiO ₂); Calcite (CaCO ₃); Halite (NaCl); Portlandite (Ca(OH) ₂); Iron Oxide Hydroxide (FeO(OH)); Calcium Silicate (Ca ₃ SiO ₅) [106].	40
Fig. 2-41 (a) Cl ⁻ penetration in AAFA and SPC pastes and (b) their mortars [105].	41
Fig. 2-42 Relationship between the carbonation depth and compressive strength (A) and post-carbonation total pore volume (B) of alkali-activated concretes, as a function of the content of MK incorporated in the binder [113].	42
Fig. 2-43 Natural carbonation depth (16 months exposure to ambient laboratory environment) of silicate-activated slag pastes (φ= 12.8 mm) as a function of the MgO content in the slag [114].	42
Fig. 2-44 Transverse sections of naturally carbonated pastes after 16 months exposed samples to atmospheric conditions, with the extent of carbonation revealed by a phenolphthalein indicator [114].	43
Fig. 2-45 Atomic ratios Ca/Si vs Al/Si and Mg/Si vs Al/Si, for uncarbonated and carbonated regions [18].	44
Fig. 2-46 X-ray diffractograms of alkali-activated fly ash/slag blended pastes cured for (A) 1 day or (B) 7 days and exposed for 7 days to accelerated carbonation at different CO ₂ concentrations as marked [18].	46
Fig. 2-47 Carbonation depth of mortars based on activated slag/metakaolin blended binders as a function of the GBFS/(GBFS + MK) ratio and activation concentration [124].	48
Fig. 2-48 Fourier transform infrared spectra of uncarbonated and carbonated pastes of (A;B) GBFS and (C;D) GBFS/MK blends, activated with (A;C) M _s = 2.4, (B;D) M _s = 2.0 [49].	50

Fig. 2-49 ²⁷ Al MAS NMR spectra of (A) alkali-activated fly ash and (B) alkali-activated fly ash/slag blends [18].....	53
Fig. 2-50 X-ray diffractograms of alkali-activated slag with (A) 1 day and (B) 7 days of curing, then exposed to elevated CO ₂ concentrations as marked, for 7 days [18].	55
Fig. 2-51 Porosity of partially carbonated concretes based on alkali-activated slag/metakaolin blends formulated with GBFS/(GBFS+MK) ratios of a 1.0, b 0.9 and c 0.8, as a function of the relative humidity, at 1 % CO ₂ . Error bars correspond to one standard deviation of four measurements [131].....	56
Fig. 2-52 Carbonation depth as a function of the relative humidity and time of exposure in alkali-activated GBFS/MK concretes, formulated with GBFS/(GBFS+MK) ratios of a 1.0, b 0.9 and c 0.8, at 1 % CO ₂ [131].....	57
Fig. 2-53 Water absorption of rice husk based AAM concrete mixes with partial replacement of OPC.	58
Fig. 2-54 A representation of (a) water absorption behaviour of heat-cured AAM concrete, and (b) porosity behaviour of heat-cured AAM concrete.....	59
Fig. 2-55 Relationship between the moisture and the bulk resistivity of AAM concrete.....	60
Fig. 2-56 Plots of (a) void contents of AAM concrete as a function of liquid to alkaline activate concentration, and (b) water permeability of AAM concrete as a function of liquid to alkaline activate concentration.....	60
Fig. 2-57 Curves show (a) relationship between water permeability and void content of AAM concrete, and (b) relationship between compressive strength and void ratio of AAM concrete.	61
Fig. 2-58 (a) Relationship between compaction factor and 28 days compressive strength (b) Relationship between compressive strength and RCPT at 28 days	61
Fig. 2-59 Correlation of (a) total porosity-compressive strength and (b) total porosity-water permeability of slag (AAS), metakaolin (MK) and metakaolin/slag (MGG) pervious concrete.	62
Fig. 2-60 First derivative of the cumulative pore volume of alkali-activated cements (a) before and (b) after accelerated leaching as determined by MIP [147].	64
Fig. 2-61 XRD patterns of the (d) S100 and (e) PC samples before and after accelerated leaching [147].	64
Fig. 2-62 Schematic diagram of efflorescence process in AAMs.....	65
Fig. 2-63 Alkali-activated metakaolin specimens exposed to efflorescence condition [148] 65	65
Fig. 2-64 SEM images of the efflorescence products: (a) on the surface of 28-day air aged GPC-NS1.5, and (b) the carbonation products on a fracture surface [158]	67
Fig. 2-65 Compressive strength of geopolymer specimens activated with sodium silicate [158]	67

Fig. 2-66 A vertical section of composite GB-C-S-H1.65 (Ca/Si = 1.65) with the silica layers in C-S-H oriented perpendicular to the interface: green = Ca, gold = Si, grey = Al, red = O, white = H, purple = Na [169].	70
Fig. 2-67 Stress-strain curves of GB-C-S-H composites at different Ca/Si ratios and with a crack of $2a = 20 \text{ \AA}$ and thickness of 4 \AA . [169].	72
Fig. 2-68 Failure of GB-C-S-H1.45 (Ca/Si = 1.45) composites for interface (a) parallel and (b) perpendicular to SiO ₂ layers in C-S-H.....	73
Fig. 3-1 Conceptual design flow chart for this body of work.	80
Fig. 4-1 Experimental flow chart of AAMs binder specimens	82
Fig. 4-2 Experimental procedure for efflorescence tests on AAMs samples.....	83
Fig. 4-3 Experimental procedure for leaching trials	84
Fig. 4-4 Steps involved in MD simulations.	86
Fig. 4-5 Solvation model of aluminosilicate source.....	86
Fig. 5-1 X-ray diffractograms of FA and slag showing the main mineralogical phases.	91
Fig. 5-2 Binder specimens with varying levels of slag showing surface deposition after 28 days of efflorescence	94
Fig. 5-3 Compressive strength of binder specimens after curing and efflorescence.	96
Fig. 5-4 Split tensile strength of binder specimens after curing and efflorescence.....	96
Fig. 5-5 The variation in pH with respect to leaching time in the binder specimens.	97
Fig. 5-6 The comparative plots of (a) concentration of sodium and silicates leached from hardened binder specimens, and (b) open porosities of binder specimens before and after the leaching.	98
Fig. 5-7 XRD patterns of hardened binder specimens and after 28 days of ageing under efflorescence with decreasing FA content, (a-b) 100FA0SN (C), (c-d) 90FA10SN(C), and (e-f) 70FA30SN(C).	101
Fig. 5-8 FTIR spectra of binder specimens	104
Fig. 5-9 TGA thermograms of aged AAM binder specimens	105
Fig. 5-10 MAS-NMR spectra of unreacted precursors: (a) ²⁷ Al of FA and slag	108
Fig. 5-11 ²⁷ Al MAS-NMR spectra of binders before and after efflorescence: (a) binder specimens without Na ₂ CO ₃ , and (b) binder specimens with Na ₂ CO ₃	108
Fig. 5-12 ²³ Na MAS-NMR spectra of binders before and after efflorescence: (a) binder specimens without Na ₂ CO ₃ , and (b) binder specimens with Na ₂ CO ₃	109
Fig. 6-1 Efflorescence formation on binder specimens activated with 9wt.% Na ₂ O content varying with Ca/(Si+Al) ratios.	116

Fig. 6-2 Efflorescence formation on binder specimens activated with 5 wt.% Na ₂ O content varying with Ca/(Si+Al) ratios.	117
Fig. 6-3 Cylindrical binder specimens before and after 90 days of efflorescence exposure	118
Fig. 6-4 Cubicle binder specimens after efflorescence	118
Fig. 6-5 FTIR spectra of AAMs with 9wt.% Na ₂ O content and varying Ca/(Si+Al) ratios	124
Fig. 6-6 FTIR spectra of AAMs with 5wt.% Na ₂ O content and varying Ca/(Si+Al) ratios	125
Fig. 6-7 (a) and (b) Differential thermograms of AAMs with 9wt.% and 5wt.% Na ₂ O content	128
Fig. 6-8 ²³ Na NMR spectra of (a) 9 wt.% and (b) 5 wt.% Na ₂ O AAMs	130
Fig. 6-9 ²⁷ Al MAS-NMR spectra of raw materials	131
Fig. 6-10 ²⁷ Al MAS-NMR spectra of binder specimens with 9wt.% Na ₂ O content and varying Ca/(Si+Al) ratios.....	134
Fig. 6-11 ²⁷ Al MAS-NMR spectra of binder specimens with 5 wt.% Na ₂ O content and varying CA/(Si+Al) ratios.....	136
Fig. 6-12 Compressive strength of binder specimens	138
Fig. 6-13 Split tensile strength of binder specimens	139
Fig. 6-14 Concentration of sodium leached from AAM specimens at 30, 60 and 90 days (a) 9wt.% Na ₂ O specimens (9A-9D) and (b) 5wt.% Na ₂ O (5A-5D) specimens	140
Fig. 6-15 The porosity of binder specimens before and after efflorescence.....	141
Fig. 7-1 X-ray diffractograms of FA and slag.	147
Fig. 7-2 Structure of Sodalite.....	150
Fig. 7-3 Amorphous N-A-S-H structure.....	150
Fig. 7-4 Solvation model of N-A-S-H structure	151
Fig. 7-5 Amorphous N-A-S-H gel structure at 300 K and 1 bar pressure	151
Fig. 7-6 (a-c) leached fractions of Na as a function of time and (d-f) leached fractions of Si as a function of time.....	155
Fig. 7-7 (a) Effect of slag on leaching fractions of Na and (b) Effect of slag on leaching fractions of Si.....	155
Fig. 7-8 (a) Concentrations of Ca and Al in leachate and (b) pH profiles of selected binder mixes	155
Fig. 7-9 (a) FTIR spectra of binder mixes after activation and (b) after leaching	156
Fig. 7-10 FTIR spectra of binder mix after curing and leaching activated with 5 wt.% Na ₂ O and varying slag content.....	158

Fig. 7-11 FTIR spectra of binder mixes as a function of activator content (a) 0wt.% slag, (b) 5 wt.% slag, (c) 10 wt.% slag and (d) 30 wt.% slag.....	159
Fig. 7-12 MAS-NMR spectra of unreacted precursors: (a) ^{27}Al of FA and slag, (b) ^{23}Na of unreacted slag	160
Fig. 7-13 MAS-NMR (^{27}Al) spectra of blended precursors before activation.....	160
Fig. 7-14 ^{23}Na MAS-NMR spectra of binder mixes with varying slag content after curing and leaching (a) 9 wt.% Na_2O , (b) 7 wt.% Na_2O and (c) 5 wt.% Na_2O	162
Fig. 7-15 ^{27}Al MAS-NMR spectra of binder mixes activated with 9 wt.% Na_2O and varying slag contents (a) after curing and (b) after leaching.....	163
Fig. 7-16 ^{27}Al MAS-NMR spectra of (a-c) binder mix with varying Na_2O content and 0 wt.% slag content, and (d-f) binder mixes with varying Na_2O content and 30 wt.% slag content.	166
Fig. 7-17 (a-b) ^{27}Al MAS-NMR spectra of binder mixes activated with 7 wt.% Na_2O , 5 and 10 wt.% slag content. (c-d) binder mixes activated with 5 wt.% Na_2O , 5 and 10 wt.% slag content.	167
Fig. 7-18 Water clusters around Amorphous N-A-S-H gel and Na ions.....	169
Fig. 7-19 Distance between Al atoms of N-A-S-H and Na ions at atmospheric condition .	169
Fig. 7-20 Distance between Al atoms of N-A-S-H and Na ions at after 1ns.....	170
Fig. 7-21 Electrostatic interaction energies between AlO_4 and Na ions.....	171
Fig. 7-22 Electrostatic interaction energies between AlO_4 and water.....	171
Fig. 7-23 Electrostatic interaction energies between Na and water	172
Fig. 7-24 X-ray diffractograms. (a-c) binder mixes with varying Na_2O and 0 wt.% slag content. (d-f) binder mixes with varying Na_2O and 30 wt.% slag content	174
Fig. 7-25 Physical properties of binder mixes (a) Capillary absorption after curing, (b) Open porosity values after curing (c) Dry density after curing (d) Compressive strength behaviour after curing and leaching and (e) Split tensile strength behaviour after curing and leaching.	177
Fig. BS-1	187
Fig. BS-2	187
Fig. BS-3	188
Fig. BS-4	189
Fig. BS-5	190
Fig. BS-6	191
Fig. BS-7	192

Fig. BS-8	193
Fig. BS-9	193
Fig. BS-10	193
Fig. BS-11	194
Fig. BS-12	194
Fig. BS-13	195
Fig. BS-14	195
Fig. BS-15	195
Fig. BS-16	196
Fig. BS-17	196
Fig. BS-18	197
Fig. BS-19	197
Fig. BS-20	198
Fig. BS-21	198
Fig. BS-22	198

LIST OF TABLES

Table 2-1 Chloride migration coefficients of concretes determined from the NordTest accelerated method as a function of curing age. Values in parentheses are standard deviations of 4 samples.....	39
Table 2-2 Simulation details of N-A-S-H geopolymer gels.....	71
Table 2-3 Interatomic potential parameters used for M (Si/Al/Na)-Oh and Oh-H interaction.[168].....	72
Table 5-1 Chemical compositions of FA and GGBFS as determined by XRF. Loss on ignition (LOI) is shown at 1000 °C.....	90
Table 6-1 Compositional details of the precursors used in this study	113
Table 6-2 Mix design details of AAMs	114
Table 6-3 Effect of efflorescence on Chemical shift and areas determined through deconvolution of FTIR spectra	126
Table 6-4 Effect of efflorescence on Chemical shift and areas determined through MAS-NMR	137
Table 7-1 Chemical compositions of FA and GGBFS as determined by XRF. LOI is the loss on ignition at 1000 °C.	146
Table 7-2 Mix proportions and curing conditions of binders.....	147
Table 7-3 Effect of leaching on Chemical shift and areas determined through MAS-NMR... ..	168

CHAPTER 1 INTRODUCTION

Cement and concrete are vital construction materials for modern civilization. These materials are extensively used in the construction of buildings, roads, bridges, dams, and sewer systems. Ordinary Portland cement (OPC) concrete is the widely used substance next to the water, and 10 billion tonnes of cement concrete is produced every year [1,2]. OPC concrete is still the choice for engineers because of its service life and fire resistance. Apart from these properties, OPC concrete structures also offer an average lifespan of 100 years.

In recent years, the cement industry is under scrutiny from environmental and sustainability perspectives. The cement industry is responsible for the serious depletion of natural resources caused by the extraction of raw materials. Moreover, the cement industry also contributes to $\approx 8\%$ of global CO_2 [2,3] emissions and consumes $\approx 10\%$ of the total energy used [4,5]. As a result, the cement industry is keen to reduce energy consumption and greenhouse gas emissions and actively pursue suitable sustainable alternatives to tackle these concerns. Resources such as fly ash (FA), ground granulated blast furnace slag (GGBFS) and rice husk ash (RHA) are supplementary sources of cementitious materials for developing novel eco-efficient binders such as calcium aluminate cements [6–8], calcium sulfoaluminate cements [9–13], super-sulphated cements [14–16] and alkali-activated binders or alkali-activated materials (AAMs) [17–24]. Among these, commercially available alkali-activated materials, also known as geopolymers are very promising [25,26].

The AAMs or geopolymers have gained attention as a new type of cement and concrete production, with the advantages of OPC, but with a significant reduction in carbon dioxide (CO_2) production. AAMs also exhibit engineering properties like high compressive strength, acid resistance and sulphate resistance. AAMs have emerged as cost-effective sustainable construction materials with the potential to reduce the cost of construction materials and CO_2 emissions posed by OPC [27–30].

AAMs and geopolymer cement/concrete have been investigated for composition, reaction mechanisms, chemical and mechanical properties. However, durability aspects such as efflorescence and leaching behaviour, testing methods and

standardization of testing methods are still under evaluation and discussion [31,32,41–43,33–40].

This body of work aims to understand the durability aspects of FA-slag based AAMs under efflorescence and leaching exposure. The first part of the research work (chapter 5) discusses the efflorescence in alkali-activated materials as a strong function of precursor and activator composition, which dictates their engineering properties and durability. In this study, the efflorescence of naturally cured NaOH/Na₂SiO₃ alkali-activated FA and alkali-activated FA-slag binder mixes was assessed with an alkali concentration of 9 wt.%, and 10 to 30 wt.% of slag, and compared with binder mixes with 9 wt.% Na₂O, and 10 to 30 wt.% of slag along with 2 wt.% Na₂CO₃. The effects of efflorescence were assessed using visual and leaching inspections. The compressive and split tensile strengths were determined post activation. Atomic absorption spectrometry was used to quantify free alkalis in the leachate, and X-ray diffraction and Fourier transform infrared spectroscopy, magic-angle-spinning nuclear magnetic resonance and thermo-gravimetric analysis were performed to analyse the phase changes in binder mixes after efflorescence. The increased slag content facilitated the formation of calcium aluminosilicate hydrate (C-A-S-H) gel in binder mixes and enhanced the mechanical properties of binder mixes. Subsequent exposure of binder specimens to efflorescence conditions aided the formation of carbonate products, degradation of sodium aluminosilicate hydrate and sodium calcium aluminosilicate hydrate (N-A-S-H and N-(C)-A-S-H) gel, and a decrease in split tensile strength in the binder specimens.

The second part of the research work (chapter 6) discusses the effect of calcium and Na₂O content on the efflorescence behaviour of FA- slag based AAMs. In this study, eight low-calcium based AAMs varied with calcium and activator content were exposed to 90 days of efflorescence condition. The compressive and split tensile strengths were assessed at different time intervals. Microstructural features such as changes in N-A-S-H/N-(C)-A-S-H was observed using FTIR, MAS-NMR and TGA. The AAMs with 9 wt.% Na₂O and Ca/(Si+Al) = 0.0-0.25 exhibited excessive efflorescence and resulted in severe damage to AAMs specimens. Significant dealumination in Al[IV] environment of N-A-S-H/N-(C)-A-S-H gels, higher mobility of Na⁺ ions and natural carbonation was observed in these binder mixes. Conversely

AAM specimens with 5 wt.% Na_2O and $\text{Ca}/(\text{Si}+\text{Al}) = 0.0-0.25$ exhibited negligible efflorescence and higher stability after exposure. The binder mixes with 5 wt.% Na_2O and $\text{Ca}/(\text{Si}+\text{Al}) = 0.25$ exhibited dealumination and the carbonated product was observed. However, AAM specimens with 5 wt.% Na_2O and $\text{Ca}/(\text{Si}+\text{Al}) = 0.0-0.10$ showed the inclusion of Al[IV] and Si into aluminosilicate gels under efflorescence exposure. The relationship between the effect of calcium and activator content on phase changes and mechanical properties of AAMs under efflorescence exposure facilitates in developing key indicators in AAMs compositional design and applications.

The third part of the research work (chapter 7) discusses the effect of FA-slag ratio and Na_2O content on the leaching behaviour of AAMs. In this study, the long-term leaching behaviour of alkali-activated materials (AAMs) has been investigated in this work. A series of FA-slag based AAM binder mixes with varying slag content (0-30 wt.%) and varying Na_2O content (5, 7 and 9 wt.%) has been synthesized and exposed to leaching conditions for 90 days. The inclusion slag content has significantly enhanced mechanical properties along with reducing the porosity, which is attributed to the formation of C-A-S-H gel along with N-A-S-H gel. The low porosity in AAMs with slag content has reduced the leaching potential of Na^+ and Si^{4+} from binder mixes. However, the long-term exposure of binder mixes in these conditions triggered the leaching of Ca^{2+} and Al[IV] from the structural gels such as N-A-S-H/N-(C)-A-S-H gels showed degradation binder gels. The degradation of AAM phases under leaching affected mechanical properties such as compressive and split tensile strength.

CHAPTER 2 LITERATURE REVIEW

AAMs or geopolymers are synthesized at room temperature or at a slightly elevated temperature (23° C - 85° C, 50% relative humidity). Initially, geopolymers include an aluminosilicate source and alkaline-silicate solution, and the reaction between these at ambient temperature initiates a reaction or series of reactions that facilitate the formation of a geopolymer network, which possesses cementitious properties. OPC consists of calcium hydroxide and calcium silicate hydrate (C-S-H) as major binding constituents, but in geopolymer, a three-dimensional amorphous silicate network is assumed as a binding agent.

Fig. 2-1 and Fig. 2-2 show the comparison between the conventional Portland cement and geopolymerization process. Portland cement consists of two phases, namely calcium silicate hydrate and calcium hydroxide. However, geopolymer consists of an aluminosilicate phase. Besides, there is no calcination process in geopolymer, which reduces the carbon emission during synthesis [44].

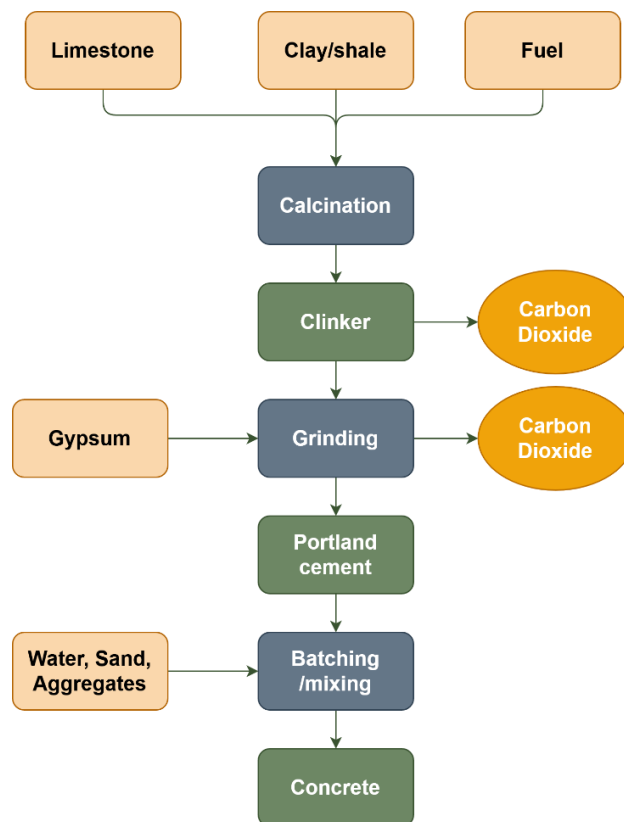


Fig. 2-1 A schematic of the cement manufacturing process showing the major raw materials and steps.

Fig. 2-2 also shows the distinct phases involved in AAMs, with fly ash (FA), blast furnace slag, and metakaolin as the most common materials. Although the production of these materials is cheaper, the reaction mechanism involved in the alkali activation process is complex and elusive, attracting numerous endeavours to understand and develop the explanatory models of the alkali activation process, which are discussed here [44].

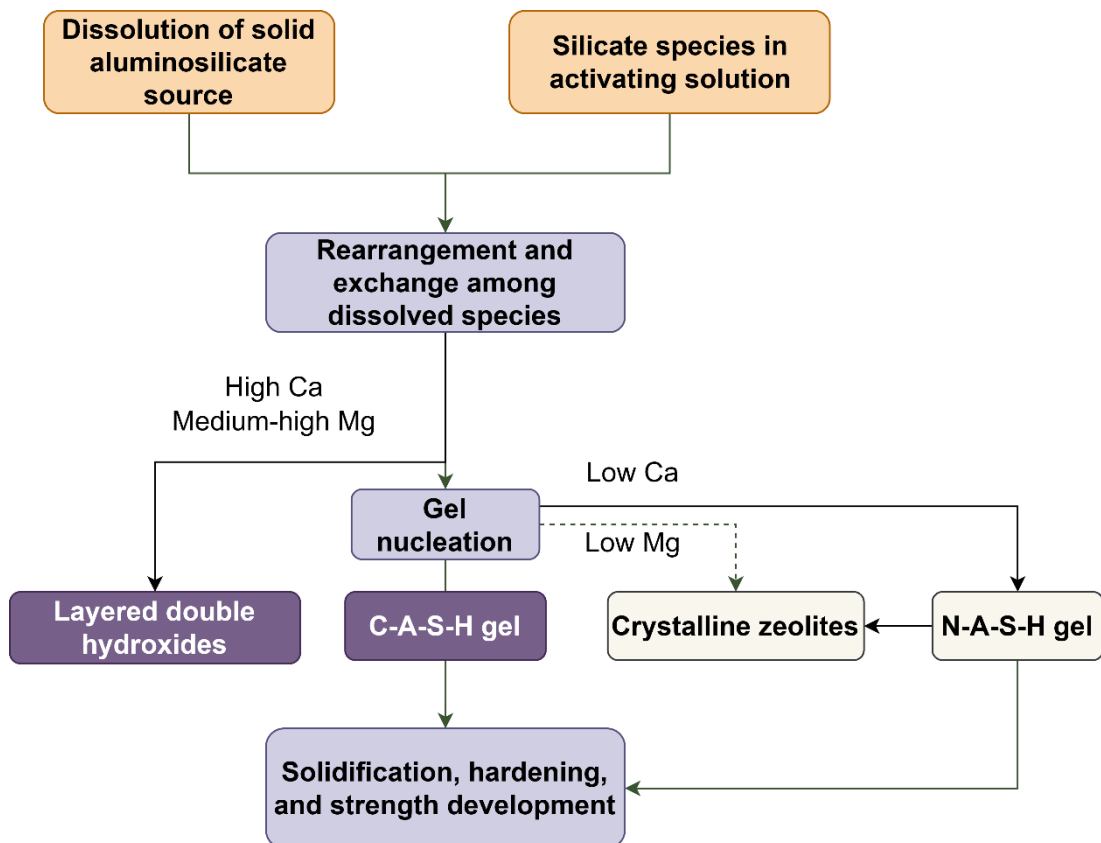


Fig. 2-2 A schematic of alkali-activated cement or geopolymerization process showing the main phases and intermediate steps.

According to Glukhovsky's model of the alkali activation process, the alkali activation consists of three stages. Initially, in the destruction-coagulation stage, Si-O-Si, Al-O-Al, and Si-O-Al bonds are dissociated from the source material. Secondly, in the coagulation-condensation stage, the dissociated products interact mutually to form a coagulated structure and undergo polycondensation. Finally, condensation-crystallisation takes place, where solid and microparticles interact and condense to form a solid phase [45]. Davidovits further developed Glukhovsky's model to describe the geopolymer process. Davidovits model described the mechanism of the alkali-activation reaction as being similar to a Zeolite formation process. Subsequently,

Fernandez-Jimenez and Palomo extended Davidovits' model for FA-based alkali-activated materials. Both specify the first stage as nucleation, where the aluminosilicate source interacts with an alkali solution, inducing the dissolution of the amorphous phase present in the solid material to release aluminates and silicates. The subsequent stage depends on thermodynamic and kinetic parameters, which are different from Gluhovsky's first two stages. The monomers released during the first stage subsequently interact with each other to form dimers, which in turn react mutually to form trimers and tetramers to form a three-dimensional, solid aluminosilicate network [25,46].

Today, the widely accepted FA/metakaolin based AAMs envisages the initial formation of aluminium rich (Si/Al ratio \cong 1-1.3) N-A-S-H gel (alkaline-aluminosilicate hydrate). As the reaction continues, the release of Si-O groups increases to the system. The Zeolite precursor or N-A-S-H gel present in the system reacts with silicon groups to form a hardened gel (Si/Al ratio \cong 2). The hardened gel exhibits substantial mechanical strength [46].

Al species present in the precursor material plays a vital role in the reactivity of AAMs. This is because of the rapid dissolution of Al species or Al-O interactions. It has been reported that Al-O interaction is weaker than Si-O interactions. It has been reported that the reaction kinetics of AAMs is primarily controlled by the amount and dissolution rate of aluminosilicates, which would, in turn, evolve as thermodynamically stable phases. Reactivity, dissolution, and coagulation are quick processes, evaluating these properties at the same time is challenging [46].

To obtain a geopolymer mix that is durable and possesses adequate mechanical strength, it is imperative to understand the effect of precursors, activators, and curing temperature on alkali activation and reaction products. The subsequent sections discuss the formation of reaction products or phases in various AAM systems, the effect of phases on mechanical properties, degradation of phases under durability conditions and decrease in mechanical properties after the degradation of phases.

2.1 Type of precursors and their alkali-activation products

Over the past few decades, researchers have used several precursors to develop alkali-activated materials (AAMs). Ground granulated blast furnace slag (GGBFS), FA,

metakaolin and their blends are widely used precursor materials in the field of alkali-activated cements. A range of activator solutions has been combined with these precursors to produce AAMs with substantial mechanical properties. The mechanical properties depending on the materials used during the time of activation such as precursor ratios, curing conditions, activator type and concentration, influence the formation and stability of phases or reactions products of AAMs. The subsequent sections discuss the formation of phases in different alkali-activated systems. Effect of different precursors, activators, and dosage of activators on phase formation and mechanical properties.

2.1.1 Alkali-activated slag (AAS)

Alkali-activated slag or AAS cements are produced by activating slag or GGBFS with different activators such as NaOH, Na₂SiO₃, Na₂CO₃ and KOH. Alkali-activated slag cement is considered an alternative to OPC. AAS has advantages over OPC such as high and rapid strength development and resistance to chemical attack [47,48]. The formation of calcium silicate hydrate/calcium aluminosilicate hydrate (C-S-H/C-A-S-H) gel is observed as the major reaction product in the alkali-activated slag materials.

The initial stages of hydration of AAS include the dissolution of calcium from slag. Concomitantly, activator content in AAS facilitates the dissolution of Al and Si from the slag and subsequently followed the precipitation of C-S-H/C-A-S-H gel with partial substitution of Al for Si in the final reaction product. Irrespective of the activator used, C-S-H gel with a low Ca/Si ratio is the main reaction product in alkali-activated slag materials. In NaOH activated AAS, disordered C-S-H(I) was observed at the initial stages of activation. In Na₂SiO₃ activated AAS, the C-S-H gel remained disordered after one year of curing [47,48].

Minor traces of crystalline compounds such as merwinite, gehlenite, quartz, calcite, gypsum, and akermanite were detected in slag before alkali activation [18,49–52]. Fig. 2-3 shows the X-ray diffractograms of slag before and after activation cured for 8 days, 14 days and 3 years. The AAS with NaOH (4M) and Na₂SiO₃ (2M) developed C-S-H as the major reaction product after 28 days of curing. With an increase in the curing time, the intensity of the peak attributed to the calcium silicate hydrate (C-S-H) gel increased. Along with the C-S-H gel, other phases like gehlenite (Ca₂Al(AlSiO₇)), gismondine (CaAl₂Si₂O₈·4(H₂O)), thomsonite (NaCa₂[Al₅Si₅O₂₀]·6H₂O), katoite

($\text{Ca}_3\text{Al}_2[\text{Si}(\text{OH})_4]_3$), calcite (CaCO_3), dicalcium silicate hydrate, tobermorite and hillebrandite ($\text{Ca}_6\text{Si}_3\text{O}_9(\text{OH})_6$), and vaterite (CaCO_3) were observed. Other than C-S-H, the early formation of hydrotalcite ($\text{Mg}_6\text{Al}_2\text{CO}_3(\text{OH})_{16}\cdot 4\text{H}_2\text{O}$) was observed in AAS specimens with high MgO content. Also, hydrated calcium aluminate (AFm) ($[\text{Ca}_2(\text{Al,Fe})(\text{OH})_6]\cdot \text{X}\cdot x\text{H}_2\text{O}$) phases were observed in AAS specimens. The high-temperature curing of AAS systems confirmed the presence of sodium silicate hydrate (N-A-S-H) and tobermorite structures in alkali-activated slag systems at 150 °C [53]. The intensities of the peaks of phases such as gismondine are higher in 14 days cured specimens. The phases from 3-year cured AAS specimens showed Ca/Na aluminosilicates with a zeolitic structure such as thomsonite [54]. The hydrothermal curing condition led to the partial conversion of gismondine to alumina-rich thomsonite. Besides, the presence of metastable phases such as calcite, the 14-day cured specimens showed the formation of vaterite in 3 years cured specimens, which indicates the initial stages of carbonation in binder specimens. Also, the presence of katoite/siliceous hydrogarnet ($\text{Ca}_3\text{Al}_2[\text{Si}(\text{OH})_4]_3$) and albite ($\text{Na}(\text{AlSi}_3\text{O}_8)$) were observed in 3-year cured AAS specimens activated with Na_2SiO_3 . High silica content present in the system leads to the formation of katoite instead of AFm phases [18].

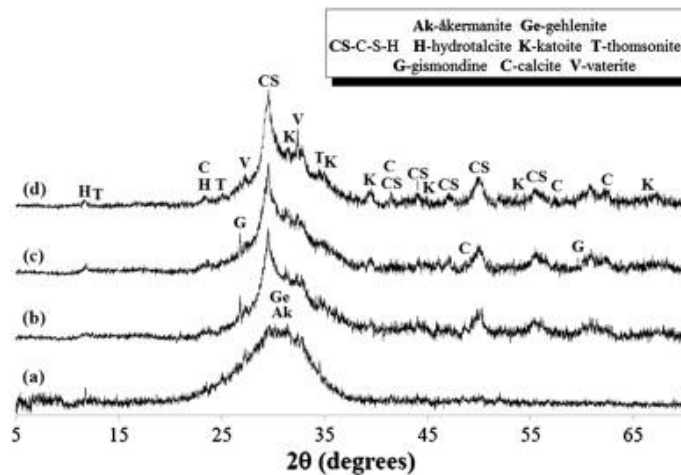


Fig. 2-3 X-ray diffractograms of (a) unreacted slag, and unexposed alkali-activated slag after (b) 8 days, (c) 14 days, and (d) 3 years of curing [55].

The alkali-activated slag activated with varying concentrations of NaOH and Na_2SiO_3 ($M_s = 1.6, 2.0,$ and 2.4) exhibited the formation of phases like gehlenite ($\text{Ca}_2\text{Al}(\text{AlSiO}_7)$) in AAS with $M_s = 2.4$, C-S-H and aluminosilicate zeolite gismondine ($\text{CaAl}_2\text{Si}_2\text{O}_8\cdot 4(\text{H}_2\text{O})$). The low pH and high soluble silica content during the time of activation lead to the formation of C-S-H and gismondine in these binder mixes.

Sodium ions dissolved during the activation resides in the pore solution or non-crystalline reaction products [49]. The decrease in M_s content increases the concentration of NaOH in the binder system and increases the pH during the activation. Hence, the phases such as sodium-calcium silicate hydrate (Na-C-S-H/N-A-S-H) were favoured in the specimens activated with $M_s=2.0$.

The effect of alumina (Al_2O_3) content on the compressive strength is shown in Fig. 2-4. The slag with high alumina and low alumina content (7.0wt.%, 14.1wt.%, and 16.7wt.%) were activated with NaOH and Na_2SiO_3 . The high Al_2O_3 content slightly slowed the hydration reaction in both NaOH and Na_2SiO_3 activated mixes. At the end of 28 days, a similar degree of the reaction was observed in AAS specimens activated with NaOH and Na_2SiO_3 . Regardless of Al_2O_3 content in slag, the compressive strength of AAS in specimens activated Na_2SiO_3 specimens showed higher compressive strength and low porosity [56]. The formation of C-S-H gel in AAS with high and low alumina content activated with NaOH is shown in Fig 2-5 and Fig. 2-6. A thin layer of C-S-H gel formation around slag particles was observed at the initial stages with the formation of hydrotalcite platelets. The formation of hydrotalcite was also higher in high alumina AAS specimens [56].

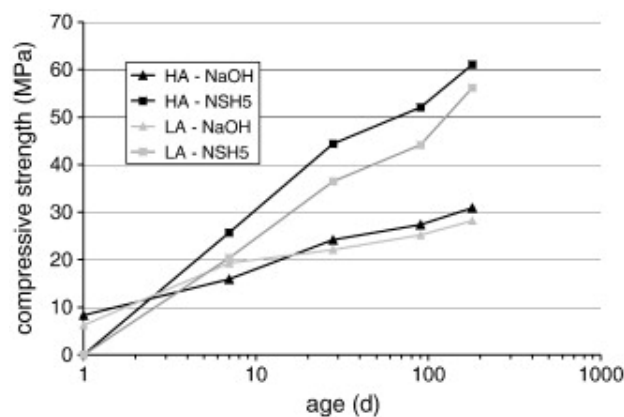


Fig. 2-4 Compressive strength development in the different alkali-activated systems [56].

The varying concentrations of Al_2O_3 in slag slows the rate of hydration reaction in AAS during the initial stages of the alkali activation. Regardless of alumina content, the coarse porosity in Na_2SiO_3 -activated AAS specimens was lower compared with NaOH-activated AAS specimens for the same curing period. Also, higher alumina content in slag increased the Al uptake and influences the Al/Si ratios in C-S-H gels.

The Al/Si ratios in C-S-H gel increased from 0.11 to 0.3 in slag with 17wt.% alumina content. At the initial stages, the Mg/Al ratio was ~2 for AAS with 17wt.% alumina content, the Mg/Al ratio decreased to 1.3 at the end of 1 year of curing [57]. The variations in Al content influenced the Mg/Al and Al/Si ratios in reaction products and the formation of phases such as C-S-H, hydrotalcite and strätlingite ($\text{Ca}_2\text{Al}_2\text{SiO}_7 \cdot 8\text{H}_2\text{O}$).

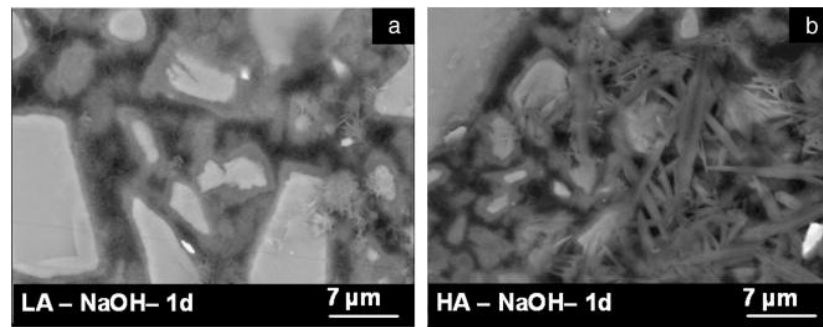


Fig. 2-5 Microstructure of NaOH activated slag at early ages of curing showing the C-S-H layer around the slag particles as well as platelets of hydrotalcite. (a) Low alumina slag with NaOH, and (b) High alumina slag with NaOH [56].

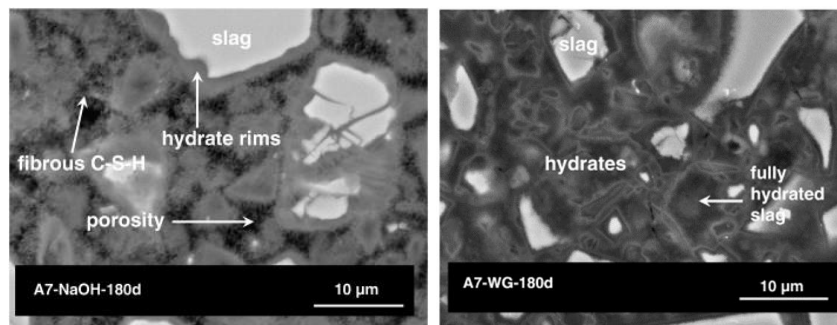


Fig. 2-6 SEM images of AAS activated with NaOH and Na_2SiO_3 at later stages [57].

The effect of MgO content (6.4wt.%, 6.6wt.%, and 7.2wt.%) on the hydration of AAS activated with NaOH and Na_2SiO_3 showed the phases such as C-S-H, magnesium-rich layered double hydroxides, gismondine ($\text{CaAl}_2\text{Si}_2\text{O}_8 \cdot 4(\text{H}_2\text{O})$), and garronite ($\text{Na}_2\text{Ca}_5\text{Al}_{12}\text{Si}_{20}\text{O}_{64} \cdot 27\text{H}_2\text{O}$) [51,52,59]. The formation of phases such as gismondine and garronite in AAS specimens, the formation of gismondine was favoured in systems with activator concentrations, the increase in the activator dosage (15 wt.% Na_2O) or pH during alkali activation suppress the formation gismondine and favours the Na/Ca exchange process to develop garronite phases [59].

The varying concentrations of MgO (7.7 wt.%, 10.5 wt.% and 13.2 wt.%) on compressive strength and porosity of NaOH and Na₂SiO₃ activated AAS is shown in Fig. 2-7. The specimens activated with Na₂SiO₃ low hydration compared with NaOH activated specimens at initial stages. The compressive strength results showed a similar trend, where the compressive strength of NaOH activated specimens were lower compared with sodium silicate activated AAS specimens. The samples with low MgO content activated with Na₂SiO₃ showed lower heat of hydration and compressive strength at early ages. At later stages, a similar degree of hydration was observed in all mixes with varying MgO contents. Irrespective of MgO contents in slag, the NaOH activated specimens showed the same level of hydration and compressive strength at all stages. The Na₂SiO₃ activated specimens showed comparatively higher compressive strength values compared with NaOH specimens. Also, the AAS specimens with high MgO content activated with Na₂SiO₃ showed higher compressive strength and lower porosity. The compressive strength is also a function of porosity. The Na₂SiO₃ activated specimens showed significantly lower porosity which led to higher compressive strength in AAS specimens. The increase in the formation of magnesium-based hydrates in AAS with high MgO contents reduced the overall porosity by 50-80% and enhanced the compressive strength.

The SEM images of AAS specimens activated with NaOH and sodium silicate with 13wt.% MgO cured for 1 year is shown in Fig. 2-8. NaOH activated AAS specimens have denser C-S-H gels with more pores compared with AAS specimens activated with sodium silicate solution. Besides, the reaction products were more homogenous in sodium silicate activated AAS specimens. The AAS specimens with higher MgO content has less porosity and less unreacted slag grain compared with AAS specimens with low MgO content [60]. This indicates that the MgO and Na₂SiO₃ in AAS favour the formation of secondary reaction products such as hydrotalcite. The formation of hydrotalcite reduces the overall porosity and enhances the compressive strength of AAS.

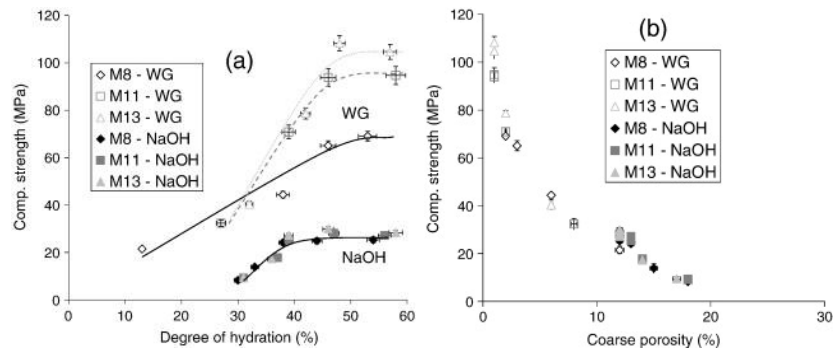


Fig. 2-7 Compressive strength of the pastes vs. (a) degree of hydration and (b) coarse porosity of AAS activated with NaOH and Na_2SiO_3 [60].

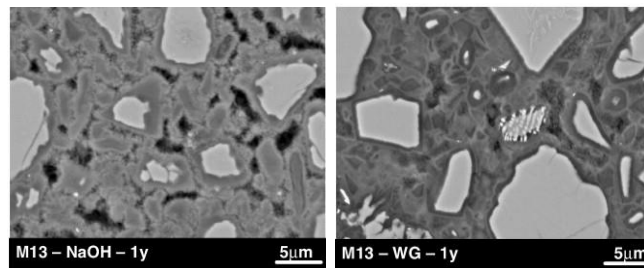


Fig. 2-8 SEM-image of NaOH and Na_2SiO_3 activated slag with 13wt.% of MgO after 1 year [58].

Regardless of activator type, concentration, and curing regime, the alkali activation of slag favoured the formation of C-S-H/C-A-S-H gel as the primary reaction product, which significantly contributed to the mechanical and durability properties of the AAS materials. An increase in activator concentration facilitated the formation of N-A-S-H gel as the secondary reaction product along with the C-S-H. The concentration of activators favoured the partial substitution of Al in C-S-H gels, which led to the formation of C-A-S-H phases. The presence of higher Al_2O_3 favoured the formation of strätlingite with an increase in Al content in C-S-H gel and higher MgO content favoured the formation of hydrotalcite with higher Mg/Al content. The Na_2SiO_3 activated AAS showed significantly higher compressive strength and lower coarse porosity compared with NaOH activated AAS. Other than C-S-H, gismondine, garronite, thomsonite, gehlenite, AFm and katoite are some of the reaction products found in AAS systems. However, the effects of durability conditions on these reaction products and phase transformation of these reaction products are discussed in subsequent sections. Polymorphs of calcite such as vaterite and aragonite are the by-products of surface carbonation in alkali-activated slag materials.

2.1.2 Alkali-activated fly ash (AAFA)

Alkali-activated fly ash or AAFA cements are produced by activating FA with different activators such as NaOH, Na₂SiO₃, Na₂CO₃ and KOH. AAFA cement is considered an alternative to OPC. AAFA cements are famous for their durability properties. The formation of sodium aluminosilicate hydrate (N-A-S-H) gel is observed as the major reaction product in the AAFA system.

The hardened AAFA materials possess adequate mechanical properties, which are useful construction materials. The widely accepted reaction mechanism of AAFA is as follows. Initially, the aluminosilicate precursor (FA) dissolves in an alkali solution, through the scission of Si-O-Si, Al-O-Al, and Al-O-Si bonds in the aluminosilicate precursor. Concomitantly, complexes and polymerized species of Si-O-Na, Si-O-Ca-OH, Al(OH)₄, Al(OH)₂₅, and Al(OH)₃₆ are formed during the activation. Subsequently, a condensation reaction takes place, where dissolved species forms a coagulated structure [61] or N-A-S-H gel, at later stages of the reaction, N-A-S-H gel will evolve as a three-dimensional pseudo zeolitic structure that resembles the zeolitic structure. This section discusses the parameters such as type of activators, the dosage of activators, and curing temperature that affects mechanical properties and reactions products in the AAFA system.

The XRD patterns of fly ash and AAFA specimens activated with varying amounts of silicate and Na₂O cured at 40 °C for 28 days are shown in Fig. 2-9 and Fig. 2-10. The raw fly ash showed phases such as mullite and quartz. When cured for 28 days, the AAFA specimens activated with various SiO₂ content showed N-A-S-H based reaction products such as hydroxysodalite (Na₄Al₃Si₃O₁₂(OH)) and faujasite (Na_{1.84}Al₂Si₄O_{11.92}·H₂O). In AAFA specimens with varied Na₂O concentrations, only faujasite was observed as a reaction product [62]. The high-temperature curing of AAFA specimens activated with NaOH+Na₂SiO₃ solutions favoured the formation of hydroxysodalite and amorphous aluminosilicate gels were observed after elevated temperature curing. Hydroxysodalite phases started disappearing as the nepheline phases were observed at 800 °C. At 1000 °C exposure, jadeite (NaAlSi₂O₆) was observed. At 1200 °C exposure, NaAlSi₂O₆, albeite (NaAlSiO₈) and Na-feldspars (AlNa(SiO₄)) was observed. The use of potassium-based activators such as KOH and K₂SiO₃ solutions favoured the formation of phases such as kalisite (KAlSiO₄) and

leucite (KAlSi_2O_6) after activation [63]. The use of a potassium-based activator led to the formation of potassium aluminosilicate hydrate (K-A-S-H) instead of N-A-S-H gels.

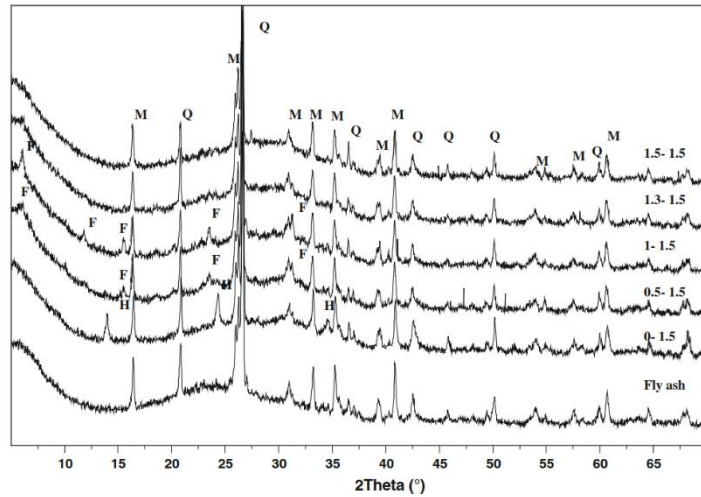


Fig. 2-9 XRD of alkali-activated fly ash with various SiO_2 content Q: quartz (SiO_2), M: mullite ($\text{Al}_{4.8}\text{O}_{9.54}\text{Si}_{1.2}$), H: hydroxysodalite ($\text{Na}_4\text{Al}_3\text{Si}_3\text{O}_{12}(\text{OH})$), F: faujasite ($\text{Na}_{1.84}\text{Al}_2\text{Si}_4\text{O}_{11.92}\text{H}_2\text{O}$) [62]

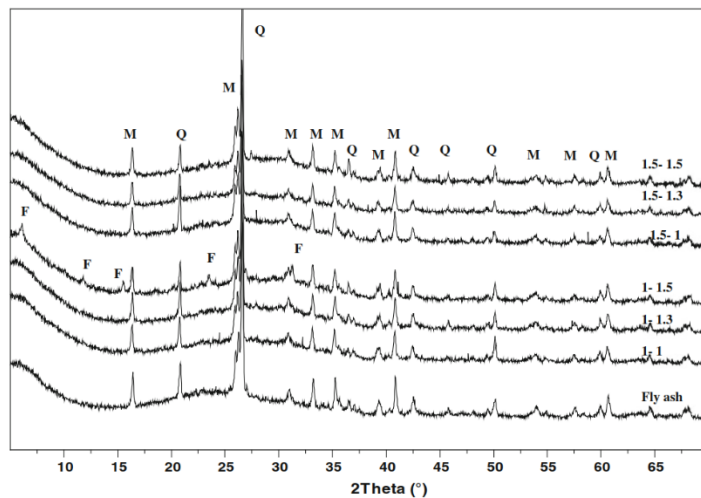


Fig. 2-10 XRD of alkali-activated fly ash with various Na_2O contents, Q: quartz (SiO_2), M: mullite ($\text{Al}_{4.8}\text{O}_{9.54}\text{Si}_{1.2}$), F: faujasite ($\text{Na}_{1.84}\text{Al}_2\text{Si}_4\text{O}_{11.92}\cdot 7\text{H}_2\text{O}$) [62]

The SEM images of AAFA specimens at various stages of alkali activation is shown in Fig. 2-11 and Fig. 2-12. It can be observed in Fig. 2-12 that the deterioration of spherical FA particles under dissolution at 85°C temperature. The Si and Al species from the FA spherical particles dissolve and interact with the Na ions of activators. The dissolution of Al and Si from FA increases Si/Al ratios in N-A-S-H gel which leads to the enhancement of mechanical properties of AAMs. The degree of reaction

at this stage was 45.35% (Fig. 2-13), with a Si/Al ratio of 1.6 and an N-A-S-H phase was observed at this stage. With an increase in curing time, the reaction progresses, the formation of zeolitic products and the complete disappearance of FA spheres can be observed (Fig. 2-11 and Fig. 2-12). The degree of reaction after 20 h curing was observed to be increased at 50% with the Si/Al ratio of 1.8-2.0 [64]. The elevated curing condition accelerates the reaction kinetics, as the curing time increases the Si/Al ratio in the reaction products increases, indicating higher Si content in reaction products. Thus, an increase in Si content in the AAFA reaction products enhances mechanical properties.

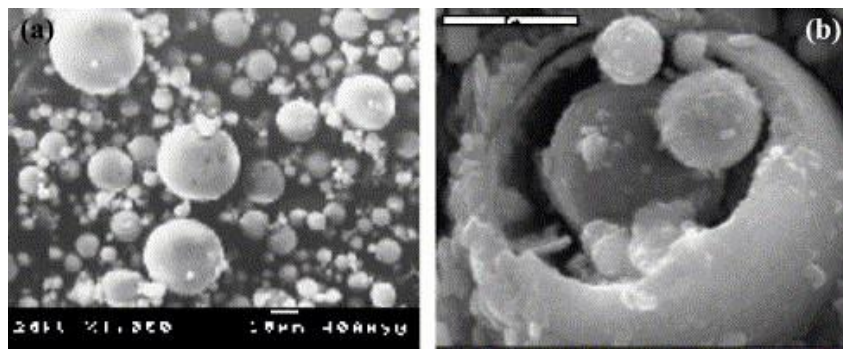


Fig. 2-11 SEM pictures: (a) raw FA, (b) FA activated with 8 M NaOH for 5 h at 85 °C [64]

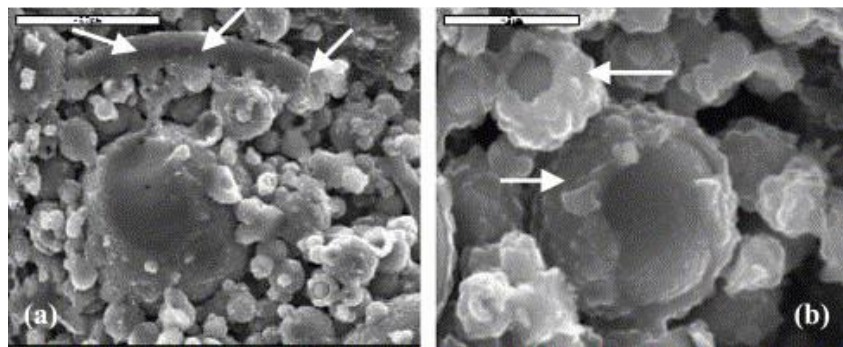


Fig. 2-12 SEM pictures. FA activated with 8 M NaOH for 20 h at 85 °C; (a) reaction process of a large sphere, (b) singular details of the reaction of some small spheres [64].

The evolution of mechanical strength and rate of strength gaining of AAFA specimens as a function of curing time is shown in Fig. 2-13 and Fig. 2-14. The increase in temperature accelerates the rate of reaction concomitantly with an increase in compressive strength of AAFA specimens [61]. The AAFA specimens cured at 85 °C showed a significant increase in mechanical strength compared with AAFA specimens cured at 65 °C and 45 °C within the first 25 h of activation. Regardless of the

temperature after 25 h showed a similar trend in strength gain in the specimens cured at different temperatures. The significant amount of dissolution of Si and Al from FA at higher temperatures accelerates the rate of reaction and increases the number of reaction products in AAFA specimens, which would contribute to the mechanical strength gain of AAFA specimens.

The ^{29}Si and ^{27}Al MAS-NMR spectra of raw FA are shown in Fig. 2-15 (A). In ^{29}Si environments, five peaks were detected at -83, -91.8, -96.9, and -103 ppm, which indicate the presence of vitreous material in FA. The peak at -87.4 ppm indicates the presence of mullite and peaks at -109.3 and -114 ppm indicate the distinct silica phases. The dissolution of raw FA in hydrogen fluoride dissolves the reactive components and leaves behind the inert components of FA (Fig. 2-15 (B)). After hydrogen fluoride attack the ^{29}Si environment showed two peaks at -87.3 and -90.5 ppm indicating the presence of mullite and a distinct peak at -109.1 ppm was observed indicating the presence of quartz, with a broad peak at -100.6 ppm indicating the presence of unreacted FA. Fig. 2-15 (C) shows a ^{27}Al environment of FA, showing two peaks centred at 51.6 ppm indicating the presence of tetrahedral aluminium and a peak at 1 ppm indicating octahedral aluminium [61]. The MAS-NMR study indicates the presence of reactive Si and Al peaks in raw FA. During the alkali activation, the reactive Si and Al dissolve and new peaks evolve indicating the formation of reaction products.

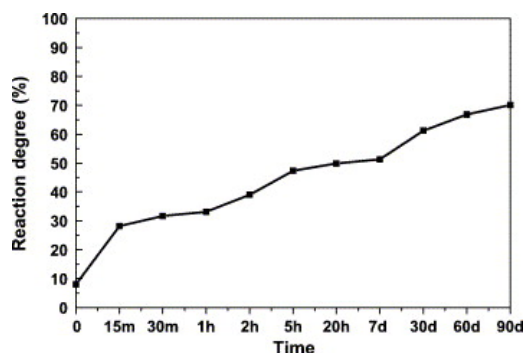


Fig. 2-13 Evolution of the reaction degree of FA activated with an 8 M NaOH dissolution. Curing temperature: 85 °C [64].

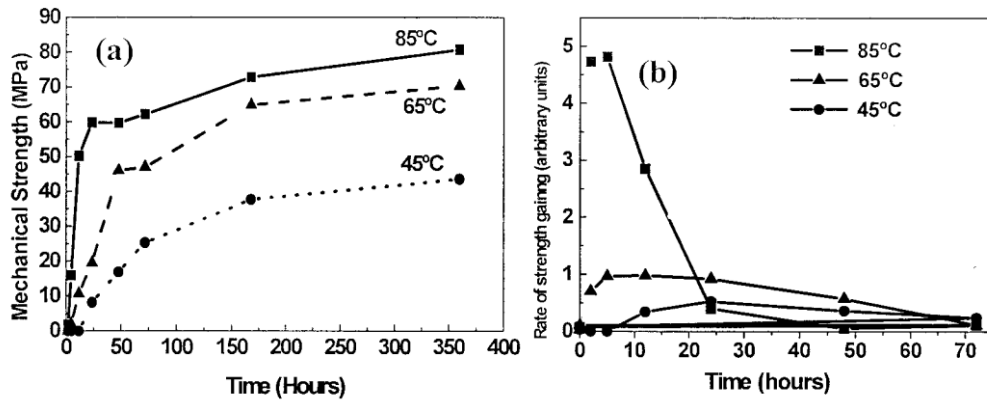


Fig. 2-14 (a) Evolution of the mechanical strength of the activated FA mortars as a function of time; (b) rate of mechanical strength gaining. Mortars were cured in the stove for (2, 5, 12, and 24 h) at 45°, 65°, and 85°C, and then were kept at $23 \pm 1^\circ\text{C}$ and 95% relative humidity for 1, 2, 3, 7, and 15 d [61].

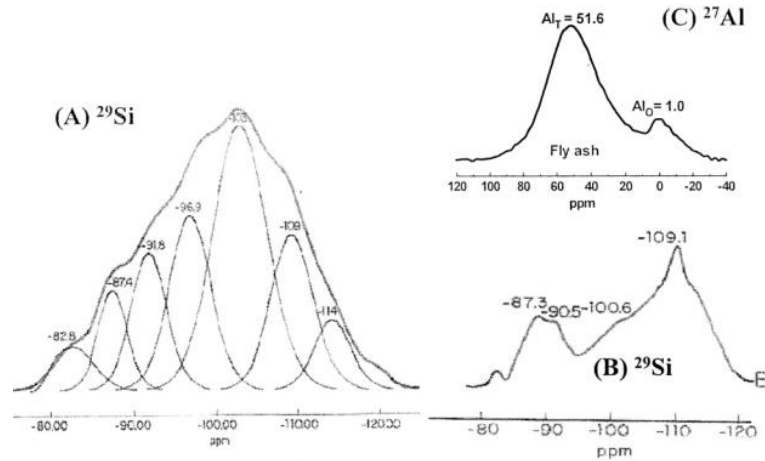


Fig. 2-15 ^{29}Si NMR spectrum of (A) original FA, and (B) FA attacked with HF, and (C) ^{27}Al NMR spectrum of original FA [61].

MAS-NMR spectra of AAFA specimens activated at 85°C with NaOH for 5h and a week is shown in Fig. 2-16. Changes were observed in the ^{29}Si environment, the main peak (Fig. 2-16(B)) appears at -86.7 ppm indicating the formation of tectosilicate rich in aluminium. Additional signals at -96.8, -103.3 and -109.2 ppm were detected indicating the formation of unreacted FA and a low degree of reaction ((Fig. 2-16(C) and Fig. 2-16(D)).

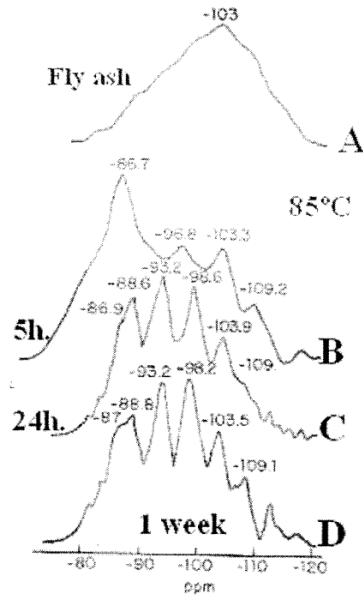


Fig. 2-16 ^{29}Si MAS-NMR spectra of (A) the original FA; (B) alkali-activated FA 5 h at 85°C ; (C) 24 h at 85°C ; and (D) 1 week at 85°C [61].

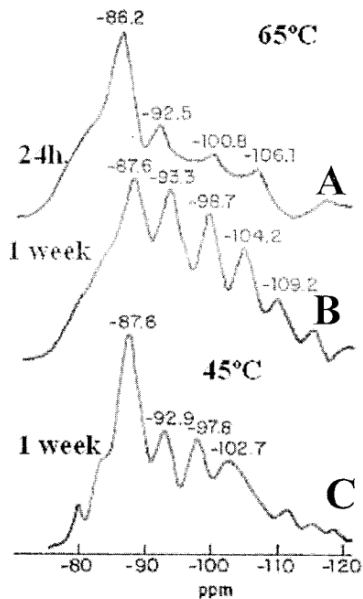


Fig. 2-17 ^{29}Si NMR MAS spectra of the alkali-activated FA at (A) 24 h at 65°C , (B) 1 week at 65°C , and (C) 1 week at 45°C [61].

The AAFA specimens activated at 65°C for 24 h, 65°C for 1 week and 45°C for 1 week is shown in Fig. 2-17. Five peaks were detected at -88.8, -93.2, -98.2, -103.5, and -109.1 ppm indicating the dissolution of Si and Al from FA and increase in Si and Al content in hardened binder specimens after 1 week (Fig. 2.17(B)). However, The intensity of the signals at 93.2, -98.2, -103.5, and -109.1 ppm were lower in AAFA specimens cured at 45°C (Fig. 2-17(C)) and the intensity of the peak at -87 ppm

increases indicating the presence of a higher fraction of mullite in unreacted FA [61]. This indicates that high-temperature curing increases the dissolution of Al along with the increasing rate of reaction, hence increasing the amount of reaction products after activation.

The curing time and activator concentration favoured the formation of different zeolite phases such as hydroxysodalite after activation in AAFA specimens activated with 7wt.% Na₂O content and with a Si/Al=1.0, at Si/Al=2.0, phases such as Na-chabazite or herschelite ((Na₂,K₂,Ca,Sr,Mg)₂[Al₂Si₄O₁₂]₂·12H₂O) was formed. However, the amount of hydroxysodalite remained unchanged with the increase in curing time and the amount of herschelite kept growing as the silica content in the AAFA system increased. Further curing time increases the Si/Al ratio and zeolite Y phases were observed at Si/Al =2.4 (Na_{1.88}Al₂ Si_{4.8} O_{13.54}·9H₂O), and zeolite P phases were observed after 180 days of curing with Si/Al=3.4. The formation of different zeolitic phases or precursors such as N-A-S-H, hydroxysodalite and chabazite form stable zeolitic structures such as analcime (Na(AlSi₂O₆)·H₂O). Further increase in the Si/Al ratio hindered the formation of zeolitic structures in the AAFA system [65]. The increase in soluble silica content decreases the rate of reaction and favoured the formation of herschelite, sodium carbonate and thermonatrite (Na₂CO₃·H₂O) [66,67].

The FA activated with concentrations such as 5, 8 and 12 M NaOH favoured the formation of the chabazite, zeolite (X, 4A and NaP1) and sodalite structures in the AAFA system. However, zeolite X and 4X structures appeared in specimens activated with 5M NaOH. Zeolite NaP1 appeared in the specimens activated with 8 and 12 M NaOH [68,69,70]. The FA activated with only sodium silicate solution led to the formation of distinct types of zeolitic phases in the specimens, which belong to the ABC-6 family consisting of six-member rings. Hydroxycancrinite ([Na₆(OH)₂][Na₂(H₂O)₂](Si₆Al₆O₂₄)), sodalite, levyne, chabazite and offretite (KCaMg(Si₁₃Al₅)O₃₆·15H₂O) are some of the identified phases in the study [71]. The phases such as cancrinite (Na₈(Si₆Al₆O₂₄)(H_{0.88}(CO₃)_{1.44})(H₂O)₂) and franzinite ((Na, Ca)₇(Si, Al)₁₂O₂₄(SO₄, OH, CO₃)₃·H₂O) in the specimens cured at 20 °C for 365 days. Apart from these, the levyne (Ca (Al₂Si₄O₁₂) ·6H₂O) phase was also present in specimens cured at 60 °C for 365 days [72].

AAFA system primarily exhibited the N-A-S-H based phases such as hydroxysodalite, faujasite, NaP1 zeolites and analcime. The formation of the reaction products in the AAFA system showed a strong dependence on the nature of the precursor, Na₂O type, Na₂O concentration and curing temperature. The elevated curing accelerated the rate of reaction and increased the mechanical properties of the AAFA system. Similar to other alkali-activated systems, AAFAs also show adequate mechanical properties and resistance to durability properties such as carbonation. However, the effect of Al₂O₃, MgO, and Fe content on the reaction products of AAFA is still unexplored.

2.1.3 Alkali-activated metakaolin (AAMK)

Metakaolin powder is obtained by calcination kaolin powder at 900 °C, which is rich in Si and Al. The alkali activation of metakaolin can be categorised into two stages, i.e., the first stage involving the dissolution of silicate and aluminate monomers, and the second stage involving the dissolved silicate and aluminate monomers mutually interacting and developing as aluminosilicate oligomers. These oligomers favour the formation of geopolymeric phases. The concomitant reactions of geopolymeric phases lead to the cross-linkage of Al and Si tetrahedral units to form inorganic geopolymer gels, which resembles a pseudo zeolitic structure [73].

XRD patterns of raw metakaolin and AAMK specimens activated with varying concentrations of NaOH solution is shown in Fig. 2-18 and Fig. 2-19. Minor traces of quartz, kaolinite and halloysite was observed in the metakaolin before activation. After activation, there was a shift in the broad peak from 15-35° to 40° and the weakening of peaks attributed to kaolinite and halloysite indicate the geopolymerization reaction and formation of amorphous phases in these systems. With an increase in NaOH concentration, new phases such as hydroxysodalite and zeolite A was observed (Fig. 2-19), indicating a higher degree of reaction in these systems [73]. Minor traces of sodium carbonate were observed in AAMK specimens, which is the result of superficial carbonation.

FTIR spectra of raw metakaolin and AAMK specimens activated with varying NaOH concentrations is shown in Fig. 2-20. In raw metakaolin, the bands at 465 cm⁻¹ are attributed to (T = tetrahedral Al or Si) bending vibrations in TO₄ tetrahedra.

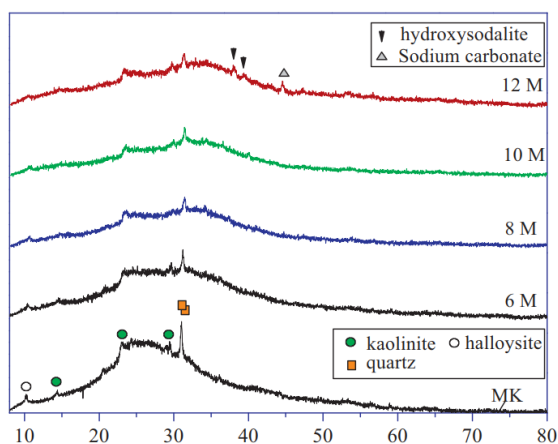


Fig. 2-18 XRD patterns of AAMK after activation with NaOH solution of 6–12 mol/L at 30 °C for 72 h (kaolinite, $\text{Al}_2\text{Si}_2\text{O}_5(\text{OH})_4$; halloysite, $\text{Al}_2\text{Si}_2\text{O}_5(\text{OH})_4 \cdot 2\text{H}_2\text{O}$; quartz; hydroxysodalite, $\text{Na}_8\text{Al}_6\text{Si}_6\text{O}_{24}(\text{OH})_2 \cdot 2\text{H}_2\text{O}$; sodium carbonate, Na_2CO_3) [73].

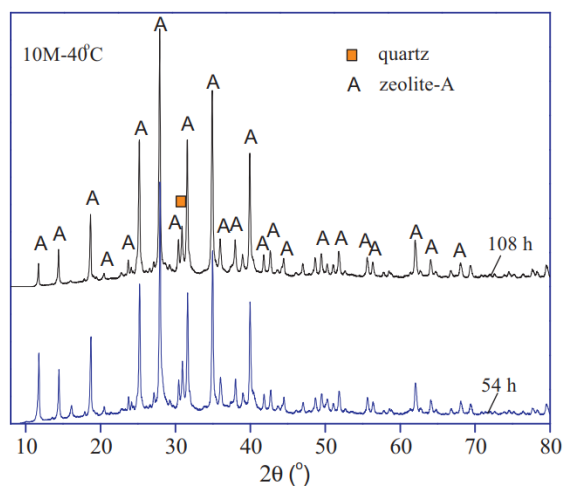


Fig. 2-19 XRD patterns AAMK activated with NaOH solution 10 mol/L at 40 °C (zeolite A, $\text{Na}_{96}\text{Al}_{96}\text{Si}_{96}\text{O}_{384} \cdot 216\text{H}_2\text{O}$) [73].

The band at 800 cm^{-1} is assigned to the bending of octahedral Al in metakaolin. After geopolymerization, the intensities of the aforementioned bands decrease and the band at 710 cm^{-1} intensifies, indicating the formation of Al[IV] in the Al environment. The band centred at $\sim 600\text{ cm}^{-1}$ indicates the T=O vibration in double rings of zeolite precursors. The increase in alkali activator concentration such as 10M NaOH formed a new peak at 557 cm^{-1} , indicating the vibrations in double rings in zeolites A. The shift in broad peak from $\sim 1080\text{ cm}^{-1}$ in MK to $\sim 1000\text{ cm}^{-1}$ indicates the presence of silica-rich geopolymer product. The bands at 1440 cm^{-1} are attributed to the bending of O-C-O bonds of CO_3^{2-} , which is the result of natural carbonation. After alkali activation, two new bands appeared at $1005\text{--}990\text{ cm}^{-1}$ and $960\text{--}944\text{ cm}^{-1}$ and $960\text{--}944\text{ cm}^{-1}$ which

are attributed to the asymmetric stretching vibrations of Si-O-T bonds in aluminosilicate network and asymmetric stretching of Si-O-Na non-oxygen bridging sites [73].

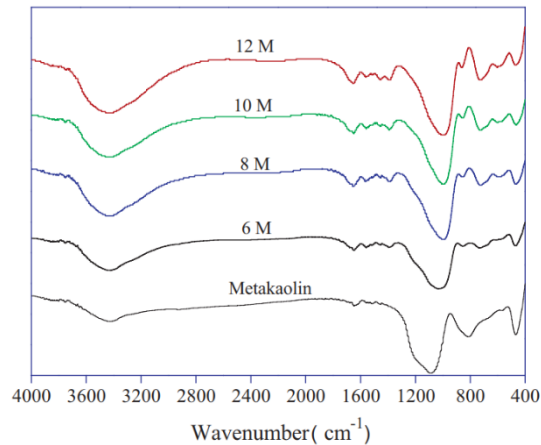


Fig. 2-20 FTIR spectra of MK and the geopolymerization products after activation with NaOH solution at 30 °C for 72 h. [73].

The SEM images of fractured surfaces of AAMK specimens activated with varying concentrations of NaOH is shown in Fig. 2-21. With an increase in NaOH concentration metakaolin particles transformed into a porous, particulate phase and showed a platelike morphology. These images indicate the formation of zeolites in AAMK specimens with low Si/Al ratios [74].

The compressive strengths of AAMK specimens after 24h and 72 h are shown in Fig. 2-22. Because of the rapid setting of metakaolin, it gains strength within 24 h of reaction. In binder specimens with $M_s=1.2$ shows the increase of compressive strength values from 22 MPa to 40 MPa within 72 h of activation. However, mechanical properties are a function of several factors such as gel/metakaolin, alkali content, cross-linking and compaction during the time of binder preparation [74].

Metakaolin specimens blended with amorphous Al_2O_3 and silica and activated with NaOH led to the formation of phases such as gibbsite ($Al(OH)_3$), sodium aluminosilicate hydrate and thermonatrites at higher alumina content Si/Al=0.5. As the silica content in the alkali-activated system increased from 0.5 to 2, the number of amorphous phases in the AAMK system increased. At Si/Al = 2.0, a crystalline zeolitic phase was observed [75].

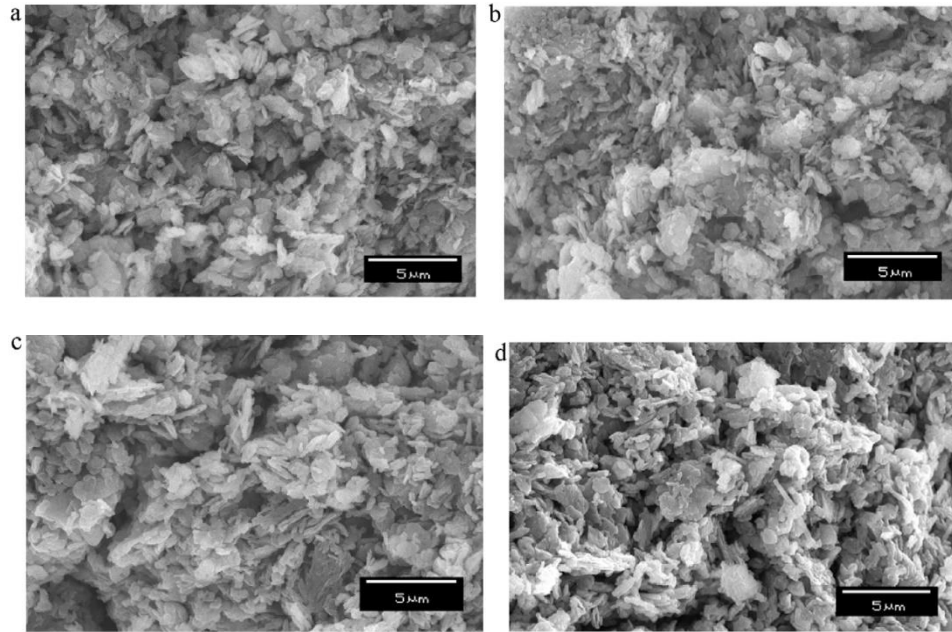


Fig. 2-21 SEM micrographs of the fracture surfaces of geopolymerization products of MK activated with NaOH solution: (a) 6 mol/L, (b) 8 mol/L, (c) 10 mol/L and (d) 12 mol/L. [74].

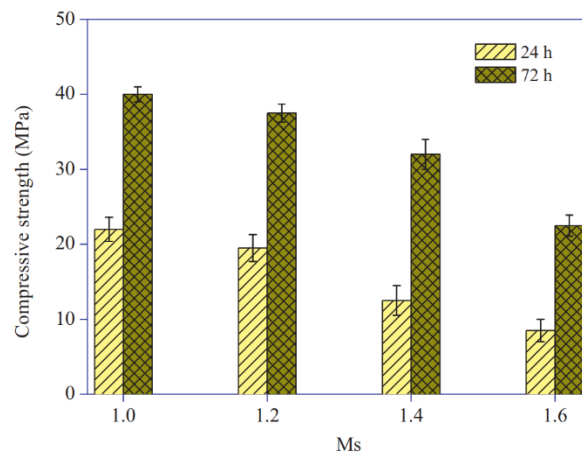


Fig. 2-22 Compressive strengths of hardened binders synthesized with liquid/solid ratio of 0.65 mL/g at 25 °C [74].

The elevated temperature curing on AAMK systems favoured the formation of distinct phases after alkali activation. AAMK activated with NaOH+Na₂SiO₃ facilitated the formation of minor traces of hydroxysodalite and zeolite A (Na₉₆Al₉₆Si₉₆O₃₈₄·216 H₂O) at 85 °C curing temperature. As the curing temperature increased from 85 °C to 150 °C, faujasite (Na₂Al₂Si_{2.4}O_{8.8}·6.7H₂O) and zeolite A were observed. At 200 °C, sodalite syn (Na₈Al₆Si₆O₂₄(OH)₂·2H₂O) was detected [76]. The use of KOH+K₂SiO₃ led to the formation of potassium-based phases such as leucite (KAlSi₂O₆) and

kaliophilite (KAlSiO_4) AAMK system at 600-1000 °C. At 1000 °C, minor traces of leucite were observed but the intensity of kaliophilite phase slightly increased. [77,78].

The AAMK systems favour the formation of N-A-S-H or zeolitic products after activation. The high Al content present in metakaolin led to the formation of N-A-S-H with high Al/Si ratios. Also, the faster dissolution of Al from metakaolin accelerates the rate of reaction and strength gain of AAMK specimens.

2.1.4 Blended alkali-activated system.

When the availability of raw precursors for AAM synthesis is limited, precursors like FA/slag are partially incorporated in OPC in the development of high/ultra-high-performance concretes, to enhance the mechanical and durable properties. This limits the potential application of AAM in the construction industry, also the limited supply of raw materials is another impediment in the application of AAMs in the construction industry. The blended AAMs can be produced by blending slag with cost-effective and widely available precursors such as metakaolin and FA. Hence, blended activation systems such as slag-metakaolin, slag-FA and metakaolin-FA are developed as commercially attractive alternative AAMs, with substantial mechanical and durable properties. The structural and durability properties of blended AAMs depend on precursor ratios, type of activators used, activator concentrations and curing conditions [59].

The blending of precursors leads to the simultaneous activation of precursors and facilitates the coexistence of different reaction products after alkali activation. In the activation of the slag-FA system the formation of calcium-sodium-alumino-silicate hydrate or sodium-calcium-alumino-silicate-hydrate (C-(N)-A-S-H/N-(C)-A-S-H) gel can be observed, the amount of the final reaction product depends on the precursor ratio and activator concentration. Because of the blending of different precursors, minor traces of Na-Ca based phases are also observed [59].

2.1.4.1 Alkali-activated slag-metakaolin system (AASMK)

AASMK systems are produced by mixing slag and metakaolin powder in different ratios. The inclusion of metakaolin increases the Al content in the system and enhances the Al content in the final reaction products. Phases such as N-(C)-A-S-H/C-(N)-A-S-H is the major reaction products of AASMK systems.

The blended slag and metakaolin by varying slag content from 0wt.% to 100wt.% with NaOH+Na₂SiO₃. The calcium and aluminium rich phases in the AASMK system were observed after activation. The elemental analyses performed on the aluminosilicate gel showed changes in calcium concentrations in the hydration phases. The decrease in the Al/Si ratio was observed when slag content in the aluminosilicate gel increased. The average aluminosilicate elemental composition of the specimens activated with M_s=2 changed from Na_{0.53}Ca_{0.07}SiAl_{0.46} (20wt.% slag) to Na_{1.1}Ca_{0.5}SiAl_{0.24} (80wt.% slag) and from Na_{0.89}Ca_{0.05}SiAl_{0.46} (20wt.% slag) to Na_{1.7}Ca_{0.25}SiAl_{0.24} (80wt.% slag) for M_s=1.2. In addition to this Na/Si and Ca/Si ratios increased as the metakaolin content decreased in aluminosilicate gel. Thus, excess silicate and lack of aluminium in the alumina-rich phase hindered the formation of the larger oligomer or N-A-S-H formation in the AAM system. Further to this as the Na content increases (M_s = 2.0 to 1.2) in the system, would increase the pH of the activation system, and suppress the formation of C-A-S-H/C-S-H gel initially and promotes the formation of Si/Al-rich N-A-S-H gel. Hence, the excess calcium present in the system precipitate in the form of CaOH₂ and forms C-S-H gel [79].

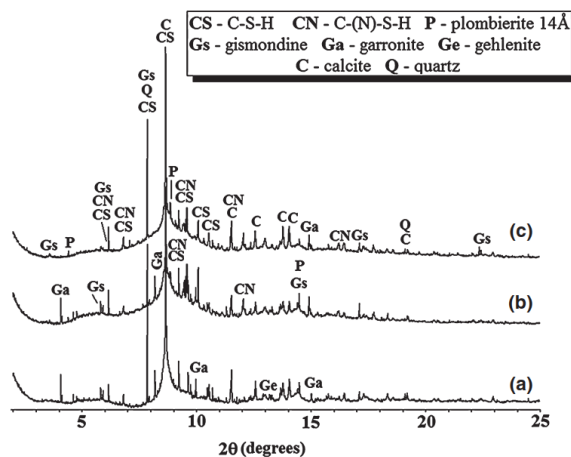


Fig. 2-23 High-resolution synchrotron X-ray diffraction patterns ($k = 0.458\ 879\ \text{\AA}$) of 28-d cured alkali-activated pastes with GBFS/(GBFS + MK) ratios of (A) 1.0, (B) 0.9 and (C) 0.8 [59].

The XRD patterns of AASMK specimens activated with varying GGBFS/(GGBFS + MK) ratios of 1.0, 0.9, and 0.8 is shown in Fig. 2-23. Two distinct calcium silicate-based reaction products were identified after activation. A hybrid (C, N)-A-S-H type gel develops around slag and metakaolin particles and C-A-S-H gel with a low Ca/Si ratio. Along with these phases, the gismondine type zeolitic products were observed in AASMK specimens with higher metakaolin content. The formation of gismondine

phases indicates the reduction in Na^+ content during activation, as Na^+ was consumed by rapid dissolution of metakaolin under activation. The addition of metakaolin also increases Al uptake in C-A-S-H and (C, N)-A-S-H gels [59].

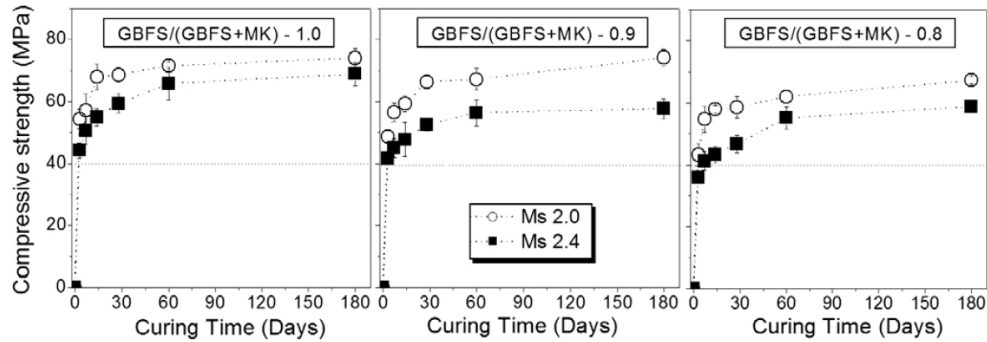


Fig. 2-24 Compressive strength of mortars based on silicate activated GBFS/MK blends [80].

AASMK specimens show a strong dependence on $\text{SiO}_2/\text{Na}_2\text{O}$ ratios. The higher $M_s=2.4$ shows lower compressive strength because of less heat of hydration during activation (Fig. 2-24). The inclusion of metakaolin slightly decreases final mechanical strength. The workability increases with the addition of metakaolin to slag [80].

Ageing or curing time and concentration of alkali in the activator solution influences the phase formation of AASMK binders [59,81]. The increased intensities of phases such as C-S-H, gehlenite, gismondine and calcite with an increase in curing time. A significant increase in peaks of Na-C-S-H and gismondine as the curing time advances. Also, phase intensities of Na-C-S-H and gismondine are higher with $M_s=2.0$ compared to $M_s=2.4$. The significant alkalinity in the $M_s=2.0$ solutions generates enough alkalinity to dissolve Al^{3+} and Na^+ in metakaolin that facilitates the formation of Al and Na rich silicates. Further, incorporation of metakaolin in low content (10wt.% and 20wt.%) to the slag and activating at the high Na_2O content (10.6wt.% to 12wt.%) at low modulus 0.9-1.0 developed reaction products such as calcium silicate hydrate, sodium-calcium silicate hydrate, gismondine and garronite ($\text{NaCa}_{2.5}(\text{Si}_{10}\text{Al}_6)\text{O}_{32}\cdot 13\text{H}_2\text{O}$). Gismondine and garronite were observed in AASMK systems with 10wt.% metakaolin content. Besides, low MgO content present in the slag favoured the formation of gismondine instead of hydrotalcite. The partial substitution of Na for Ca favoured the formation of garronite at high alkali concentrations. In addition to this plombierite ($\text{Ca}_5\text{Si}_6\text{O}_{16}(\text{OH})_2\cdot 7\text{H}_2\text{O}$), a hydrated member of tobermorite group was observed in AASMK systems with 10wt.% metakaolin content. The intensities of C-

(N)-A-S-H gel observed to be higher in the binder systems with a high content of metakaolin. The phases such as gismondine and garronite were absent in the AASMK systems with 20wt.% metakaolin. A multiphase system with a high content of metakaolin will induce the Na-Ca ion exchange process to form C-(N)-A-S-H gels. Also, the higher metakaolin content consumes Na^+ ions in the pore solution to form an aluminosilicate gel. Thus, the reduced availability of Na^+ ions reduce the alkalinity and favours zeolite growth. The incorporation of metakaolin to slag up to 70wt.% and activated with NaOH solutions were exposed to 80 °C for 28 days, the XRD data showed the presence of phases such as zeolite X (Al/Si=0.85), zeolite A (Al/Si=1), and zeolite P (Al/ Si=0.6) [82].

The inclusion of metakaolin in the AASMK system favours the coexistence of N-(C)-A-S-H/C-(N)-A-S-H gels and Al uptake in C-A-S-H gels. The addition of metakaolin in slag slightly decreases the compressive strength and increases the overall porosity of AAMs.

2.1.4.2 Alkali-activated fly ash – metakaolin system (AAFMK)

AAFMK systems are produced by mixing slag and metakaolin powder in different ratios. The AAFMK systems favour the formation of N-A-S-H or aluminosilicate gel irrespective of the precursor ratios. The high content of metakaolin inclusion leads to the formation of N-A-S-H products with low Al/Si ratios. The increase in FA content favours the formation of N-A-S-H products with high Al/Si ratios [76].

The compressive strength and porosity values of metakaolin and AAFMK specimens cured at varying temperatures are shown in Fig. 2-26. The AAFMK specimens showed higher compressive strengths and lower porosity values [76]. AAFMK specimens cured at 150 °C showed a significant increase in compressive strength and low porosity values. The increase in temperature accelerates the rate of reaction and facilitates the faster dissolution of Al and Si from Fa-metakaolin and leads to the formation of zeolitic products with substantial mechanical strength [76].

The AAFMK specimens (50wt.% FA and 50wt.% metakaolin) with $\text{NaOH} + \text{Na}_2\text{SiO}_3$ with 7.4wt.% Na_2O (Fig. 2-25). The high thermal curing conditions (85 °C) of AAFMK specimens revealed the formation of hydroxysodalite (Fig. 2-26) and minor traces of Zeolite A ($\text{Na}_{96}\text{Al}_{96}\text{Si}_{96}\text{O}_{384} \cdot 216 \text{H}_2\text{O}$) at 85 °C curing temperature. At 150

°C, faujasite ($\text{Na}_2\text{Al}_2\text{Si}_{2.4}\text{O}_{8.8} \cdot 6.7\text{H}_2\text{O}$) and zeolite A were observed. At 200 °C, sodalite syn ($\text{Na}_8\text{Al}_6\text{Si}_6\text{O}_{24}(\text{OH})_2 \cdot 2\text{H}_2\text{O}$) was detected. The intensities of zeolites formed in AAFMK specimens are lesser compared to AAFAspecimens [76].

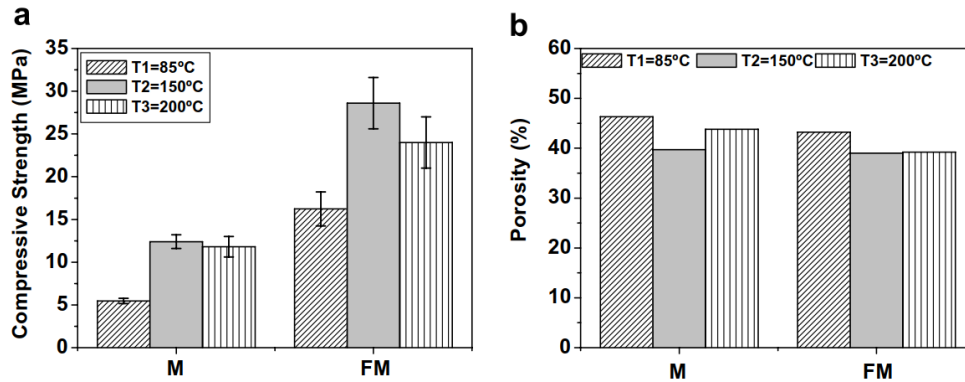


Fig. 2-25 (a) Compressive strength development; (b) porosity values [76].

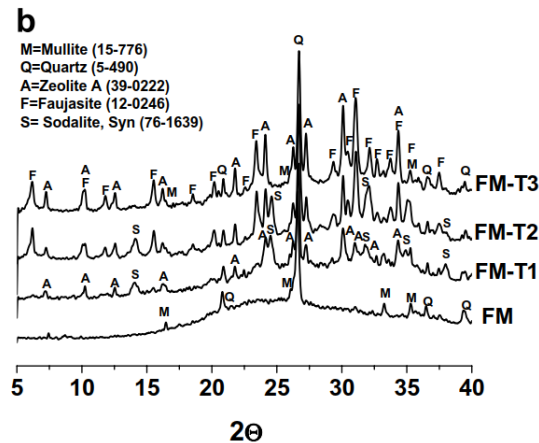


Fig. 2-26 X-ray diffraction patterns of FA metakaolin blends [76].

The AAFMK system is produced by mixing FA and metakaolin in different ratios. Regardless of the precursor ratios and activator concentrations, the major reaction product is N-A-S-H. The curing temperature significantly alters the phases and facilitates the formation of zeolites.

2.1.4.3 Alkali-activated slag-fly ash system (AASFA)

Slag and FA blend is the common choice of precursor sources in the production of AAMs and their activation mechanism has been under investigation in past decades. The slag and FA blends are mixed at different precursor ratios and activated using NaOH, Na_2SiO_3 , Na_2CO_3 , KOH, K_2SiO_3 and different blends. The dosage of Slag/FA,

activator concentrations influence the phase evolution and microstructures. AAS - FA system is famous for its structural, mechanical and durability properties [19].

The compressive strength as a function of slag content and curing time is shown in Fig. 2-27. Regardless of activator concentration, the inclusion slag enhanced the compressive strength in AAS - FA specimens. the compressive strength varied between ~32.00 MPa to ~ 120.0 MPa [83].

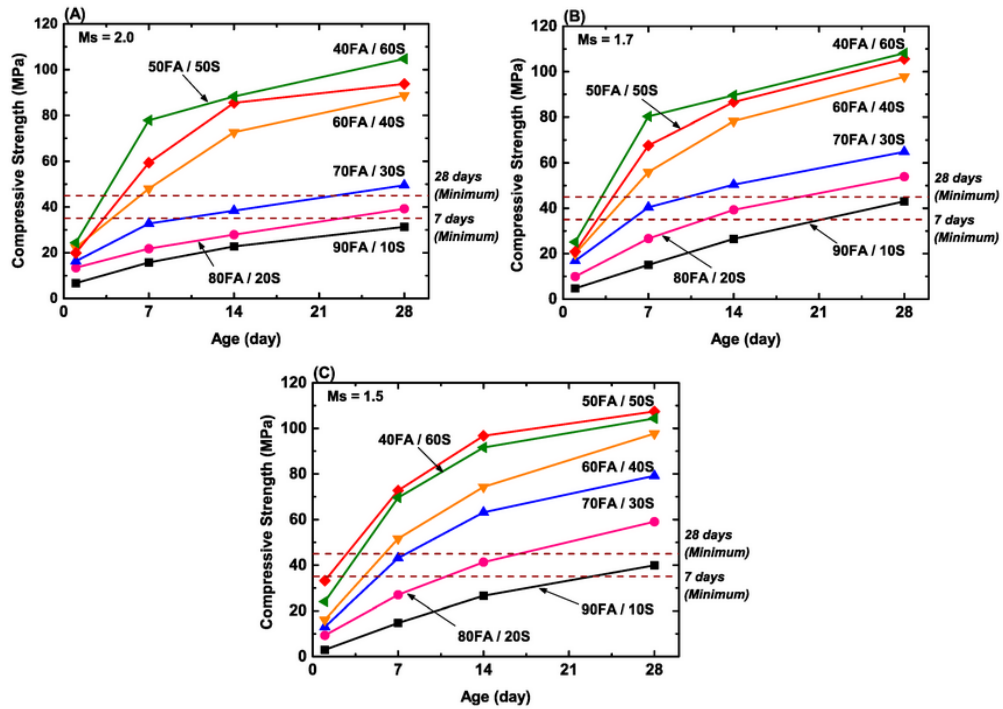


Fig. 2-27 Effect of ageing time on compressive strength and effects of blast furnace slag content on the rates of compressive strength development of airtight ambient cured geopolymers mortars [83]

The alkali-activated FA slag blends (50wt.%FA:50wt.% slag) with 10M NaOH and cured specimens at 65 °C exhibited the presence of reaction products such as calcite, hydrotalcite, and calcium hydroxide [84]. The FA and slag blend with de-sulphurised gypsum, slaked lime, burkeite ($2\text{Na}_2\text{SO}_4 \cdot \text{Na}_2\text{CO}_3$), and lignosulfonate. Also, ettringite and C-S-H gels in reaction products [85].

The XRD patterns of AAS FA blends with varying FA content is shown in Fig. 2-28. In 75 wt.% slag/25 wt.% FA, disordered C-S-H was observed. The intensity of peaks of C-S-H gel was increased as the FA (50 wt.% slag/50 wt.% FA) content in the AAS FA system. The inclusion of FA up to 50% delayed C-A-S-H formation because of the dissolution of Al and Si from FA. Also, an increase in FA content decreases the

availability of Ca^{2+} ions and favoured the formation of C-A-S-H phases with lower $\text{Ca}/(\text{Si}+\text{Al})$ ratios. In pastes with 75wt.% FA content, authors have observed the reduced intensity of C-A-S-H gel phases compared to low FA contents at the early ageing of curing. As curing progressed, 28 days of crystalline products with phases like garronite (instead of gismondine) and zeolite Na-P1 were observed. Authors have reported that the Na-Ca ion exchange process at high alkali content led to the transformation of gismondine to garronite phases. Increased FA content (at 75wt.%) and sodium, reduced the availability of Ca and favoured the formation of zeolite Na-P1 structure [18,19].

The disordered C-S-H gels in the AAS FA specimens with 20wt.% slag content were cured at 23 °C for 90 days. The elevated curing conditions (80 °C) favours the transformation of poorly crystalline C-S-H gels to zeolitic phases such as analcime ($\text{NaAlSi}_2\text{O}_6 \cdot \text{H}_2\text{O}$) and tobermorite and C-A-S-H phases with 30wt.% slag incorporation [86]. The elevated curing of AAFA specimens between 200 - 800 °C for 2 hours, favoured the formation of anhydrite sulphate (CaSO_4), akermanite ($\text{Ca}_2\text{MgSi}_2\text{O}_7$) and gehlenite ($\text{Ca}_2\text{Al}_2\text{SiO}_7$). The decomposition of the reaction product C-A-S-H gel was observed at 600 °C. Further increase in the temperature (800 °C) intensified the formation of akermanite and gehlenite. At this temperature, the new crystalline phases such as nepheline (NaAlSiO_4), wollastonite ($\text{Ca}_3\text{Si}_3\text{O}_9$) and anorthite ($\text{CaAl}_2\text{Si}_2\text{O}_8$) were observed [87]. The slag-FA blends activated with $\text{NaOH}+\text{Na}_2\text{SiO}_3$ solutions are exposed to different curing temperatures varying from 23 °C, 300 °C to 600 °C favoured the formation of C-S-H, maghemite (Fe_2O_3 , $\gamma\text{-Fe}_2\text{O}_3$) and calcite phases [88]. The formation of C-S-H, hydrotalcite and katoite (C_3AH_6) were observed in AAS FA specimens with an increase in the Na_2O content from 4wt.% to 8wt.% they observed the formation of portlandite $\text{Ca}(\text{OH})_2$ [89].

The activation mechanism AAS FA system activated with 5 and 10wt.% sodium carbonate (Na_2CO_3) behaved differently. The addition of Na_2CO_3 slightly reduces the pH of the mix because of the partial neutralization of Na_2CO_3 to Na_2O and CO_3^{2-} ions. At the initial stages, the Ca^{2+} from the slag reacts with CO_3^{2-} to form CaCO_3 based phases such as gaylussite and calcite.

Q - Quartz M - Mullite A - Aragonite C - Calcite C-S-H - Calcium silicate hydrate
 HT - hydrotalcite HM - Hematite GN - Garrisonite Na-P1 - Zeolite

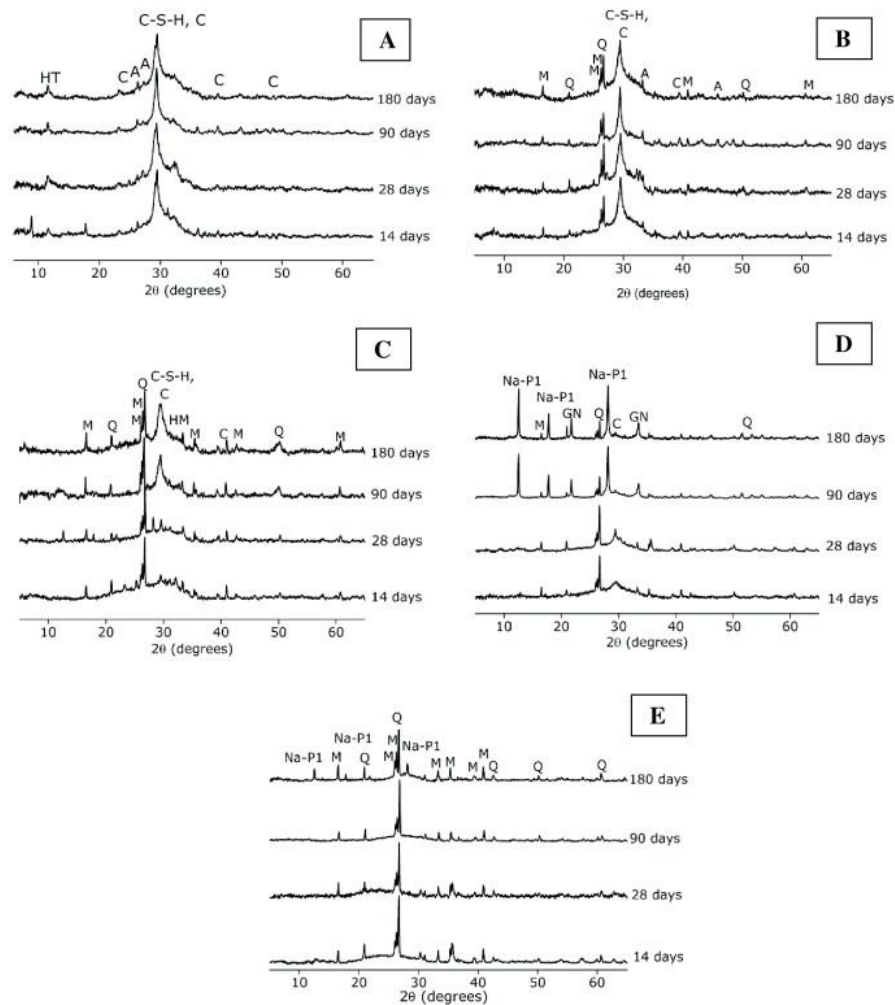


Fig. 2-28 X-ray diffractograms of alkali-activated slag/fly ash binders, as a function of the slag/fly ash ratio and the time of curing: (A) 100 wt.% slag, (B) 75 wt.% slag/25 wt.% fly ash, (C) 50 wt.% slag/50 wt.% fly ash, (D) 25 wt.% slag/75 wt.% fly ash and (E) 100 wt.% fly ash [19].

The Al and Si components of slag/FA reacts with Na_2O separately and favour the formation of N-A-S-H products. The low pH developed during the time of activation slows down the rate of reaction eventually leading to low mechanical properties at the initial stages of curing. Once the CO_3^{2-} is exhausted, the activation reaction behaves similar to NaOH activated systems. It has been reported that at later stages of curing, Na_2CO_3 activated AAS FA systems exhibit substantial mechanical properties [90]. Calcite, vaterite, aragonite, gaylussite and zeoliteNaA ($\text{Na}_{12}\text{Al}_{12}\text{Si}_{12}\text{O}_{48} \cdot 18\text{H}_2\text{O}$) were observed as reaction products. The partially dissolved Ca^{2+} in slag and CO_3^{2-} species in the activator solution led to the formation of the zeolite NaA structure. However,

with an increase in curing time authors have observed the reduction of zeolite NaA and gaylussite traces, as the formation of Ca-rich zeolite heulandite ($\text{CaAl}_2\text{Si}_7\text{O}_{18}\cdot n\text{H}_2\text{O}$, $n = 3.5\text{--}6$), calcium aluminium silicate hydrate (C-A-S-H), Al-rich tobermorite ($\text{Ca}_5\text{Si}_6\text{O}_{18}\cdot 5\text{H}_2\text{O}$) and layered double hydroxide (LDH) ($\text{Mg}_6\text{Al}_2\text{CO}_3(\text{OH})_{16}\cdot 4\text{H}_2\text{O}$) increased. A significant increase in intensities of C-A-S-H, hydrotalcite, heulandite and minor traces of Na-Ca carbonates was observed at the end of 180 days of curing [19].

The activation of slag with Na_2CO_3 + sodium metasilicate, favoured the formation of polymorphs of calcium carbonate, pirssonite ($\text{Na}_2\text{Ca}(\text{CO}_3)_2\cdot 2\text{H}_2\text{O}$), and hydroxysodalite phases. The increase in intensities of polymorphs of calcium carbonate, as the curing time increases. The addition of sodium metasilicate in the system favoured the formation of pirssonite instead of gaylussite, hydroxysodalite and analcime ($\text{NaAlSi}_2\text{O}_6$). As the reaction continues, both analcime and hydroxysodalite were consumed and favoured the formation of LDH and tobermorite phases at the initial stages of curing. The presence of Mg^{2+} in slag significantly influence the precipitation of calcium carbonate. As the reaction continues, the Mg^{2+} species in the system are consumed by calcium to form layered double hydroxides structures [92].

The alkali-activation of slag and FA led to the formation of N-(C)-A-S-H gels with a high amount of tetracoordinated Al charge-balanced by Na ions. The increase in the amount of slag increases the Ca-based phases in the system. Similarly, high FA content increases the amount of N-A-S-H in the mixes. The activator concentration also influences the development of reaction products. The high activator concentration increases the pH of the system and suppresses the precipitation of C-A-S-H during the initial stages of activation. The optimal $\text{SiO}_2/\text{Na}_2\text{O}$ (Ms) ratio for the AAS FA system is between 1-1.5. The inclusion of FA in slag results in improved setting time and higher compressive strength.

2.2 Durability

Concrete structures and cement products may deteriorate when exposed to harsh or aggressive environmental conditions, classified as physical or chemical environments. Physical deterioration caused by abrasion, freeze and thaw and fire. Chemical deterioration is because of the sulphur attack, chloride ingress, leaching and carbon dioxide penetration.

2.2.1 Sulphate resistance

Concrete structures can suffer from acid attacks when exposed to acidic media such as sulphur, hydrochloric, acetic, and nitric compounds. Most commonly acid-induced failures can be seen in the sewer system because of the formation of sulphuric acid [93–95]. AAMs derived from high calcium precursors show better acid resistance compared to Portland cement concrete. This acid resistance of AAMs can be attributed to low permeability, pH of the alkaline solution and low CaO/SiO₂ ratio in the AAMs system [96]. Several attempts were made to understand the effect of acidic concentrations on the corrosion mechanism of AAMs. Higher acidic concentrations (sulphuric acid) react with cations (calcium and sodium) present in the hardened geopolymer paste induce an electrophilic interaction on the aluminosilicate network resulting in the removal of aluminium from the aluminosilicate network. The cations present in the pore solution diffuse and react with the acid in the solution, precipitating in the form of crystals (gypsum) inside the hardened gel. Exposure of AAMs to severe acidic concentrations will reduce the compressive strengths, degradation of materials, and mass loss [97].

An excessive amount of sulphate content in cement and concrete products cause sulphate transport. The factors influencing sulphate transport is the following factors, the presence of excessive amounts of sulphate contents in cement, binders or aggregates, penetration of sulphates because of environmental conditions. The sulphate penetration concrete will t in the porous matrix will facilitate the formation of ettringite crystals (Fig. 2-29). The formation of ettringite will create expansive stress on the surrounding area. Thus, concrete materials fail because of cracking. Several studies show the better performance of AAMs over OPC concrete under Sulphate attack [98]. In contrast to OPC based materials where expansion cracking of concrete specimen was observed, the AAM based materials show the development of ettringite phases were observed as secondary products. Studies report that exposure of AAM specimens to Na₂SO₄ leads to structural evolution of AAMs [99]. However, exposure of AAMs to MgSO₄ solutions leads to degradation geopolymeric phases such as N-A-S-H/C-A-S-H phases subsequently compressive strength of AAMs (Fig. 2-30, 2-31 and Fig. 2-32) [100,101].

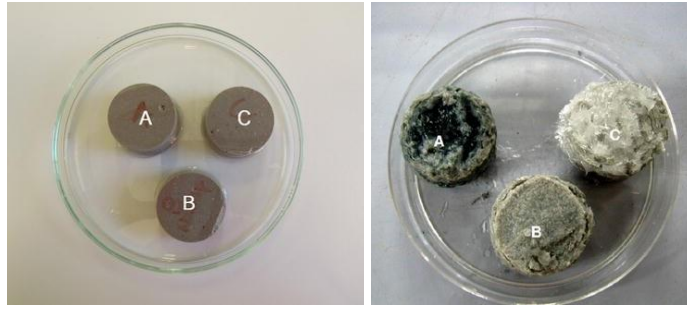


Fig. 2-29 Physical condition of samples: A w/b 0.40; B w/b 0.50; and C w/b 0.60, after immersion in Na_2SO_4 and MgSO_4 for 90 days [99].

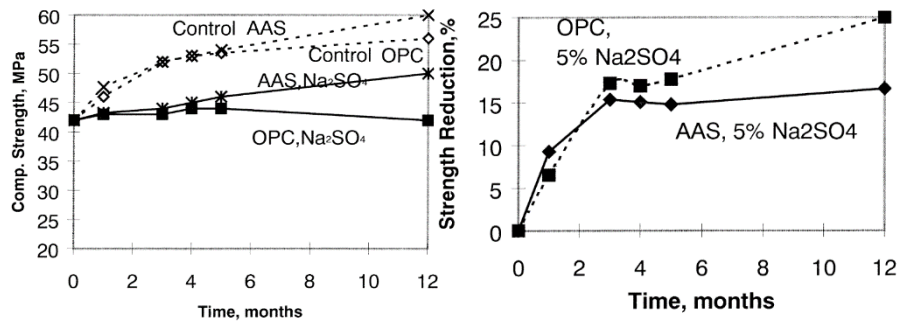


Fig. 2-30 Compressive strength of AAS concrete subjected to 5 wt.% Na_2SO_4 solution and compressive strength reduction of AAS and OPC samples subjected to sulphate attack in 5 wt.% Na_2SO_4 solution [100].

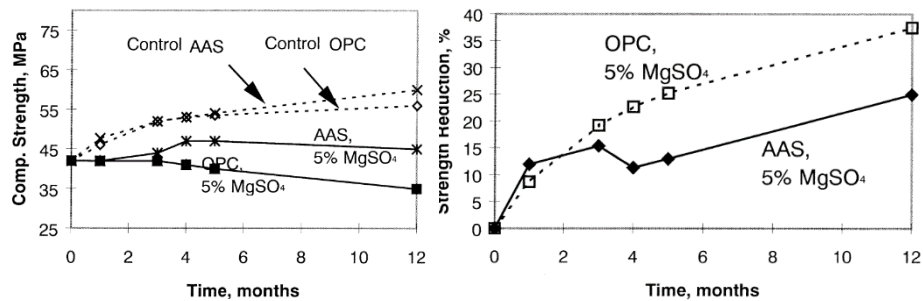


Fig. 2-31 Compressive strength of AAS concrete subjected to 5 wt.% MgSO_4 solution and compressive strength reduction of AAS and OPC samples subjected to sulphate attack in 5 wt.% MgSO_4 solution [100].

XRD patterns of AAMs exposed to Na_2SO_4 solutions with varying concentrations is shown in Fig. 2-33. After the exposure, the sulphate, and silicate-based phases such as thenardite (Na_2SO_4) and wollastonite (CaSiO_3) phases were observed [101].

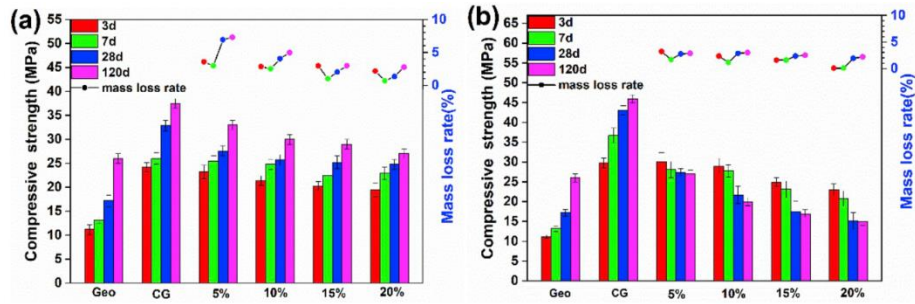


Fig. 2-32 The compressive strengths of specimens before and after the sulphate exposure for 3, 7, 28, and 120 days: (a) A3 of PVA and PP fibre reinforced geopolymers, (b) B9 of PVA and WS fibre reinforced geopolymers (Pure geopolymer-Geo & Control group with fibres-CG) [101].

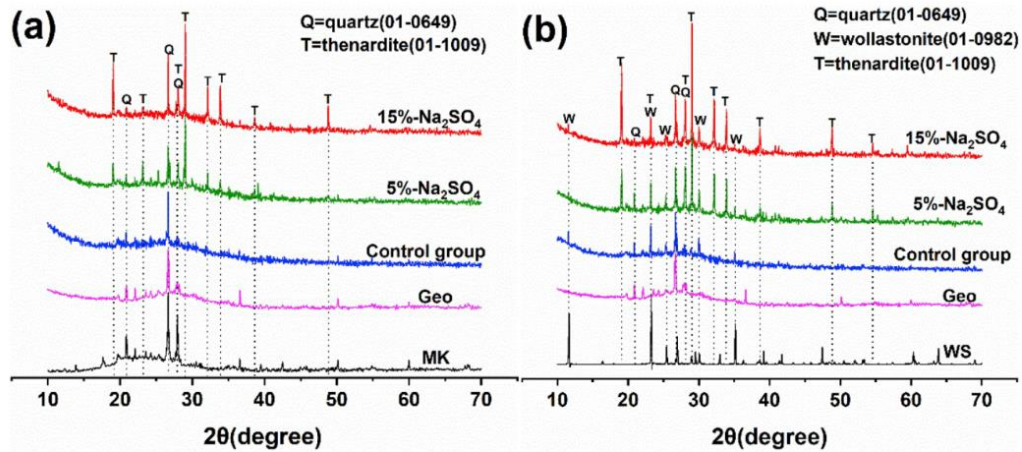


Fig. 2-33 The XRD pattern of samples exposed to sulphate for 28 days: (a) A3 of PVA and PP fibre reinforced geopolymers, (b) B9 of PVA and WS fibre reinforced geopolymers [101].

The backscatter images of FA-slag based AAM specimens exposed to $MgSO_4$ environment for 6 months is shown in Fig. 2-34. Angular particles represent unreacted slag and spherical particles represent FA. This study reveals that after exposure the Mg^{2+} induces the decalcification of C-A-S-H phases and favours the formation of M-(A)-S-H gel and released Ca^{2+} in pore solution during sulphate exposure precipitate as gypsum. Precipitation of gypsum can in Fig. 2-36 (Ca and S), after Ca^{2+} and SO_4^- reaction in pore solution [102].

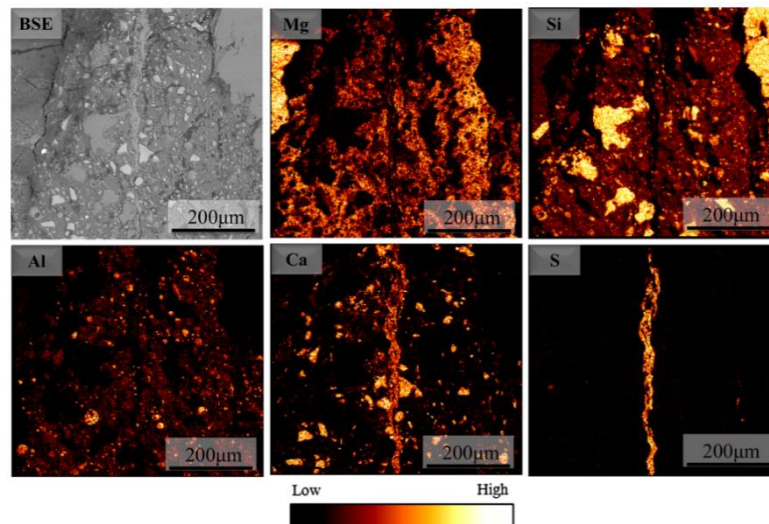


Fig. 2-34 BSE image and elemental maps of alkali-activated 75 wt.% slag/25 wt.% fly ash concrete with 28 d curing after 6 months of magnesium sulphate exposure [102].

Most of the available literature shows the role of the calcium content in the performance of AAMs under acid attack. Still, it needs more investigations to draw the correlations between calcium content on the durability aspects of AAMs.

2.2.2 Freeze-thaw resistance

This phenomenon is dependent on water saturation and porous structure concrete materials. Under complete saturation, the water content in the porous structure freezes because of a temperature drop in the surrounding environment. The ice formed inside occupies $\approx 9\%$ more volume than water. The increase in volume because of ice formation induces hydrostatic stresses on walls of the pores wall surfaces, the additional hydrostatic stresses result in cracking of the concrete materials. The freezing temperature of OPC and AAMs differs because of the ionic strength of the pore solution, pore volume, and pore radius. The relationship between pore structure and frost resistance in AAMs is governed by mixed design and precursor materials [98].

The mass-loss rates in alkali-activated caned and uncalcined coal gangue - slag specimens after freeze-thaw exposure are shown in Fig. 2-35 and Fig. 2-36. The concrete specimens were exposed to water and saltwater freeze cycles. With the increase in freeze-thaw cycles, the mass loss in coal gangue geopolymer concrete was predominant. With the increase in coal-gangue-substitution percentage, the mass loss

increased from 8.00% to 19.44% for 100 % substitution. After 100 cycles, mass-loss rates in slag-based concrete increased to 7.2% and 8.6%. In saltwater freeze-thaw cycles agglomeration of NaCl, crystal salts were observed and the internal crystal pressure was greater than interface pressure and the damage was severe when concrete was exposed to saltwater freeze-thaw cycles [103].

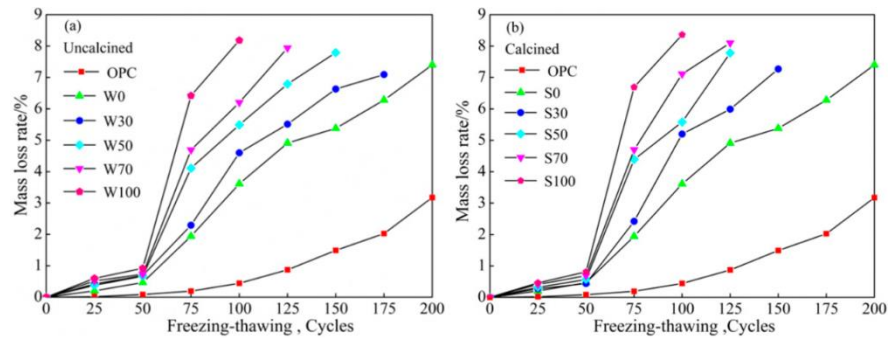


Fig. 2-35 The relationship between the number of freezing-thawing cycles and the mass-loss rate of (a) uncalcined and (b) calcined [103].

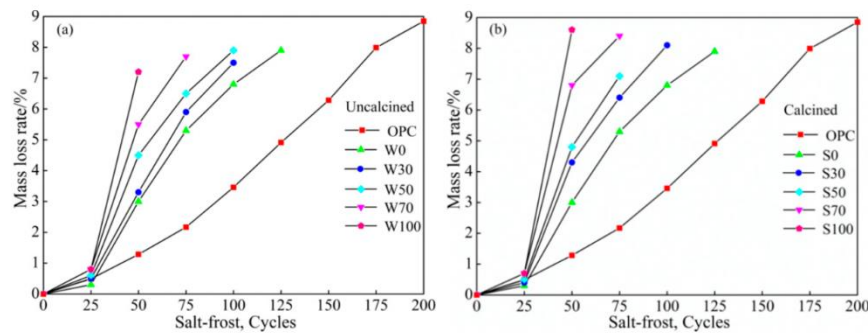


Fig. 2-36 The relationship between cycle times of salt freeze-thaw and mass-loss rate of (a) uncalcined and (b) calcined [103].

The changes in relative dynamic modulus of geopolymer concrete exposed to saltwater freeze-thaw cycles are shown in Fig. 2-37. At the end of 50 cycles, the calcined and uncalcined concrete showed a fall in dynamic modulus to 58.3% and 54.3%. The damage because of saltwater freeze-thaw cycles increased with an increase in salt concentration. With the increase in the saturation levels of the concrete, NaCl in the pore solution reacts with reaction products such as C-S-H and $\text{Ca}(\text{OH})_2$ to precipitate an expansive Friedel's salt ($3\text{CaO} \cdot \text{Al}_2\text{O}_3 \cdot \text{CaCl}_2 \cdot 10\text{H}_2\text{O}$), which leads to decalcification and cracks in concrete (Fig. 2-38). Also, the increase in the chloride ions in the pore solution favours the reduction of pH in the system and accelerated chloride ion penetration and decalcification [103].

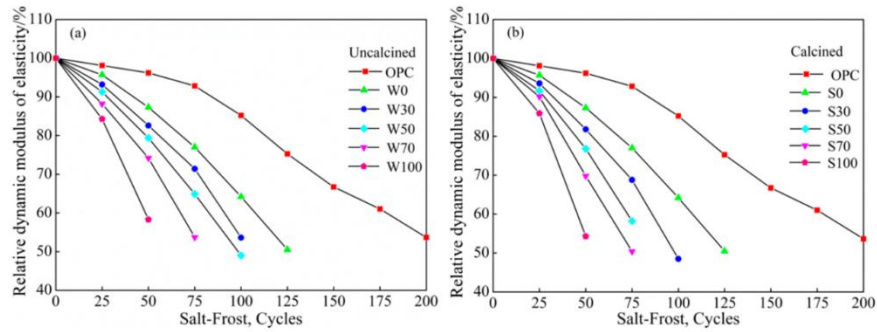


Fig. 2-37 The relationship between the salt-frost and the relative dynamic modulus of elasticity of (a) uncalcined and (b) calcined [103].

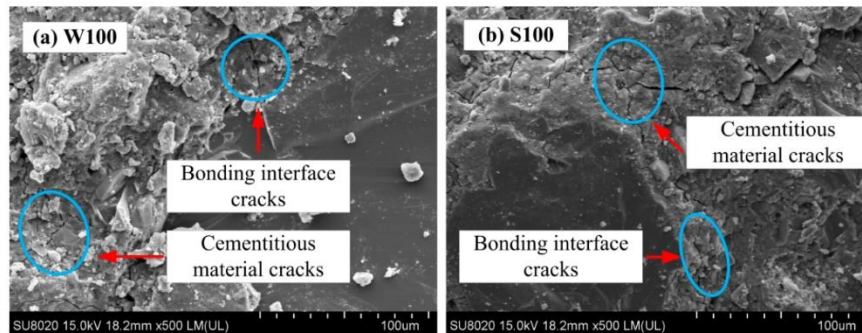


Fig. 2-38 SEM image of ACSC freeze-thaw cycles of (a) W100 and (b) S100 [103].

2.2.3 Chloride resistance

Chloride attack has been noted as one of the most concerning aspects of concrete durability. Chloride penetration is detrimental to reinforced steel bars and initiates electrochemical corrosion of steel reinforcement. However, chloride ingress usually causes no harm to the concrete matrix or structural integrity between binder, sand and gravels, the intensity of structural change caused by chloride penetration is typically low in OPC products and even lower in AAMs.

In general, the AAMs have higher porosity compared with OPC materials. However, the ongoing geopolymeric reaction and microstructural changes slow down the chloride ingress in AAMs. Fig. 2-39 shows the chloride penetration in alkali-activated FA-slag and OPC specimens. Table 2-1 shows the chloride diffusion coefficients, measured following the Nordtest accelerated method as a function of curing age. From the fig and the table, it can be inferred that the performance of AAMs is better compared with OPC. The diffusion coefficient measured in 100 wt.% slag specimens is almost negligible [104]. Another study where chloride penetration in alkali-activated FA specimens (Fig. 2-41) corroborate the aforementioned behaviour [105].

Table 2-1 Chloride migration coefficients of concretes determined from the NordTest accelerated method as a function of curing age. Values in parentheses are standard deviations of 4 samples.

Sample (wt.% slag/wt.% FA)	Chloride migration coefficient (Dp) ($\times 10^{-12} \text{ m}^2/\text{s}$)	
	28 days	90 days
100/0	1.02 (0.75)	0.51 (0.18)
75/25	0.24 (0.21)	0.65 (0.21)
50/50	1.24 (0.29)	2.01 (1.20)
OPC	18.6 (4.1)	16.8 (0.1)

XRD patterns of AAMs exposed to chloride penetration. The calcium and silicate-based phases such as calcite (CaCO_3) and calcium silicate (Ca_3SiO_5) are shown in Fig. 2-40. The chloride-based phase such as halite (NaCl) and Friedel's salt ($\text{Ca}_2\text{Al}(\text{OH})_6\text{Cl}\cdot 2\text{H}_2\text{O}$) was observed in AAM specimens. The presence of NaCl and Friedel's salt has attributed the reaction of Cl^- ions with Na^+ in pore solution, which precipitates as aforementioned salts [104,105].

Also, studies reveal that C-A-S-H gels have more affinity towards chloride ions and can adsorb chloride ions without any microstructural change. However, N-A-S-H gel is more porous in nature and it can absorb more chloride ions because of higher surface area, which favours the formation of salts upon drying. With the decrease in slag content, the final Ca/Si ratio binder mix reduces along with the alkali content binder mixes. Also, studies (Fig. 2-41) reveal that the presence of hydrotalcite phases in slag-based cement enhances the chloride binding capacity. Hence, the presence of hydrotalcite reduces the free chloride content in binder mixes and hinders the chloride ion to reach the reinforcement, thus delaying corrosion in AAMs [104].

Thus far, many studies have been conducted to understand the chloride penetration, however, these factors in general compared with OPC materials and still, there is insufficient information describing the chloride penetration AAMs. A comprehensive testing methodology and the development of a standard code of practice is required [98].

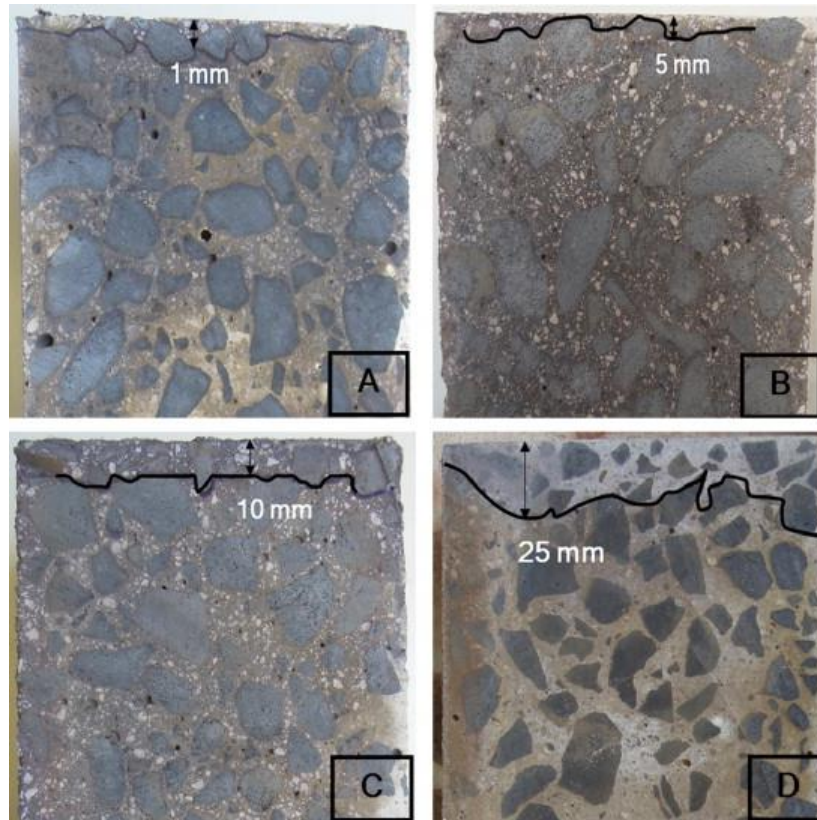


Fig. 2-39 Results of application of AgNO_3 to concretes at the end of the ponding test for concretes with 28 days of curing, as a function of slag/FA proportion: (A) 100 wt.% slag, (B) 75 wt.% slag/25 wt.% FA, (C) 50 wt.% slag/50 wt.% FA, and (D) OPC [104].

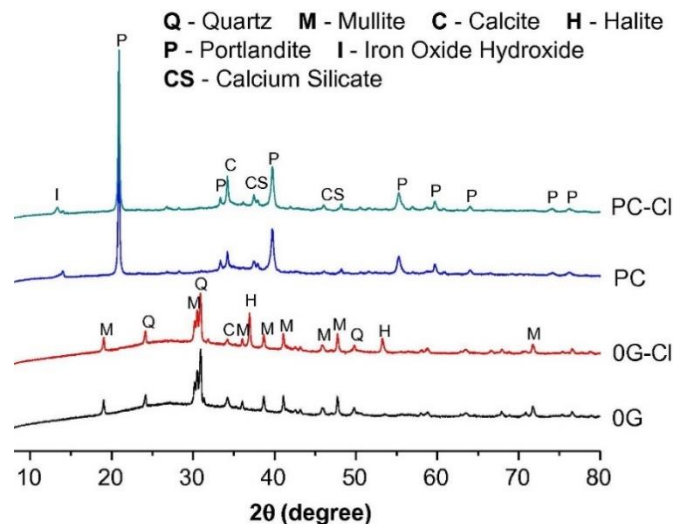


Fig. 2-40 XRD diffractograms of 100% FA geopolymer and PC samples before or after the ponding test. Mullite ($\text{Al}_{4.56}\text{Si}_{1.44}\text{O}_{9.72}$); Quartz (SiO_2); Calcite (CaCO_3); Halite (NaCl); Portlandite ($\text{Ca}(\text{OH})_2$); Iron Oxide Hydroxide ($\text{FeO}(\text{OH})$); Calcium Silicate (Ca_3SiO_5) [106].

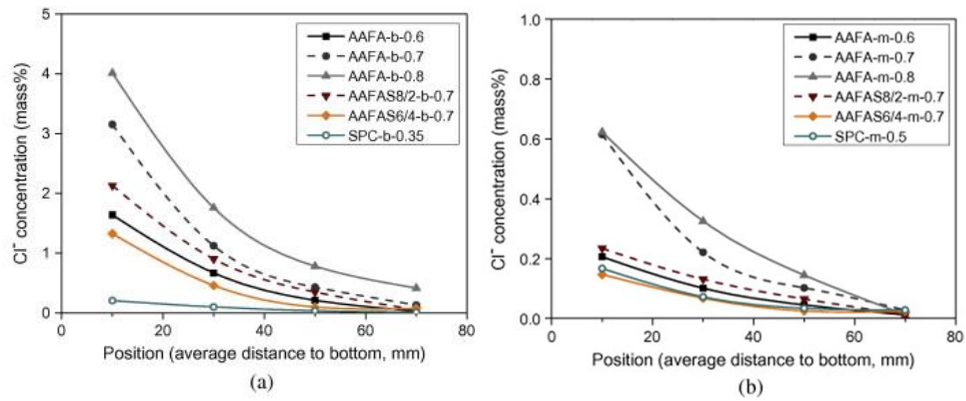


Fig. 2-41 (a) Cl^- penetration in AAFA and SPC pastes and (b) their mortars [105].

2.2.4 Carbonation resistance

Carbonation is the reaction that takes place between cementitious materials and carbon dioxide in the atmosphere, creating carbonates inside the cement concrete. The pH of the pore solution in the cementitious system controls the degree and extent of carbonation. In Portland cement, pH is controlled by $\text{Ca}(\text{OH})_2$ and in AAMs, it is controlled by pore solution. Thus, the carbonation in AAMs occurs at two stages. First, a reduction of pH in the pore solution occurs because of CO_2 penetration. Second, precipitation of Na-rich carbonates occurs, resulting in decalcification of the structure gel and deterioration of the geopolymer [18,107–110].

The key mechanisms of the carbonation process are controlled by the reactivity and diffusivity of CO_2 . Pore structure and exposure of the material dictate the diffusivity of CO_2 , reactivity depends on concentration, the type of binder, the gel maturity, and the chemistry of the pore solution [111]. Amount and type of precursor significantly influence the carbonation of AAMs. It is reported that the variation of slag content from $400 - 500 \text{ kg/m}^3$ and water to binder ratio, increase the carbonation resistance of AAMs, but this leads to the development of microcracks. Hence, an optimum dosage of slag content is required to minimize the carbonation effect and microcracks [24,50,112].

2.2.4.1 Role of precursors in carbonation

Accelerated carbonation tests were carried on blast furnace slag (GGBFS)/metakaolin (MK) ($\frac{\text{GGBFS}}{\text{GGBFS}+\text{MK}} = 1.0, 0.9, \text{ and } 0.8$) blend system and sodium silicate as an activator. Specimens were exposed at $3.0 \pm 0.2\%$, $\text{RH} = 65 \pm 5\%$ and $20 \pm 2^\circ\text{C}$ for 340 - 540 h. The addition of metakaolin into the binder formulations increased the carbonation

depths (Fig. 2-42). The higher water/binder ratio (0.47) used in this study contributed to the rapid carbonation of AAMs. Also, incorporation of MK in AAMs reduced the compressive strength after 340 and 540 h of carbonation [50]. However, the presence of MgO content in the slag significantly affected carbonation depths. With the increase in MgO content, the carbonation depths decreased, the 7.44wt.% MgO in the slag showed the least carbonation depths (Fig. 2-43 and Fig. 2-44). The inclusion of metakaolin slightly decreased the compressive strength and enhanced total pore volume which contributes to the enhancement of carbonation reaction [113,114].

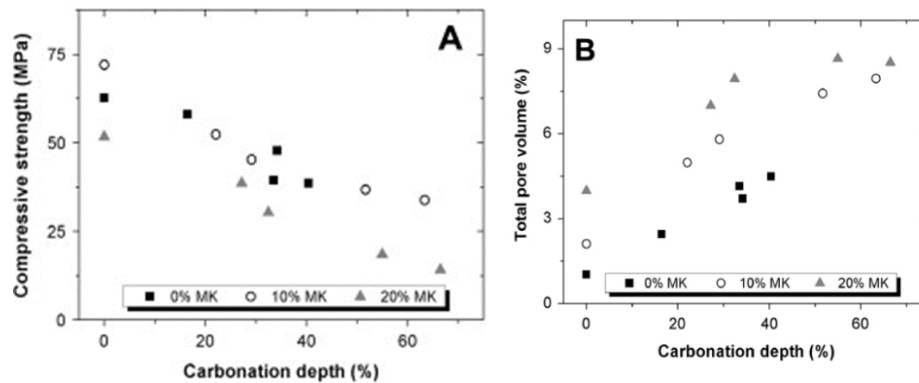


Fig. 2-42 Relationship between the carbonation depth and compressive strength (A) and post-carbonation total pore volume (B) of alkali-activated concretes, as a function of the content of MK incorporated in the binder [113].

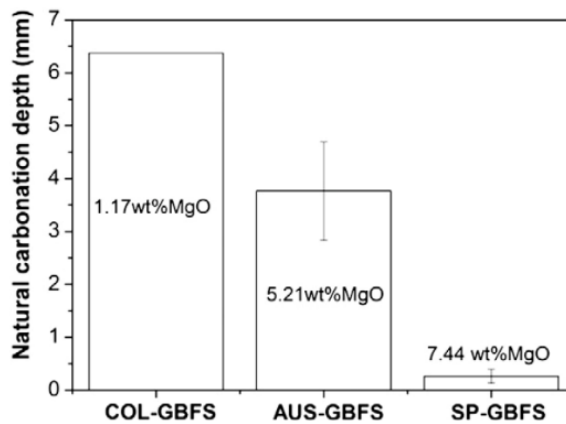


Fig. 2-43 Natural carbonation depth (16 months exposure to ambient laboratory environment) of silicate-activated slag pastes ($\phi = 12.8$ mm) as a function of the MgO content in the slag [114].

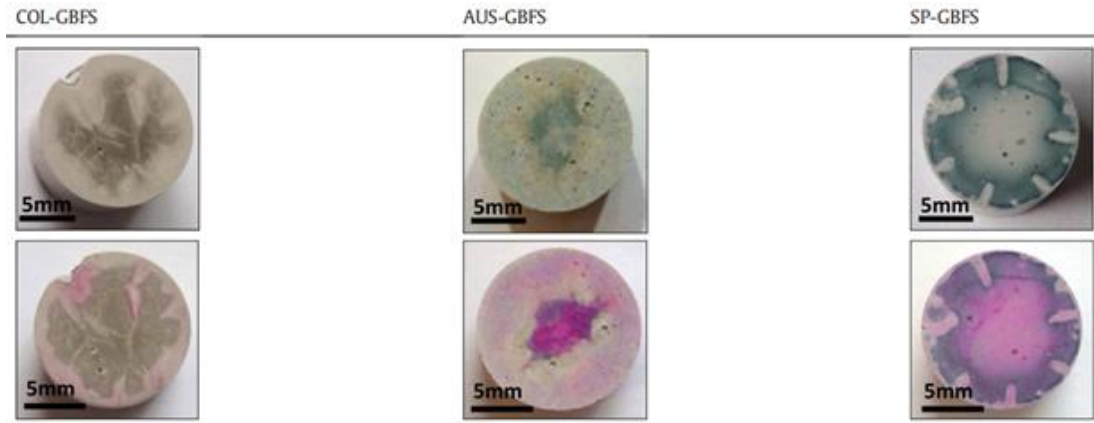


Fig. 2-44 Transverse sections of naturally carbonated pastes after 16 months exposed samples to atmospheric conditions, with the extent of carbonation revealed by a phenolphthalein indicator [114].

XRD studies on uncarbonated GGBFS/MK systems exhibited the amorphous phase as gehlenite ($\text{Ca}_2\text{Al}_2\text{ASiO}_7$) and unreacted GGBFS phases like quartz (SiO_2) and calcite (CaCO_3). Reaction products such as C-S-H ($\text{Ca}_6\text{Si}_3\text{O}_{12}\cdot x\text{H}_2\text{O}$) and aluminosilicate zeolite gismondine ($\text{CaAl}_2\text{Si}_2\text{O}_8\cdot 4\text{H}_2\text{O}$) were observed. Any sodium-based phases were not observed, the Na^+ ions in the binder must be present in the pore solution or non-crystalline reaction products [18,50].

The crystalline phases like C-S-H, calcium - aluminosilicate (gismondine) and quartz were observed along with calcium carbonates (CaCO_3) in this study after carbonation. Trona ($\text{Na}_3\text{H}(\text{CO}_3)_2 \cdot \text{H}_2\text{O}$) was identified as a secondary carbonation product. The addition of MK to the GGBFS system significantly influenced compressive strengths and carbonation depths. The incorporation of MK up to 20wt.% reduced the compressive strength of uncarbonated AAMs from ≈ 75 MPa to 50 MPa. However, a 60% reduction in compressive strength in AAMs with 20wt.% MK was observed. Along with compressive strength addition of MK increased the porosity of binders from $\approx 4.5 - 9\%$ [50]. Besides, the Ca/Si and Al/Si ratios significantly decreased after carbonation (Fig. 2-45), this indicates decalcification of gels through the formation of carbonates. The Mg/Si ratio and Al/Si ratios were also observed to be decreased after carbonation which is because of the consumption of phases other than hydrotalcite and AFm phases [18].

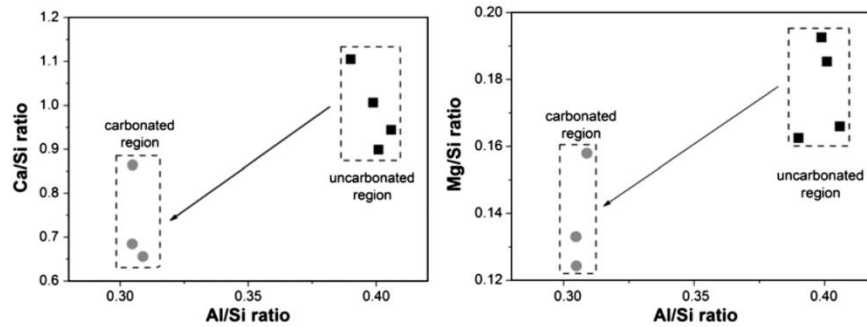


Fig. 2-45 Atomic ratios Ca/Si vs Al/Si and Mg/Si vs Al/Si, for uncarbonated and carbonated regions [18].

In GGBFS based alkali-activated concrete specimens, slag content increase from 400 kg/m³ to 500 kg/m³ showed a considerable influence on the carbonation effect. After 180 days of curing only significant difference porosities were observed between specimens with low slag content (400kg) and high slag content (500 kg). However, capillary sorptivity in specimens with higher slag content was observed. This property was attributed to the formation of thermal microcracks because of the increased slag content. The carbonation rates of geopolymers specimens with higher slag content under accelerated carbonation (1% CO₂) condition, showed better resistance to the specimens with lower slag content. Nevertheless, the specimens under different water/binder ratios (0.42 and 0.48) and at varying Na₂O (4wt.% and 5wt.%) content behaved differently under natural carbonation [115]. In addition to the above-mentioned factors, GGBFS+MK activated specimens showed a different rate of CO₂ diffusion under accelerated carbonation (1% CO₂, 65% RH and 1000 h of exposure). The specimens with 400 kg/m³ and 500 kg/m³ slag contents gave a carbonation depth of 13.3 mm and 10.9 mm respectively at a water/binder ratio of 0.42. This shows that accelerated carbonation rates predict natural carbonation rates [18,115,116].

The XRD patterns of FA-slag based AAMs activated exposed to accelerated carbonation for 7 days is shown in Fig. 2-46. After carbonation, the phases such as CaCO₃ (calcite, aragonite and vaterite) were observed in these specimens. The presence of Mg-Ca based carbonate such as huntite was also observed in these specimens. Three types of GGBFS with different MgO content (1.17wt.%, 5.21wt.% and 7.44wt.%) were activated using sodium silicate and cured for 14 days at 23 °C. X-ray diffraction studies on uncarbonated specimens revealed the presence of hydrotalcite (Mg₆Al₂CO₃(OH)₁₆·4H₂O) in alkali-activated specimens at higher MgO content (5.21wt.% and 7.44wt.%) instead of gismondine. Phases like thomsonite

($\text{NaCa}_2\text{Al}_5\text{Si}_5\text{O}_{20}\cdot 6\text{H}_2\text{O}$) and katoite were observed after 180 days of curing. However, X-ray diffraction studies of carbonated specimens at different CO_2 (0.2, 0.4 and 1% accelerated carbonation conditions) and RH at $65 \pm 5\%$, shows the carbonate polymorphs calcite, vaterite and aragonite at 1.17wt.% MgO content. In the case of AAMs with 5.21wt.% MgO content, phases vaterite, aragonite, nahcolite (NaHCO_3), Thermonatrite ($\text{Na}_2\text{CO}_3\cdot\text{H}_2\text{O}$), hunite ($\text{CaMg}(\text{CO}_3)_4$), and gaylussite ($\text{Na}_2\text{Ca}(\text{CO}_3)_2\cdot 5\text{H}_2\text{O}$) were observed with this mix composition. The intensity of vaterite and aragonite phases was decreased at 7.44wt.% MgO content. The intensity of hunite was observed to be higher in this mix composition [50]. Besides, ^{27}Al MAS-NMR studies on carbonated specimens (1.17wt.% MgO) showed minor concentration of unreacted slag content at 10 ppm. The intensity of this peak was observed to be intense for the carbonated geopolymer specimens at higher MgO contents. This indicates that CO_2 sorption increases with an increase in the MgO content of GGBFS, eventually forming magnesium carbonate phases. The decalcification of C-S-H gel in geopolymer specimens was also observed in NMR studies after accelerated carbonation. NMR studies show that structural changes in C-A-S-H gel because of carbonation [50].

Also, ^{27}Al MAS-NMR studies on carbonated specimens (1.17wt.% MgO) showed minor concentration of unreacted slag content at 10 ppm. The intensity of this peak was observed to be intense for the carbonated geopolymer specimens at higher MgO contents. This indicates that CO_2 sorption increases with an increase in the MgO content of GGBFS, eventually forming magnesium carbonate phases. The decalcification of C-S-H gel in geopolymer specimens was also observed in NMR studies after accelerated carbonation. NMR studies show that structural changes in C-A-S-H gel because of carbonation [50].

Natural carbonation studies were conducted FA/GGBFS geopolymer (Type 1 =75wt.%FA+25wt.%GGBFS and Type 2 =70wt.% FA+30wt.% GGBFS) system for 8 years. The type 1 system was activated with a combination of potassium hydroxide (KOH) and sodium hydroxide (NaOH) along with Na_2SiO_3 (sodium silicate). The type 2 system was activated with KOH and NaOH solutions. After the field exposure for eight years, carbonation depths of 23.5 – 27.5 mm for Type 1 and 8 – 14 mm for Type 2 specimen was observed [117].

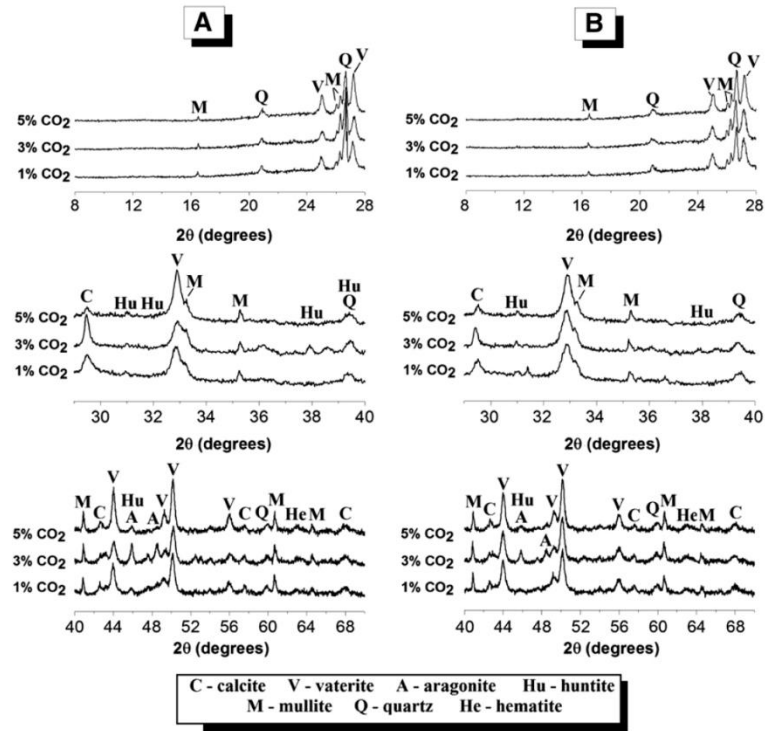


Fig. 2-46 X-ray diffractograms of alkali-activated fly ash/slag blended pastes cured for (A) 1 day or (B) 7 days and exposed for 7 days to accelerated carbonation at different CO₂ concentrations as marked [18].

The addition of Titanium dioxide (TiO₂ in 1, 3, and 5wt.%) to FA based AAMs, activated with Na₂SiO₃ and NaOH, showed improved carbonation resistance. The specimens were carbonated under accelerated carbonation (20% CO₂ and 65 ± 5%) condition for 3, 7, 28, 90 and 180 days [118]. The incorporation of micro silica (5wt.%, 10wt.% and 15wt.%) in GGBFS based AAMs with NaOH as an activating solution was considered for carbonation study. This study also considered the effect of water and plastic wrap curing on carbon penetration depths. According to this study, no significant changes were observed when specimens were water cured. However, the carbonation depths were significantly higher in plastic cured specimens. Also, the correlation of carbonation effect with residual compressive strength exhibited the decreasing trend, the lower compressive strength (65 – 70 MPa) was observed at higher carbonation depth (8 – 9 mm), and higher compressive strength (90 – 95 MPa) was observed at lower carbonation depths (5 – 6 mm) [119].

In low calcium FA or class – F FA AAMs, MgO content was artificially varied from 0 – 12 wt.%, the system was activated using NaOH solution. The study showed the increase in compressive strength of carbonated (20% CO₂) specimens to uncarbonated

specimens. They have also shown the shift Si: Al stoichiometry towards Si region and Mg: Si towards MgO region under CO₂ rich environments [120]. The GGBFS content was varied from 0 – 100 wt.% in FA/GGBFS AAMs. Compositions were activated using NaOH and Na₂SiO₃ solution. These specimens were carbonated at laboratory conditions (0.038% CO₂, 55% RH and 20 °C) for 1 year. The carbonation depths were decreased (28 -0 mm) as the slag content increased from 0 – 100wt.% [121].

In FA based AAMs low calcium FA or class – F FA shows increased carbonation resistance and low porosity, compared to high calcium FA or class - C FA. It is reported that Class – C (high calcium) FA based AAMs are more prone to CO₂ penetration, corrosion, and permeability when these mixes are exposed under 5% CO₂ because of the low pH of the pore solution [122]. In slag/FA blends, the co-existence of C-A-S-H and N-A-S-H gel is found. If C-A-S-H gel constituents are higher than N-A-S-H gel, it will lead to the higher alkalinity of the pore solution with large porosity, this state of materials can be readily carbonised [18].

2.2.4.2 Effect of activators in carbonation

Activators influence the carbonation process, the type and concentration of activators are crucial to the carbonation process [123]. Studies have reported that GGBFS based AAMs were activated by Na₂SiO₃ and NaOH solutions. The prepared slag specimens were cured for 28 days at 98% RH and carbonated at 43.2% RH. These specimens were carbonised in a CO₂ saturated chamber for 1, 2 and 4 weeks. Their TGA (Thermo Gravimetric Analysis) from 0 °C – 600 °C studies indicated no significant difference in weight loss between carbonated and uncarbonated specimens. The TGA studies have indicated that the presence of carbonates is lower in NaOH – slag-based specimens than in Na₂SiO₃ specimens. However, the MAS – NMR studies indicated that the nature of alkali activators caused no changes in accelerated carbonation pastes. Nevertheless, the same pastes were carbonated for 4 and 8 months, the compressive strength of Na₂SiO₃ slag pastes exhibited a 14% decrease in compressive strength after 4 months of carbonation, no further change in compressive strength was observed after 8 months of carbonation. However, NaOH – slag pastes exhibited a 93% increase in compressive strength after 4 months and no change in compressive strength after 8 months of carbonation. The total porosity of Na₂SiO₃ slag pastes decreased slightly,

but the average pore size increased significantly. In NaOH – slag pastes total porosity and average pore diameter decreased significantly [124].

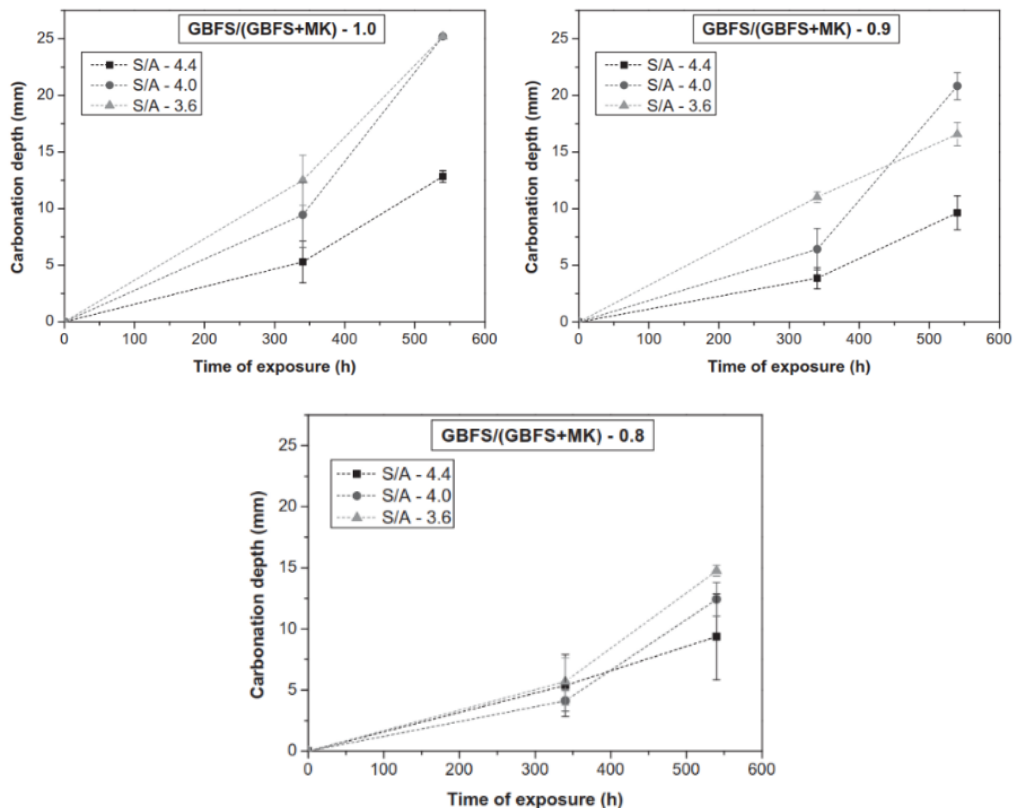


Fig. 2-47 Carbonation depth of mortars based on activated slag/metakaolin blended binders as a function of the GBFS/(GBFS + MK) ratio and activation concentration [124].

The carbonation depth of slag-metakaolin based AAMS exposed to 340 h and 540 h of carbonation is shown in Fig. 2-47. The specimens with Si/Al = 3.6, 4.0 and 4.4 showed carbonation depth of 21%, 42% and 37% respectively. After 540 h of exposure, the specimens with Si/Al = 4.4 showed a carbonation depth of 51%. However, other specimens showed 100% carbonation. However, in binder specimens with 10wt.% metakaolin, a similar trend was observed, where the AAMS specimens with Si/Al = 3.6 showed 8% higher carbonation depths compared with slag only specimens. However, the Si/Al= 4.4 showed 65% reductions in the carbonation depths. A similar trend was also observed in mortar specimens with 20 wt.% metakaolin content. The use of slag with a higher amount of MgO (8.9wt.%) content in these AAMS has favoured the formation of hydrotalcite-like phases. These phases enhance the carbonation resistance and bind CO₂ in alkali-activated slag binders [124].

Studies show that variation of M_s (1.6, 2.0 and 2.4) of Na_2SiO_3 affects the carbonation process. The GGBFS+MK specimens with M_s of 1.6 were rapidly carbonised at $3.0 \pm 0.2\%$ CO_2 concentration and RH of $65 \pm 5\%$. However, specimens with $M_s = 2.4$ showed the lowest carbonation depths after 340 and 540 h of carbonation. This study shows that an increase in alkalinity increases carbonation rates. Further to this, uncarbonated specimens with higher M_s have exhibited compressive strengths up to 67MPa. However, their compressive strength decreased drastically by 60% (38 MPa) after 540 h of carbonation. According to this study, higher M_s values increases mechanical strength initially, but after carbonation significant decrease in mechanical properties were observed at higher M_s content. Along with carbonation, M_s values also influence capillary sorptivity. Higher sorptivity and shrinkage was observed in AAMs specimens prepared at $M_s = 1.6$ [125].

FTIR spectra of AAM binder specimens activated with $M_s = 2.0$ and 2.4 and exposed to carbonation conditions is shown in Fig. 2-48. After carbonation bands assigned to O-C-O bending of CO_3^{2-} bending was shifted to 1438 cm^{-1} to 1417 cm^{-1} with increasing intensity. The bands assigned to Si-O-T stretching 983 cm^{-1} shifted to 1001 cm^{-1} with decreasing intensity. This shows the decalcification of binder gel and the formation of carbonation products in these specimens. An increase in intensity 880 and 870 cm^{-1} assigned to calcite formation was observed, along with the formation of a new peak at 833 cm^{-1} indicating the formation of HCO_3^- ion, which indicates the formation of trona. The inclusion of 10wt.% metakaolin shifts Si-O-T stretching to 1005 cm^{-1} , indicating a higher degree of polymerization and higher uptake of Al content in binder gel in these mixes. The carbonation of these mixes also exhibited the reduction in asymmetric stretching of Si-O-T bonds a shoulder at 1158 cm^{-1} , indicating higher intensity carbonation in these binder specimens. The formation of trona was not observed in these specimens. The carbonation of these specimens led to the formation of higher intensity of calcite phases and a formation of HCO_3^- at 836 cm^{-1} . Incorporation of metakaolin to these specimens showed similar trends with AAMs with 10wt.% metakaolin activated with $M_s=2.4$ [49].

TGA ($25 - 1100 \text{ }^\circ\text{C}$) analysis conducted on uncarbonated and carbonated specimens showed free and bound water loss at $60 - 160 \text{ }^\circ\text{C}$. Dehydration of C-S-H gel in uncarbonated specimens activated at lower M_s was observed above $380 \text{ }^\circ\text{C}$. However,

decomposition of CaCO_3 was observed between 660 – 680 °C. The amount of CaCO_3 was observed in specimens with higher M_s content (2.0 and 2.4) indicate the presence of a higher amount of calcite content in carbonated samples.

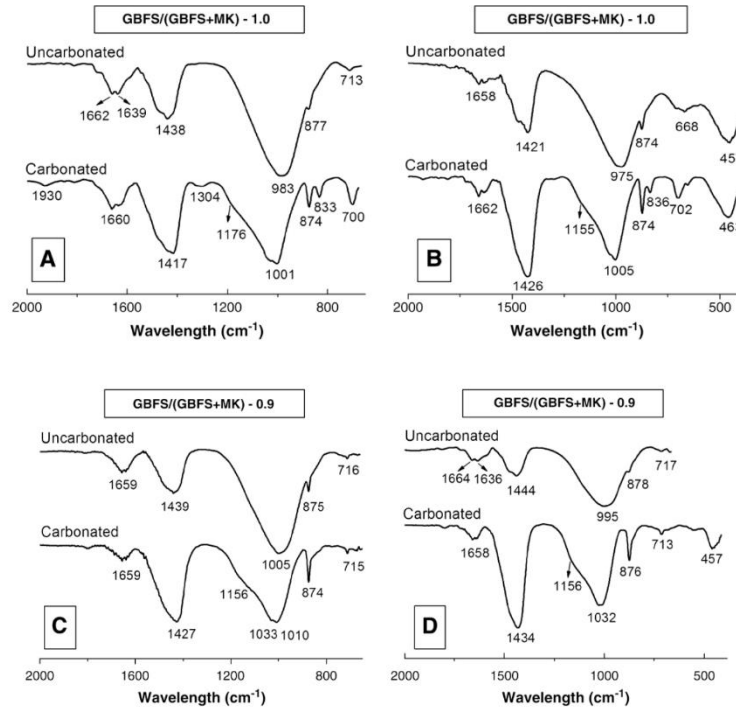


Fig. 2-48 Fourier transform infrared spectra of uncarbonated and carbonated pastes of (A;B) GBFS and (C;D) GBFS/MK blends, activated with (A;C) $M_s = 2.4$, (B;D) $M_s = 2.0$ [49].

In GGBFS+MK specimens, Na_2O content significantly influenced the carbonation process. After 7 years of natural carbonation, the depth of carbonation measured in 5wt.% Na_2O specimens was ten times higher than 4wt.% Na_2O specimens. However, the total porosity of 5wt.% Na_2O specimens after 90 and 180 days of curing, were lower than 4wt.% Na_2O specimens. This reveals that the diffusivity of CO_2 is independent of the water/binder ratio (0.42 and 0.48). Thus, CO_2 diffusivity into the specimens with a higher content of alkaline activator enhances the carbonation rate. Further to this, the diffusion rate of CO_2 in concrete can be linked to the permeability phenomenon. However, along with permeability, higher concentration Na_2O in alkaline pore solution, attract the CO_2 and accelerates CO_2 diffusion rate in a porous matrix-forming carbonic acid. Thus, a decrease in pH of the pore solution leads to decalcification of the C-S-H gel of AAMs [115].

In comparison with OPC, FA based AAMs showed better carbonation resistance. According to this study, M_s (1.00 and 1.25) of activator had a significant influence on the carbonation of AAMs. Other studies claim that variation of M_s (0, 0.5, 1.0 and 1.5) values strongly influence the carbonation process. Slag mortars activated with NaOH performed better than Na_2SiO_3 activated slag mortars. The residual compressive strength (after carbonation) values of Na_2SiO_3 activated specimens decreased up to 25.8% with increase in M_s values [18,49,50,115,122,124].

2.2.4.3 Effect of CO_2 in carbonation

Carbon-di-oxide concentration must be considered during the carbonation tests. Accelerated carbonation tests with extremely high CO_2 concentration is not advisable, these conditions normally fail to simulate the appropriate environmental conditions. Also, high CO_2 content does not influence carbonation, it enhances the diffusivity of CO_2 [126,127].

In OPC concrete, CO_2 concentrations significantly influence the compressive strength. Higher the CO_2 concentration higher the carbonation depth was identified. Concrete samples with different grades (30 MPa, 40 MPa, and 50 MPa) were carbonated from 2.5% to, 100 % and carbonation depths were determined after 7, 14, 28 and 56 days. Carbonation depths were increased as the CO_2 concentration increased from 2% - 20%. However, this increasing trend reduced drastically at 20% - 50% CO_2 concentrations. Further, the increase in CO_2 concentrations after 50% did not influence carbonation depths. The same trends were observed in all grades of concrete.

Effect of CO_2 concentration was studied on OPC, blended with limestone powder, GGBFS, FA and micro silica. Each concrete mix has resulted in different CaO content varying from 41.43wt.% (fly ash-based OPC) to 64.24wt.% (OPC with no blend). These concrete specimens were carbonated at CO_2 concentrations of 0.045% (laboratory exposure), 1% and 4%. Few other concrete samples were exposed outdoors (sheltered and unsheltered). Carbonation coefficients (K_{ACC} for accelerated carbonation and $K_{\text{N, S}}$ for natural carbonation) were calculated after exposing specimens for 28 days. K_{ACC} is a function of carbonation depth (d_k), initial carbonation depth (A) and the square root of time (\sqrt{t}). The slope of K_{ACC} (0.61 for 1% CO_2 and 0.12 for 0.045% CO_2) decreased with an increase in CO_2 concentrations.

Under natural carbonation condition $K_{N,S}$ of unsheltered concrete specimens was 2.5 times higher than sheltered concrete specimens. In the case of accelerated carbonation condition, the gradient of K_{ACC} for normal OPC concrete was slightly higher than blended mixtures. This study claims that CO_2 concentrations increase from 1 – 4 % has less significance in the carbonation process [128].

MK based geopolymers (activated using Na_2SiO_3) were carbonated under endogenous (20 °C), natural (20 °C, atmospheric CO_2 concentration and 95% RH) and at accelerated (20 °C, 50% CO_2 and 50% RH) conditions. The specimens were carbonated for 1, 3, 5, 7 and 14 days for the accelerated condition and up to 365 days for natural and endogenous carbonation. The pore solution from geopolymer specimens was extracted at above mentioned time intervals and pH profiles were plotted against time. Titration analysis was conducted to measure the mass of Na_2CO_3 formed after carbonation. In the case of endogenous carbonation initial pH value was 13.9, 13.0 after three days, 12.8 after seven days and the value stabilized slightly over 12 for the rest of the period.

The pH of the solution under natural carbonation was showed a similar trend, but the higher reduction in pH values at the end of one year. The pH was 12 after 14 days and reduced to 10.5 at the end of one year. However, in accelerated curing condition pH values dropped to 12.0 at the end of 14 days of carbonation. The mass of Na_2CO_3 present in the porous matrix was observed to be increased from 16.1 g/L to 30.9 g/L.

This study proposes that carbonation occurs in two phases. In phase 1, during the first two weeks, pore solution under natural conditions forms Na_2CO_3 salts and the pH value reduces to 12. In phase 2, the equilibrium between carbonate/bicarbonate maintains the pH value around 10.5, no significant changes were observed between 6 months to 1 year. Also, their accelerated carbonation studies conclude that the accelerated carbonation test for geopolymers resulted in no significant effect [129].

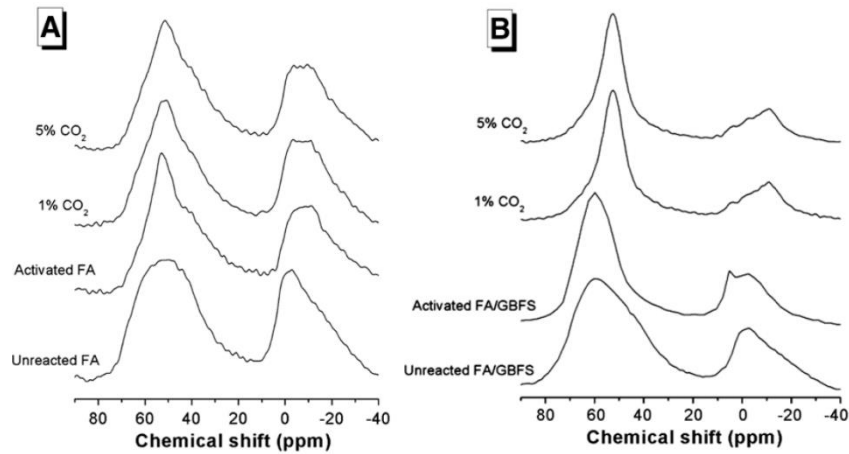


Fig. 2-49 ^{27}Al MAS NMR spectra of (A) alkali-activated fly ash and (B) alkali-activated fly ash/slag blends [18].

The GGBFS based AAMs were activated using solid anhydrous sodium metasilicate, these specimens were cured for 28 days and carbonated at 7% CO_2 at 65% RH. Also, another set of samples were extracted and crashed after 7 days of curing, accelerated carbonation test was performed on these samples at 1%, 3% and 5% CO_2 concentrations for 7 days. Besides, specimens were extracted after 14 days of curing and exposed to natural carbonation in a laboratory for 3 years.

The carbonation depths of AAMs specimens under accelerated conditions (7% CO_2) are higher than natural carbonation depths. Similar trends were observed with OPC concrete when specimens were carbonated in accelerated and natural conditions [54,130]. Fig. 2-49 shows the effect of carbonation on FA-Slag based binder specimens. Exposure to elevated CO_2 conditions C-A-S-H gels are more susceptible to change. The ^{27}Al MAS-NMR results shows complete removal of Al[IV] sites from C-A-S-H and movement of Al[IV] chemical shifts to lower ppm, which is consistent with ^{29}Si results [18].

In comparison with accelerated carbonation (1%, 3% and 5%), naturally carbonated specimens showed carbonate-based phases (calcite, vaterite and aragonite) and hydrous phases such as natron and several double salts (Fig. 2-50). The phases and concentrations of phases of carbonated samples at high CO_2 concentrations differed significantly. XRD studies reveal the absence of a strong calcite peak and an increase in intensities of vaterite and aragonite at high CO_2 concentrations. Other major differences such as the absence of bicarbonates in natural carbonation and the presence of bicarbonates in accelerated carbonation. The presence of thermonatrite in the

samples favoured the formation of bicarbonate such as nahcolite over natron. The thermonatrite ($54.96 \text{ cm}^3/\text{mol}$) and nahcolite ($38.66 \text{ cm}^3/\text{mol}$) occupy less molar volume compared to natron ($196.56 \text{ cm}^3/\text{mol}$). Hence, thermonatrite and nahcolite occupy less space and decrease the degree of pore blockage, when they grow inside the porous matrix.

The pore blockage is a crucial factor in the case of AAMs, where phases of AAMs binders, occupy less space and reduce diffusion of CO_2 compared to OPC. Also, another consequence of thermonatrite presence in the sample forms alteration in solid phases of the binder matrix; this would change the phase equilibrium of carbonate/bicarbonate. Thus, the change in the equilibrium of carbonate/bicarbonates will govern the pH of the pore solution. Determination of pH of pore solution will further assist in identifying potential risk of steel bars corrosion of concrete [54,130].

When alkali-activated slag/metakaolin systems were carbonated at 1% CO_2 concentration, a decrease in capillary absorption was observed [131]. However, a further increase of CO_2 concentration decreased the pH of the pore solution, led to the decalcification of C-A-S-H gel. Decalcification of the gel can alter the porosity and gel structure [18]. Along with these, a combination of cations present in the gel and internal relative humidity can also influence the CO_2 diffusion and precipitation of bicarbonate salts [18].

In naturally carbonated AAMs, at $23 \text{ }^\circ\text{C}$ the formation of natron is favoured. However, a slight increase in CO_2 concentration will change the phase equilibrium and favour the trona formation. Further, the incorporation of 10wt.% MK into this system will hinder the formation of trona. The addition of MK influences the alumina dissolution and binds the sodium in aluminosilicate gels. The unavailability of sodium for CO_2 will reduce the carbonate formation in the geopolymer binder. Further increase in CO_2 concentration (above 0.2%) will facilitate the formation of natron or trona [54].

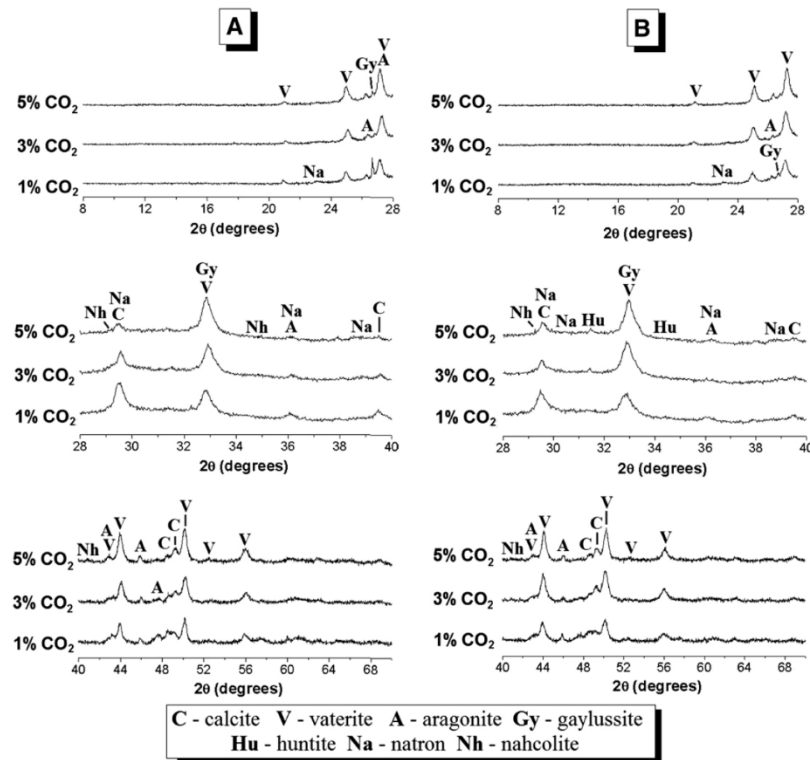


Fig. 2-50 X-ray diffractograms of alkali-activated slag with (A) 1 day and (B) 7 days of curing, then exposed to elevated CO₂ concentrations as marked, for 7 days [18].

2.2.4.4 Effect of relative humidity (RH) in carbonation

Studies have reported that relative humidity influences the carbonation process. High RH (RH>80%) reduce the carbonation effect in AAMs. At high RH content normally AAMs are saturated and the porous network inside is filled with moisture. Thus, resulting in the blocking of pores inside and reducing the rate of diffusion of CO₂. On the other hand, low RH (RH<50%) also reduce the carbonation effects because of the low saturation of CO₂ in porous volume [131]. In this case, low moisture content inside hinders the solvation and hydration of CO₂ to form carbonic acid [132]. In slag/metakaolin based AAMs, RH of 65±5% (Fig. 2-51) is required to create a partially saturated environment, for the maximum diffusion of CO₂, which leads to the highest volume of permeable porosity and accelerate the carbonation process [132–136].

GGBFS and GGBFS+MK based AAMs were evaluated for carbonation varying RH (50 ± 5%, 65 ± 5% and 80 ± 5%) content for 250, 500 and 1000 h at 1% CO₂ concentration (Fig. 2-51 and Fig. 2-52)). The carbonation depth observed was increased with an increase in time of exposure and the lowest carbonation depth was observed at 80% RH. Specimens with higher MK incorporation exhibited rapid

carbonation at intermediate humidity (65% RH). At higher 80% RH content, the rate of carbonation was slower because of the total saturation of the porous matrix of geopolymer specimen [54,130,137].

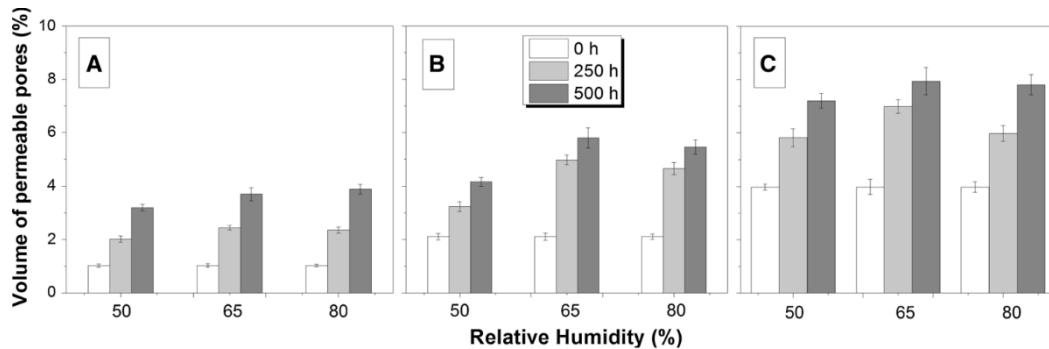


Fig. 2-51 Porosity of partially carbonated concretes based on alkali-activated slag/metakaolin blends formulated with GBFS/(GBFS+MK) ratios of a 1.0, b 0.9 and c 0.8, as a function of the relative humidity, at 1 % CO₂. Error bars correspond to one standard deviation of four measurements [131].

Carbonation of calcium-based alkali-activated systems developed following solid phases. The major reaction product of CaO (free lime) after carbonation (RH = 80%, at 0.03-0.04% CO₂) for 24 h was calcite, other major phases of calcium after carbonations were aragonite and vaterite formed at RH content of 20-60% [138]. In Alkali activate slag systems surface cracks were observed because of drying and carbonation shrinkages when carbonation tests were carried at 15% CO₂ concentration and RH = 52%. Also, the pre-drying of AAMs have influenced the permeability phenomenon and microstructural properties of AAMs. However, if the pre-drying process is skipped, then the CO₂ diffusion rate would be delayed because of low saturation, which can significantly reduce the rate of carbonation AAMs because of low porosity [139].

FA based AAMs with activation solutions NaOH and Na₂SiO₃ were heated 85 °C for 5, 12, and 20 h and 7 days. These specimens were cured under two different conditions, moulds were kept in an airtight container with a certain amount of water (method 1) and moulds were completely immersed in water (method 2). The specimens subjected to method 2 curing showed carbonate phases irrespective of heat treatment [140].

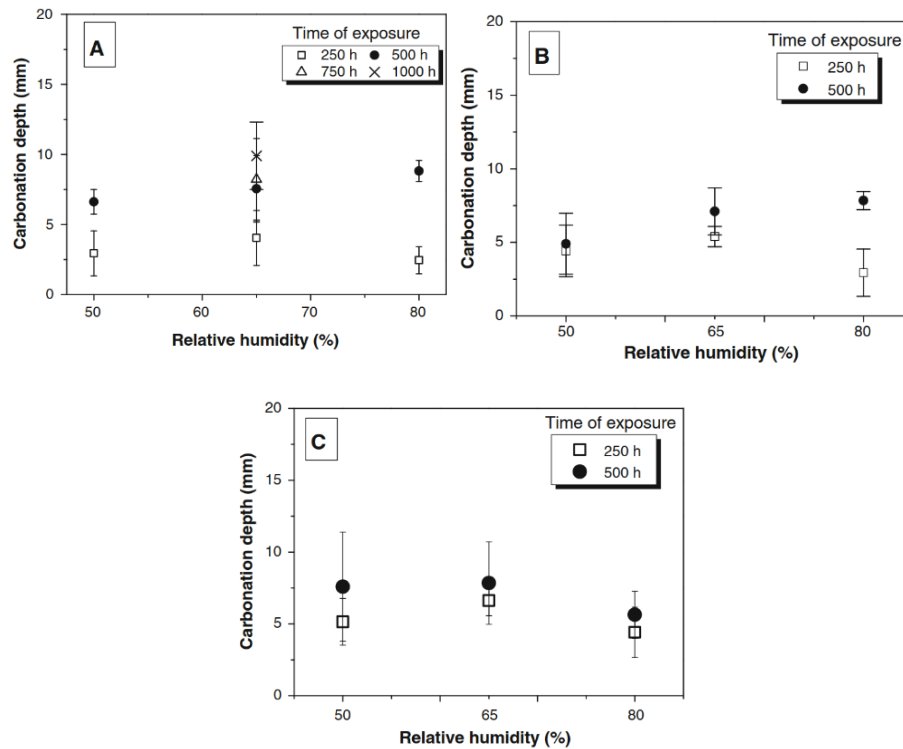


Fig. 2-52 Carbonation depth as a function of the relative humidity and time of exposure in alkali-activated GBFS/MK concretes, formulated with GBFS/(GBFS+MK) ratios of a 1.0, b 0.9 and c 0.8, at 1 % CO₂ [131].

The study claims that during the initial stages of curing concrete specimens interact with the atmosphere and carbonation occurs rapidly. Typically, the carbonation rates were higher at 45 – 75%RH. The carbonation rate was decelerated above 80% RH because of waterlogging in the porous matrix. However, carbonation was not observed below 25% RH content, because of less water content present inside the specimens. The development of sodium carbonate and bicarbonate phases during carbonation reduced the pH of the pore solution and the rate of aluminosilicate formation [140].

The atmospheric exposure played a key role in the reactive kinetics of geopolymer specimens. Method 1 specimens were not exposed to the atmosphere, hence higher degrees of the reaction were observed in these specimens. However, in method 2 specimens atmospheric CO₂ reacts with sodium content present in the AAMs and forms sodium bicarbonates. Hence, sodium carbonates species decreases the pH of the pore solution and decelerates the rate of aluminosilicate reaction [46,140].

2.2.5 Permeability behaviour of AAMs

The flow of water through the pores of cementitious materials is regarded as permeability. Permeability in concrete affects the durability factors such as

carbonation, efflorescence, chloride ion penetration, and leaching. The continuous flow of water through concrete leads to an increase in the porosity of concrete because of the i) leaching of cementitious materials from the concrete, ii) the increase in porosity increases the permeability coefficient of concrete followed by cavitation, iii) degradation of concrete, and iv) reduction in mechanical properties.

The permeability of AAMs can be reduced by adding OPC or slag. The addition of 15 wt.% OPC to rice husk based AAMs refined the pore structure and strengthened the nucleation sites which decreased the water absorption up to 4.42% at the end of 90 days of ageing (Fig. 2-53) [141]. This indicates that the inclusion of OPC favours the formation of C-A-S-H based phases, which tend to fill pore volume and increase the degree of tortuosity. Also, a decrease in porosity increases the electrical resistivity in AAM concrete. Thus OPC inclusion decreased the chloride ion penetration and increased electrical resistivity in concrete from 2018 Coulombs to 1037 Coulombs. The main factors responsible for the reduction in charge passed and, thus, the enhancement in chloride penetration resistance were: (1) pore refinement because of OPC inclusion as mentioned previously, (2) dense and compact matrix, and (3) reduction in conductivity of pore solution [142].

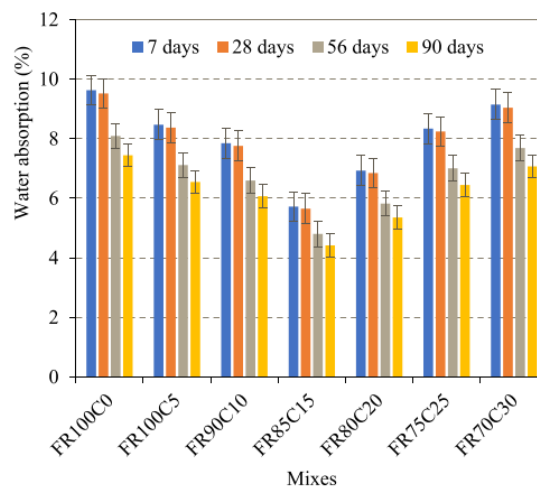


Fig. 2-53 Water absorption of rice husk based AAM concrete mixes with partial replacement of OPC.

The curing temperatures of AAM concrete refined the porosity and water absorption rates (Fig. 2-54(a) and (b)). Heat cured AAM concrete showed a lesser water absorption value of (5.4-6.0%) compared with heat-cured OPC concrete (6.3-7.1%). The curing of AAM concrete at 75 °C for 18 h reduced the porosity from $\approx 16\%$ to \approx

13.7%. The decrease in porosity delayed the saturation of AAM concrete to 9 days and the water absorption of AAM concrete [142].

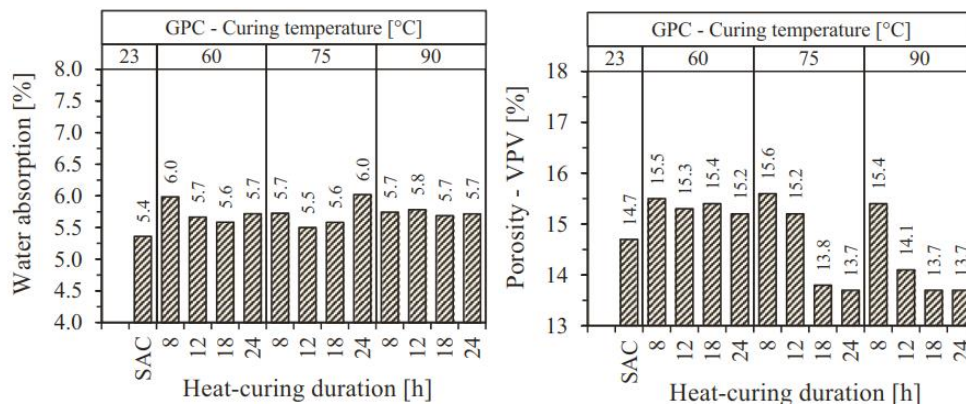


Fig. 2-54 A representation of (a) water absorption behaviour of heat-cured AAM concrete, and (b) porosity behaviour of heat-cured AAM concrete.

The relation between bulk resistivity and the moisture content is shown in Fig.2-55. The curves show an exponential increase in bulk resistivity with a decrease in moisture content. The free alkalis in the concrete conduct electricity, and these free alkalis are present in pore solution. The resistivity of the saturated concrete is controlled by the pore volume, pore network, concentration of ions in the pore solution [142]. The electrical resistivity in concrete is not significantly affected when the concrete is fully saturated. In the surface dry condition a marginal increase ($<2 \text{ k}\Omega \text{ cm}$) can be observed in the bulk resistivity. When the concrete is dried at $50 \text{ }^\circ\text{C}$ for more than 15 days, where the entrapped water in the large voids is removed, a strong increase in the electrical resistivity can be observed [142]. When the water in the capillary pores is removed, exponential increases in the bulk resistivity can be observed. The AAM samples cured for 24 h at $75 \text{ }^\circ\text{C}$ exhibited higher bulk resistivity. This behaviour is attributed to the low permeability coefficient and low pore connectivity in AAM concrete [143].

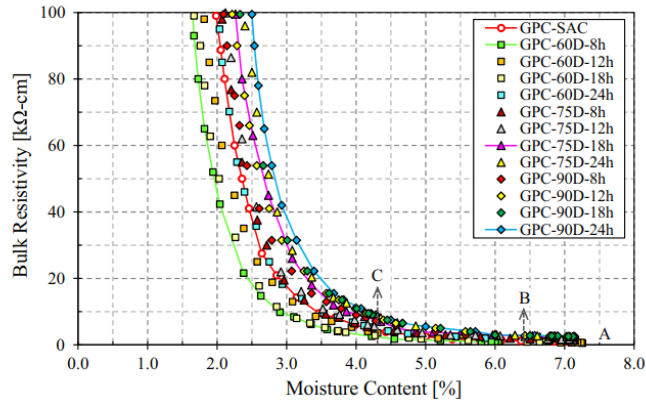


Fig. 2-55 Relationship between the moisture and the bulk resistivity of AAM concrete

The effect of alkali concentration on void content is shown in Fig.2-56(a) and (b). An increase in alkaline activator content decreases the void content in the concrete mix. The increase in alkali concentration enhanced the alkali activation reaction and paste content relatively developing dense AAM concrete [144].

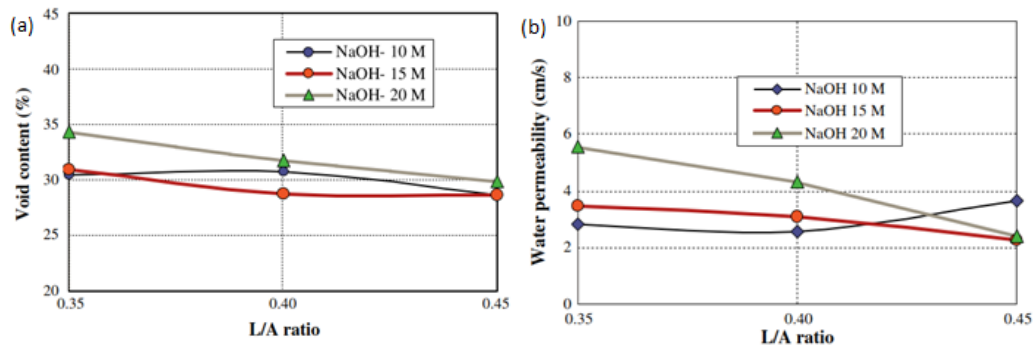


Fig. 2-56 Plots of (a) void contents of AAM concrete as a function of liquid to alkaline activate concentration, and (b) water permeability of AAM concrete as a function of liquid to alkaline activate concentration.

The relationship between void content and water permeability is shown in Fig.2-57(a). The increase in void content increased the water permeability in AAMs [144]. The increase in permeability is controlled by various factors such as low activator concentration, type of precursors, type of aggregates and compaction factor of concrete [144]. The relationship between compressive strength and void content is shown in Fig.2-57(b). An increase in void content significantly decreased the compressive strength of the AAM concrete mix and increased the permeability coefficient of AAM concrete mixes.

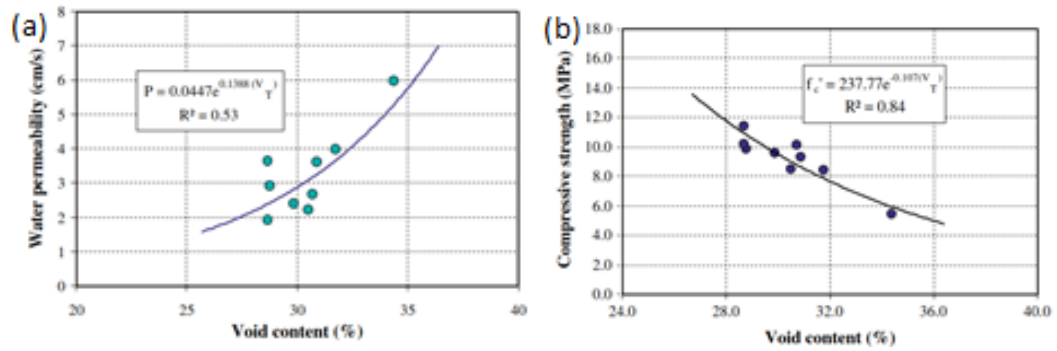


Fig. 2-57 Curves show (a) relationship between water permeability and void content of AAM concrete, and (b) relationship between compressive strength and void ratio of AAM concrete.

The relation between compaction factor and compressive strength is shown in Fig. 2-58(a) with the increase in compaction factor generally workability increases along with the water/solids ratio [144]. Hence, there will be an increase in the porosity and a decrease in the compressive strength. Therefore, a lower water/solids ratio decreases the permeable voids. Also, an increase in OPC content or slag content increases the C-A-S-H phases in AAMs. This would also enhance the tortuosity in AAM concrete. This behaviour can be observed in Fig.2-58(b) where increases in compressive strength decrease the chloride ion penetration in concrete [144].

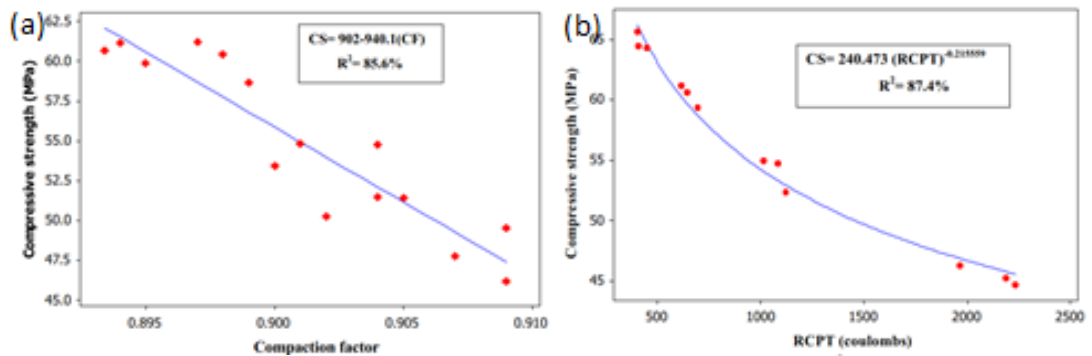


Fig. 2-58 (a) Relationship between compaction factor and 28 days compressive strength (b) Relationship between compressive strength and RCPT at 28 days

The effect of precursors on the total porosity and compressive strength of AAM concrete is shown in Fig. 2-59(a). In comparison with slag and metakaolin based AAM concrete, metakaolin/slag based blended AAM concrete showed lower porosity and higher compressive strength. The formation of C-N-A-S-H gels in blended AAM mixes enhances compressive strength and decreases the porosity. Similarly, the water

permeability also decreased with the increase in slag content in metakaolin based AAM concrete [145].

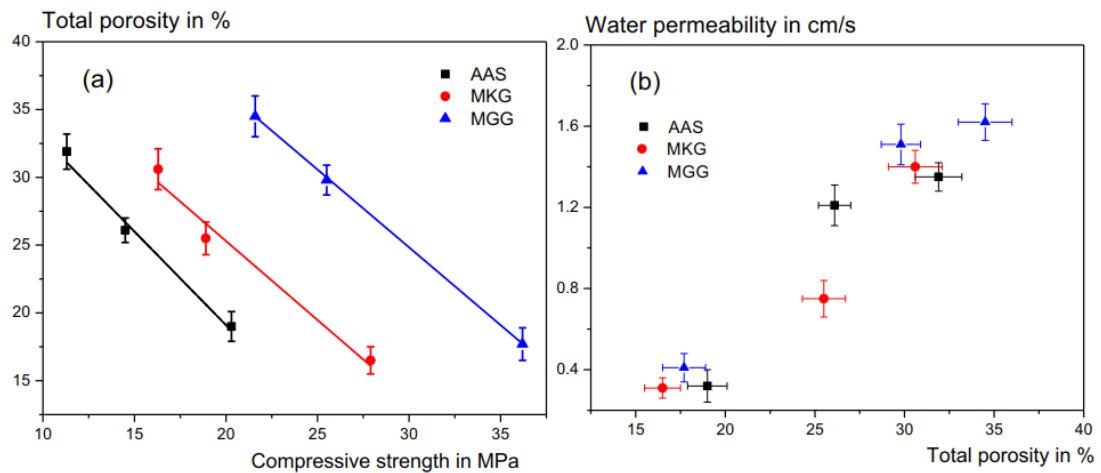


Fig. 2-59 Correlation of (a) total porosity-compressive strength and (b) total porosity-water permeability of slag (AAS), metakaolin (MK) and metakaolin/slag (MGG) pervious concrete.

From the literature, it can be observed that carbonation, leaching, efflorescence and chloride penetration is all dependent on the permeability behaviour of AAM concrete. Also, the overall trend of permeability is the function of porosity, size of pores and tortuosity of the pore network. Low porosity and degree of tortuosity in the AAM concrete significantly affect the durability behaviour of AAMs.

2.2.6 Leaching behaviour

Leaching is a phenomenon, in which reacted products inside the geopolymer gel flow out in the presence of a liquid medium. Leaching depends on the pH of the liquid medium, working temperatures, and dissolution rate of aluminium and silicon.

Studies have reported the leaching kinetics of metakaolin, using 5 or 8M NaOH at 25 or 85 °C as working temperatures. Atomic absorption spectrophotometer (AAS), Inductively coupled plasma (ICP), XRD and MAS-NMR and liquid NMR techniques were extensively used in this study to understand the reaction kinetics [46]. These techniques have confirmed the formation of N-A-S-H gel and the dissolution of reactive compounds (Si and Al) at an early stage of alkali activation. On the other hand, liquid NMR spectra of geopolymers did not reflect the formation of the final structure of reaction products [46].

Metakaolin samples were mixed with 5N and 8N NaOH (1 MK: 25 solutions). The solutions were stored at 25 °C or 85 °C and assessed at time intervals from 10min to 36 days. ICP analysis was conducted on these samples, leaching of Si and Al in 25 °C solutions (≈ 5000 ppm) were higher compared to 85 °C solutions (≈ 3000 ppm). This shows that temperature significantly influences the leaching behaviour of AAMs. They have reported the formation of silica ($\text{SiO}_2(\text{OH})_2^{2-}$ and $(\text{SiO}(\text{OH})_3)^-$ along with the formation of aluminium phases ($\text{Al}(\text{OH})_4^-$ monomers in liquid NMR techniques. The MAS-NMR studies on solid phases showed the unreacted MK, Si and Al phases during the leaching period. However, the temperature played a significant role here, the amount of unreacted Si and Al phases in the specimens activated at 25 °C were higher compared to the specimens activated at 85 °C [46].

The GGBFS samples were activated with deionised water, 0.01M, 0.1M and 1.0 M NaOH solutions. ICP and atomic absorption spectroscopic techniques were used for leachate analysis. The concentrations of cations (Ca, Si and Al) leached at different time intervals were quantified. It was observed that, at higher concentrations of NaOH, leaching of calcium ions was decreased. However, at higher concentrations of NaOH, Si and Al leaching were increased [146].

The change in pore diameters of binder specimens using mercury intrusion porosimetry (MIP) before and after leaching is shown in Fig. 2-53. Before leaching, the pure FA binder specimens show the highest fraction of pore diameters varying from ~ 30 nm and 13 nm before leaching. After leaching the 13 nm pores showed decreasing trend and those at 30 and 60 nm, which is attributed to the dissolution of binder mixes. The specimens with 30wt.%, 70wt.% and 100wt.% slag showed pore diameters below 10 nm, which significantly lower compared to FA based AAMs. After leaching, binder mixes with slag content showed a significant decrease in pores. The specimens with 30 and 70wt.% slag content showed an increase in pores with 100-1,000 nm diameter. This may be because of the leaching of hydration products and binder gel.

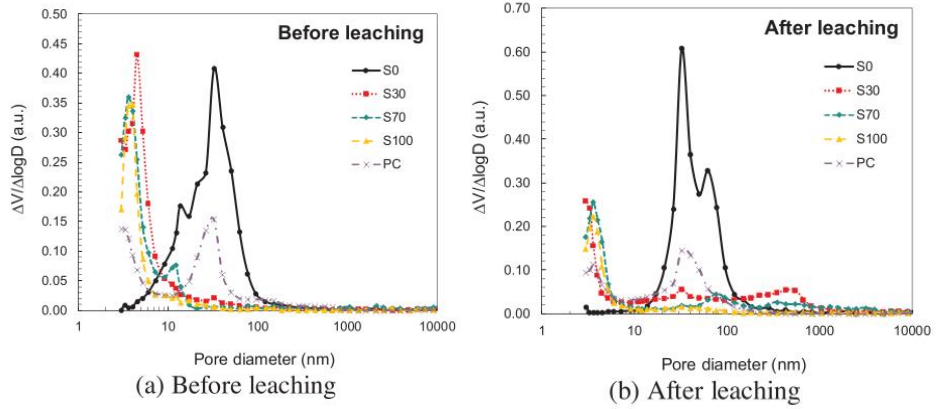


Fig. 2-60 First derivative of the cumulative pore volume of alkali-activated cements (a) before and (b) after accelerated leaching as determined by MIP [147].

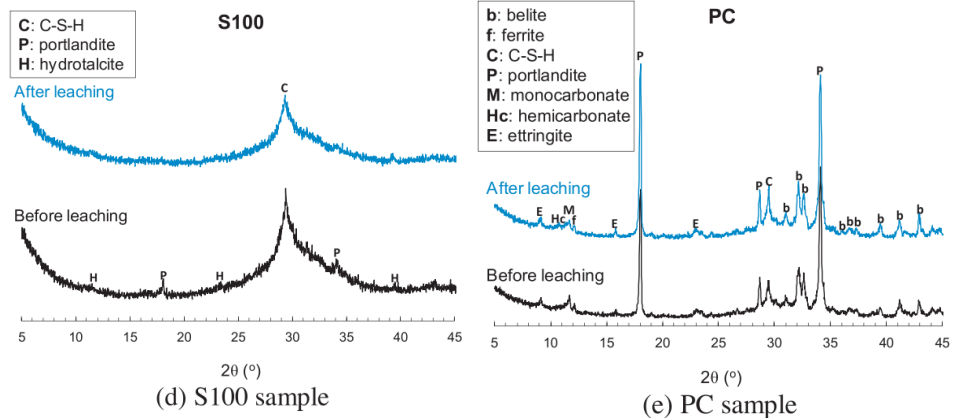


Fig. 2-61 XRD patterns of the (d) S100 and (e) PC samples before and after accelerated leaching [147].

The XRD patterns of AAMs before and after leaching is shown in Fig. 2-54. After activation, phases such as C-A-S-H, portlandite and hydrotalcite were observed. Significant reduction in N-A-S-H/C-A-S-H gel was observed after leaching, which indicates the dissolution binder and hydration products under leaching conditions, which is consistent with MIP studies. [147]

2.2.7 Efflorescence

Deposition of salts on the surface of bricks, mortar and concrete under natural and artificial environment is regarded as efflorescence. The formation of salt crystals on the surface may be because of material constituents or surrounding environment and the chemical reaction that caused evaporation of moisture and formation of the salt solution [149,150]. In traditional cement-based materials efflorescence is the reaction between $\text{Ca}(\text{OH})_2$ inside the pozzolanic material and CO_2 to form CaCO_3 crystals.

This process goes through six distinct stages from the diffusion of CO_2 inside the cement matrix and formation of aqueous species, alkali release, $\text{Ca}(\text{OH})_2$ dissolution, diffusion of reactants through the solution and precipitation of CaCO_3 [151].

In AAMs made of Class – F FA (low calcium) consists of open microstructure and porosity. Unreacted reaction material inside the matrix reacts with CO_2 to form hydrous alkali carbonate and appears on the surface of AAMs through moisture transfer (Fig. 2-55 and Fig. 2-56). The high porosity, high alkalinity of pore solution and weak binding property of alkali ions in AAMs cause more efflorescence than OPC [149,152–154].

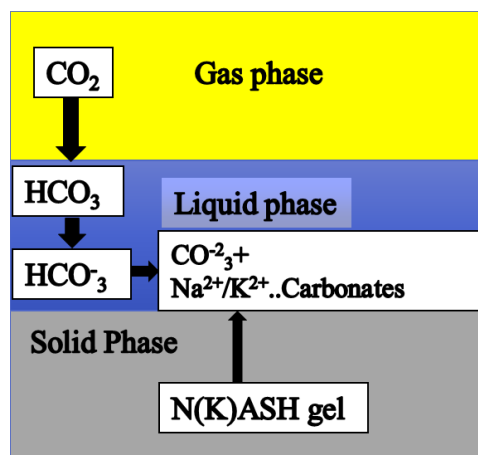


Fig. 2-62 Schematic diagram of efflorescence process in AAMs.



Fig. 2-63 Alkali-activated metakaolin specimens exposed to efflorescence condition

[148]

Many researchers have reported that efflorescence products (whitish) are not detrimental but aesthetically undesirable and not expansive [93,151]. In contrast, other studies (considering environmental factors) have reported that efflorescence products precipitated on the concrete surface might be not harmful and can be easily removed by washing the surface. However, subfluorescence (efflorescence below the surface can form following crystals $\text{Na}_2\text{CO}_3 \cdot n\text{H}_2\text{O}$, NaHCO_3 , K_2CO_3 and KHCO_3) can induce stresses to the surrounding, this can be harmful to the structure [93,155]. Other studies have reported that the formation of CaCO_3 crystals during efflorescence in FA–blast furnace based AAMs can significantly affect compressive strength, microstructure, shrinkage behaviour, reduction of alkaline pH in the pore solution and steel reinforcement corrosion. These studies show that efflorescence is a durability issue and not an aesthetic issue [93].

Efflorescence can be controlled by adjusting the chemical composition of alkali activators; changing curing conditions (temperature curing or hydrothermal curing) and using different admixtures to form a dense microstructure of AAMs. The addition of alumina in metakaolin/slag-based blends and hydrothermal curing reduced the efflorescence effect. This method improves the dissolution rate of Al species, cross-linking of N-A-S-H gel, mechanical properties and constrains the mobility of ions alkali ions from further reactions. Curing AAM specimens at 65 °C could initiate local reorganization and crystallization of geopolymer gels, this can reduce the efflorescence rate [156].

The type of alkali activators also influences the efflorescence rate, alkali contents like Na_2O and soluble Si content present in the activator solution can restrict efflorescence rate at curing temperature 25 °C (room temperature) and promotes efflorescence at 80 °C. This is because of the distribution of finer pore sizes in AAMs at curing temperature 25 °C, than in specimens cured at 80 °C. Authors have suggested that the presence of a low quantity of sodium or potassium and Ca^{2+} ions in the formation of C-S-H gel reduced the efflorescence rate in FA (32wt.% - 60wt.%) and Portland cement (30wt.% - 40wt.%) blends [157]. The SEM images of efflorescence products such as carbonates formed on the binder specimens are shown in Fig. 2-57. The reaction between alkali pore solution and atmospheric CO_2 led to the formation of hydrated carbonates, after efflorescence [158].

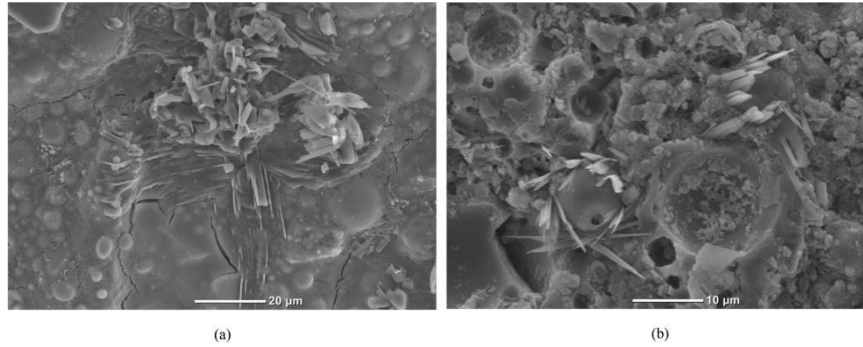


Fig. 2-64 SEM images of the efflorescence products: (a) on the surface of 28-day air aged GPC-NS1.5, and (b) the carbonation products on a fracture surface [158]

Studies show, the use of KOH over NaOH as an activator to reduce the efflorescence rate because potassium ions strongly interact with geopolymer gel phases [159]. In contrast, other studies have reported the leaching of sodium and potassium ions from N(K)ASH gel, without comprising compressive strength [153]. Other studies have observed the strong Na-O interactions in partially formed Na-O-Al (Si) structure and weak interactions of Na with water molecules in the form of $\text{Na}(\text{H}_2\text{O})^{n+}$. According to this investigation, the authors are sceptical about the earlier leaching investigation report. They have proposed a hypothesis that alkalis in the geopolymer gel exist in two different states and each state has its leaching rate [156]. The compressive strength and compressive modulus of binder specimens before and efflorescence exposure is shown in Fig. 2-58. There was a slight increase in compressive strength in binder specimens exposed to air. However, the binder specimens partially and fully immersed in water showed a decreasing trend in compressive modulus and strength, which indicates the degradation of hydration and binder gel when exposed to efflorescence conditions [158].

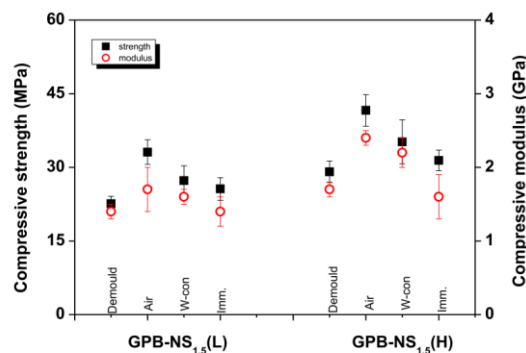


Fig. 2-65 Compressive strength of geopolymer specimens activated with sodium silicate [158]

The interesting fact is that the differentiation between efflorescence and the natural carbonation process is still unclear. Some authors claim that both are different because carbonation involves pH reduction, gel deterioration and formation of carbon reaction products in the cement sample, which may or may not be visible in natural conditions. On the other hand, efflorescence involves the precipitation of salts that are visible to the naked eye [149,159]. However, recent studies are reporting the reduction of pH, deposition of alkali salts on the surface and acceleration of corrosion process as the outcomes of the efflorescence process. These conditions may be detrimental for some of the AAMs properties. Moreover, reduction (diffusion towards the surface in the form of salts) of alkali ions in the pore structure during efflorescence will hinder the formation of geopolymer gel at later stages [155,156].

By considering the facts mentioned by several authors, the studies related to microstructure and compressive strength after efflorescence or during efflorescence has not been investigated.

2.3 Molecular dynamics simulations

The geopolymerization process depends on oligomer formation and the stability of the gel formed. Dissolution of aluminosilicates and repolymerization can be considered as one of the complex and important reactions to be understood. There are quite a few attempts made by researchers to understand the key mechanism behind the transformation of aluminosilicates solution in an alkali media into the geopolymer gel. However, experimental methodologies to understand the exact mechanism of atomistic reactions occurring at the evolution of geopolymer gel has made research challenging. Most of the experimental methods are unable to effectively provide the information because of the quick and complex nature of the reaction and transition [25,26,46,160,161].

In recent decades, continuum mechanics approaches like Finite element methods and granular mechanics were used in predicting the macroscopic properties of granular materials like solids. Most of these methods fail to predict the nature of materials because of several factors like particle size variation, irregular geometry, geological formation, chemical composition, and environmental history [162]. Hence, it requires a fundamental understanding of the nature of the material at the micron and sub-micron level to predict its macroscopic properties. Approaches like Discrete Element

techniques are used to explain the behaviour of particulate matter. But these methods fail to predict atomic and molecular properties of any material, to explain, molecular level reactions, phase transitions and interaction energies involved in any complex interactions [163].

Molecular Dynamics (MD) simulations and Monte Carlo (MC) simulations are widely used computational techniques to predict the atomic properties of materials. These methods overcome the limitations of Discrete and Finite element methods. For the modelling of geopolymer gel evolution, molecular dynamics simulations would be one of the effective tools [163].

Molecular dynamics (MD) simulation is a computational method that is used to determine the trajectories of atoms and molecular interactions using Newton's laws of motion. MD simulations were first used by Stillinger and Rahman (1974) to simulate water. MD technique is based on Newton's second law of motion $F = ma$, where 'F' is the force exerted by on an atom, 'm and a' are the mass and acceleration of an atom. For the set of 'N' number of atoms, the second law of motion can be denoted using Equation 2-1 [163]:

$$m_i a_i = - \frac{dU_{total}}{dr_i} = F_i \quad (2-1)$$

Where m_i and a_i is the mass and acceleration of an atom I respectively; U_{total} or $E_{system} = E_{bond} + E_{over} + E_{under} + E_{val} + E_{pen} + E_{tors} + E_{conj} + E_{vdwals} + E_{Coulomb}$ is the total potential energy of the system, r_i is the position of an atom i and F_i is the force exerted on atom i . Recent studies have reported that the elastic modulus of MD simulated geopolymers increases with the increasing Si/Al ratios. They have also reported that the failure of geopolymer gel is initiated by the failure of Al-O bond breakage. Besides, ultimate tensile strength and elastic modulus of geopolymer gel were recently reported by researchers by performing MD simulations. They have reported that ultimate tensile strength is directly proportional to Si/Al ratios. The water content in the geopolymer network had no significant effect on the Si-Al network. However, the presence of water in geopolymer cavities influenced the deformation dynamics of geopolymers. Also, water content enhanced the diffusion coefficient of Na ions [164–166].

Table 2-2 shows the details of MD simulation studies run on N-A-S-H, using simulator packages like LAMMPS, Material studio and TREMOLOX. Also, much of the works carried to measure mechanical properties of N-A-S-H and C-A-S-H gels. However, developing an accurate MD model that depicts the behaviour of the N-A-S-H system is not straightforward because of the disordered nature of reaction products [167]. Some researchers tried to produce mechanical properties of N-A-S-H and C-A-S-H phases. Fig. 2-59 shows the composite of geopolymer-C-S-H gel with $\text{Ca/Si} = 1.65$. Table 2-3 shows the interatomic or potential parameters of distinct species of N-A-S-H gel [168]. LAMMPS software used to run these simulation and ReaxFF forcefields were used to simulate the breaking of bonds. Fig. 2-60 shows the failure of the GB-C-S-H composite under tensile stress, the stress-strain properties are shown in Fig. 2-61 as a function of Ca/Si ratios, the composite with $\text{Ca/S} = 1.2$ exhibited higher mechanical strength [169].

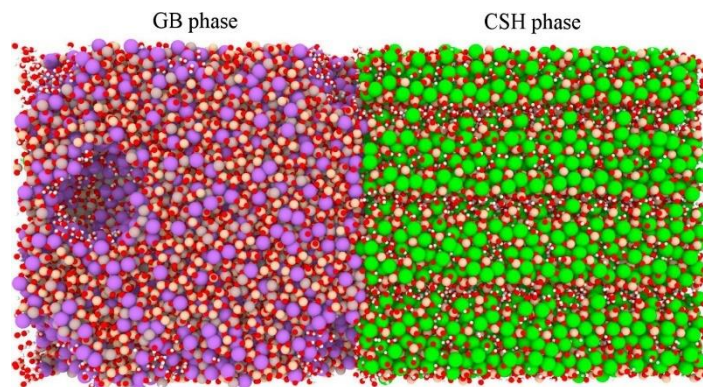


Fig. 2-66 A vertical section of composite GB-C-S-H1.65 ($\text{Ca/Si} = 1.65$) with the silica layers in C-S-H oriented perpendicular to the interface: green = Ca, gold = Si, grey = Al, red = O, white = H, purple = Na [169].

Because of the amorphous nature of N-A-S-H gel, it is challenging to develop an accurate MD model and it needs more thermo-chemical details, which cannot be represented through classical forcefields. However, recent developments in reactive forcefields are shown some promising results which describe the bond formation and breaking during polymerization. However, significant gaps still exist in the behaviour of N-A-S-H gel in MD and experimental results. Because of variation like precursor and activator, it is still challenging to get accurate mechanical properties. In addition to this, the development of suitable forcefields and molecular description is required to produce an accurate MD model [167].

Table 2-2 Simulation details of N-A-S-H geopolymer gels.

Study	Platform	Model	Density	Potential	Ensemble	Research Target
Kupwade-Patil et al. 2013	Materials Studio	Connected N-A-S-H chains	1.06 g/cm ³	COMPASS (Non-reactive)	NPT, NVT	Gel properties
Sadat et al. 2016	LAMMPS	3D N-A-S-H network	Not given	Buckingham Potential (Non-reactive)	NVE, NPT, NVT	Gel properties
Sadat et al. 2016	LAMMPS	NAS glass	Not given	Morse potential (Non-reactive)	NVT, NPT	Gel Properties
Bagheri et al. 2017	Materials Studio	N-A-S-H oligomers	About 2.00 g/cm ³	Dreiding (Non-reactive)	NPT	Gel Properties
Wan et al. 2017	Materials Studio	No details	1.04 g/cm ³	Not given	NPT, NVT	Binding energy
Bagheri et al. 2018	Materials Studio	N-A-S-H layered structure	Not given	COMPASS (Non-reactive)	Not given	Ion diffusion
Sadat et al. 2018	LAMMPS	3D N-A-S-H network	Not given	Morse & Buckingham Potentials (Non-reactive)	NPT, NVT	Mechanical properties
Sadat et al. 2018	LAMMPS	3D N-A-S-H network	2.08 g/cm ³	ReaxFF (Reactive)	NVT, NPT	Mechanical properties
Zhang et al. 2018	TREMOLO-X	Silicate and aluminate monomers	1.32 g/cm ³	Feuston and Garofalini potentials (Reactive)	NVT	Polymerization
Lolli et al. 2018	LAMMPS	Crystalline, amorphous and defective crystal structures	1.66, 2.13 and 2.28 g/cm ³	ReaxFF (Reactive)	NPT, NVT	Mechanical properties
Zhang et al. 2018	LAMMPS	NAS glass	2.59 g/cm ³	ClayFF (Non-reactive)	NVT	Ion adsorption
Hou et al. 2018	LAMMPS	NAS glass	2.59 g/cm ³	ReaxFF (Reactive)	NVT, NPT	Polymerization & gel properties
Lyngdoh et al. 2019	LAMMPS	Albite mineral	1.825 and 2.120 g/cm ³	ReaxFF (Reactive)	NPT, NVT	Polymerization & gel properties
Hou et al. 2020	LAMMPS	NAS glass	2.41 g/cm ³	ClayFF (Non-reactive)	NVT	Ion immobilization
Wang et al. 2020	Materials Studio	Na ₂ SiO ₅ glass	2.69 and 2.94 g/cm ³	COMPASS (Non-reactive)	NPT, NVT	Gel Structure
Chitsaz et al. 2020	Materials Studio	Walkley oligomer model	1.7 g/cm ³	Universal (Non-reactive)	NVT	Gel modulus

Table 2-3 Interatomic potential parameters used for M (Si/Al/Na)–O_h and O_h–H interaction.[168].

Atoms	Charge	Atoms	Charge
Al	+1.8	O _h	-0.856
Na	+0.6	H	+0.256
2-body Buckingham potential parameters			
Atomic pair	A (eV)	P (Å)	C (eV Å ⁶)
Si-O _h	12433.827	0.193817	54.681
Al-O _h	9701.4170	0.195628	31.997
Na-O _h	2629.3649	0.258583	33.831
O _s -O _h	2029.2233	0.343645	192.58
O _h -H	100.0	0.25	0.0
Morse potential parameters			
Atomic pair	D (eV)	A (Å ⁻¹)	r ₀ (Å)
O _h -H	7.0525	1.8	0.9485
a Structural oxygen; b Hydroxyl oxygen			

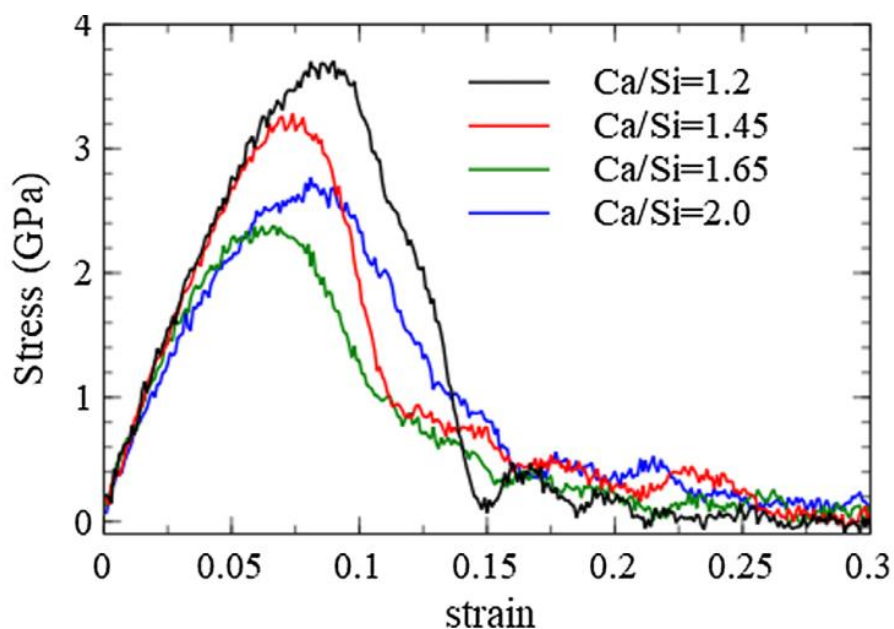


Fig. 2-67 Stress-strain curves of GB-C-S-H composites at different Ca/Si ratios and with a crack of $2a = 20 \text{ \AA}$ and thickness of 4 \AA . [169].

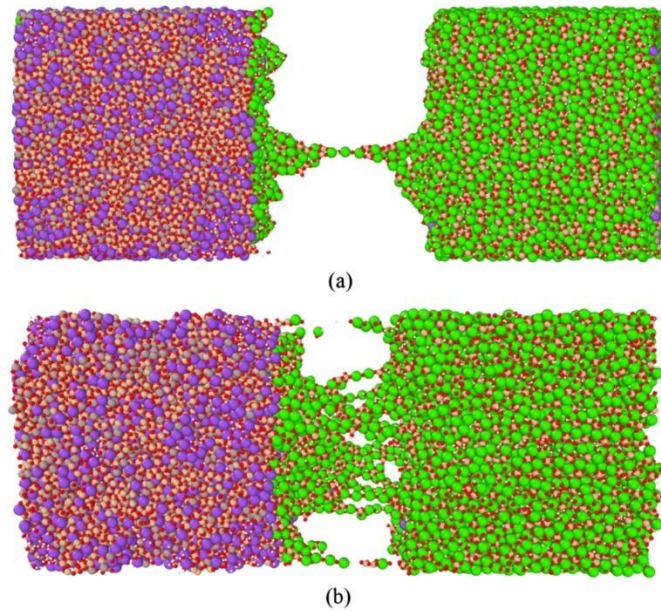


Fig. 2-68 Failure of GB-C-S-H1.45 ($\text{Ca/Si} = 1.45$) composites for interface (a) parallel and (b) perpendicular to SiO_2 layers in C-S-H.

2.4 Literature summary and conclusions

The reviewed literature shows that AAMs qualify as construction materials. However, most of the existing literature focused on using a diverse range of several precursors, alkaline activators, mixing parameters, and curing temperatures. Parametrical and cementitious mechanical properties and durability of AAMs were determined to gain an understanding of the effect of the aforementioned materials and process parameters. Following are some of the key highlights of the literature survey.

In general, AAMs are prepared with precursors such as FA, slag, metakaolin and their blends. Depending on the type and dosage of precursors the AAM phases formed. In slag activated materials C-A-S-H is the dominant reaction product and N-A-S-H is in FA based AAMs. The phases such as N-(C)-A-S-H and C-(N)-A-S-H would be developed as the final binder mixes, which is the function of FA and slag dosages. Also, sodium-based activators for Na based aluminosilicates and potassium-based activators develop potassium-based aluminosilicates. The activator concentration also plays a key role in AAM mixes. The higher activator concentration in FA-slag binder mixes leads to higher pH, which hinders/delay the precipitation of C-A-S-H gel.

The properties such as compressive strength higher slag based AAMS compared with FA and metakaolin based AAMs. The development of C-A-S-H gel in slag based AAMs significantly contribute to mechanical properties. The presence of higher MgO

content in slag significantly contribute to the compressive strength and develop Ca-Mg based phases such as hydrotalcite.

Significant works have been carried to understand the durability behaviour of AAMs. The carbonation behaviour of AAMs has been significantly addressed in the literature. The effect of precursors, activators, the concentration of CO₂ and RH studies suggest that 1% CO₂ and 65±5% RH is adequate for the carbonation process. The carbonate phases such as trona, nahcolite, natron, hunite, gaylussite, sodium carbonates and sodium bicarbonates are some of the observed phases under carbonation. These phases are formed because of the reaction between atmospheric CO₂ and N-A-S-H/C-A-S-H gel. The presence of hydrotalcite phases significantly reduced the carbonation process and carbonation depths in alkali-activated slag and its blends. The use of sodium silicates is another factor that significantly reduces the carbonation process in AAMs.

AAMs performance is better against chloride and sulphate penetration. The presence of phases such as hydrotalcite plays a vital role in binding free chloride content in AAM specimens, which would slow down the corrosion of rebars in AAM concretes. Sodium chloride and Friedel's salts are some of the commonly observed phases in AAMs exposed to an excessive chloride environment. The AAMs performed better in the sodium sulphate environment, compared with the magnesium sulphate environment. The presence of Na₂O content in sodium sulphate contributes to the structural evolution of AAMs. When AAMs exposed to magnesium sulphate significant deterioration was observed because of the degradation of structural gel and formation of Mg-based phases and ettringite during the exposure. AAMs exposure under freeze and thaw resistance showed some significant damages after 50 cycles. However, research studies related to this area is quite limited.

The performance of AAMs under leaching is less known and fewer studies are available. The FA and FA-slag based performed better in leaching environment compared with pure slag-based environments. There was a slight dissolution of C-A-S-H gel in AAM in slag based AAMs. The ²⁹Si and ²⁷Al environment also showed significant degradation of the N-A-S-H/C-A-S-H environment.

Efflorescence behaviour of AAMs is another phenomenon that is less understood. When AAMs exposed to efflorescence natural carbonation, leaching and efflorescence

process takes place simultaneously. Hence, it is challenging to decouple these reactions in a simulated environment. However, some works show the use of slag in AAMs restrict the movement of free alkalis in AAMs. Carbonate salts are observed as the by-product of efflorescence behaviour. However, complete information about the evolution of phases during efflorescence is absent in the literature.

MD simulation is a powerful tool to understand the phase formation, degradation, and mechanical properties at the atomistic scale. However, the lack of an accurate description of the formation and behaviour of N-A-S-H gel and studies related to the development of potential parameters for AAMs is limited. Hence, the MD simulation of AAMs is another area where significant works related to AAMs is limited.

A range of experimental methodologies and properties and variations in durability is seen in AAM behaviour. Furthermore, a general lack of standard testing methods and standard code of practices further perplex practising engineers and researchers, weakening confidence in using AAMs for structures. These aspects and the associated limited directionality have diminished the commercial value and applicability of AAMs in the building and construction industry.

Following are the research gaps identified from the literature.

- Existing standards on the long-term behaviour of AAMs are often compared with OPC standards. The difference in binder chemistry and structure between OPC and AAMs could induce errors while adopting these standards.
- Most of the existing literature on carbonation discuss the behaviour of AAMs under accelerated carbonation ageing. The published results related to the natural carbonation of AAMs are limited. Besides, investigation on the effect of gel chemistry, CO₂ concentration, RH factors, and correlation of atmospheric and accelerated CO₂ condition is required.
- The rate of alkali leaching from AAMs hardened paste needs further investigation. These studies would be successful in providing important insight into long-term performances and reaction processes at different AAMs.
- The studies on the effect of efflorescence on FA and low calcium FA-Slag based AAMs is limited. Furthermore, the effect of FA/slag ratio, activator

content, long-term exposure, and different activators on phase changes under efflorescence is required.

- The studies related to the effect of, the effect of FA/Slag ratio, activator content, long term exposure and different activators on phases changes under long term leaching needs further investigation.

CHAPTER 3 OBJECTIVES AND CONCEPTUAL FRAMEWORK

3.1 Objectives

The comprehensive analysis of the behaviour of FA/slag based AAMs under efflorescence and leaching conditions is the focus of this thesis, with a concentration on how phases such as N-A-S-H and C-A-S-H gels dictate mechanical properties.

This thesis aims to address a long-standing challenge of correlating phase degradation of reaction products with mechanical properties under efflorescence and leaching conditions. From a precursor standpoint, the effect of calcium content in slag, and the effect of Na₂O content on efflorescence and leaching are investigated, correlating them with N-A-S-H and C-A-S-H gel formation in the AAM binders.

The four specific objectives are detailed as follows:

1. Effect of activator content on efflorescence behaviour of AAMs

The Na₂O content in AAMs varies between 3-10 wt.%. A higher alkali content in AAMs will result in binder mixes with better mechanical properties. The presence of higher alkali content leads to higher efflorescence formation, further leading to phase degradation and decreased mechanical properties. The following sub-objectives were evaluated in this objective.

- Effect of Na₂O on compressive strength and split tensile strength of FA/FA-slag based AAMs.
- Effect of Na₂O content on efflorescence rate and residual mechanical properties.
- Effect of alkali content on the phase changes of FA-slag based AAMs under efflorescence.

2. Effect of slag content on efflorescence behaviour of AAMs

The presence of calcium content in the precursor material (blast furnace slag and FA) or external addition of calcium content to low calcium precursor material and activating using an alkaline solution (Na₂CO₃, NaOH, Na₂SiO₃ and Na₂SO₄) improves the physical properties (compressive strength and low porosity) of hardened AAM pastes. This behaviour is attributed to the coexistence of both N-A-S-H and C-A-S-H gel in the mix. From the literature review, it can be inferred that leaching and efflorescence in C-A-S-H gel affect structural properties. The increased concentration of calcium content replaces the activated product from N-A-S-H gel to C-A-S-H gel

gradually. At an intermediate calcium content, both C-A-S-H and N-A-S-H gels co-exist.

The effect of slag/calcium content in AAMs under efflorescence condition was evaluated in this objective. The following mechanisms were assessed in this objective.

- Effect of slag/calcium content on mechanical properties, before and after efflorescence.
- Effect of slag/calcium content on the phase changes under efflorescence condition.

3. Effect of slag content on leaching behaviour of AAMs

The addition of slag refines the pore structure. Thus, contributing to the lower porosity of AAMs. The immersion of AAMs specimens in water for a prolonged period can leach the Na^+ , Ca^{2+} , Al^{3+} and Si^{4+} ions from the binder structure. The leaching of several ions changes the microstructure, phases, and mechanical properties. The following mechanisms would be evaluated in this objective.

- Effect slag/calcium concentration on leaching behaviour of alkali ions and phase degradation of C-A-S-H gel under leaching exposure in AAM pastes.
- Effect of slag on the relationship between porosity, mechanical properties and leaching of alkali ions in AAM pastes.
- Effect of slag on leaching potential Na^+ , Ca^{2+} , Al^{3+} and Si^{4+} ions from AAM binder pastes

4. Effect of Na_2O content on leaching behaviour of AAMs

The aluminosilicate network formed at the end of geopolymer reaction consists of sodium-aluminosilicates. Most of the other reaction products or residual ions will reside in the porous network of three-dimensional aluminosilicate structure [170]. The removal of alkali ions alters the aluminosilicate network. Also, Na^+ ions significantly interact with the AlO_4 groups of the aluminosilicate structure to balance the negative charge. The removal of alkali ions under leaching significantly change the N-A-S-H/C-A-S-H structure.

To understand the leaching behaviour of AAMs AAS, FTIR, MAS-NMR, XRD and MD simulations were performed. This objective is aimed at understanding the effect of Na_2O content on the leaching of AAMs through experimental and MD simulation studies. Following key mechanisms addressed in this study.

- Effect of Na₂O content on leaching behaviour of AAM binder pastes and phase degradation of N-A-S-H/N-(C)-A-S-H gel under leaching
- Effect of Al/Si ratio and Na₂O content on leaching behaviour of AAMs through MD studies.
- Computation of non-bonded interaction between Al-O, Si-O, alkali ions and water
- Computation of non-bonded interaction energies between Na – (Al-O) ions under leaching condition

3.2 Conceptual framework

The research conducted in this body of work is depicted as a conceptual design diagram (Fig. 3-1). The chemical composition of FA and slag were determined using X-ray fluorescence technique and XRD studies. The precursors were blended with suitable activators and the water/solid (w/s) ratio was fixed through trial and error. The compressive strength of binder pastes was measured after 7 and 28 days of curing. The w/s ratio, activator content and precursor ratios of the binder mixes were redesigned if the compressive strength of binder pastes failed to reach the adequate level (20-50 MPa). After measuring compressive strength the specimens were crushed and microstructural studies were performed. Once the acceptable level of compressive strength was achieved, the specimens were exposed to efflorescence and leaching conditions. The microstructural studies and mechanical performance on binder pastes were performed after efflorescence/leaching to correlate the relationship between phase changes and mechanical properties.

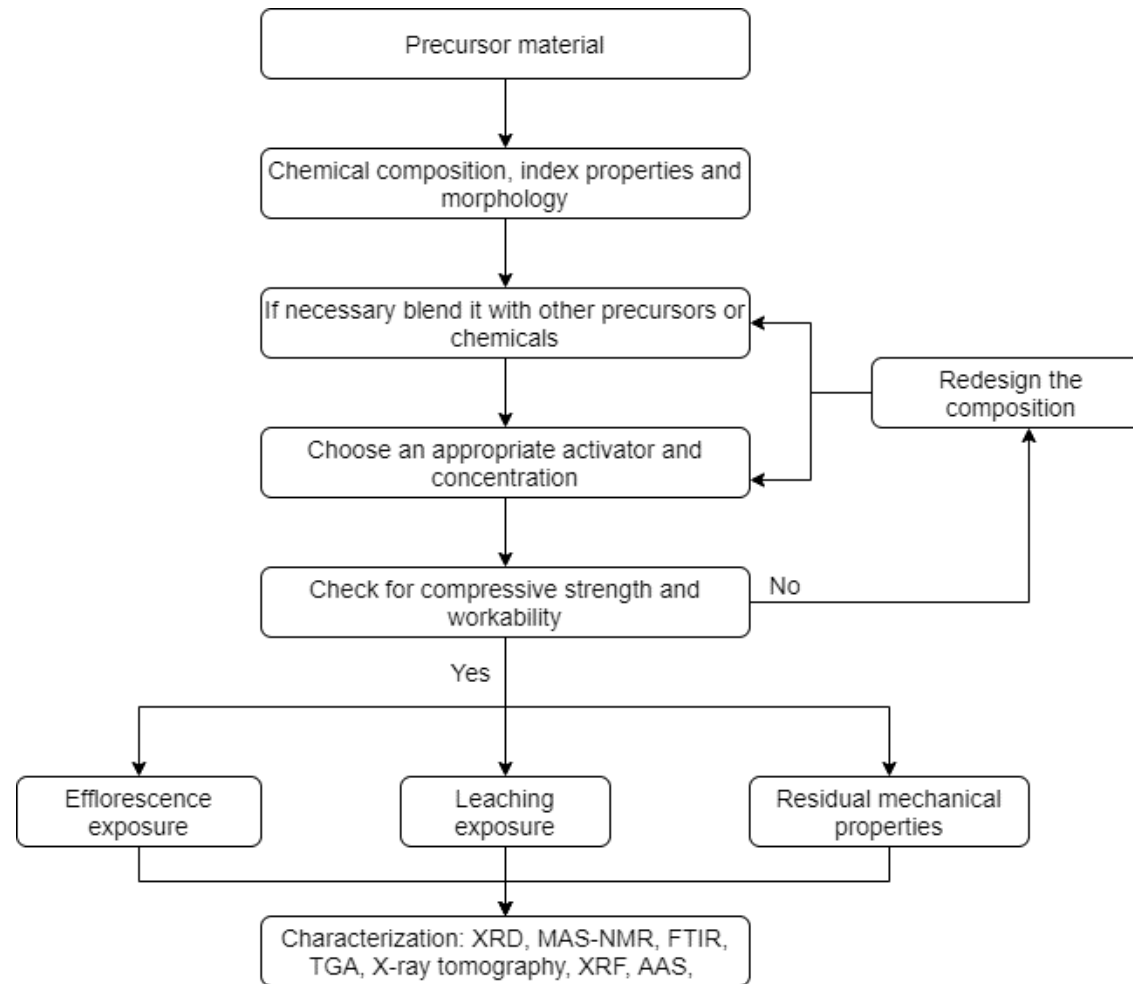


Fig. 3-1 Conceptual design flow chart for this body of work.

CHAPTER 4 METHODOLOGY

This chapter provides an overview of the basic properties of precursors, activators, characterisation details and techniques performed in this study. The specific details of mechanical property testing and characterization techniques are provided in Chapters 5-7.

4.1 Materials and methods

Alkali-activated materials synthesis consists of two types of materials, i.e., precursor and alkaline activator. The use of FA, ground granulated blast furnace slag, metakaolin and blending of different precursor materials according to requirements and binder chemistry is performed. In this study, FA with slag as precursor materials were used. FA and slag were obtained from Neilsen's group in Queensland, Australia. X-ray fluorescence (XRF) was used to determine the mineralogical compositions of FA and slag. According to ASTM C 618 [171], FA is categorised as class F and has a high concentration of SiO₂ and a low concentration of CaO. Laboratory grade NaOH pellets, Na₂CO₃ powder were obtained from Chemsupply Adelaide, Australia. Na₂SiO₃ solution (Na₂O = 14.7 wt.%, SiO₂ = 29.4 wt.% and H₂O = 52.7 wt.%) with M_s = 2.0 (SiO₂/Na₂O ratio) were obtained from PQ Australia, Dandenong, Australia.

4.1.1 Geopolymer synthesis

Geopolymer binders were prepared by mixing dry FA with calcium oxide and ferric oxide. Initially, dry FA was mixed in a Hobart mixer with dry calcium oxide for 2 min. The concentrations of calcium oxide were varied from 0wt.% - 30wt.% or [(Ca/Fe)/(Si+Al)] = 0 - 0.25 ratio. Sodium carbonate solution was added to this mixture and mixed for another 5 min. The M_s (SiO₂/Na₂O) was fixed at 1.4. Fresh geopolymer binder mix was poured into moulds of dimensions 25 mm diameter and 50 mm height. The specimens were cured at 25 ± 2 °C for 7 and 28 days.

The cured specimens were tested for compressive strength, leaching and efflorescence at specific timelines. The methodology of conducting these experiments is discussed in the next section. To attain the aimed compressive strength, efflorescence and leaching experiments were conducted on the geopolymer specimens. Fig. 4-1 shows

the tests conducted on binder specimens. The experimental methodology of the relevant experiments is discussed in subsequent sections.

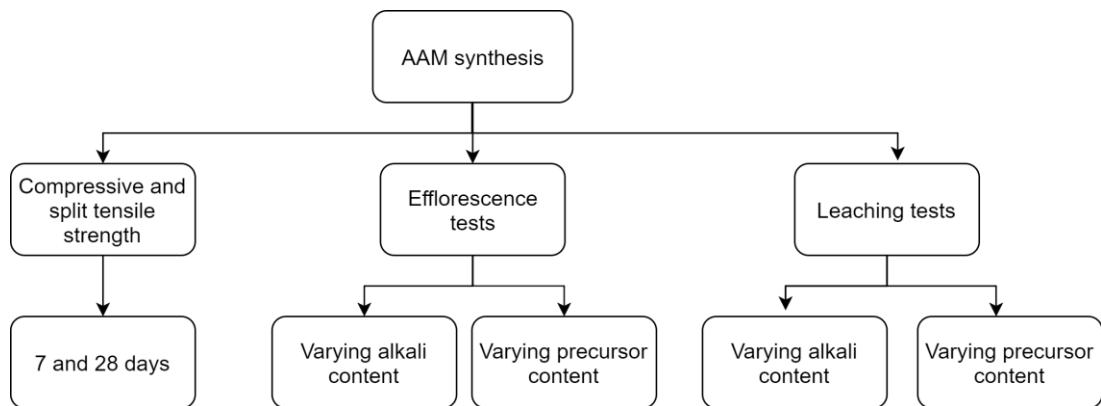


Fig. 4-1 Experimental flow chart of AAMs binder specimens

4.2 Property testing

4.2.1 Compressive strength and split tensile strength determination

The compressive strength of geopolymer specimens was determined using the material testing system or MTS following AS 1012.9:2014 Methods of testing concrete: Method 9: Compressive strength tests - concrete, mortar, and grout specimens. Cylindrical binder specimens were prepared with dimensions of 20 mm diameter \times 20 mm height (l/d ratio = 2) for split tensile strength determination. Cubic specimens with 30 mm \times 30 mm were prepared for compressive strength determination.

4.2.2 Efflorescence testes

AAMs specimens were subjected to natural efflorescence tests. The specimens were partially immersed in water to a height of 5 mm from the bottom surface and efflorescence were observed at different time intervals. The binder pastes and salt deposition on the specimens were assessed for microstructural analysis. Residual compression strength was measured after the tests at specific time intervals. Fig. 4-3 shows the efflorescence methodology showed used in this study.

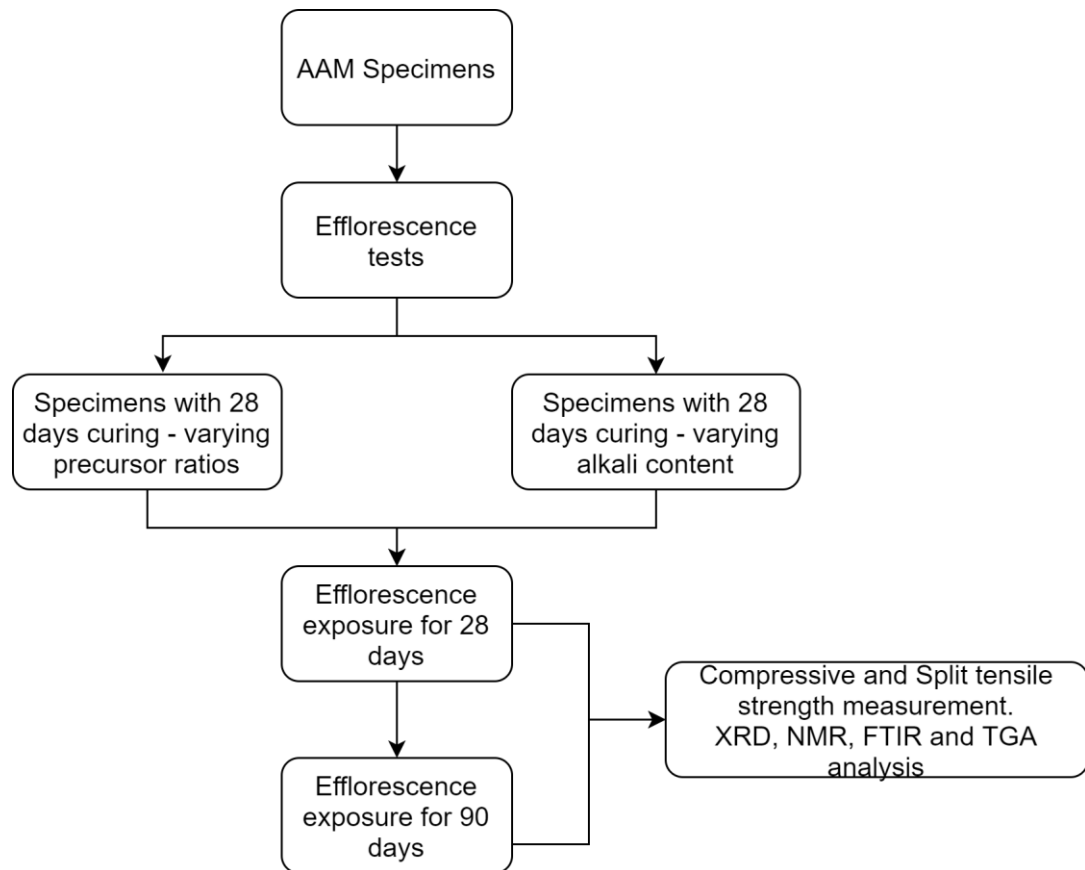


Fig. 4-2 Experimental procedure for efflorescence tests on AAMs samples

4.2.3 Leaching tests

Leaching tests were conducted on geopolymer specimens. The methodology is shown in Fig. 4-3. Atomic absorption spectrophotometer was used for the determination of alkali loss. XRD, FTIR and NMR tests were done on solid residues for the phase determination [46, 96-99].

4.3 Microstructural characterization

Characterization techniques like Atomic absorption spectroscopy (AAS), Fourier transforms infrared spectroscopy (FTIR), X-ray diffraction (XRD) and magic angle spinning – nuclear magnetic resonance were used in this study (MAS – NMR).

4.3.1 Atomic absorption spectroscopy (AAS)

AAS was used to determine Na^+ , Si^{4+} , Al^{3+} and Ca^{2+} ions in leachate. The initial calibration curve was prepared by alkali concentration in pure reagents. The concentration of alkali in the leachate was plotted against the calibration curve to determine the alkali concentration in the leachate [172,173].

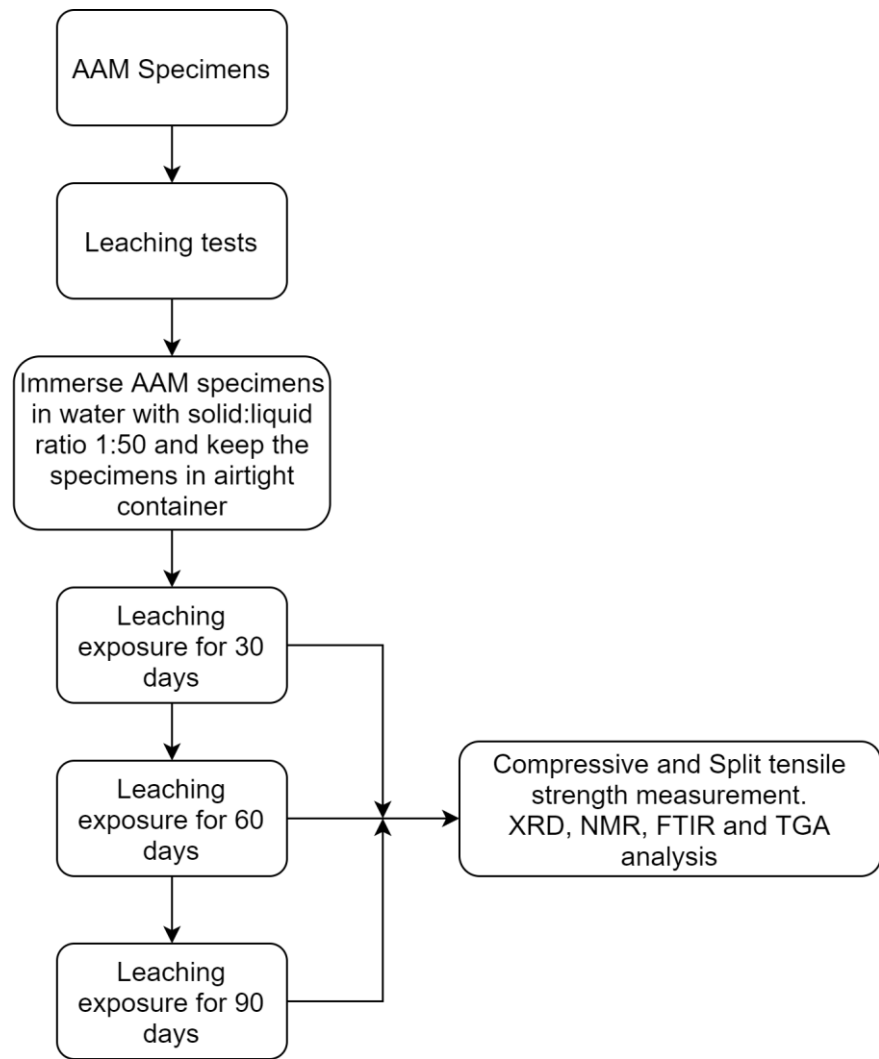


Fig. 4-3 Experimental procedure for leaching trials

4.3.2 X-ray diffraction studies

XRD patterns of powder samples were studied to identify solid phases present in geopolymer samples using Cu-K α radiation and scanned from 5° to 90° (2 θ) at a rate of 5° /min (with the step of 0.04). Obtained spectra were compared with the Joint Committee on Powder Diffraction Standards or JCPDS patterns to identify solid phases [174].

4.3.3 Fourier transform infrared spectroscopy (FTIR)

Crushed AAMs powder was taken and FTIR analysis was performed over the range 4000 – 400 cm $^{-1}$ [175].

4.3.4 Magic angle spinning – nuclear magnetic resonance (MAS – NMR)

Environments were generated around ^{29}Si and ^{27}Al to get MAS-NMR for the solid activated matrix. NMR spectra were recorded at 79.49 and 104.23 MHz (9.4T magnetic field), by spinning the samples at the magic angle ($54^{\circ}44'$) using an NMR equipped with a Fourier transform unit. 10000 cps was used as the spinning speed with pulse lengths of 4 μs and 215 μs and recycle delays were 10 s and 5s for ^{29}Si and ^{27}Al , respectively. Tetramethylsilane (TMS) for ^{29}Si and 1M AlCl_3 for ^{27}Al was used as representative samples. Chemical shifts were reported in ppm (parts per million) [46,96,97,150].

4.3.5 Conceptual molecular model

To accomplish the established objectives, the solvation model consists of alumina and silicates was built initially, and these models were equilibrated for several nanoseconds. Another solvation box of water molecules was built around the aluminosilicate-solvation model. Fig. 4-4 and Fig. 4-5 show the steps in the MD simulation and conceptual solvation model of aluminosilicates, respectively. This system was further equilibrated for a few nanoseconds before measuring atomistic properties. These simulation models were further expanded to understand the interaction of the aluminosilicate source in a sodium/calcium-rich environment. Not Another Molecular Dynamics (NAMD) [176] was used to perform MD simulations. Gaussian Version 9 [177] was used to develop the stiffness constants of the bond, angles and dihedrals of the structure. Virtual Molecular Dynamics (VMD) [178] was used for post-processing and interactive studies.

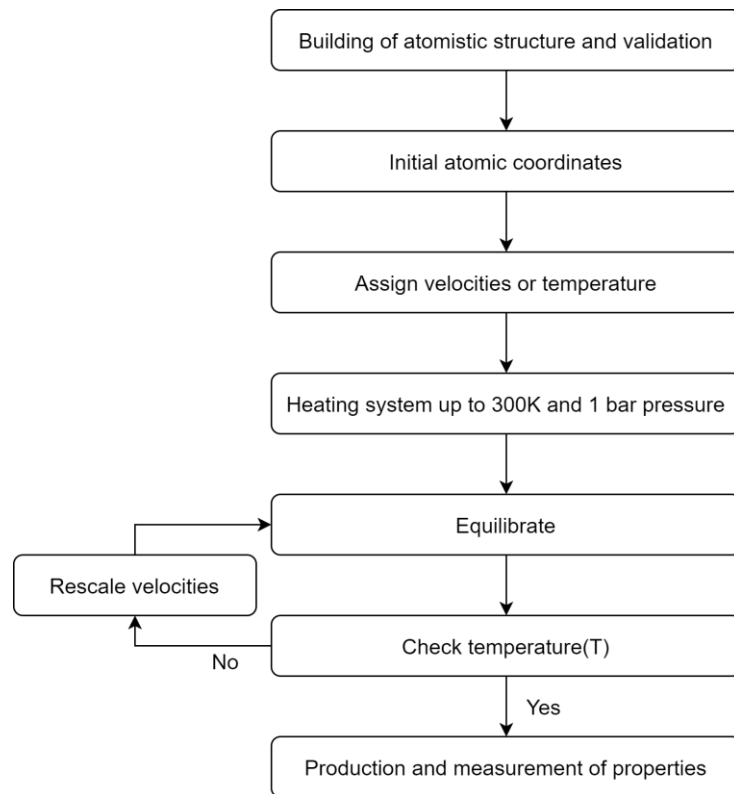


Fig. 4-4 Steps involved in MD simulations.

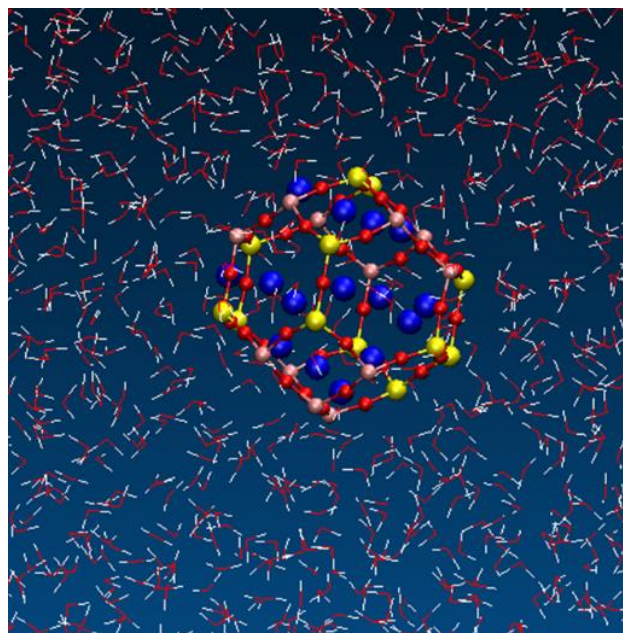


Fig. 4-5 Solvation model of aluminosilicate source

CHAPTER 5 PHASE CHANGES UNDER EFFLORESCENCE IN ALKALI-ACTIVATED MATERIALS WITH MIXED ACTIVATORS

5.1 Introduction

Alkali-activated materials (AAMs) or geopolymers have gained attention as a class of alternative cement possessing properties comparable to ordinary Portland cement (OPC), but with a large overall reduction in carbon dioxide (CO_2) emissions [179]. AAMs are produced by mixing solid aluminosilicate precursors in an alkaline environment in the form of binder mixes, which gain adequate strength upon curing and used potentially in construction. Common aluminosilicate precursors include industrial by-products such as fly ash (FA), ground-granulated-blast-furnace-slag (slag/GGBFS), and calcined clays (metakaolin/MK), and their blends [19]. The use of activators such as sodium hydroxide (NaOH), sodium silicate (Na_2SiO_3), and sodium carbonate (Na_2CO_3) produces a highly alkaline environment, which aids in activating and curing to generate aluminosilicate phases that exhibit adequate engineering properties [91].

The aluminosilicate phases are developed in two stages in binder mixes, with elevated alkaline conditions facilitating initially the dissolution of reactive components in the precursor, and subsequently, the condensation reactions [46]. The development of hardened phases in binder mixes such as sodium aluminosilicate hydrate (N-A-S-H gel) occurs in pure-FA-activated AAMs and calcium aluminosilicate hydrate (C-A-S-H gel) in slag-activated AAMs. The co-existence of both C-(N)-A-S-H/N-(C)-A-S-H is a consequence of FA–slag alkali activation [21,99], which is a function precursor ratio and the activator content. The activation of slag and FA together increases the dissolution of Ca and Al, producing dominant tetrahedral-coordinated-Al binder phases along with a substantial increase in mechanical properties and durability, compared to pure FA-based AAMs [180].

The inclusion of a Na_2SiO_3 activator combined with the NaOH solution reduces the pH of the activator solution, where the additional silicate content from the Na_2SiO_3 causes increases in electrostatic forces between the reactive phases during dissolution. This increased intensity of electrostatic forces causes increases in mechanical properties of hardened binder mixes in turn [91]. Recent studies show how Na_2CO_3 can be a cost-effective activator and an alternative to NaOH in FA–slag AAM [90].

The Na₂CO₃-activated AAMs exhibit a) low compressive strength at an early age, b) an increase in initial setting time, and c) a low pH during activation because of the partial neutralization of pH in early ages of activation. The presence of carbonated compounds from the dissolved Na₂CO₃ enhances their compressive strength at later stages, up to 60 MPa at 28 days [91,181] in contrast to NaOH-activated AAMs [182].

Apart from engineering properties, durability aspects such as efflorescence and leaching behaviours of free alkalis from the AAMs are critical for their industrial application. Efflorescence particularly is observed as deposits of salts on the surface of cement structures and masonry resultant of physicochemical reactions [101,158,183]. Efflorescence is initiated by the free alkalis in the AAM binders that react with CO₂ in the atmosphere. The dissolution of free alkalis and diffusion of CO₂ from the atmosphere to the binder matrix causes precipitation of hydrated, carbonated phases upon drying [148]. Furthermore, the continuous hydration and movement of alkalis in the pore solution towards the dried surface enhance the degree of efflorescence [158]. Previous works also showed the development of subflorescence caused because of the dissolution of diffused CO₃²⁻ ions in alkali pore solution, and subsequent formation of salt crystals in the pore network [158]. The geological origin of precursors, physical/chemical properties, reactivity, and the ratio of precursor blends dictate the extent of efflorescence in AAMs [184]. However, there is an overall insufficiency of a method to interpret these effects effectively with the degree of efflorescence, which is currently qualified through ASTM D 7072-04 standard that categorizes the saturated surface as ‘none, slight, moderate or severe’, based on the colour contrast between white efflorescence products on a grey cement surface [185]. Image analysis and curettage methods [186], and indirect methods such as leaching tests and microstructural characterization are also applied to quantify efflorescence [86].

In general, efflorescence is considered as an aesthetic issue in OPC structures. However, high activator content used in AAMs during activation leads to leaching, and subsequent precipitation of leached alkalis in the form of carbonate salts from binders leads to efflorescence to be a durability concern [175]. The excessive efflorescence or subflorescence in AAMs significantly affects their service life. Previous studies show the partial replacement of slag in FA based AAMs caused the

formation of a tortuous pore network and inhibited the leaching of alkalis from AAM binders [175]. Also, the use of Na_2SiO_3 as an activator reduced the efflorescence extent in FA- and MK-based AAMs [175,183]. The additional silica content in Na_2SiO_3 caused low porosity and impeded the leaching of alkalis from AAMs. Furthermore, the potassium-based activators, thermal curing, and calcium-alumino cements were used to reduce the degree of efflorescence in AAMs [183]. However, the inclusion of higher proportions of slag in FA is cost-prohibitive, which leads to natural carbonation and decreases the setting time in AAMs [187]. Similarly, the excessive use of Na_2SiO_3 is also cost-prohibitive, affects the reactivity of AAM precursors and leads to a higher amount of sodium content in the binder mix, which aids efflorescence [188]. Because of the wide variability in the nature of precursors, activators, and the complex physicochemical reactions involved in efflorescence formation in AAMs, this field remains relatively less explored, and with a limited understanding. Despite several advances in the field of AAMs and efflorescence formation of FA–slag based AAMs, the a) effect of slag content or the calcium content on the efflorescence formation and b) the phase degradation of reaction products, specifically N-A-S-H and N-(C)-A-S-H gel under efflorescence exposure stays unexplored, which is investigated in detail in this work.

The main objective of this work is to design and investigate zero- and low-calcium AAMs with a focus on N-A-S-H/N-(C)-A-S-H phases under efflorescence. Pure FA was used to develop N-A-S-H gel and slag was incorporated in FA to develop N-(C)-A-S-H gel in binder mixes. Additionally, the target mean compressive strength of 28 days naturally cured AAMs was designed in the range of 20 MPa to 50 MPa in the final binder mix. Furthermore, to design the aforementioned binder mixes with target compressive strength, the $\text{NaOH} + \text{Na}_2\text{SiO}_3$ with a modulus ($\text{SiO}_2/\text{Na}_2\text{O}$) of $M_s = 1.4$ was fixed with 9wt.% Na_2O content, and the water/solid (w/s) ratio was fixed at 0.35. Additionally, another set of FA and FA–slag based AAMs were designed and 2wt.% dissolved Na_2CO_3 was used combined with $\text{NaOH} + \text{Na}_2\text{SiO}_3$ to investigate the effect of Na_2CO_3 on the activation and efflorescence behaviour. Visual inspection and leaching tests were carried on AAM specimens to evaluate the degree of efflorescence. Compressive and split tensile strength of binder specimens were determined after activation and efflorescence. A leaching test was performed on the cured unbroken cylindrical specimens as an indirect method to measure the efflorescence potential.

The Atomic absorption spectrometry (AAS) was used to quantify the free alkalis in the leachate of binder specimens after the leaching test. The calibration curve with 4 points was prepared by measuring the concentration of alkalis in distilled water and pure reagents with varying concentrations. X-ray diffraction (XRD), Fourier transform infrared spectroscopy (FTIR), magic-angle-spinning nuclear magnetic resonance (MAS-NMR) and thermo-gravimetric analysis (TGA) were performed to analyse the phase changes of binder specimens after activation and efflorescence.

5.2 Materials and methods

5.2.1 Precursors and activators

Class F fly ash (FA) and GGBFS a.k.a slag were obtained from Neilsen's group in Queensland, Australia. X-ray fluorescence (XRF) was used to determine the mineralogical compositions of FA and GGBFS (Table 5-1). The FA contains high concentrations of SiO₂ and low concentrations of CaO and can be categorised into Class F, according to ASTM C 618 [171].

Table 5-1 Chemical compositions of FA and GGBFS as determined by XRF. Loss on ignition (LOI) is shown at 1000 °C.

	Weight Fraction (wt.%)								LOI
	SiO ₂	Al ₂ O ₃	CaO	MgO	K ₂ O	Na ₂ O	Fe ₂ O ₃	P ₂ O ₅	
FA	55.830	34.280	2.880	0.778	0.819	0.269	2.430	0.111	0.24
GGBFS	33.680	14.540	42.49	6.010	0.320	0.180	0.551	0.022	0.07

In cured AAMs, a total of 9.0 wt.% of Na₂O content was maintained. Fig. 5-1 shows the X-ray diffractograms of FA and slag. In FA, major reflections of quartz and mullite, and minor reflections of maghemite were seen. In slag, minor traces of tri-calcium silicate and traces of aragonite were observed.

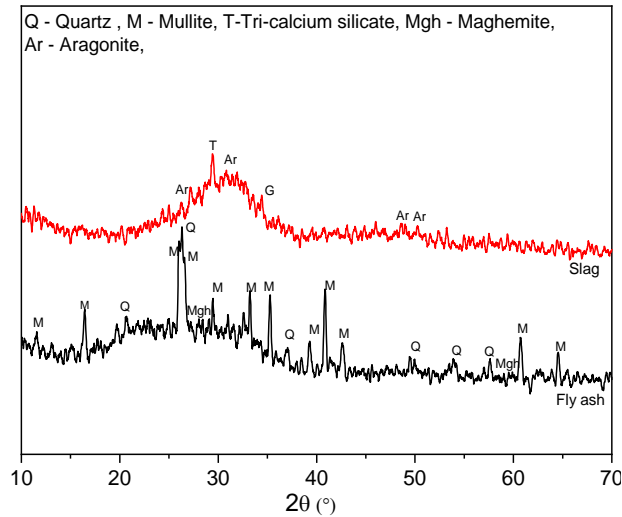


Fig. 5-1 X-ray diffractograms of FA and slag showing the main mineralogical phases.

5.2.2 AAM preparation

Analytical grade NaOH pellets and Na₂CO₃ powder were obtained from Chemsupply, Adelaide, Australia. D-grade Na₂SiO₃ solution (Na₂O = 14.7 wt.%, SiO₂ = 29.4 wt.% and H₂O = 52.7 wt.%) with M_s = 2.0 (SiO₂/Na₂O ratio) was obtained from PQ Australia, Dandenong, Australia. The activator solution was prepared by mixing NaOH+ Na₂SiO₃ and NaOH+ Na₂SiO₃+Na₂CO₃ and cooled to room temperature at least 3 h before mixing with solids. The modulus (M_s) = 1.4 (SiO₂/Na₂O ratio) was achieved in the final activator solution through and 10wt.% - 30wt.% slag was blended with FA to obtain an acceptable level of compressive strength (between 20 MPa – 50 MPa)

AAMs were prepared by mixing the precursors with activator for 5 min in a planetary mixer, with additional water being added to achieve workability to achieve at total w/s = 0.35. This was poured into 30 mm × 30 mm × 30 mm cubes and Φ 23 mm × 23 mm cylindrical moulds. The prepared specimens with specific mix proportions were sealed and kept in a plastic box and demoulded after 28 days of natural curing at 23 ± 2 °C and of relative humidity (RH) ≥ 90%. Table 5-2 Table 2 shows the final mix proportions, mix ID (100FA0SN – 100 wt.% FA+0 wt.% slag+(NaOH+Na₂SiO₃) and 100FA0SN – 100 wt.% FA+ 0 wt.% slag+(NaOH+Na₂SiO₃+Na₂CO₃), M_s, total Na₂O content, w/s ratio and curing time.

Table 5-2 Mix proportions and curing conditions of binders

Mix ID	FA (wt.%)	Slag (wt.%)	M _s	Total Na ₂ O (wt.%)	Na ₂ CO ₃ (wt.%)	w/s ratio	Curing time (days)
100FA0SN	100	0	1.4	9.0	0	0.35	28
90FA10SN	90	10	1.4	9.0	0	0.35	28
70FA30SN	70	30	1.4	9.0	0	0.35	28
100FA0SNC	100	0	1.4	9.0	2	0.35	28
90FA10SNC	90	10	1.4	9.0	2	0.35	28
70FA30SNC	70	30	1.4	9.0	2	0.35	28

5.2.3 Testing and characterization

The binder specimens were cured for 28 days and subsequently subjected to 30 days of efflorescence. To reach the partially saturated conditions in the efflorescence test, the bottom surface of the specimens was submerged in water to a height of 10 mm, with the top surface of the specimens allowed to be exposed freely to air. Efflorescence tests were carried in a laboratory environment at 23 ± 2 °C and RH of $55 \pm 5\%$.

Leaching tests were carried on unbroken specimens, immersing binder specimens in de-ionised water. A larger solid/liquid ratio of 1:20 was considered for the leaching test to make sure that even dispersion of solid ions. The test was carried following ASTM D 3987 and ASTM E 1908-16 [172,173]. The specimens were kept in plastic boxes at 23 °C and $\geq 90\%$ RH and sealed to avoid water evaporation. A pH meter was used to measure the pH values of the leachate at specific time intervals. Sodium and silicon concentrations were measured from leachate using an AAS after 28 days of leaching.

Compressive strength of specimens measured after 7 and 28 days of curing and 28 days of efflorescence. The split tensile strength of binder specimens was measured after 28 days of curing and efflorescence. A minimum number of 5 specimens were tested for the compressive and split tensile strength measurements. MTS universal mechanical testing machine with a strain rate of 0.5 mm/min was used to measure mechanical properties, following AS 1012.10 and AS 1012.9:2014 [189,190]. After determining mechanical properties, samples were crushed, dried at 60 °C to equilibrate weight, and sieved through a 75 µm sieve. These crushed powders were also used for XRD, FTIR, TGA, and MAS-NMR analyses. XRD analysis was carried using PAN Analytical Xpert Pro with Cu-K_α radiation, operated at 30 mA and 40 kV, with a step size of 0.020°, 2θ range of 5 - 70° and scan time of 0.85 s/step. FTIR analyses were

carried on binder specimens using an FTIR spectrometer, with a wavelength range from 400 cm^{-1} to 4000 cm^{-1} . A sample at approx. 1 mm to 2 mm depth was sampled for mineralogical characterization, which was stored in airtight containers.

NMR studies were conducted using a JEOL (ECX400) solid-state NMR (11.7T) at 400 MHz using a probe of 4 mm, with a spinning speed of 10 kHz to measure the chemical shift of ^{27}Al (transmitter frequency = 156 MHz, scans = 3072), and ^{23}Na (transmitter frequency = 132 MHz, scans = 3072) nuclei. The pulse width of $6\text{ }\mu\text{s}$ and a relaxation delay of 2 s were used for all samples. A TA SDT 650 thermo-gravimetric analyser was used to perform the TGA analysis on binder specimens, using a heat rate of $20\text{ }^\circ\text{C}/\text{min}$, between $50\text{ }^\circ\text{C}$ to $1000\text{ }^\circ\text{C}$.

The open porosity of the leached specimens was measured by following a method established in the literature [158]. Initially, the specimen was crushed to a size of 5 mm thick particles. The crushed particles were cleaned in compressed air and dried at $105\text{ }^\circ\text{C}$ for 24 h to attain an equilibrium mass in a desiccator. The samples were cooled and then the mass of individual particle was measured and mass M_1 was measured. Later the particles were placed in a vacuum desiccator with a suction pressure of 90 kPa for 4 h until full saturation was attained. Later, specimens were immersed in a hot water bath under vacuum, the saturated surface dry mass M_2 and buoyant mass M_3 of samples were measured and open porosity was calculated using the Equation 5-1.

$$P = (M_2 - M_1)/(M_2 - M_3) \times 100\% \quad (5-1)$$

5.4 Results and discussion

5.4.1 Visual analysis

Visual inspection imagery of efflorescence in binder specimens after 28 days of ageing is shown in Fig.5-2. A significant quantity of effloresced salts was observed on the surface of 100FA0SN (0wt.% slag) specimens. The effloresced salts are often attributed to subfluorescence that is driven by carbonate crystal growth confined to the subsurface in the specimens. In 90FAS10N (10wt.% slag) and 70FAS30N (30wt.% slag) specimens, there was a slight increase in the salt deposition because of the decrease in N-A-S-H gel content in the binder mixes because of the reduction in FA content and increase in the unreacted alkali content in the binder mixes. The specimens with Na_2CO_3 showed higher deposition of salts on the surface, with small visible

cracks and deposition of salts at the top surface. The specimens with 2 wt.% Na_2CO_3 , i.e., 100FA0SNC (0wt.% slag and 2wt.% Na_2CO_3), 90FA0SNC (10wt.% slag and 2wt.% Na_2CO_3), and 70FA30FNC (30wt.% slag and 2wt.% Na_2CO_3) showed a higher amount of salt deposition compared to binder specimens without Na_2CO_3 . The addition of Na_2CO_3 partially neutralised the pH of the binder mix [191]. Therefore, the low pH developed during the activation hinders the development of geopolymer gel during activation and increases the presence of unreacted free alkalis in the system [191].

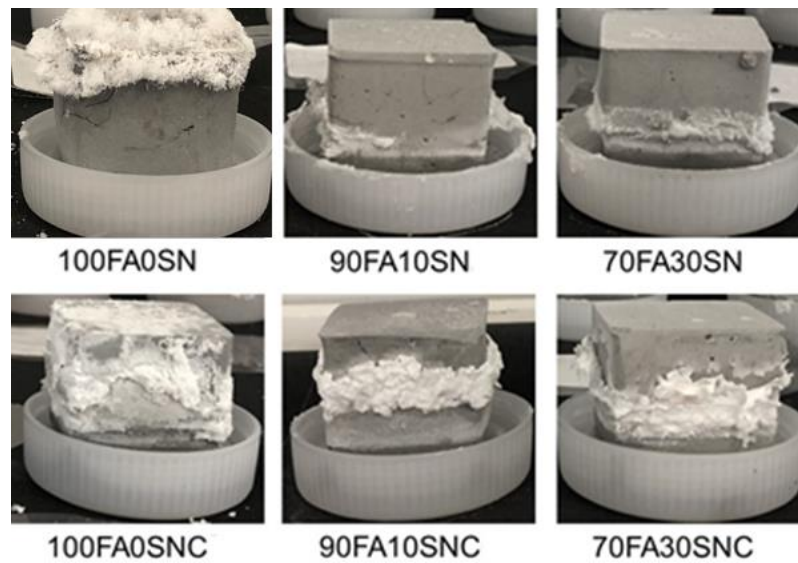


Fig. 5-2 Binder specimens with varying levels of slag showing surface deposition after 28 days of efflorescence

5.4.2 Mechanical property assessment

Compressive strength and split tensile strength of binder specimens were analysed after curing and efflorescence. The compressive strength values of binder specimens after 7 days and 28 days of curing are shown in Fig.5-3. At 7 days, the 100FA0SN (100 wt.% FA) control specimens exhibited a compressive strength of 6.45 ± 0.39 MPa. In specimens with 10 and 30 wt.% slag (90FA10SN and 70FA30SN), the compressive strength was 15 ± 0.75 MPa and 26 ± 1.3 MPa, respectively, as expected with slag addition. In specimens with 2 wt.% Na_2CO_3 , i.e., 100FA0SNC, 90FA10SNC and 70FA30SNC, the compressive strength values at 7 days were 5.42 ± 0.25 MPa, 13.62 ± 0.65 MPa and 16.71 ± 0.8 MPa. With the addition of Na_2CO_3 , compressive strength showed a decrease because of reduced reactivity in the binder mixes [91].

At 28 days, the compressive strength values of 100FA0SN, 90FA10SN and 70FA30SN were 22.15 MPa, 29 ± 1.45 MPa and 48 ± 1.2 MPa, respectively. Compressive strengths of 100FA0SNC, 90FA10SNC, and 70FA30SNC were 22 ± 1.1 MPa, 28 ± 1.4 MPa, and 40.35 ± 2.4 MPa, respectively. These increases in compressive strength can be attributed to the addition of calcium within slag, and the resultant formation of calcium-based, strength-enhancing reaction products [192].

The compressive strength values of 100FA0SN, 90FA10SN and 70FA30SN after 28 days of efflorescence were observed to be 28.65 ± 1.4 MPa, 33.8 ± 1.57 MPa and 49.54 ± 2.3 MPa, respectively. Compressive strengths of 100FA0SNC, 90FA10SNC and 70FA30SNC were observed as 26.33 ± 1.3 MPa, 32.87 ± 1.6 MPa and 41.86 ± 2.05 MPa, respectively. Overall, a minimum increase of 20% to 30% in compressive strength was observed in binder specimens, except 70FA30SN and 70FA30SNC. The compressive strength increase in binder specimens after efflorescence ageing was attributed to the slow, ongoing alkali reactions under ageing. In these ongoing alkali reactions, free alkalis in the pore solution react with unreacted precursors, i.e., FA and slag in the binder mixes [175].

The split tensile strength data of binder specimens at 28 days of efflorescence ageing are shown in Fig.5-4, with a decrease in split tensile strength of over 60%, compared to the 28-day curing case. This decrease shows the effect of subfluorescence occurring within the solid binders. The a) CO_3^{2-} absorbed from the atmosphere, and b) free alkalis in the binder matrix react and precipitate in the form of carbonate salts inside the porous network of hardened AAM specimens [158]. Upon deposition of salt inside these pores because of subfluorescence, crystallization pressure starts to build inside the binder mixes [193] and a further increase in this crystallization pressure causes cracking in binder specimens further decreasing the split tensile strength [193]. The specimens activated with 2 wt.% of Na_2CO_3 showed a decrease in split tensile strength values under efflorescence. However, the split tensile strength of these samples showed a major decrease (>90%). From the visual inspection of efflorescence, it was clear that the extent of efflorescence was higher in binder specimens with Na_2CO_3 , when compared to samples without Na_2CO_3 .

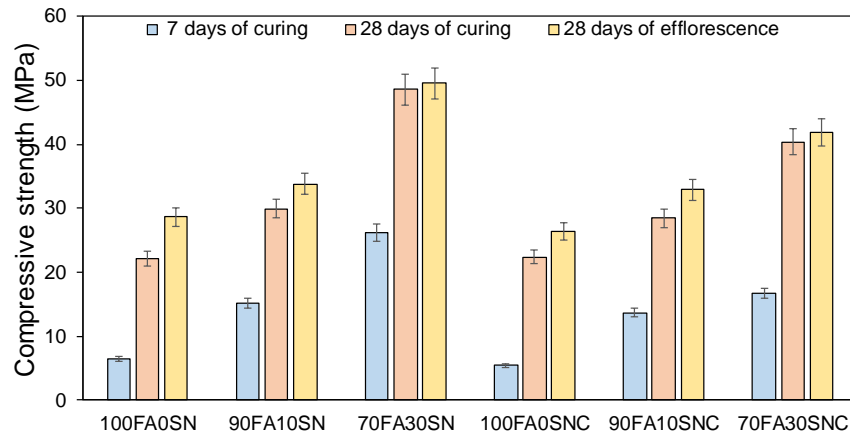


Fig. 5-3 Compressive strength of binder specimens after curing and efflorescence.

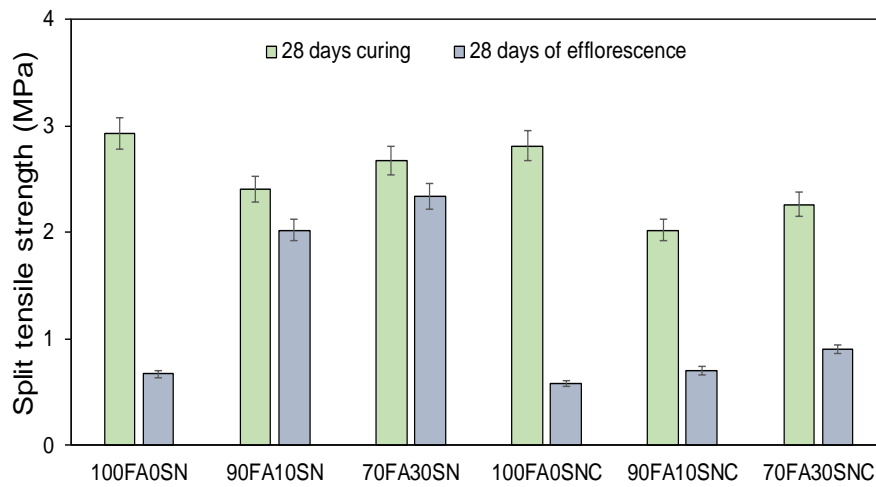


Fig. 5-4 Split tensile strength of binder specimens after curing and efflorescence

5.4.3 Leaching behaviour of hardened AAMs

The pH values of leachate collected at 28 days determined through AAS for hardened binder specimens are shown in Fig.5-5. The pH values ranged from 10.5 to 12.0, and the pH increased to their respective maxima at 24 h of immersion. The pH values of all specimens approached 10.0 upon 30 min of immersion.

The sodium and silicate concentrations in the leachate after 28 days of leaching are shown in Fig.5-6a. With the inclusion of slag, ~16% reduction in Na and ~60% reduction in Si leaching in 90FA10SN mixes. A further reduction in leaching of Na and Si was observed with an increase in slag content. The binder mixes with 30wt.% slag content (70FA30SN) showed up to ~44% reduction in Na leaching and ~83% reduction in Si leaching potential. This behaviour indicates the addition of slag content hinders the leaching of alkalis and leads to less efflorescence in binder mixes. The

inclusion of slag content reduced the porosity and developed complex tortuosity to reduce the leaching of alkalis from the mixes. In the bulk binder specimens, the presence of a dense microstructure and low porosity led to slower transport of alkalis to the surface. The binder specimens with 2 wt.% Na_2CO_3 also exhibited a similar trend, however, the concentration of alkalis leaching out of the binder mix was observed to be higher compared with specimens with no Na_2CO_3 , which was attributed to the low reactivity in mixes containing Na_2CO_3 [91].

AAM materials leach 40 to 60 wt.% of Na from the solid matrix within 45 h of immersion in an acidic environment [194]. Moreover, the alkali concentration in the leachate attained a 100 - 150 ppm level within the first 24 h of leaching [86]. The Na fraction in leachate and the alkali concentration trends were not observed in this study, which can be surmised as an effect of the slow rate of leaching because of the use of bulk specimens instead of crushed samples used in general.

The open porosity of binder specimens before and after leaching are shown in Fig. 5-6b. The inclusion of slag reduced the open porosities from ~36% to 30% in binder mixes after activation. The binder specimens with Na_2CO_3 showed a decreasing trend of porosity from ~39% to 36% as slag content increased from 0wt.% to 30wt.% after activation. Nevertheless, the overall porosity in the binder specimens with Na_2CO_3 was 2% to 5% higher compared to the binder specimens without Na_2CO_3 . After leaching, there was an increase in open porosity up to 2% to 5% in binder specimens because of the leaching of alkalis. This indicates the increase of porosity values of binder mixes after leaching which may lead to increased efflorescence formation.

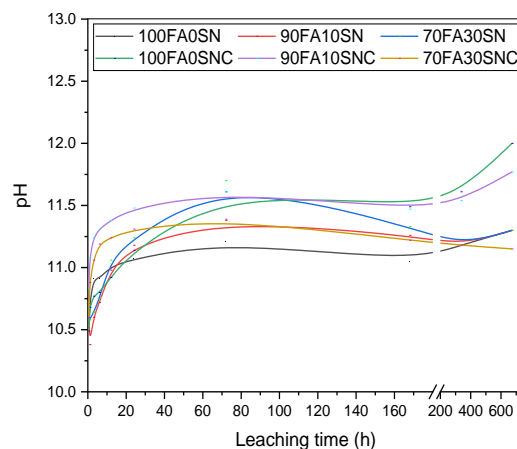


Fig. 5-5 The variation in pH with respect to leaching time in the binder specimens.

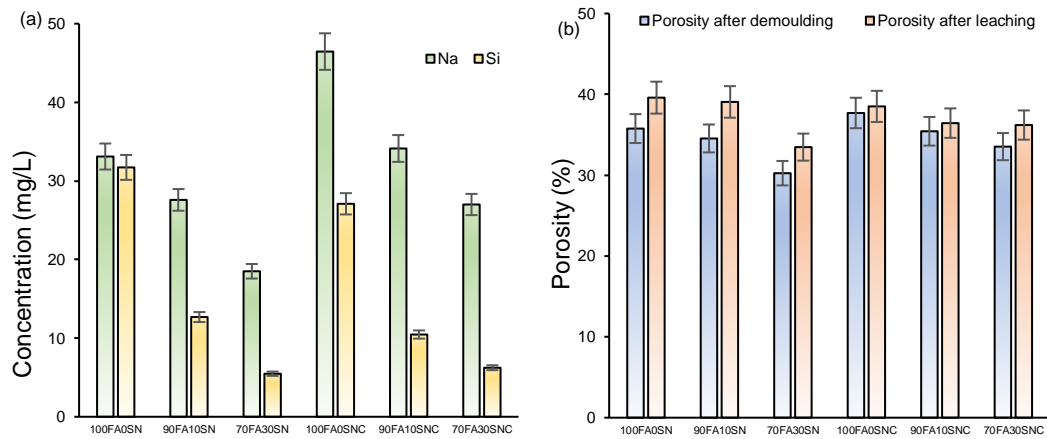


Fig. 5-6 The comparative plots of (a) concentration of sodium and silicates leached from hardened binder specimens, and (b) open porosities of binder specimens before and after the leaching.

5.4.4 XRD analysis

The XRD patterns of unreacted FA, slag, and binder specimens after 28 days of curing and efflorescence are illustrated in Fig.5-7, showing crystal phases including quartz, mullite and maghemite in all reaction products.

The XRD patterns of 100FA0SN samples before and after efflorescence are shown in Fig. 5-7a, displaying a shift in a broad feature between $2\theta = 20^\circ - 35^\circ$ upon activation, indicating the formation of disordered aluminosilicate gel after activation. Reaction products such as zeolite/Na-P1 phase resembling a gismondine structure ($\text{Na}_6\text{Al}_6\text{Si}_{10}\text{O}_{32}$, #PDF-01-074-1787) were observed at $2\theta = 33.25^\circ$ and 30.9° in these samples. Na-P1 zeolites are observed in NaOH-activated AAMs cured at elevated temperatures [195]. The higher alkali content from NaOH and Na_2SiO_3 , and low calcium content present in these mixes favoured the formation of zeolitic structures [76]. The intensity of peak attributed to quartz and mullite between $2\theta = 26^\circ - 27^\circ$ increased after activation, indicating the availability of additional silicate content from the Na_2SiO_3 solution. After efflorescence, low-intensity peaks associated with hydrous Na_2CO_3 ($\text{Na}_2\text{CO}_3 \cdot 7\text{H}_2\text{O}$, #PDF-00-025-0816) were observed in both samples (100FA0SN and 100FA0SNC) and intensities attributed to zeolitic phases were observed to be decreasing. This indicates leaching of Na^+ ions from the N-A-S-H gel and formation of sodium carbonate phases, which is attributed to partial neutralization of binder specimens under the influence of natural carbonation, where the dissolved

CO₂ in pore solution creates an acidic environment to react with free Na⁺ and OH⁻ of binder specimens and precipitates in the form of carbonates [175].

The XRD patterns of 100FA10SNC samples are shown in Fig. 5-7b after curing and efflorescence. Na-P1 zeolites were observed in these samples after curing, with their intensity decreasing with an increase in efflorescence time. Minor reflections of Na₂CO₃ (Na₂CO₃·7H₂O, #PDF-00-025-0816) were observed after efflorescence. When the XRD patterns of pure FA mixes with and without Na₂CO₃ are compared, no significant differences were observed before after efflorescence.

The XRD patterns of binder specimens before and after efflorescence with 10wt.% slag (90FA10SN) are shown in Fig. 5-7c. The reaction products detected in these binder specimens were mullite, quartz, zeolite/Na-P1, and maghemite, which were similar to the binder specimens with no slag content. The inclusion of slag facilitated the formation of a peak $2\theta = 29.5^\circ$ resembling a weak, crystalline C-A-S-H gel (#PDF-00-022-0600) in binder mixes, which was previously identified as the main product in alkali-activated FA–slag systems [196] containing a higher slag content. Another minor reflection of the zeolitic phase, i.e., garronite (NaCa_{2.5}Al₆Si₁₀O₃₂·14H₂O, #PDF-00-059-0383) was observed in mixes [19,59,197] as well. The presence of garronites was attributed to Na/Ca exchange process in FA–slag based AAMs with higher alkalinity. In this study, the reduction of FA content, the inclusion of slag, and higher alkalinity from NaOH/Na₂SiO₃ can be surmised to favour the Na-Ca exchange process to produce garronite [198]. After efflorescence, the peak intensity corresponding to C-A-S-H gel at $2\theta = 29.5^\circ$ increased in 90FA10SN. The increase in the intensity at $2\theta = 29.5^\circ$ is attributed to the formation of calcite phases and sodium-calcium carbonates (Na₂Ca(CO₃)₂·7H₂O, #PDF-00-025-0816) were observed at the end of efflorescence [99]. The XRD patterns of 90FA10SNC samples are shown in Fig. 5-7d after curing and efflorescence. Na-P1 zeolites, garronites, minor reflections of C-A-S-H gel and reaction products were observed in these samples after curing.

After efflorescence, minor reflections of Na₂CO₃ were observed in these binder mixes along with the decrease in the intensities attributed to zeolitic phases. However, unlike 90FA10SN, an increase in the intensity of C-A-S-H gel was not evidenced after efflorescence.

The XRD patterns of 70FA30SN after curing and efflorescence are shown in Fig. 5-7e, illustrating increases in peak intensities at $2\theta = 29.5^\circ$ showing the formation of a highly-crystalline C-A-S-H gel [57]. The increased slag content favoured the formation of C-A-S-H gel and suppressed the formation of Na-P1 zeolitic products. The higher slag content favoured the formation of zeolitic products such as garronite. After efflorescence, the intensity of peaks corresponding to the zeolitic products decreased, indicating the degradation of geopolymer gel under efflorescence. Concomitantly, the peaks corresponding to phases such as hydrous Na_2CO_3 and calcite were identified in these samples, as expected.

The XRD patterns of 70FA30SNC binder specimens with Na_2CO_3 after curing and efflorescence are shown in Fig. 5-7f. A lower intensity of C-A-S-H gel was observed in these specimens compared with 70FA30SN, along with a decreased intensity of zeolitic products under efflorescence. The binder mixes with Na_2CO_3 showed lower intensities of N-A-S-H/N-(C)-A-S-H gel phases after activation and showed a significant reduction of zeolitic phases after efflorescence. The formation of higher amount effloresced salts because of lower reactivity developed by Na_2CO_3 inclusion in binder mixes.

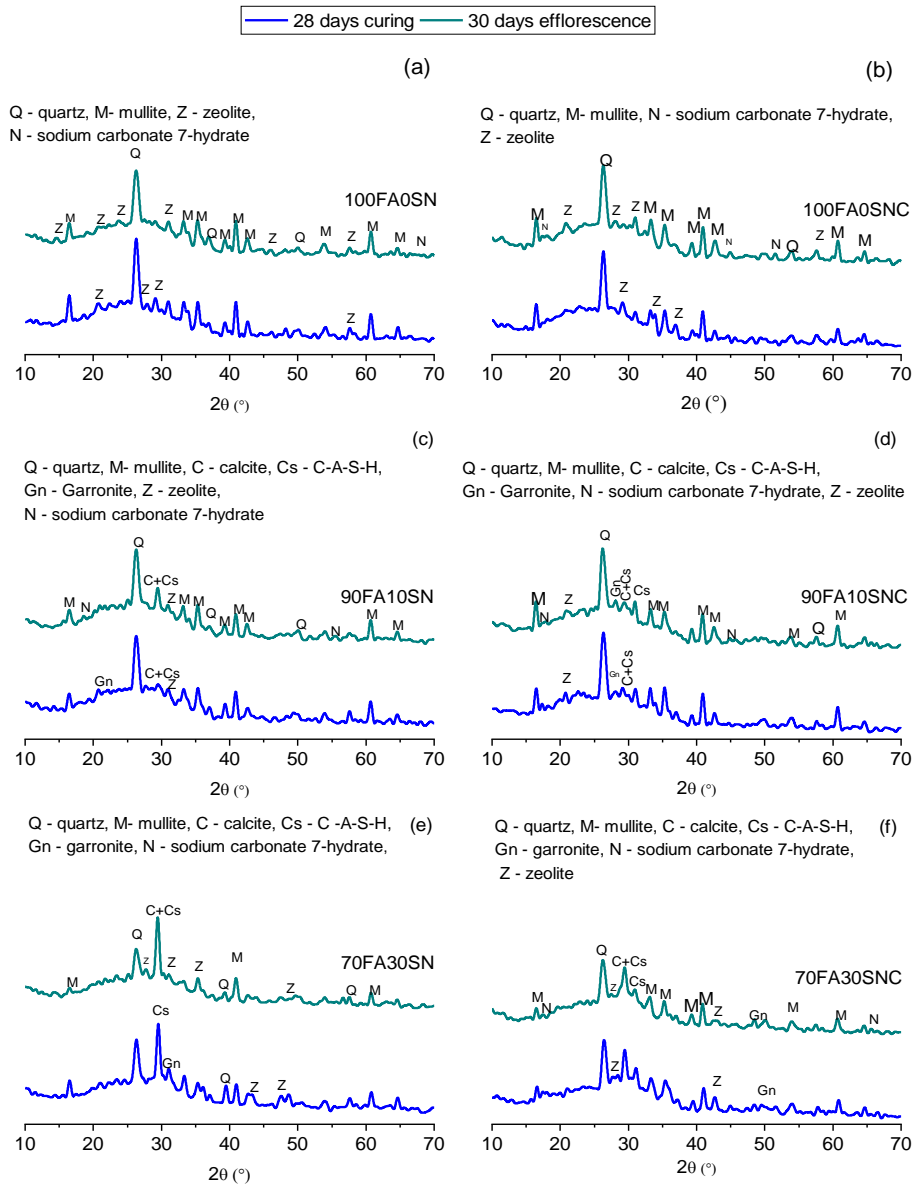


Fig. 5-7 XRD patterns of hardened binder specimens and after 28 days of ageing under efflorescence with decreasing FA content, (a-b) 100FA0SN (C), (c-d) 90FA10SN(C), and (e-f) 70FA30SN(C).

5.4.5 FTIR Analysis

The FTIR spectra of binder specimens with and without Na_2CO_3 after curing and efflorescence are presented in Fig. 5-8a and 8b, respectively. The broad band from 900 to 1100 cm^{-1} is attributed to the asymmetric stretching vibration of tetrahedral Si-O-T (T = Si or Al) bonds. In all specimens, bands centred at 545 cm^{-1} , 553 cm^{-1} , 555 cm^{-1} and 669 cm^{-1} were detected, which are attributed to the symmetric stretching vibration of Si-O-Si bonds [199]. A band detected at 848 cm^{-1} (Fig. 5-8a and Fig. 5-8b) was correlated to asymmetric stretching of CO_3^{2-} in binder specimens. Traces of carbonates were identified at 1415 cm^{-1} , 1450 cm^{-1} , and 1480 cm^{-1} that indicate asymmetric

stretching of O-C-O bond of CO_3^{2-} . In the 10 wt.% (90FA10SN and 90FA10SNC) and 30 wt.% slag (70FA30SN and 70FA30SNC) specimens, the 871 cm^{-1} and 873 cm^{-1} shoulders were attributed to bending vibrations of AlO_4 groups [200].

The broad band at 1004 cm^{-1} in 100FA0SN (Fig. 5-8a) is assigned Si-O-T vibration of N-A-S-H gel. Given that FA is an alumina-rich precursor, Al from FA facilitates the formation of highly-polymerised N-A-S-H or aluminosilicate gel (geopolymer gel) [19] in the presence of low calcium content. The 987 cm^{-1} band is assigned to the Si-O-T vibration of N-(C)-A-S-H gel 90FA10SN (Fig. 5-8a) specimens. The replacement of FA with 10 wt.% slag shifted Si-O-T bands to lower wavenumbers, indicating the formation of C-A-S-H gel, and concomitant reduction of Al content in N-A-S-H gel [19]. The high FA content and low slag content mixed with an activator with high Na_2O (9 wt.%) can simultaneously activate both FA–slag and promote the coexistence of N-A-S-H and C-A-S-H gels [19]. The FA to slag ratio and the activator concentration dictates the intensity of co-existence of these gels. When low slag and high FA systems are activated with a high dosage of activator, the formation of N-(C)-A-S-H gel is favoured, with N-A-S-H gel as the dominant reaction product. Further increase in slag content ($\geq 25\text{ wt.}\%$) suppresses the formation of N-A-S-H gel and causes the formation of C-A-S-H gels as the dominant reaction product [80]. With the activation of 70FA30SN samples, the Si-O-T vibration band further shifted to 972 cm^{-1} , indicating the formation of N-(C)-A-S-H gel with more substitution of Ca^{2+} into the gel in the place of Al.

At 28 days of efflorescence, no shift was observed in the asymmetric stretching of Si-O-T in 100FA0SN (Fig. 5-8a) specimens. However, the intensity at 870 cm^{-1} , assigned to vibration of AlO_4 groups showed a reduced intensity, indicating the dealumination in tetrahedral Al environment of N-A-S-H gel after efflorescence. The frequencies attributed to Si-O-T stretching of binder specimens with 10 wt.% (90FA10SN) and 30 wt.% (70FA30SN) slag shifted to higher wavenumbers, indicating the formation of silica-rich gel and decalcification of calcium from the N-(C)-A-S-H gel under efflorescence. The intensity of the shoulder at 873 cm^{-1} increased, indicating carbonation in binder specimens and the formation of calcite phases in these specimens.

The Si-O-T stretching vibrations in 100FA0SNC specimens were observed at 995 cm^{-1} (Fig.5-8b). The presence of Na_2CO_3 in these specimens caused a lower pH and affected the kinetics of the alkali activation process at early ages, favouring the formation of low-cross-linked N-A-S-H gel [201]. The Si-O-T stretching shifted to lower wavenumbers with an increase in slag content, similar to the binder specimens without Na_2CO_3 . After efflorescence (Fig. 5-8b), Si-O-T stretching vibrations in 100FA0SNC shifted to 991 cm^{-1} , indicating degradation of N-A-S-H gel after efflorescence. However, this shift was not observed in 90FA10SNC (Fig. 5-8b) specimens with 10 wt.% slag, where the Si-O-T stretching band moved to higher wavenumbers (987 cm^{-1}) during efflorescence, indicating the removal of calcium and formation of a silica-rich gel in the system [125].

The 70FA30SNC (Fig. 5-8b) did not show significant changes in Si-O-T vibration, with a minor shift of bands towards higher wavenumbers (972 cm^{-1}) was observed. The 873 cm^{-1} and 871 cm^{-1} bands showed increased intensity after efflorescence indicating the formation of calcite phases [202]. The binder mixes activated with Na_2CO_3 showed the lesser movement of asymmetric Si-O-T stretching, exhibited higher degradation of N-A-S-H/N-(C)-A-S-H gel and significant development of carbonation products under efflorescence conditions. This behaviour is attributed to the presence of unreacted precursors because of the lower reactivity developed because of the addition of Na_2CO_3 , which leads to the formation of a higher degree of efflorescence formation and development of carbonation products.

5.4.6 TGA Analysis

Differential thermograms of binder specimens without Na_2CO_3 after 28 days of efflorescence are shown in Fig. 5-9a and 9b. The thermograms show a major mass loss occurring below $200\text{ }^\circ\text{C}$. Mass loss below $105\text{ }^\circ\text{C}$ (I peak) is attributed to the removal of loosely bound water in N-A-S-H gel and N-(C)-A-S-H gels. In 100FA0SN samples, the I mass-loss peak at $100\text{ }^\circ\text{C}$ is assigned to the mass loss of water loosely-bound to the gel, and the II mass-loss peak at $174\text{ }^\circ\text{C}$ (Fig. 5-9a) is assigned to the loss of water held within small pores [55]. The mass loss at higher temperatures (peaks IV and V) between $550\text{ }^\circ\text{C} - 650\text{ }^\circ\text{C}$ and $695\text{ }^\circ\text{C} - 795\text{ }^\circ\text{C}$, respectively are attributed to the decomposition of Na_2CO_3 phases.

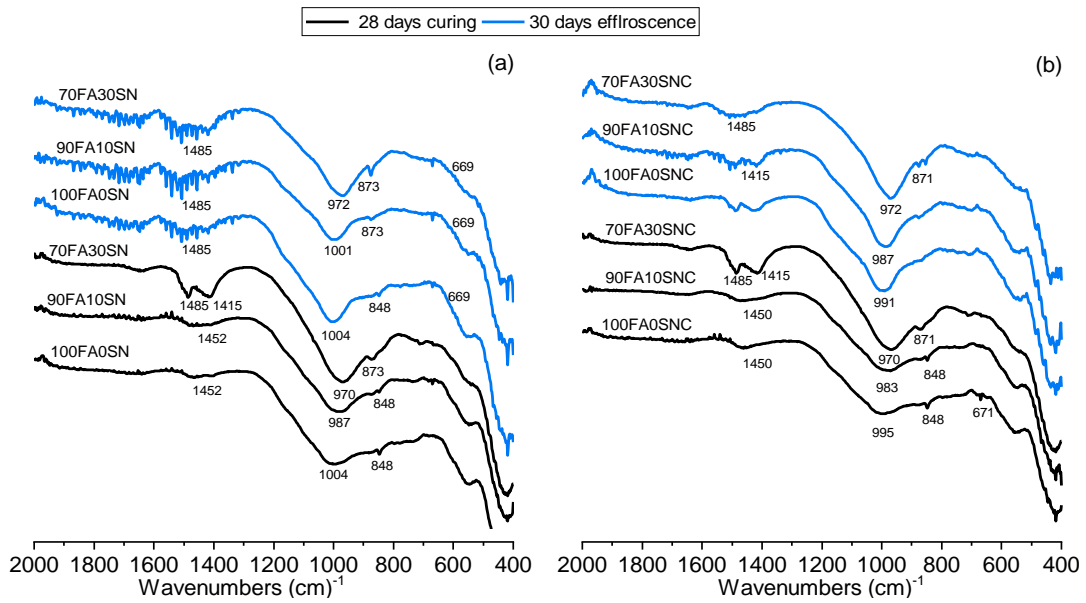


Fig. 5-8 FTIR spectra of binder specimens

In 90FA10SN (Fig. 5-9a) and 70FA30SN samples (Fig. 5-9a), the I mass loss peak, i.e., the loosely bound water evaporation was observed at 137 °C and 146 °C, respectively. The dehydration of loosely bound water was observed at higher temperatures in these specimens. The shift of I peak to a higher temperature was correlated to the formation of zeolites [19]. The II and III mass loss peaks in 90FA10SN samples were attributed to the decomposition of carbonate phases. The II mass loss peak between 450 °C – 550 °C in 70FA30SN samples was attributed to the decomposition of C-A-S-H phases, and III mass loss peak from 650 °C – 850 °C is attributed to the mass loss of the Na_2CO_3 and calcite phases, indicating the occurrence carbonate phases under efflorescence.

Differential thermograms of binder specimens with 2 wt.% Na_2CO_3 are shown in Fig. 5-9b. The mass loss occurred below 200 °C, with the corresponding I mass loss peak in 100FA0SNC at 100 °C assigned to the mass loss of loosely bound water within the gel. The 2nd mass loss peak (II) at 176 °C was attributed to the mass loss of water from pores. The III and IV mass loss peaks were attributed to the decomposition of the Na_2CO_3 phases.

In 90FA10SNC, the mass loss peak I was observed at 136 °C indicating the presence of zeolites. The II mass loss peak at 185 °C is attributed to the physisorbed water. The mass loss peak between 650 °C – 750 °C (III) is attributed to the decomposition of carbonate phases [19].

In 70FA30SNC samples, the mass loss peak I is attributed to free water loss observed at 100 °C. Along with the mass loss, widening of this curve was observed between 133 °C – 303 °C, indicating the occurrence of natural carbonation in these samples [55]. The II and III mass loss peaks at $T > 600$ °C are attributed to the decomposition of Na_2CO_3 and calcite phases. The increase in the mass loss peak III of 70FA30SNC compared to 90FA10SNC and 100FA0SNC indicates the presence of a greater fraction of carbonated phases formed in the samples, which is caused by efflorescence and natural carbonation [125].

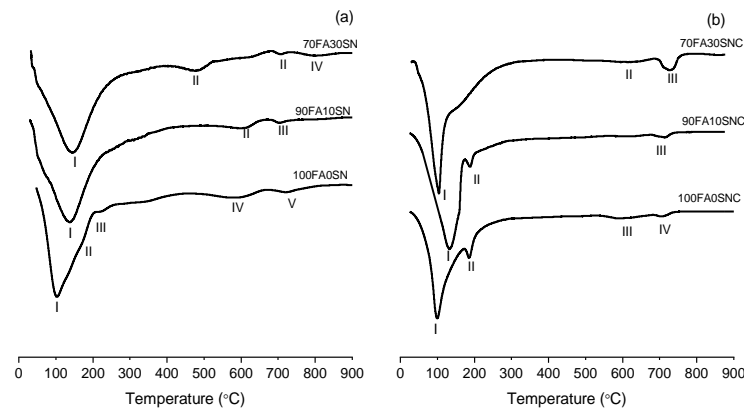


Fig. 5-9 TGA thermograms of aged AAM binder specimens

5.4.7 MAS-NMR analysis

The MAS-NMR spectra of ^{27}Al environment of unreacted precursors are shown in Fig. 5-10. The FA spectra show a) broad signal centred at $\delta_{\text{obs}} = 0$ ppm (Al[VI]) attributed to the resonance of octahedral Al[VI] in FA, b) a broad shoulder in FA between $\delta_{\text{obs}} = 40$ ppm to 60 ppm exhibiting the pentahedral aluminium (Al[V]) resonance, and c) $\delta_{\text{obs}} = 66$ ppm (Al[IV]) attributed to the resonance of tetrahedral aluminium in glassy phases [203]. In the ^{27}Al environment of unreacted slag (Fig. 5-10), a broad feature at $\delta_{\text{obs}} = 66$ ppm correlated to tetrahedral aluminium was detected [91]. The low-intensity broad resonance peaks at $\delta_{\text{obs}} = 0$ ppm to 13 ppm are attributed to the octahedral resonance of aluminium in unreacted slag [204].

The ^{27}Al MAS-NMR spectra of 100FA0SN, 90FA10SN and 70FA30SN specimens after curing and efflorescence are shown in Fig. 5-11a. The broad peaks corresponding to Al[VI] (0 ppm) in unreacted precursors were transformed after alkali activation, which causes aluminium from Al[V] and Al[VI] to dissolve and react, to develop Al[IV] sites. Hence, in the alkali-activated specimens, the $\delta_{\text{obs}} = 0$ ppm peaks exhibited

lower intensities, which are indicative of residual Al[VI] sites. Upon activation, 100FA0SN samples showed increased intensity in Al[IV] resonance ($\delta_{\text{obs}} = 60$ ppm), assigned to a highly-polymerized N-A-S-H gel structure in a Q⁴ environment [22,205]. In 90FA10SN and 70FA30SN samples, the Al[IV] resonance detected at chemical shifts at $\delta_{\text{obs}} = 62$ ppm and 63 ppm, respectively, which are higher than 100FA0SN samples and attributed to the presence of N-(C)-A-S-H gels.

The Al[IV] chemical shifts of 100FA0SN (Fig. 5-11a) samples was recorded at $\delta_{\text{obs}} = 60$ ppm, indicating dealumination under efflorescence. The Al[IV] chemical shifts in 90FA10SN ($\delta_{\text{obs}} = 60$ ppm) (Fig. 5-11a) and 70FA30SN ($\delta_{\text{obs}} = 61$ ppm) shifted to lower ppm, indicating the decalcification of N-(C)-A-S-H gel under efflorescence, which is consistent with TGA and FTIR analyses. After efflorescence, lower chemical shifts in Al[IV] environment in 100FA0SN, 90FA10SN and 70FA30SN were recorded.

The aforementioned change in intensities to lower chemical shifts in Al[IV] environment is unique to carbonation, where intensities associated with Al[IV] of C-A-S-H phases disappear because of C-A-S-H gel decalcification [55]. It can be surmised that the changes in N-(C)-A-S-H environments under efflorescence are similar to a carbonation process, where decalcification of C-A-S-H gel in binder specimens causes a shift to lower resonances within an Al environment.

The ²⁷Al MAS-NMR spectra of binder samples 100FA0SNC, 90FA10SNC, and 70FA30SNC are shown in Fig. 5-11b. The spectra of these samples were similar to the spectra of binder samples without Na₂CO₃ (Fig. 5-11b), displaying an increase in Al[IV] resonance intensity upon activation, assigned to N-A-S-H/N-(C)-A-S-H gel phases at $\delta_{\text{obs}} = 60$ ppm, $\delta_{\text{obs}} = 61$ ppm, and $\delta_{\text{obs}} = 62$ ppm, respectively. After efflorescence, Al[IV] resonances attributed to N-(C)-A-S-H phases of 90FA10SNC and 70FA30SNC samples moved towards lower chemical shifts at $\delta_{\text{obs}} = 60$ ppm from 61 ppm, and $\delta_{\text{obs}} = 61$ ppm from 62 ppm, respectively.

The ²³Na MAS-NMR spectra of 100FA0SN, 90FA10SN and 70FA30SN samples after activation and efflorescence process are shown in Fig. 5-12a. The 100FA0SN exhibited a disordered, partially-hydrated sodium environment of N-A-S-H phases at $\delta_{\text{obs}} = -4.9$ ppm (Fig. 5-12a) [206]. The chemical shifts of binder specimens with

10wt.% and 30wt.% slag contents were observed at lower resonances, i.e., $\delta_{\text{obs}} = -4.0$ ppm (90FA10SN, Fig. 5-12a) and $\delta_{\text{obs}} = -3.5$ ppm (70FA30SN, Fig. 5-12a) respectively. After efflorescence, the peak resonances of 100FA0SN, 90FA10SN and 70FA30SN shifted to $\delta_{\text{obs}} = -2.0$ ppm, $\delta_{\text{obs}} = -3.5$ ppm, and $\delta_{\text{obs}} = -1.8$ ppm, respectively.

Fig. 5-12b shows the ^{23}Na MAS-NMR of 100FA0SNC, 90FA10SNC and 70FA30SNC specimens after activation and efflorescence. The chemical shifts of 100FA0SNC, 90FA10SNC and 70FA30SNC were recorded at $\delta_{\text{obs}} = -4.0$ ppm, $\delta_{\text{obs}} = -3.9$ ppm, and $\delta_{\text{obs}} = -3.1$ ppm, respectively. After efflorescence, these resonances shifted to positive values, i.e., $\delta_{\text{obs}} = -3.1$ ppm (100FA0SNC), $\delta_{\text{obs}} = -3.5$ ppm (90FA10SNC) and $\delta_{\text{obs}} = 0.09$ ppm (70FA30SNC). Overall, the ^{23}Na MAS-NMR spectra of the binder specimens indicate the shift of resonances to positive values because of efflorescence.

The trend displayed in ^{23}Na MAS-NMR spectra can be correlated with the interaction of Na^+ ions in N-A-S-H gels that balance the charge in two ways. The first peak resonance at $\delta_{\text{obs}} = -4$ ppm is attributed to the charge-balancing Na in aluminosilicate gel. The second peak resonance at $\delta_{\text{obs}} = 0$ ppm is associated with the Na in pore solution, which balances the $\text{Al}(\text{OH})_4^-$ groups [27,207]. The shift of Na to negative values in dehydrated aluminosilicate gel is widely reported, confirming the strong interaction between oxygen and Na atoms [208]. The movement of resonances to positive values indicates hydration or development of a solvation shell around Na atoms upon the increase in the water content [209]. The movement of ^{23}Na resonance to positive values indicates the development of an isotropic Na environment under hydration [210]. The development of hydration shell around Na atom reduces the interaction between oxygen atoms of aluminosilicate structure and Na atoms, by decreasing the electric field gradient at Na nucleus and lead to depolymerisation of aluminosilicate gel [210]. Therefore, the movement of resonance to positive values in this study supports the depolymerisation of aluminosilicate gel under efflorescence.

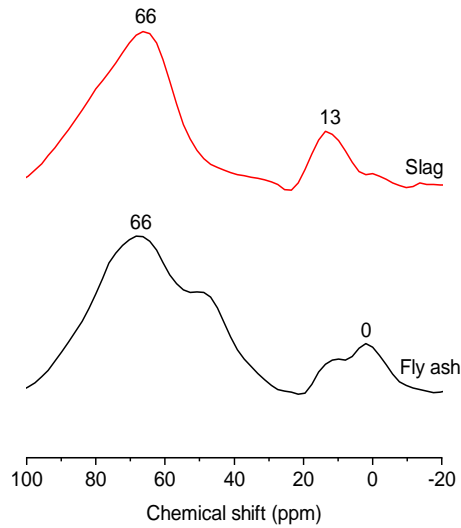


Fig. 5-10 MAS-NMR spectra of unreacted precursors: (a) ^{27}Al of FA and slag

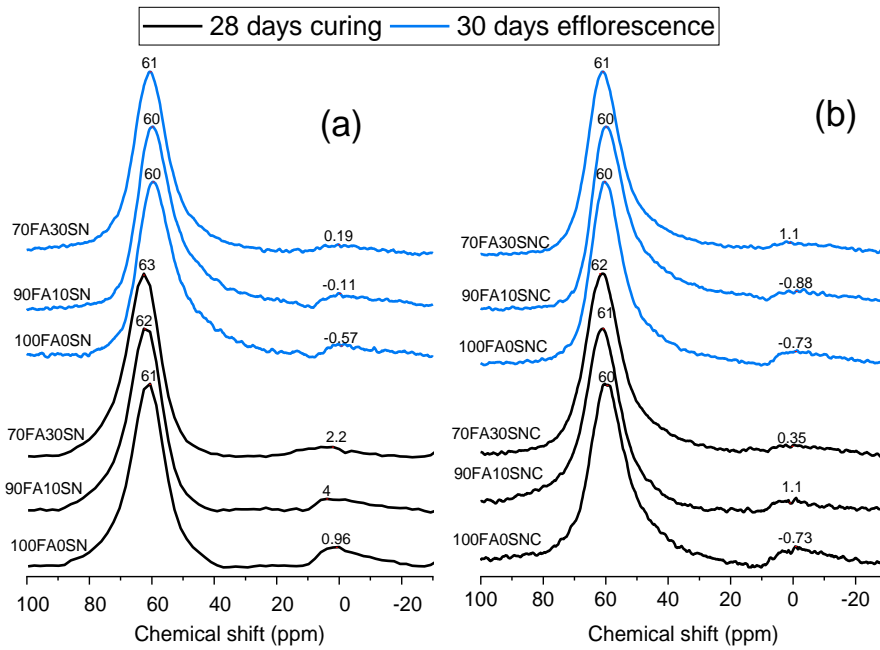


Fig. 5-11 ^{27}Al MAS-NMR spectra of binders before and after efflorescence: (a) binder specimens without Na_2CO_3 , and (b) binder specimens with Na_2CO_3 .

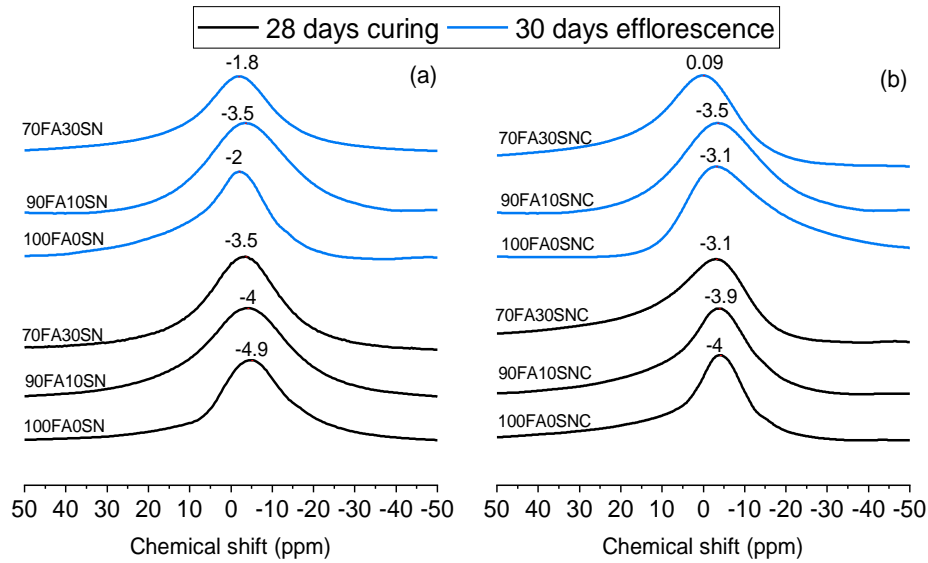


Fig. 5-12 ^{23}Na MAS-NMR spectra of binders before and after efflorescence: (a) binder specimens without Na_2CO_3 , and (b) binder specimens with Na_2CO_3 .

5.5 Conclusions

The degree of efflorescence in naturally-cured FA and FA–slag based AAM with mixed activator $\text{NaOH}+\text{Na}_2\text{SiO}_3$ and Na_2CO_3 investigated in this work. The inclusion of slag content in minor quantities such as 10 wt.% and 30 wt.% reduced the open porosity, leaching of alkalis and efflorescence behaviour of AAM. Furthermore, the inclusion of slag caused increased compressive and split tensile strength after curing. The amount and extent of efflorescence products formed were higher in binder mixes with 2 wt.% Na_2CO_3 . The compressive strength of binder specimens increased under efflorescence, but the development of crystallization pressure because of the deposition of salts inside the binder matrix reduced the split tensile strength of the binder specimens. Simultaneous progress of alkali activation and development of efflorescence products in binder specimens led to an increase in compressive strength under efflorescence.

The XRD and FTIR analysis showed a significant amount of geopolymer gel at the time of curing. After efflorescence, a slight degradation in N-A-S-H phases, increase in silica content accompanied by the development of carbonate phases was demonstrated, further supported by the TGA analysis in pure FA based AAM. The binder specimens with slag showed a simultaneous increase in the silica content and decalcification of N-(C)-A-S-H gel. The inclusion of Na_2CO_3 in binder specimens

induced a slight delay in the development of reaction products. Also, the addition of Na_2CO_3 accelerated the efflorescence. Under efflorescence, FTIR, XRD and TGA studies indicated the development of carbonated phases in all binder mixes with Na_2CO_3 .

The ^{27}Al MAS-NMR analysis indicated the movement of the Al[IV] environment towards lower chemical shifts under efflorescence ageing, because of the degradation in the tetrahedral aluminium environment of N-A-S-H/N-(C)-A-S-H gel. The movement in chemical shifts towards positive values in the ^{23}Na environment after efflorescence is attributed to the movement of bound-Na ions from the aluminosilicate framework, corroborating the degradation of N-A-S-H/N-(C)-A-S-H gel under efflorescence.

CHAPTER 6 EFFECT OF FLY ASH/SLAG RATIO AND ACTIVATOR CONCENTRATION ON EFFLORESCENCE OF FLY ASH/SLAG-BASED ALKALI-ACTIVATED MATERIALS

6.1 Introduction

Alkali-activated materials (AAMs), also called geopolymers, are a group of cementitious materials possessing the potential to provide a new class of binders, additional to traditional types of cement [25,148]. AAMs are described as materials with better mechanical strength, resistance to elevated temperature, fire, and acid, the potential to immobilize hazardous materials, and low carbon emissions, compared with ordinary Portland cement [211,212].

AAMs are synthesised by mixing solid aluminosilicate precursors, such as fly ash (FA), ground granulated blast furnace slag (GGBFS a.k.a. slag), metakaolin (MK) and combinations thereof (i.e., blended precursors), with an alkaline activator (e.g., NaOH, Na₂SiO₃, and KOH) to develop a binder paste. The hardened binder paste consists of a three-dimensional amorphous N-A-S-H (sodium aluminosilicate hydrate) gel structure interconnected with silica and alumina tetrahedral units resembling zeolitic structures [213], with alkali ions (Na⁺ or K⁺) neutralizing the charge deficit developed because of the isomorphic substitution of Al³⁺ instead of Si⁴⁺ in tetrahedral units of aluminosilicate framework [214]. The resulting aluminosilicate framework creates a strong ionic interaction by developing a Na-O-Al(Si) network, with a stoichiometric ratio of Na/Al = 1.02 and Si/Al = 2.2 [215]. Also, because of the charge deficiency in the aluminosilicate network, the position of Na⁺ or K⁺ around Al-O-Si sites is more plausible compared with Si-O-Si sites. Furthermore, the alkalis in the aluminosilicate network are in the state of Na(H₂O)_n⁺ in the pore solution [207,216] and weakly bound to the structural gel, which often leads to an unstable state when the binder is exposed to efflorescence and leaching.

The presence of unreacted activator in the form of residual free alkalis in binder mixes, which often leads to the formation of efflorescence in AAMs [158]. The understanding of efflorescence, which affects the durability of AAMs, is ongoing. In partially saturated AAM structures, efflorescence starts at the point of water contact assisted by capillary forces, followed by the leaching of free alkalis to the outer surface under

hydration, and reaction with atmospheric carbon dioxide forming carbonate salts on the surface of the structures [74,158,175]. Also, atmospheric CO₂ diffused into the binder mix reacts with water content to form HCO₃²⁻, which further reacts with alkalis in the pore solution to develop salt crystals inside the porous network, which is a phenomenon termed as subflorescence [158]. The excessive formation of salt crystals in the porous network is detrimental to the tensile strength of AAMs [158]. Previous studies have reported an excessive amount of alkali leaching up to 16% in FA and 55% in MK based AAMs [175,217,218]. The high leaching potential in AAMs decreases the ionic interaction between Al-O-Si and alkali ions, which weakens the Al-O-Si bonds and the structural integrity of the aluminosilicate network [219]. Also, the leached alkalis precipitate in the form of efflorescence or subflorescence salts and can cause severe damage to AAMs.

The partial inclusion of slag or calcium-rich precursors in FA based AAMs reduces efflorescence potential [175]. Slag inclusion in AAMs enhances mechanical properties and leads to the development of higher tortuosity in the porous network [220,221]. Hence, increased tortuosity impedes the movement of alkalis in AAMs and decreases the efflorescence potential in AAMs. The concentration of calcium in an aluminosilicate gel facilitates the formation of calcium aluminosilicate hydrate (C-A-S-H) gel [222]. The coexistence of N-A-S-H and C-A-S-H such as C-(N)-A-S-H/N-(C)-A-S-H is often observed in hardened AAMs, comprising of blended precursors [223]. The formation of C-(N)-A-S-H gel in the hardened AAMs depends on the relative ratio of slag and FA, i.e., the ratio of Ca to Al. A high-Ca/low-Al combination in the precursors leads to the formation of high calcium C-(N)-A-S-H gel in the resultant AAMs [56,59]. Specifically, the lower pH developed because of the presence of calcium in slag favours the formation of C-(N)-A-S-H and hinders the evolution of N-A-S-H as the dominant gel. Conversely, a low-Ca/high-Al combination in a high-alkaline environment favours the formation of N-(C)-A-S-H gel. A higher pH caused by the activator inhibits the dissolution of calcium from the precursor and favours the formation of a low-calcium N-(C)-A-S-H gel [224,225]. Though the inclusion of slag hinders alkali movement in AAMs, the inclusion of a high fraction is cost-prohibitive and carbonation prone. Besides, the study related to the stability of N-A-S-H and N-(C)-A-S-H gels under long-term efflorescence exposure is not explored.

To that end, this work aims to understand the effect of efflorescence on AAMs with different Ca and pH by varying slag and activator contents. The designed binder mixes were subjected to long-term efflorescence conditions. Microstructural studies were performed after curing and efflorescence to observe specifically the changes in Al environment in aluminosilicate gel, Na stability and mechanical properties. In this study, the efflorescence behaviour of NaOH+Na₂SiO₃ activated FA and FA/slag blended AAMs specimens with low Ca/(Si+Al) ratios (0 to 0.25) were assessed with two different Na₂O content (5 wt.% and 9 wt.%). The compressive and split tensile strengths were measured before and efflorescence. The phase changes before and after efflorescence were assessed using Fourier Transform Infrared Spectroscopy (FTIR), and Thermogravimetric Analysis (TGA). The changes in aluminium (²⁷Al) and sodium (²³Na) environment were analysed by and Magic Angle Spinning – Nuclear Magnetic Resonance (MAS-NMR) spectroscopy.

6.2 Materials and Methods

Class F FA or FA and a ground granulated blast furnace slag or GGBFS with a basicity coefficient K_b of 1.005 and hydration modulus (HM) of 1.9 was used and provided by Nielsen's group, Queensland, Australia. The X-ray fluorescence technique was used to determine the mineralogical composition of precursors and the results are summarised in Table 6-1.

Table 6-1 Compositional details of the precursors used in this study

	FA	GGBFS
	%	
SiO ₂	55.83	33.68
Al ₂ O ₃	34.28	14.54
CaO	2.88	42.49
Fe ₂ O ₃	2.43	0.55
MgO	0.78	6.01
K ₂ O	0.82	0.32
Na ₂ O	0.27	0.18
P ₂ O ₅	0.11	0.02
LOI	0.24	0.07

The 5 wt.%, 10 wt.% and 30 wt.% slag was mixed with FA to obtain the desired Ca/(Si+Al) ratios of 0.07, 0.10 and 0.25 mixed in a dry condition for 5 minutes. The activating solutions were produced using laboratory-grade NaOH pellets with 99% purity obtained from Chemsupply, Australia. D-grade Na₂SiO₃ (Na₂O=14.7 wt.%,

SiO₂ = 29.4 wt.% and H₂O = 52.7 wt.%) with M_s=2.0 (SiO₂/Na₂O) was procured from PQ Australia. The obtained NaOH pellets were dissolved in deionised water and mixed with Na₂SiO₃ solution to obtain M_s = 1.4 with 5 wt.% and 9 wt.% Na₂O and cooled to room temperature. The activator solution was prepared 3 h before mixing with solid precursors.

6.3 AAM synthesis and efflorescence conditioning

Table 6-2 shows the final mixes with different atomic ratios and Na₂O content.

Table 6-2 Mix design details of AAMs

Mix ID	Na ₂ O (wt.%)	FA (wt.%)	Slag (wt.%)	Al/Si	Ca/Si	Na/Al	Ca/(Si+Al)	Curing time (days)	Water/solid ratio (w/s)
9A	9	100	0	0.57	0.0	0.37	0.0	28	0.35
9B	9	95	5	0.56	0.11	0.38	0.07	28	0.35
9C	9	90	10	0.55	0.16	0.39	0.10	28	0.35
9D	9	70	30	0.52	0.36	0.44	0.25	28	0.35
5A	5	100	0	0.61	0.0	0.20	0.0	28	0.35
5B	5	95	5	0.60	0.12	0.21	0.07	28	0.35
5C	5	90	10	0.59	0.17	0.22	0.10	28	0.35
5D	5	70	30	0.56	0.40	0.25	0.25	28	0.35

AAMs specimens were prepared by mechanically mixing precursors with an alkaline activator (NaOH+Na₂SiO₃) for 5 min, with additional water added to achieve suitable workability and a final water/solid (w/s) ratio of 0.35 was achieved. The prepared binder mix was poured to cubical moulds of dimensions 30 mm × 30 mm × 30 mm and cylindrical moulds of dimensions Φ 25 mm × 25 mm (height). The prepared AAMs specimens were wrapped with plastic sheets and sealed in polycarbonate containers and allowed to cure naturally for 7 and 28 days under ambient conditions (~25°C).

6.4 Testing and characterization

The efflorescence formation was assessed by visual observation of samples after 28 days of curing following an established methodology [158,175]. To attain partially saturated conditions, the bottom portion of the specimens was immersed in water to a depth of 8 mm to 10 mm with the top surface exposed to air. The water level was regularly refilled to the initial level frequently.

After 28 days of curing, the binder specimens were tested for compressive strength, split tensile strength, and exposed to efflorescence conditions. After 28 and 90 days of exposure to efflorescence condition, the mechanical properties were measured again. A universal testing machine (MTS Insight 100) with a strain rate of 0.5 mm/min was used to measure the mechanical properties of binder specimens, following AS1012.10 and AS1012.9:2014.

The microstructural analysis was conducted by chemical characterization on a sample from the binder surface at depth < 2 mm. The collected samples were dried in an oven at 60 °C to equilibrate the weight; the dried samples were crushed and sieved through a 75- μm sieve. The powdered samples were dried again in an oven at 60 °C to evaporate the residual water content and stored in airtight containers. Microstructural characterisation of the binder specimens was assessed using X-ray computed tomography (CT) using a General Electric Phoenix v|tome|xS instrument fitted with a micro-tube. Scans were performed at 140 kV and 50 μA with a voxel size of 17 μm . 2000 images of projections recorded per specimen. The image projections were collected and merged into a three-dimensional (3D) volumetric representation of the binder mix specimens. 3D representative volumes were then extracted and used to assess the porosity within the binder mix specimens.

Shimadzu (IRAffinity-1S) ATR-FTIR was used for FTIR analyses at wavenumbers of 400 cm^{-1} (25000 nm) to 4000 cm^{-1} (2500 nm) before and after efflorescence. The spectral deconvolution between 650-1300 cm^{-1} and relative integral area under the selected peaks was performed using Origin 2020. A vendor-provided Gaussian multipeak fitting function was used to fit the spectra and $r^2 = 0.98-0.99$ was achieved throughout the deconvolution analysis.

A TA Instruments SDT 650 – thermogravimetric analyser was used to perform TGA analysis on binder samples using a heating rate of 20 °C/min and a temperature range between 30 °C – 1000 °C.

JEOL (ECX 400) solid-state NMR (11.7 T) 400 MHz with a probe of 4 mm and a spinning speed to 10 kHz was used to analyse ^{27}Al (Transmitter frequency = 156 MHz, scans = 1024) and ^{23}Na (transmitter frequency = 132 MHz, scans = 1024) environments. A pulse width of 6 μs and a relaxation delay of 2 s was used for all

samples. The obtained MAS-NMR spectra of the ^{27}Al environment are deconvoluted using Origin 2020. The Gaussian multipeak fitting functions were used to fit the spectra and $r^2 = 0.98-0.99$ was achieved throughout the deconvolution analysis.

The leaching concentrations of Na^+ ions from the bulk specimens were analysed using Shimadzu AA-7000 Atomic absorption spectrometer (AAS). The binder specimens ($30\text{ mm} \times 30\text{ mm} \times 30\text{ mm}$) after 28 days of curing were immersed in deionised water at the ratio of 1:50, in a sealed plastic box. Throughout the leaching experiment, the boxes were kept at $23 \pm 2\text{ }^\circ\text{C}$ with a relative humidity of $\geq 90\%$. Leachate of 10 ml was extracted at an interval of 30 days based on the procedure in Ref. [148,218].

6.5 Results and Discussion

6.5.1 Efflorescence formation and characterization

The efflorescence formation selected binder mixes activated with 9 wt.% and 5 wt.% Na_2O content are shown in Fig. 6-1 and Fig. 6-2 respectively. The binder mixes were exposed to partial saturation or efflorescence condition after 28 days of natural curing. Partial saturation causes water to flow through the porous network of binder mixes and dilute the salt-rich solution. The evaporation of water at the exterior surface of the binder specimens changes the solid/liquid interface system to a more energetic solid/vapour interface system [226]. Because of the increase in the energy, the capillary forces increase the water absorption and flow of pore solution towards the exterior surface. Concomitantly water evaporates from the pore solution and increases the salt concentration at the surface of the binder specimens. Furthermore, the diffusion of CO_2 from the atmosphere reacts with salts in pore solution to precipitates in the form of carbonate salts [183].

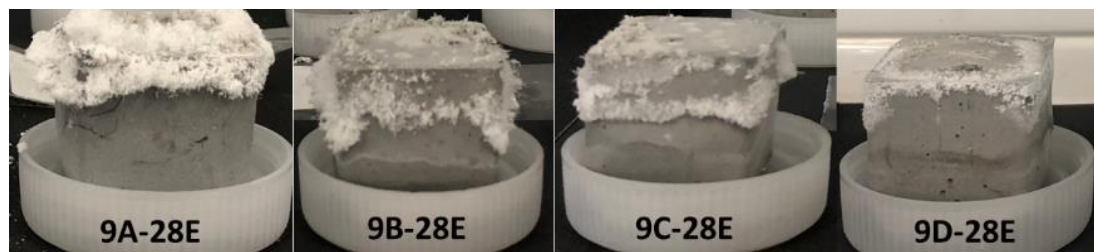


Fig. 6-1 Efflorescence formation on binder specimens activated with 9wt.% Na_2O content varying with $\text{Ca}/(\text{Si}+\text{Al})$ ratios.

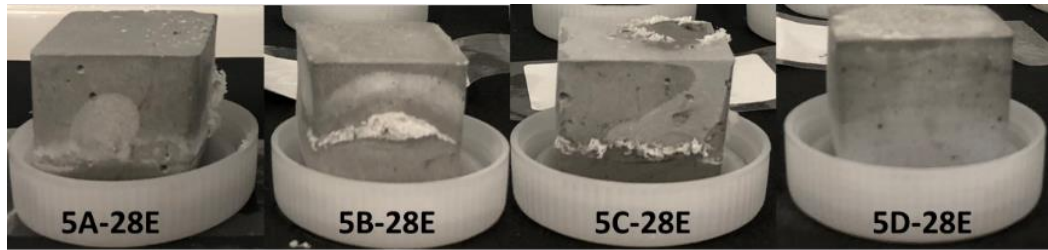


Fig. 6-2 Efflorescence formation on binder specimens activated with 5 wt.% Na_2O content varying with $\text{Ca}/(\text{Si}+\text{Al})$ ratios.

The optical characterization of binder specimens activated with 9 wt.% and 5 wt.% Na_2O contents with varying $\text{Ca}/(\text{Si}+\text{Al})$ ratios are shown in Fig. 6-3 and Fig. 6-4. The binder mixes activated with 9 wt.% Na_2O content exhibited a substantial amount of salt deposition on the surface of the specimens, indicating a higher amount of free alkali content leaching in binder mixes. After 10 days there were slight efflorescence products on the surface 9A, 9B and 9C specimens with low $\text{Ca}/(\text{Si}+\text{Al})$ ratios. At the end of 60 days, there were significant efflorescence products on the surface of the binder specimens. The binder mix with $\text{Ca}/(\text{Si}+\text{Al}) = 0.25$ showed no visible sign of efflorescence until 60 days of exposure. Previous works have demonstrated that an increase in slag content in binder mixes reduces the efflorescence potential of AAMs [175]. This behaviour is attributed to the formation of C-A-S-H gel which has more bound water and higher pore filling capacity compared with N-A-S-H gel [220]. Hence, the delayed efflorescence formation was observed in binder mixes with higher $\text{Ca}/(\text{Si}+\text{Al})$ ratios. However, the presence of higher alkali content in 9wt.% Na_2O mixes still facilitated the efflorescence at later stages. Because of the partial wetting-drying efflorescence test condition (where the top surface is dry and the bottom portion is wet), cracks started to appear on binder specimens at the end of 60 days of efflorescence exposure.

The specimens were significantly cracked at the end of 90 days of efflorescence exposure. The substantial movement free alkalis start to develop salts in the pores. With the increase in the salt deposition or subflorescence in the pores, crystallization pressure starts to develop in the surrounding area, leading to crack formation, resulting in damage of binder specimens and a decrease in tensile strength carrying capacity of binder specimens under efflorescence [158,193]. Also, FTIR, TGA and NMR data, which are discussed in subsequent sections, showed significant degradation of

aluminosilicate gel after efflorescence. The binder mixes with higher Ca/(Si+Al) also showed decalcification of aluminosilicate gel.



Fig. 6-3 Cylindrical binder specimens before and after 90 days of efflorescence exposure

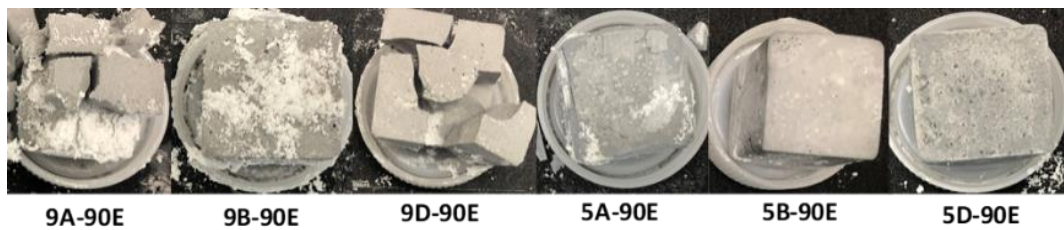


Fig. 6-4 Cubicle binder specimens after efflorescence

The binder mixes activated with 5 wt.% Na_2O content showed greater structural stability compared with 9 wt.% Na_2O mixes. A mild deposition of the salt on the specimens was seen with $\text{Ca}/(\text{Si}+\text{Al}) = 0.0$ at the end of 90 days of efflorescence and showed no cracking compared with 9 wt.% Na_2O mixes. The specimens activated with higher $\text{Ca}/(\text{Si}+\text{Al})$ ratios also assisted the reduction of the salt formation on the specimen surface.

The use of a lower amount of alkali activator in these mixes along with the increase in $\text{Ca}/(\text{Si}+\text{Al})$ ratios facilitated the formation of more C-A-S-H gel in these binder mixes because of lower pH. The presence of higher fractions of Ca in these mixes further

hindered the movement of alkalis and led to a lower efflorescence extent in binder mixes. In addition to lowered efflorescence, the inclusion of slag also refines the pore structure and restrict the movement of free alkalis. Also, FTIR results are consistent with these trends and showed increased intensity between 700-1300 cm^{-1} indicating the increase in aluminosilicate gel in 5A-5C binder mixes. The ^{23}Na NMR data revealed the low movement of Na^+ ions and ^{27}Al NMR data showed slight inclusion of Al in these binder mixes. However, TGA results showed slight carbonation in these binder mixes. The 5D binder specimen showed a significant amount of carbonation along with decalcification and dealumination of aluminosilicate gel, FTIR, TGA and NMR data are consistent with this observation.

6.5.2 FTIR Analysis

The FTIR spectra of binder specimens before and after efflorescence with varying $\text{Ca}/(\text{Si}+\text{Al})$ ratios and activated with i) 9 wt.% Na_2O and ii) 5 wt.% Na_2O is shown in Fig. 6-5 and 6-6. The spectral deconvolution is applied in the broad region between 600 cm^{-1} to 1300 cm^{-1} and the relative integral areas of selected peaks are summarised in Table 6-3. The peaks centred at $\sim 1000 \text{ cm}^{-1}$ and 940 to 960 cm^{-1} are assigned to the asymmetric stretching of Si-O-T (T = Al or Si) bonds of N-A-S-H gel and C-A-S-H gel, respectively [80,206,227]. The region beyond 1050 cm^{-1} is assigned to asymmetric stretching of Si-O-T (T = Al or Si) bonds of unreacted precursors [227]. The shoulders centred between 848 to 851 cm^{-1} are assigned to asymmetric stretching of CO_3^{2-} in binder specimens, and a sharp peak between 850 to 875 cm^{-1} is assigned to asymmetric stretching of AlO_4^- (Al-O-Si) groups [80,206].

The peaks centred between 670 to 770 cm^{-1} are assigned to Al-O-Si bending in the ring structures of aluminosilicates, indicating the formation of a geopolymer gel, with Al[IV] as the main component in the aluminosilicate gel [80,192,228–230], which necessitated further deconvolution.

Further analyses of FTIR spectra of binder mixes (9A-9D) with varying $\text{Ca}/(\text{Si}+\text{Al})$ ratios and 9wt.% Na_2O along with the deconvolution analysis are shown in Fig. 6-5(a to d) and the deconvolution of the spectra are shown in Fig. 6-5(a-28d to d-28d). The band assigned to Si-O-T stretching of N-A-S-H gel was observed at $\sim 1000 \text{ cm}^{-1}$ in 9A ($\text{Ca}/(\text{Si}+\text{Al})$ ratio of 0.0). The increase in $\text{Ca}/(\text{Si}+\text{Al})$ ratios in 9B to 9D caused a shift in the peak position of asymmetric stretching of Si-O-T bonds to lower wavenumber

(974 cm^{-1}) along with decreasing intensity and base width of the broad region between 600 to 1300 cm^{-1} (Fig. 6-5(a to d)), indicating the reduction in Al content in the binder mix, and the development of N-(C)-A-S-H phases [206,231].

The high Na_2O content in the binder mix suppresses the formation of the C-A-S-H phase because of higher pH in the mix, hence N-A-S-H gel is the dominant reaction product in these mixes [19]. Further inclusion of slag increases the availability of calcium in the mix and favours the simultaneous activation of C-A-S-H and N-A-S-H gel in the mix. The faster dissolution of calcium in these mixes initially favours the formation of C-A-S-H, delaying the formation of N-A-S-H gel in these mixes [19], causing the movement of Si-O-T stretching to lower wavenumbers after 28 days of curing. The binder mix with Ca/(Si+Al) ratio of 0.25 (Fig. 6-5(d-28d); 9D) showed two distinct peaks after deconvolution, assigned to Si-O-T stretching of C-A-S-H gel at 944 cm^{-1} , and a peak at 983 cm^{-1} was assigned to Si-O-T stretching of N-A-S-H gel.

The increase in Ca/(Si+Al) ratios decreased the Al content in the binder mixes and reduced the intensities of asymmetric stretching of AlO_4^- groups (850-875 cm^{-1}) and Al-O-Si bending (670 to 770 cm^{-1}) in the binder mix after 28 days of curing. This decrease indicates the reduction in the N-A-S-H gel [140,231] and concomitant formation of C-A-S-H gel in binder mixes [49]. The wavenumbers attributed to asymmetric stretching of unreacted precursor in the binder mixes shifted to lower wavenumbers with the increase in the Ca/(Si+Al) ratios, indicating the presence of a higher fraction of unreacted FA content in these mixes [232].

The reduction in Al content and the increase in calcium content favours the formation of alumina-substituted C-A-S-H gel. However, the presence of high Na_2O (9 wt.%) content increased pH in 9A-9D mixes, and subsequently favours the formation of N(C)ASH and N-A-S-H as the reaction product [19]. The relative integral area of asymmetric stretching of Si-O-T in N-A-S-H gel decreased with the increase in Ca/(Si+Al) ratio, with an increase in area under the asymmetric stretching of bands assigned to unreacted mullite content in FA (>1050 cm^{-1}) [218].

In addition, the area under Al-O-Si bending (670 to 770 cm^{-1}) and asymmetric stretching of AlO_4^- (850 to 880 cm^{-1}) groups decreased with an increase in the Ca/(Si+Al) ratios, indicating the reduced availability of Al in aluminosilicate gel. This

is shown by an increase in area under the asymmetric stretching of bands assigned to unreacted mullite content in FA ($>1050\text{ cm}^{-1}$) [218]. Also, the area under the Al-O-Si bending peak ($670\text{-}770\text{ cm}^{-1}$) and an asymmetric stretching peak of AlO_4^- ($850\text{-}880\text{ cm}^{-1}$) groups decreased with increasing Ca/(Si+Al) ratio, indicating a reduced availability of Al in aluminosilicate gel.

The FTIR spectra of the binder mixes (9A-9D) binder mixes (activated with 9wt.% Na_2O) after efflorescence with 9 wt.% Na_2O content is shown in Fig. 6-5(a to d) and the spectral deconvolution is shown in Fig. 6-5(a-28d to d-90d). The major changes after efflorescence were observed in the bands attributed to asymmetric stretching of Si-O-T, stretching of AlO_4^- groups and bending of Al-O-Si groups. Fig 5(a-90d to b-90d) shows the FTIR spectra of the binder mixes 9A and 9B with Ca/(Si+Al) ratios of 0.0 and 0.07, respectively. The wavenumbers assigned to the asymmetric stretching of Si-O-T shifted to lower wavenumbers and an increase in peak intensity was also measured. This indicates the degradation of geopolymer gel, and the formation of a higher fraction of Si-O-Si or silica-rich gel, because of the dissolution of silica in binder mixes [74,218].

Also, the bands and relative integral areas assigned to unreacted FA content increased with an increase in the Ca/(Si+Al) ratio. Contrary to the Si-O-T decreasing peak shift measured for binder mixes 9A and 9B, when the Ca/(Si+Al) ratio was increased to 0.10 and 0.25 in binder mixes 9C and 9D, respectively, an increasing shift was measured for the peak associated with asymmetric stretching of Si-O-T. This is indicative of a) the formation of silica-rich gel and b) decalcification of C-A-S-H in N-(C)-A-S-H environment [49,109,158].

The release of silica from the precursors during efflorescence leads to the formation of more Si-O-Si bonds, a decrease in the level of Ca^{2+} ions and the formation of silica-rich low calcium N-(C)-A-S-H gel [206]. The development of carbonates because of the CO_2 diffusion under efflorescence concomitantly decalcify the C-A-S-H gel and promote the development of carbonate salts under efflorescence [158]. Therefore, the relative integral areas after deconvolution indicate a) an increase in the area attributed to asymmetric stretching of Si-O-T, and b) a decrease in the areas attributed to the unreacted precursor content and C-A-S-H gel. The reduction in the bands and integral areas assigned to Al-O-Si bending and asymmetric stretching of AlO_4^- groups

decreased after efflorescence in 9C and 9D mixes, indicating the dealumination of Al[IV] in N-(C)-A-S-H gel after efflorescence.

The binder mixes (5A-5D) activated with 5 wt.% Na₂O content and varying Ca/(Si+Al) ratios before efflorescence are shown in Fig. 6-6(a to d) and corresponding spectral deconvolution are shown in Fig. 6-6(a-28d to d-28d). The binder mixes showed wavenumber shifts similar to 9 wt.% Na₂O binder mixes after alkali activation. The asymmetric stretching of Si-O-T in N-A-S-H gel shifted to lower wavenumbers with the increase in Ca/(Si+Al) ratios, indicating the formation of N-(C)-A-S-H gel.

The relative integral areas of asymmetric stretching of Si-O-T bands increased with an increase in Ca/(Si+Al) from 0.00 to 0.07 and 0.10, and the relative integral areas assigned to unreacted precursor content >1050 cm⁻¹ decreased in 5 wt.% Na₂O binder mixes, indicating their higher reactivity.

The binder mix 5D with Ca/(Si+Al) ratio of 0.25 exhibited two peaks after deconvolution that are assigned to N-A-S-H gel (989 cm⁻¹) and C-A-S-H gel (950 cm⁻¹). The intensity and relative integral areas of these peaks, attributed to the asymmetric stretching of AlO₄⁻ groups and Al-O-Si bending, respectively, decreased with an increase in Ca/(Si+Al) ratios indicating the reduction in Al fraction during activation.

The deconvoluted FTIR spectra of binder specimens with 5 wt.% Na₂O content and varying Ca/(Si+Al) ratios after efflorescence are shown in Fig. 6-6. The deconvoluted peaks associated with asymmetric stretching of Si-O-T bonds of binder mixes with Ca/(Si+Al) ratio of 0.0, 0.07, and 0.10 (Fig. 6-6(a to c) and 6-6(a-90d to c-90d)) shifted to higher wavenumbers with respect to the mixes before efflorescence, along with increased intensity in these bands.

The relative integral areas of the peaks attributed to N-A-S-H gel (~1000 cm⁻¹) and N-(C)-A-S-H gel (960-980 cm⁻¹) slightly increased and integral areas attributed to the unreacted precursor content (>1050 cm⁻¹) decreased after efflorescence. The increase in intensity and shift of wavenumbers can be attributed to the formation of Si-O-Si bonds in the aluminosilicate gel. An increase in the integral areas attributed to asymmetric stretching of AlO₄⁻ groups and Al-O-Si bending after efflorescence was

also seen, indicating the possible inclusion of Al tetrahedral units in the aluminosilicate gel.

The combination of lower Na₂O fraction and low Ca fraction initially inhibits the inclusion of Al during activation. However, during efflorescence, the rise in moisture content causes an increase in the pH of the pore solution and further facilitates the dissolution and inclusion of unreacted Al and Si in aluminosilicate gel. The binder mix with Ca/(Si+Al) ratio of 0.25 with 5 wt.% Na₂O content (5D, Fig. 6-6(d-28d to d-90d)) behaved differently from 5A-5C binder mixes, where the intensity of bands assigned to Si-O-T stretching of N-(C)-A-S-H gel shifted to higher wavenumbers along with a corresponding reduction in the peak intensity.

The integral area under these peaks increased, indicating the formation of Si-O-Si bonds or a silica-rich gel. The 5D mix also showed a reduction in the integral area assigned to N-(C)-A-S-H gel after efflorescence, indicating the decalcification under efflorescence, which is because of possible natural carbonation under efflorescence conditions [49]. The reduction in the integral areas assigned to AlO₄ groups and Al-O-Si bending indicated the dealumination in this binder mix.

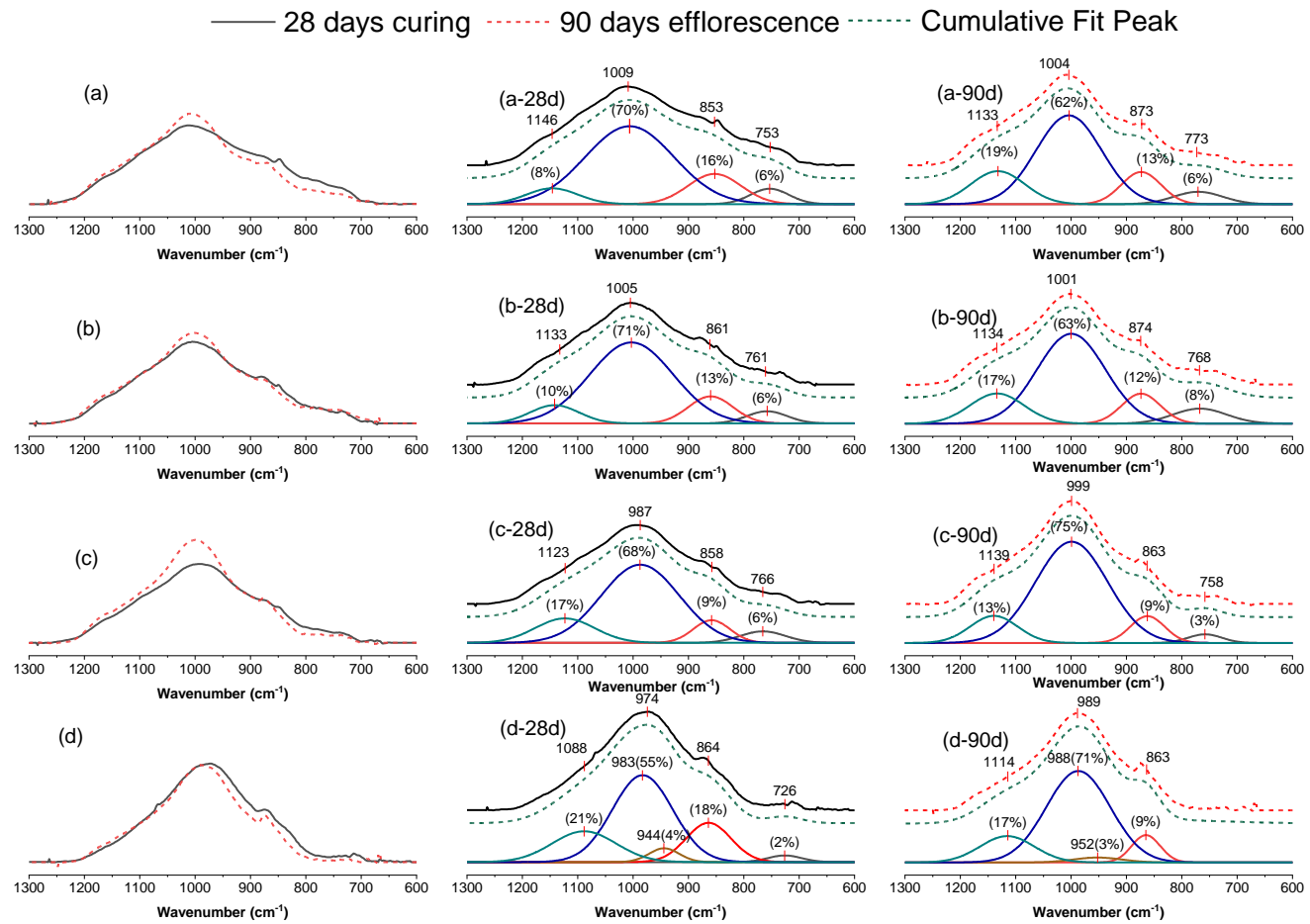


Fig. 6-5 FTIR spectra of AAMs with 9wt.% Na₂O content and varying Ca/(Si+Al) ratios

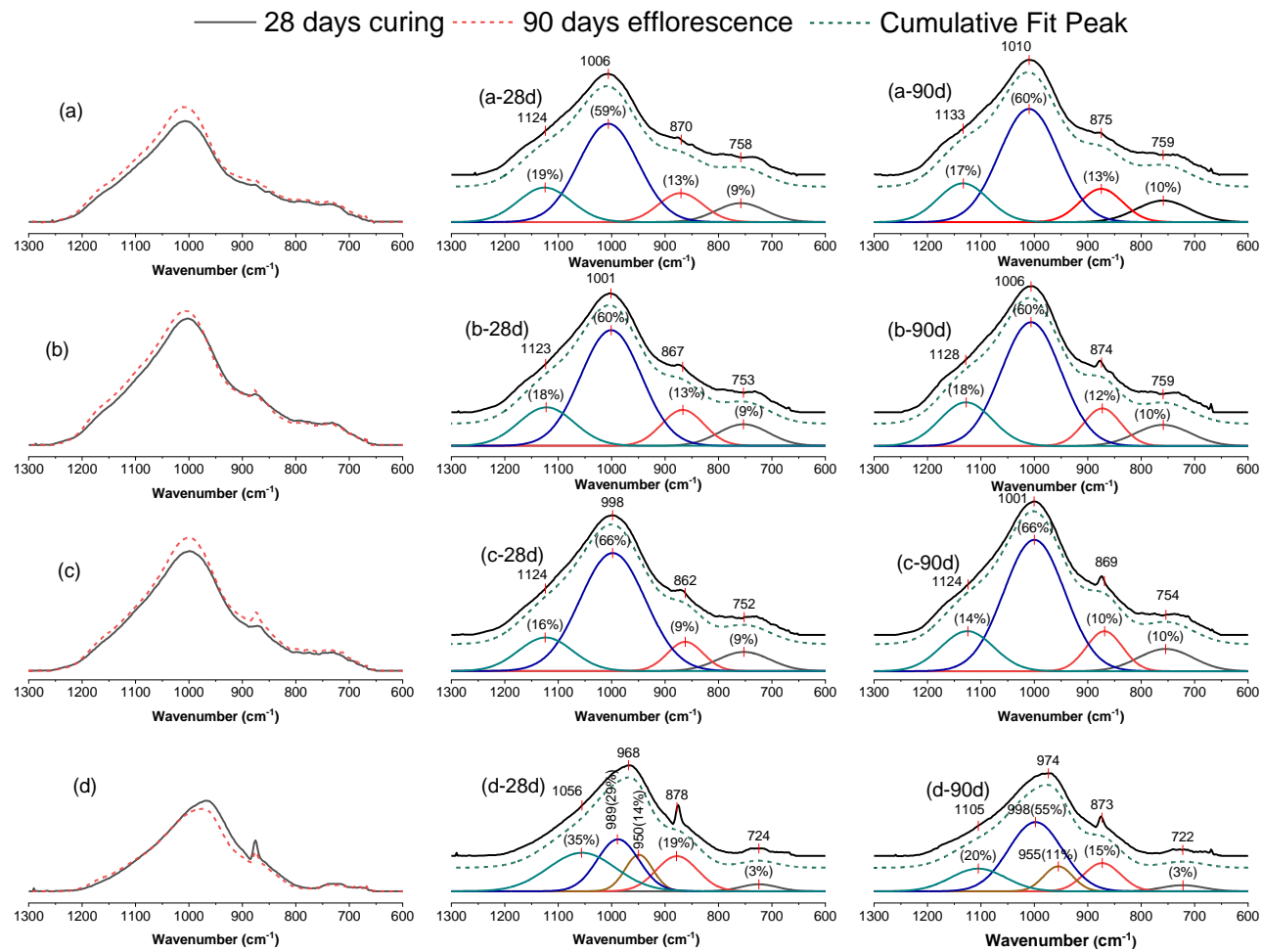


Fig. 6-6 FTIR spectra of AAMs with 5wt.% Na₂O content and varying Ca/(Si+Al) ratios

Table 6-3 Effect of efflorescence on Chemical shift and areas determined through deconvolution of FTIR spectra

Before efflorescence						After efflorescence					
Mix	670-770 cm ⁻¹	840-880 cm ⁻¹	940-960 cm ⁻¹	980-1010 cm ⁻¹	>1050 cm ⁻¹	Mix	670-770 cm ⁻¹	840-880 cm ⁻¹	940-960 cm ⁻¹	980-1010 cm ⁻¹	>1050 cm ⁻¹
Area (%)						Area (%)					
9A	6	16	-	70	8	9A	6	13	-	62	19
9B	6	13	-	71	10	9B	8	12	-	63	17
9C	6	9	-	68	17	9C	3	12	-	75	13
9D	2	18	4	55	21	9D	0	9	3	71	17
5A	9	13	-	59	19	5A	10	13	-	60	17
5B	9	13	-	60	18	5B	10	12	-	60	18
5C	9	9	-	66	16	5C	10	10	-	66	14
5D	3	19	14	29	35	5D	3	15	11	55	20

6.5.3 TGA analysis

The differential thermograms of all binder mixes before and after efflorescence activated with 9 wt.% Na₂O and 5 wt.% Na₂O are shown in Fig. 6-7a and Fig. 6-7b, respectively. The mass loss shown in the thermograms was attributable to free water evaporation between 50 °C and 200 °C in all binder mixes [19]. The binder mixes with Ca/(Si+Al) ratio of 0.0 with 9 and 5 wt.% Na₂O content, i.e., 9A (Fig. 6-7a) and 5A (Fig. 6-7b), exhibited minor mass loss peaks centred at 582 °C (9A), 716 °C (9A) and 604 °C (5A) after 28 days of curing, which are attributed to the presence of carbonate phases in mixes developed during mixing and handling [19,233].

After efflorescence, 9A and 5A mixes showed a shift in free water loss temperature from 96 °C to 114 °C in 9A and a shift from 124 °C to 144 °C in 5A, respectively. This was accompanied by an increase in mass loss peak intensity. The temperature shift indicates the possible formation of reaction products under efflorescence [19]. The secondary mass loss peak between 500 °C to 700 °C for both the 9A and 5A mixes was attributed to the decomposition of carbonates and the release of CO₂ [18]. A third peak, which occurred only in the 5A mix at 712 °C was attributed to the decomposition of sodium carbonates and nahcolite [18]. The evolution of carbonates was hence corroborated using the TGA analysis.

The specimens with a Ca/(Si+Al) ratio of 0.10, i.e., 9C and 5C show the dehydration of gel through the evaporation of free water at 133 °C in 9C and 141 °C in 5C, indicating the water-binding exhibited by zeolites. The pristine 9C and 5C specimens, showed mass loss peaks centred at 609 °C (9C), 558 °C (5C) and 635 °C (5C) were attributed to the thermal decomposition of N-(C)-A-S-H and calcite and sodium carbonate [18,90]. After efflorescence, the binder mixes 9C and 5C showed a slight increase in the intensity of free water loss peaks. The 5C mix showed major mass loss at 550 °C, which is attributed to the thermal decomposition of polymorphs of CaCO₃ and the N-(C)-A-S-H gel [90,234]. The third mass loss peak centred at 724 °C in 5C and 726 °C in 9C are attributed to the decomposition of CaCO₃ and Na₂CO₃ [90,234,235].

The binder mixes with Ca/(Si+Al) ratio of 0.25 activated with 5 wt.% Na₂O (5D) showed a mass loss peak at 99 °C correlated to the dehydration of water [18]. The 9D mixes showed three mass loss peaks at 484 °C, 597 °C and at 705 °C, which are assigned to the decomposition of N-(C)-A-S-H, traces of calcite, and sodium carbonates, respectively [18,90,234]. The 5D specimen showed a higher intensity compared with the pre-efflorescence mass loss peak as well as a shift in the peak temperature from 524 °C to 542 °C, which is assigned to the decomposition of N-(C)-A-S-H gel. The mass loss peaks at 705 °C in 9D and 713 °C in 5D are assigned to the decomposition of crystalline calcite and sodium carbonates phases [18,90]. After efflorescence, the broad differential thermograms were observed in the 5D mix exhibited free water mass loss peaks indicating dehydration of binder gel at 87 °C and decomposition of carbonate phases at 145 °C [18]. The intensity of mass loss peak at 728 °C in the 9C and 5C specimens increased after efflorescence, which indicates the formation of carbonates under efflorescence. Overall, the differential thermograms corroborate the presence of carbonate phases after efflorescence.

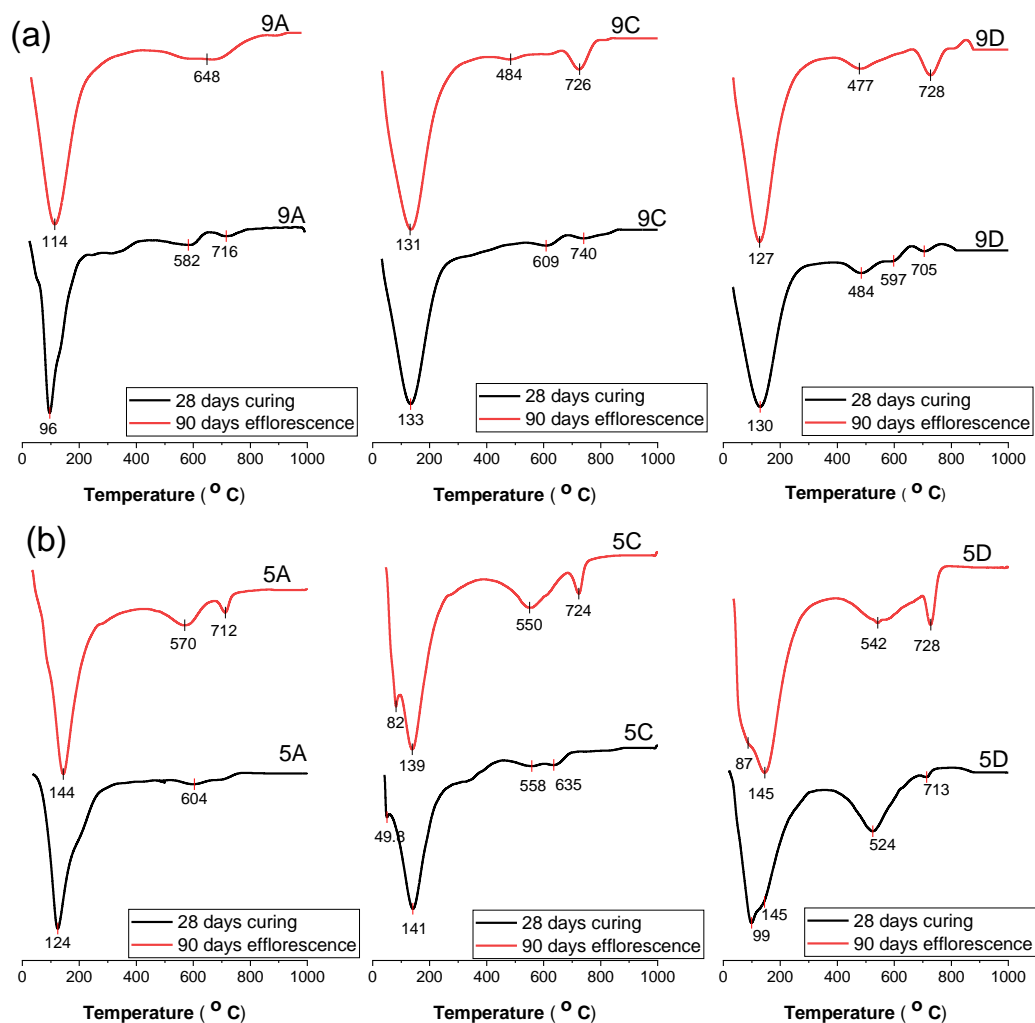


Fig. 6-7 (a) and (b) Differential thermograms of AAMs with 9wt.% and 5wt.% Na₂O content

6.5.4 MAS-NMR Analysis

6.5.4.1 ²³Na NMR

The ²³Na MAS-NMR resonances of alkali-activated binder mix with varying Na₂O content and Ca/(Si+Al) ratios before and after efflorescence are shown in Fig. 6-8a and 6-8b. The resonance centred at observed chemical shift $\delta_{\text{obs}} = -4.5$ ppm of the 9A binder mix with Ca/(Si+Al) ratio of 0.0 and 9 wt.% Na₂O (Fig. 5-8a; 9A) was attributed to the charge balancing Na⁺ ions surrounding Al centred tetrahedra or Al-O-Si sites in the N-A-S-H gel environment [203]. The increase in Ca/(Si+Al) ratios shifted the peak positions towards positive values (Fig. 6-8a; -2.8 ppm, -4.3 ppm and -3.2 ppm for binder mixes 9B, 9C and 9D, respectively, this was attributed to the Na⁺ ions surrounding N-(C)-A-S-H gel after activation [203]. The binder mixes with 5

wt.% Na₂O and Ca/(Si+Al) ratio of 0.0 showed the peak resonance values at $\delta_{\text{obs}} = -4.5$ ppm (Fig. 6-8b; 5A). The increase in Ca/(Si+Al) ratios also shifted the peak positions toward positive values (Fig. 6-8b; -3.2, -3.2 and -3.1 ppm for binder mixes 5B, 5C and 5D, respectively, and behaved similarly to 9 wt.% Na₂O content binder mixes after activation. Alkali ions in aluminosilicate gels neutralize the charges in two ways. Firstly, the resonance observed at approx. $\delta_{\text{obs}} = -4$ ppm is attributed to the bound Na⁺ ions to aluminosilicate gel balancing the charge deficit developed by Al atoms [236]. Secondly, the resonance at approx. $\delta_{\text{obs}} = 0$ ppm was attributed to the presence of Na⁺ in pore solution balancing aqueous Al(OH)₄⁻ groups [236].

After 90 days of efflorescence, the 9A (Fig. 6-8a) mix showed large deviations to the values of the chemical shifts towards positive values $\delta_{\text{obs}} = -0.56$ ppm. The spectra exhibited asymmetrical shape and extensive disorder of Na sites in AAMs, indicating changes in the N-A-S-H gel environment. The 9B, 9C and 9D binder mix shown in Fig. 8a also exhibited discernible deviations in chemical shifts towards positive values $\delta_{\text{obs}} = -1.4$, -2.6 and -1.6 ppm, respectively, which indicates changes in N-(C)-A-S-H gel environment. However, the binder mixes with an increased Ca/(Si+Al) showed comparatively less variation in both the resonance values and the shape of the NMR spectra. The resonance of the 5A binder mix after efflorescence was observed to shift from $\delta_{\text{obs}} = -4.7$ ppm to $\delta_{\text{obs}} = -3.8$ ppm (Fig. 6-8b). The resonance values of the 5B, 5C and 5D and slight shift for the 5B, 5C and 5D binder mixes observed at $\delta_{\text{obs}} = -2.9$ ppm (from $\delta_{\text{obs}} = -3.2$ ppm), $\delta_{\text{obs}} = -3.7$ ppm (from $\delta_{\text{obs}} = -3.2$ ppm) and $\delta_{\text{obs}} = -3.2$ ppm (from $\delta_{\text{obs}} = -3.1$ ppm), respectively, which indicates binder mixes with an increased Ca/(Si+Al) ratios has an insignificant effect on the chemical shift and the shape of the NMR spectra after efflorescence. The increased slag or Ca/(Si+Al) ratios in binder mixes further restricted the movement of bound Na⁺ ions in binder mixes indicating refinement of porosity because of the development of C-A-S-H gel in the mixes [220]. The chemical shift in the ²³Na environment was also observed under hydration and dehydration of aluminosilicates. The dehydrated AAMs exhibited the chemical shifts at higher negative values (-20 ppm), indicating a stronger interaction between the oxygen atoms of Al tetrahedra and Na⁺ ions [208,209]. The movement of resonances towards positive values indicates the degradation of N-A-S-H/N-(C)-A-S-H gel and changes in the position of bound Na⁺ ions because of hydration and change in the Si/Al ratios of aluminosilicate gel.

In general, Na^+ ions show a strong inclination to the Al-O-Si sites rather than the Si-O-Si sites. The movement of Na^+ ions in the binders increase the effective Na-O distance and coordination numbers, which would further decrease the ionic interaction between Na and oxygen atoms of the Al tetrahedral units of N-A-S-H/N-(C)-A-S-H gel [208,237]. The decrease in the electric field gradient at the Na^+ nucleus and decreased quadrupolar coupling exhibits a more isotropic Na^+ environment under hydration [238]. Hence, the bound Na^+ ions movement because of hydration and increase in silica content in the N-A-S-H/N-(C)-A-S-H gel exhibits the major changes in the Na environment and indicate the depolymerization of the aluminosilicate network. 9A-9D binder specimens with a 9 wt.% Na_2O showed larger movement in chemical shifts, however, the 5A-5D binder mixes (5 wt.% Na_2O) showed lesser variations in chemical shifts. The presence of a low Na_2O (5 wt.%), soluble silica and an increase in slag in 5A-5D mixes restricts the movement of Na^+ ions and therefore exhibiting more stability under efflorescence, compared to 9A-9D mixes.

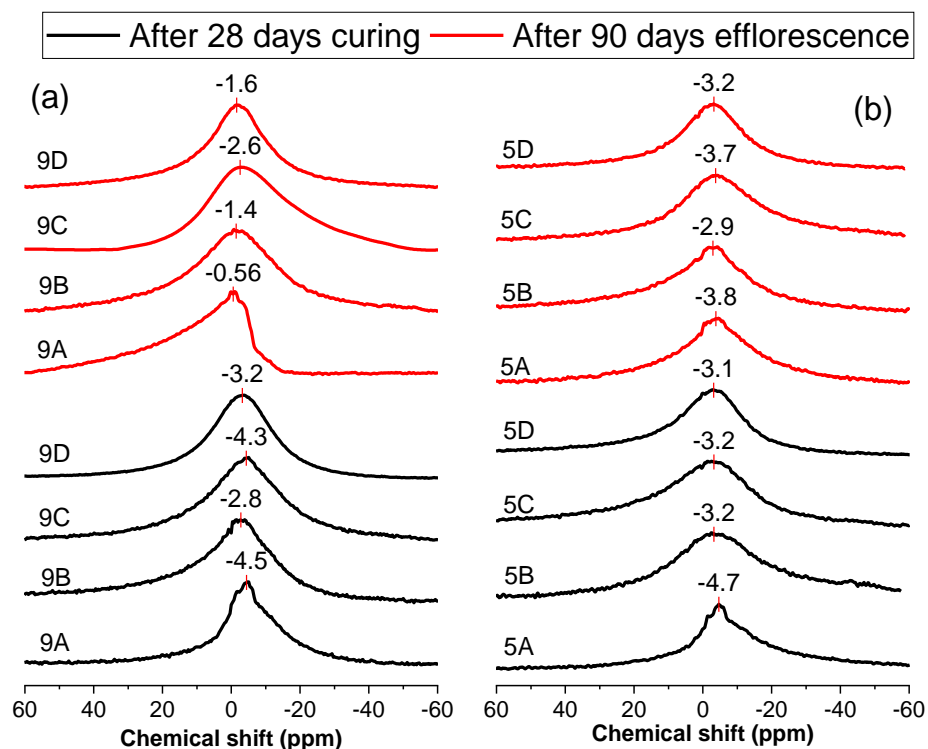


Fig. 6-8 ^{23}Na NMR spectra of (a) 9 wt.% and (b) 5 wt.% Na_2O AAMs

6.5.4.2 ^{27}Al NMR

The ^{27}Al MAS NMR environment of FA and slag precursors are shown in Fig. 6-9. the resonances centred at $\delta_{\text{obs}} = 67.6$ ppm in FA and $\delta_{\text{obs}} = 66.3$ ppm in slag is attributed

to the unreacted tetrahedral aluminium (Al[IV]) environment [115,236]. The resonance between $\delta_{\text{obs}} = 30 - 50$ ppm was assigned to unreacted penta-coordinated aluminium (Al[V]) in FA [239]. The resonances centred at $\delta_{\text{obs}} = 13.5$ ppm in the slag and $\delta_{\text{obs}} = 2.04$ ppm in the FA is assigned to the octahedral aluminium (Al[VI]) environment [115,236].

The ^{27}Al MAS-NMR spectra of binder mixes of the 9A-9D with varying Ca/(Si+Al) ratios activated with 9 wt.% Na_2O content is shown in Fig. 6-10(a to d) with the deconvoluted NMR spectra (Fig. 6-10(a-28d to d-28d)). The relative integral areas of deconvoluted peaks before and after efflorescence are shown in Table 6-4. The resonances attributed to the Al[V] and Al[VI] environment in of the 9A (Fig. 6-10(a and a-28d)); Ca/(Si+Al) ratio of 0.0) binder significantly decreased after activation. The narrow resonance at $\delta_{\text{obs}} = 60$ ppm showed an increase of Al[IV] indicating the highly polymerised N-A-S-H gel in the Q^4 environment [18,205,240].

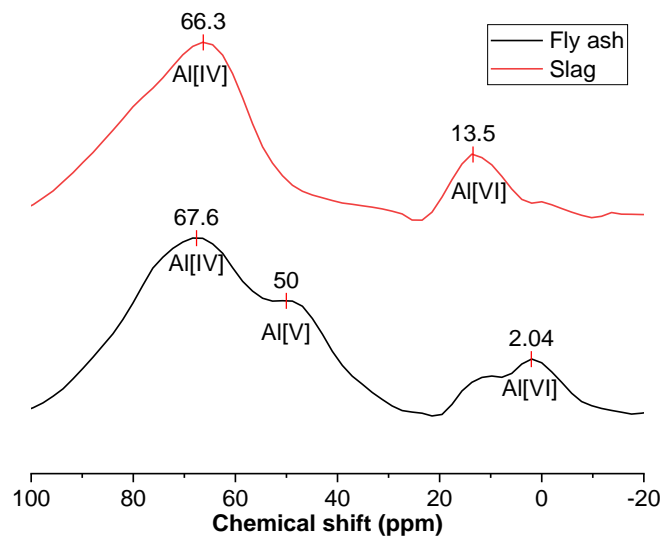


Fig. 6-9 ^{27}Al MAS-NMR spectra of raw materials

The 9B, 9C and 9D binder mixes (Fig. 6-10(b to d) and Fig. 6-10(b-28d to d-28d) with increased Ca/(Si+Al) ratios behaved similarly to the 9A binder mix, exhibiting the Al[IV] resonance at higher chemical shifts $\delta_{\text{obs}} = 62 - 63$ ppm indicating the formation of the N-(C)-A-S-H gel in these binder mixes after activation [18]. The deconvoluted NMR spectra of binder mixes 9A-9D resulted in two distinct peaks after activation attributed to the Al[IV] environment in N-A-S-H gel (9A; $\delta_{\text{obs}} = 60$ ppm), N-(C)-A-S-H gel (9B-9D; $\delta_{\text{obs}} = 62 - 63$ ppm) and Al[VI] ($\delta_{\text{obs}} = -0.8 - 3.9$ ppm) environment in the binder mixes after alkali activation.

After 90 days of efflorescence the binder mix 9A (Fig. 6-10(a and a-90d)) exhibited a shift to the Al[IV] resonances towards lower chemical shifts, $\delta_{\text{obs}} = 60$ ppm (from $\delta_{\text{obs}} = 61$ ppm) indicating dealumination and degradation of the N-A-S-H gel under efflorescence [241]. Also, broadening of the spectra was observed between $\delta_{\text{obs}} = 10 - 50$ ppm in Al[V] region after efflorescence. The 9B, 9C and 9D (Fig. 6-10(b- to d) and 9(b-90d to d-90d)) binder mixes with higher Ca/(Si+Al) ratios showed similar behaviour and the Al[IV] resonances shifted to lower values ($\delta_{\text{obs}} = 59 - 60$ ppm) and broadened in the Al[V] region indicating degradation of the N-(C)-A-S-H under efflorescence. The deconvolution of the spectra (Table 6-4) also resulted in three distinct peaks after deconvolution and they are attributed to Al[IV], a broad component between 20 to 50 ppm and Al[VI] respectively. The relative integral areas attributed to Al[IV] region decreased and areas between 20 to 50 ppm increased after efflorescence indicating changes in Al[IV] environment and degradation of N-A-S-H/N-(C)-A-S-H gel [218], which is consistent with FTIR results.

The broad component in the ^{27}Al MAS-NMR spectra was assigned to the pentahedral aluminium, distorted non-framework of the Al[IV] and tetrahedral Al[IV] environment in aluminosilicate structures [240,242]. The Al-O-Si sites in the aluminosilicate gel have a strong interaction towards the Na^+ ions to balance the charge deficiency of the Al ions [208]. The moisture movement during efflorescence can change the mobility of the bound Na^+ ions in the aluminosilicate gel, which can affect the interaction between alkalis and oxygen atoms of Al[IV] interaction. Leaching of Na^+ ions during efflorescence can lead to weaker or broken Al-O-Si bonds along with the distortion of these sites. Thus, constant leaching of Na^+ ions in the efflorescence environment can lead to the degradation of aluminosilicate gel. This has been confirmed by the ^{23}Na NMR spectra confirmed this behaviour and indicated the changes to the Na-O distance. The Na^+ ion has the ionic radius of 0.97 \AA with a charge of +1, the removal of alkalis from the aluminosilicate network changes the Na-O distance and decrease the Coulombic interaction between Al-O-Si and Na ions and change the Al coordination geometry [242]. The broadening of MAS-NMR spectra in between $\delta_{\text{obs}} = 20$ to 50 ppm region also indicates the distortion Al-O-Si bonds of Al[IV] environment. The distortion of Al-O-Si bonds increases the electric field gradient at the Al nucleus and increases the quadrupolar broadening [242]. Researchers have correlated the chemical shifts to Al-O-Si bond angles of

aluminosilicates. According to them Al-O-Si angles ($\delta_{\text{obs}} = 63$ ppm has $\theta = 138^\circ$ and $\delta_{\text{obs}} = 53$ ppm has $\theta = 146^\circ$) are higher for lower chemical shifts [243]. Hence, the movement of the chemical shift towards lower ppm values indicates the distortion of Al-O-Si bond angles after efflorescence.

The ^{27}Al MAS-NMR after spectra of the binder mixes (5A-5D) with 5 wt.% Na_2O and varying $\text{Ca}/(\text{Si}+\text{Al})$ ratios after activation along with the deconvoluted MAS-NMR spectra are shown in Fig. 6-11(a to d) and Fig. 6-11(a-28d to d-28d). The relative integral areas of the deconvoluted spectra are given in Table 6-4. After activation, the 5A (Fig. 5-11(a and a-28d)); $\text{Ca}/(\text{Si}+\text{Al})$ ratio of 0.0) binder mix showed an increased resonance intensity in the Al[IV] environment which indicates the presence of N-A-S-H gel in the mix. The 5A also exhibited broadening between $\delta_{\text{obs}} = 20$ to 50 ppm attributed to unreacted Al[V] or distorted Al-O-Si linkage in Al[IV] environment because of the decrease in Na content in the binder mix [240,244]. The deconvolution of NMR spectra the 5A binder mix after activation revealed three different peaks; $\delta_{\text{obs}} = -3.9$ ppm (Al[VI]), $\delta_{\text{obs}} = 48$ ppm (Al[V]) and $\delta_{\text{obs}} = 59$ ppm (Al[IV]) and the corresponding relative integral areas are given in Table 5-4. Increasing $\text{Ca}/(\text{Si}+\text{Al})$ or slag content in binder mixes 5B, 5C and 5D (Fig. 6-11(b to d) and Fig. 6-11(b-28d to d-28d) binder mixes shifted the Al[IV] to higher resonances $\delta_{\text{obs}} = 60$ -62 ppm indicating the presence of N-(C)-A-S-H gel in the binder mixes. The broad region between 20 to 50 ppm was observed to be narrower with an increase in $\text{Ca}/(\text{Si}+\text{Al})$ ratios and the 5D binder mix ($\text{Ca}/(\text{Si}+\text{Al})$ ratio of 0.25) showed an insignificant broadening of MAS-NMR spectrum in the 20 to 50 ppm region after activation.

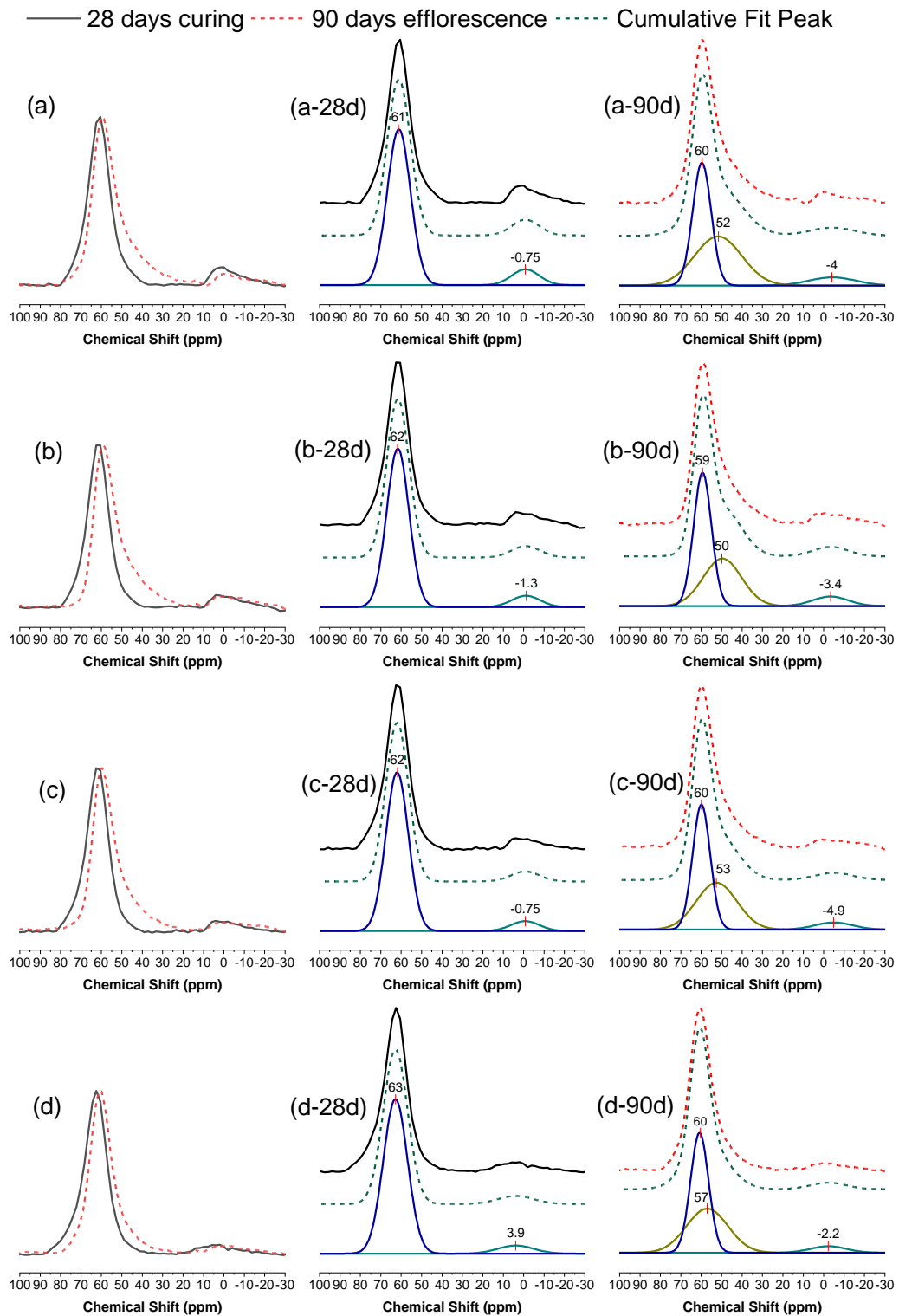


Fig. 6-10 ^{27}Al MAS-NMR spectra of binder specimens with 9wt.% Na_2O content and varying $\text{Ca}/(\text{Si}+\text{Al})$ ratios

After 90 days of efflorescence, the 5A-5C binder mixes Fig. 6-11(a to c) and Fig. 6-11(a-90d to c-90d) showed a different trend compared with 9A-9D binder mixes. The peak resonance of 5A shifted to higher values, from $\delta_{\text{obs}} = 59$ ppm to $\delta_{\text{obs}} = 60$ ppm. Additionally, narrowing of the spectra indicates the ongoing reactivity and inclusion

of Al[IV] units in the N-A-S-H environment. In contrast, the 5B and 5C binder mixes did not show any significant changes to the Al[IV] peak positions and 20 to 50 ppm broad regions of N-(C)-A-S-H environment under efflorescence. The deconvolution of the MAS-NMR spectra and calculated relative integral areas revealed an increase to the Al[IV] and a decrease to the Al[V] and Al[VI] resulting from efflorescence. However, the binder mix 5D (Fig. 6-11(d and d-90d)); Ca/(Si+Al) ratio of 0.25) showed different behaviour after efflorescence with the Al[IV] resonances shifted from $\delta_{\text{obs}} = 62$ ppm to $\delta_{\text{obs}} = 61$ ppm. This was accompanied by a slight increase in the 20 to 50 ppm region under efflorescence. The relative integral areas indicate the increased 20 to 50 ppm areas and decreased Al[IV] areas after efflorescence.

The C-A-S-H gel in the binder specimens is also prone to natural carbonation under these conditions. Researchers observed the effective movement of ^{27}Al intensity to lower chemical shifts and removal of C-A-S-H gel component from ^{27}Al environment after accelerated carbonation condition [18]. As a result, there was a higher movement in the ^{27}Al environment of the binder specimens with higher Ca/(Si+Al) ratios were observed. Comparison of the specimens containing 5 wt.% and 9 wt.% Na_2O revealed a higher amount of alkalis in the binder mix for the 9 wt.% Na_2O specimens and this was responsible for the more significant changes resulting from efflorescence.

6.5.5 Mechanical Properties and leaching analysis

The compressive strength of binder mixes before and after efflorescence exposure are shown in Fig. 6-12. Varying the Ca/(Si+Al) ratios also resulted in increased compressive strength. After 28 days of curing, the compressive strengths values of 9A – 9D specimens had a compressive strength of 22.15 ± 1.10 MPa (9A), 27.23 ± 1.50 MPa (9B), 29.90 ± 1.50 MPa (9C), and 48.59 ± 2.43 MPa (9D), respectively. The 5A-5D binder mixes had lower compressive strength values after 28 days of curing: 9.30 ± 0.46 MPa (5A), 12.21 ± 0.61 MPa (5B), 14.74 ± 0.74 MPa (5C) and 24 ± 1.2 MPa (5D), respectively.

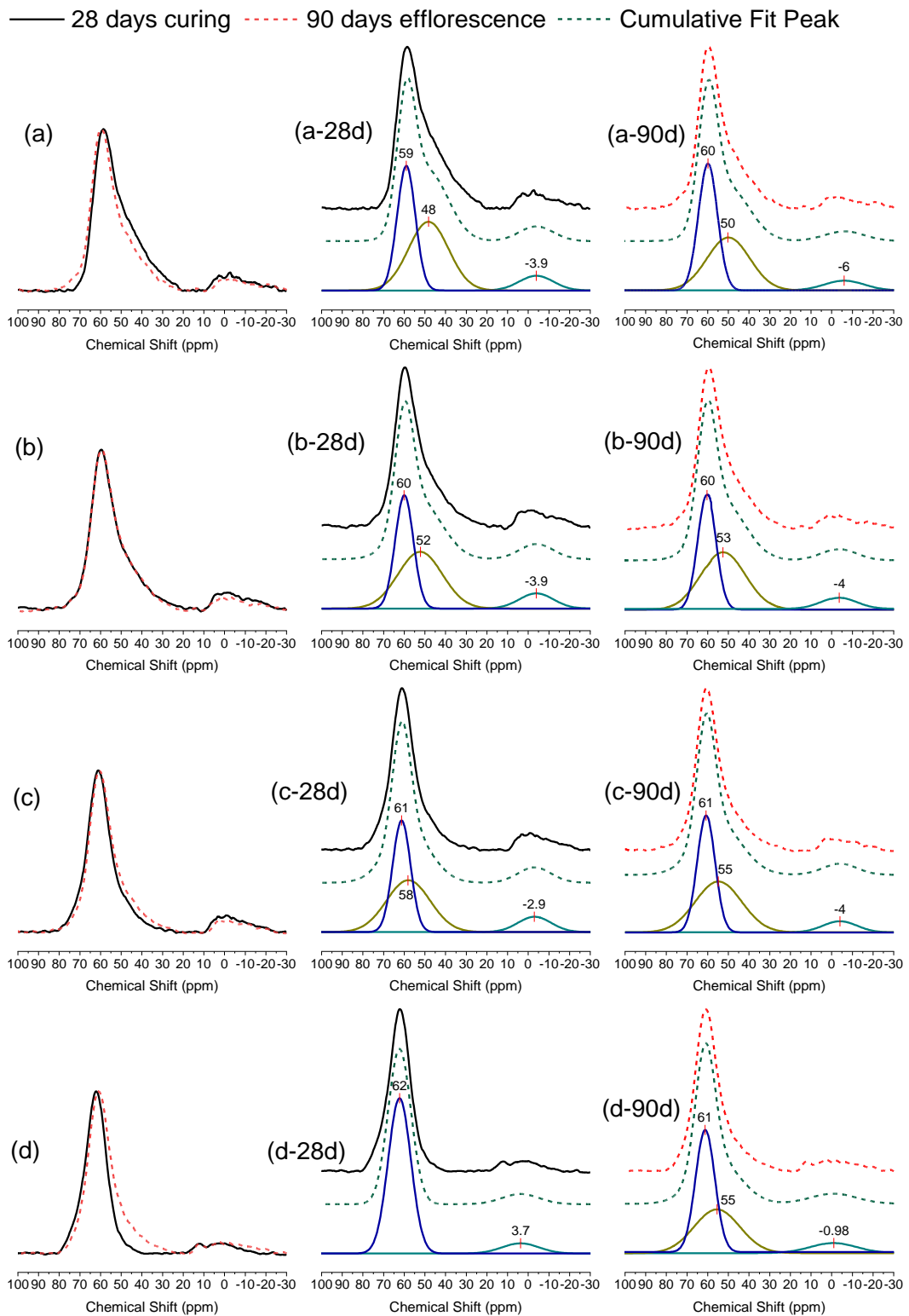


Fig. 6-11 ^{27}Al MAS-NMR spectra of binder specimens with 5 wt.% Na_2O content and varying CA/(Si+Al) ratios

Table 6-4 Effect of efflorescence on Chemical shift and areas determined through MAS-NMR

Before efflorescence							After efflorescence						
Sample ID	Chemical shift (ppm)	Area (%)	Chemical shift (ppm)	Area (%)	Chemical shift (ppm)	Area (%)	Sample ID	Chemical shift (ppm)	Area (%)	Chemical shift (ppm)	Area (%)	Chemical shift (ppm)	Area (%)
9A	61	89.4	-	0	-0.8	10.6	9A	60	45.7	52	46.7	-4.0	7.6
9B	62	91.5	-	0	-1.3	8.5	9B	59	52.5	50	40.1	-3.4	7.4
9C	62	92.7	-	0	-0.8	7.3	9C	60	50.2	53	43.6	-4.9	6.2
9D	63	92.9	-	0	3.9	7.1	9D	61	51.1	57	43.3	-2.2	5.6
5A	59	41.1	48	49.8	-3.9	9.1	5A	60	44.1	50	41.4	-6.1	7.7
5B	60	40.5	52	49.4	-3.9	10.1	5B	60	41.6	53	50.7	-3.7	7.6
5C	61	41.8	58	47.5	-2.9	10.6	5C	61	43.5	55	48.7	-4	7.7
5D	62	91.6	-	0	3.7	8.4	5D	61	45.5	55	45.7	0.98	8.8

The lower activator content (5 wt.% Na₂O) used in these binder mixes was responsible for the lower compressive strength. The higher alkali content in the binder mix (9 wt.% Na₂O) led to a higher degree of activation in binder mixes compared with 5 wt.% Na₂O binder mixes. Also, an increase in Ca/(Si+Al) ratios through the inclusion of slag leads to the formation of C-A-S-H gel and facilitates the coexistence of N-A-S-H/C-A-S-H gel, which would further enhance the compressive strength after activation.

After 28 days of efflorescence, the binder mixes with 9A-9D binder mixes showed no significant changes to compressive strength behaviour. The 9A and 9C specimens showed an increase in compressive strengths, while the 9B and 9D specimens showed a decrease in compressive strength values. Because of the slow nature of efflorescence reaction, it is difficult to observe any significant changes in compressive strengths after efflorescence. However, the variation in compressive strength observed in this study can be attributed to the effect of efflorescence on compressive strength values. After 90 days of efflorescence, it was not feasible to evaluate the compression strength of the 9A-9D specimens because of their extensive damaged, and therefore they were assumed to have negligible strength. On the other hand, the 5A-5D specimens showed increasing compressive strength with increasing efflorescence exposure. After 90 days of efflorescence, the compressive strength was 12.81±0.64 MPa, 14.94±0.75 MPa, 17.99±0.90 MPa and 26.25±1.31 MPa for the 5A-5D specimens, respectively. The higher compressive strength after efflorescence is attributed to the dissolution of silica

and alumina content under efflorescence conditions [245], and this is consistent with FTIR and MAS-NMR analysis.

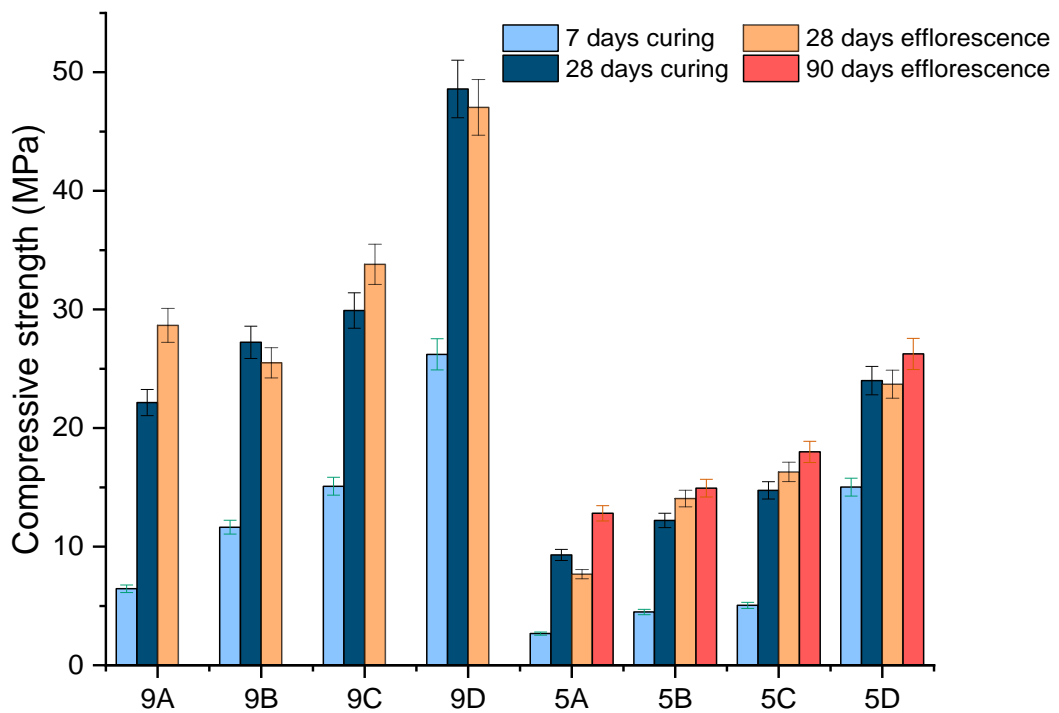


Fig. 6-12 Compressive strength of binder specimens

The split tensile strength of the binder specimens after 28 days of curing is shown in and Fig. 6-13. The binder mixes activated with 9 wt.% Na₂O with varying Ca/(Si+Al) ratios showed an increasing trend in split tensile strength values after activation. After 28 days of efflorescence, a significant decrease in split tensile strength was observed in 9A-9D binder mixes.

This is attributed to the higher extent of efflorescence which led to the development of crystallization pressure in binder mixes [193,246] and a concomitant decrease in tensile strength of binder mixes. Also, recent studies show that decreased trend in tensile strength of binder mixes with an increase in silica modulus [247]. The dissolution of silica content during the efflorescence is also a plausible reason for exhibiting a decrease in split tensile strengths.

The split tensile strength of binder mixes activated with 5 wt.% Na₂O and varying Ca/(Si+Al) showed an increasing trend after 28 days of curing. After 28 days of efflorescence, the binder mixes 5A-5C showed an increasing trend in split tensile

strength values, which is attributed to the low efflorescence formation in these binder mixes.

The FTIR and NMR results also showed ongoing alkali activation reaction and slight inclusion of Al and Si units under efflorescence conditions. The FTIR and MAS-NMR data showed degradation of aluminosilicate gel after efflorescence, where no efflorescence products were visible. However, excessive carbonates were observed in TGA analysis because of the natural carbonation of the binder mix. Hence, no change in split tensile strength could be attributed to the carbonation of the 5D binder mix.

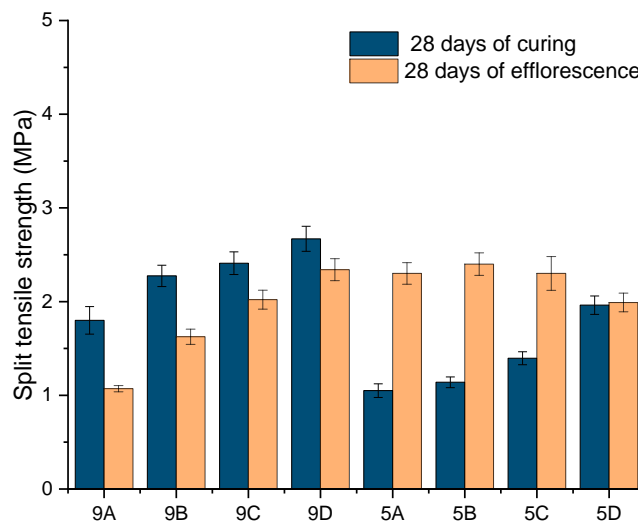


Fig. 6-13 Split tensile strength of binder specimens

The leaching concentrations of Na^+ ions from AAM binder mixes at end of 30, 60 and 90 days are shown in Fig. 6-14(a) and Fig. 6-14(b). The binder mixes with zero calcium or slag content showed higher leaching potential compared with binder mixes with higher $\text{Ca}/(\text{Si}+\text{Al})$ ratios. The increase in $\text{Ca}/(\text{Si}+\text{Al})$ significantly reduced the leaching of Na^+ ions from binder mixes. Irrespective of the alkali content, the binder mixes with $\text{Ca}/(\text{Si}+\text{Al}) = 0.25$ showed the lowest leaching potential of Na^+ ions. The decrease in leaching potential is attributed to the lower porosity values developed because of the slag addition. Fig. 6-15 shows the porosity values of selected binder mixes after activation. Irrespective of the alkali content, the binder mixes with a $\text{Ca}/(\text{Si}+\text{Al})$ ratio of 0.0 showed higher porosity values compared with binder mixes with a $\text{Ca}/(\text{Si}+\text{Al})$ ratio of 0.25.

Previous research work has demonstrated that excess calcium occupies more pore volume and refines porous network along with higher tortuosity in pore network [220]

and inclusion of slag significantly decreased the pore diameter from 47.1 nm to 9.1 nm along with the reduction in pore volume from 33% to 8% [248]. Hence, the coexistence of N-A-S-H and C-A-S-H gel, reduction in leaching potential because of the pore refinement significantly influenced the efflorescence extent and delayed the efflorescence formation. However, the excessive alkali content in 9 wt.% Na₂O binder mixes showed significant efflorescence formation after 60 days of exposure and severely damaged the binder mixes. The presence of lower Na₂O (5 wt.%) and varying Ca/(Si+Al) ratios refined the pore structure and significantly reduced the efflorescence formation and exhibited higher stability compared with 9 wt.% Na₂O binder mixes. After efflorescence, there was an increase in porosity values, which is attributed to the loss of alkalis from the binder mixes.

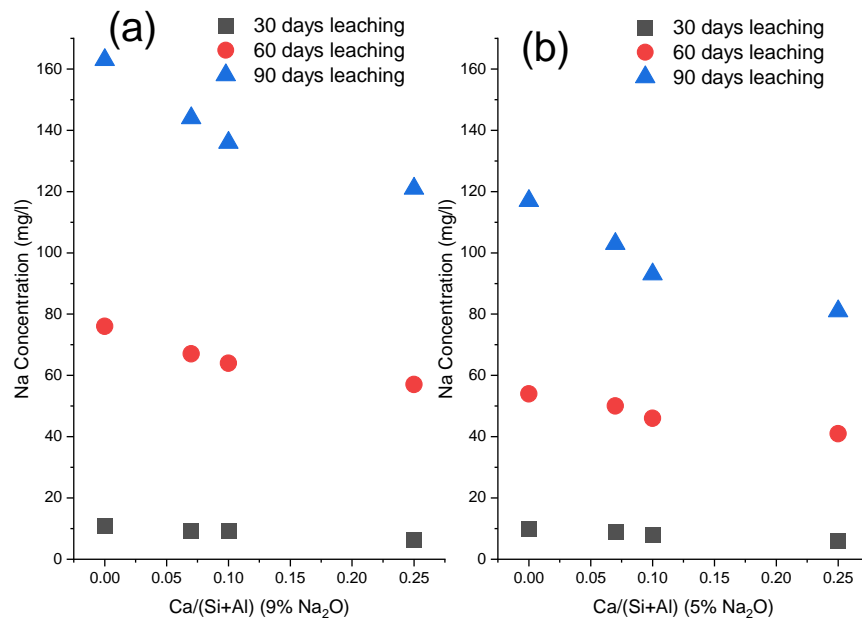


Fig. 6-14 Concentration of sodium leached from AAM specimens at 30, 60 and 90 days (a) 9wt.% Na₂O specimens (9A-9D) and (b) 5wt.% Na₂O (5A-5D) specimens

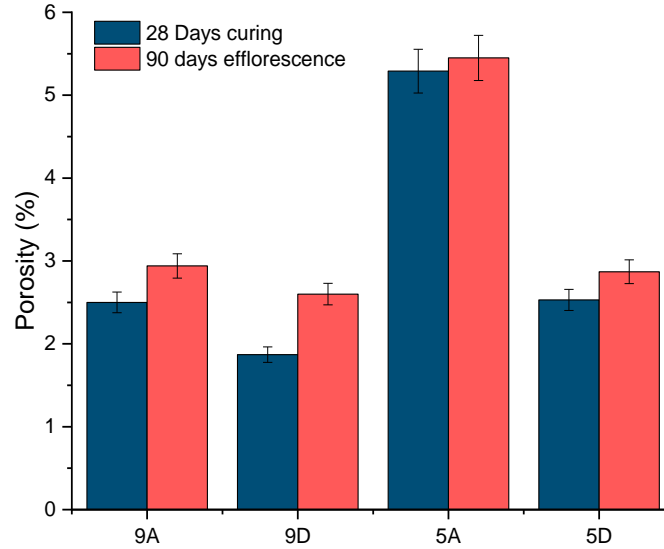


Fig. 6-15 The porosity of binder specimens before and after efflorescence

6.6 Conclusions

The efflorescence of FA/slag-based AAMs was investigated vis-à-vis FA/slag ratio and Na_2O concentration focussing on structural changes in N-A-S-H/N-(C)-A-S-H gels.

The inclusion of slag decreased the leaching potential of Na^+ ions from the FA/slag binder mixes and caused a decrease in porosity and efflorescence. The 5 wt.%- Na_2O binder mixes overall exhibited a distinct decrease in efflorescence formation and increased stability in comparison to 9 wt.%- Na_2O binder mixes. The N-A-S-H/N-(C)-A-S-H gel degradation in 9 wt.%- Na_2O binder mixes was supported by ^{23}Na and ^{27}Al MAS-NMR showing a high degree of mobility of Na^+ ions, and movement of Al[IV] environment to lower resonances. The N-A-S-H/N-(C)-A-S-H gels in the 5 wt.%- Na_2O binder mixes in opposition were stable, as supported by minor changes in ^{23}Na and ^{27}Al MAS-NMR environments.

The decrease in split tensile strength in 9 wt.%- Na_2O binder mixes was attributed to high efflorescence formation and degradation in N-A-S-H/N-(C)-A-S-H gel. The increase in split tensile strength after efflorescence in 5 wt.%- Na_2O binder mixes is attributed to the low efflorescence and slowly progressing alkali reaction. The split tensile strength in general increased with increased activator content (9 wt.% vs 5 wt.%) before efflorescence at a constant $\text{Ca}/(\text{Si}+\text{Al})$ ratio, whereas split tensile strength interestingly decreased after efflorescence with an increasing activator

content because of higher efflorescence formation and degradation of N-A-S-H/N-(C)-A-S-H gel in 9 wt. % -Na₂O binder mixes.

Overall, the 5 wt. % -Na₂O binder mixes with moderate Ca/(Si+Al) ratios exhibited greater resistance to efflorescence formation and increased mechanical properties compared with 9 wt. % Na₂O mixes with Ca/(Si+Al) ratios.

CHAPTER 7 EFFECT OF FLY ASH/SLAG RATIO AND Na₂O CONTENT ON THE LEACHING BEHAVIOUR OF ALKALI-ACTIVATED MATERIALS

7.1 Introduction

Alkali-activated materials (AAMs) or geopolymers are potential sustainable cementitious alternatives to ordinary Portland cement (OPC) which are vital to construction activities [39,245]. AAMs are widely recognised for their low carbon footprint and mechanical performance [179,249]. AAMs are generally produced with precursor materials such as fly ash (FA), slag (GGBFS) and metakaolin (MK) are activated with alkaline activators at room temperature [102]. However, availability, lack of homogeneity, the cost-effectiveness of raw materials, lack of standard code of practices and lack of understanding of durability behaviour (carbonation, acid resistance, alkali-aggregate reaction, efflorescence, and leaching) limit the dissemination of geopolymer technology [183,250]. Hence, it is imperative to understand the physicochemical behaviour that controls the performance of AAMs under harsh environmental conditions such as carbonation, acid resistance, efflorescence, chloride ingress and leaching behaviour.

The phenomenon of leaching of ions in OPC concrete is a slow process and it takes up to ~100 years [147]. whenever concrete is in contact with water, the chemical equilibrium between porous solution and reaction products is altered. Because of the change in concentration gradient between the external environment and pore solution, the diffusion of solid phases to the pore solution is observed. Subsequently, the main ionic species from the pore solution moves towards the external environment to induce new chemical equilibrium [251]. The OPC concrete under leaching at ambient temperature is affected by several factors such as porosity, water/cement ratio, pore water and pH. It has been identified that the degradation of OPC concrete in the water at 25 °C goes through four stages. Stage1 the dissolution of NaOH and KOH leads to higher pH (>12.5). Stage2 is at pH 12.5, where the dissolution of Ca(OH)₂ was observed. Stage3, when pH drops from 12.5 to 10, leaching of Ca(OH)₂, Aft, AFm and C-S-H phases were observed. Stage 4, pH below 10, calcite and mineral aggregates were observed [251,252]. The water/cement (W/C) ratio is one more key factor that influences the degradation of OPC concrete under leaching. The higher W/C ratio maintained while mixing the concrete leads to larger porosity and followed

by the higher dissolution of Ca under leaching. However, the lower W/C ratio leads to a reduction in initial precipitation of $\text{Ca}(\text{OH})_2$ and leads to extended hydration under leaching, decreasing the leaching potential of Ca[147].

Unlike OPC, there is a lack of understanding of the leaching behaviour of AAMs. Also, AAMs usually consist of 3 wt.% to 10 wt.% of alkali content, which is significantly higher than OPC[158]. Under leaching, the significant amount of unreacted free alkali content in the binder matrix is readily diffuse to the pore solution and subsequently to the external environment. However, the behaviour of bound alkalis in geopolymer structures under leaching environments is not explored. Some researchers have observed the complete leaching of alkalis from the FA and MK binders under long term leaching [253]. The leaching of alkali ions in acidic solution up to 40-60% and in water up to 12-16% and 20% - 30 % was also reported in studies[158,183]. There is also a study related to the dissolution of Ca and Al in FA-slag based AAMs under the accelerated leaching test [147]. Other factors such as density, porosity, and tortuosity, the total surface area of the specimens, curing and leaching temperatures significantly influence the leaching behaviour of AAMs.

The design of high durability AAMs depends on the type of precursors and their blends, activator type and concentration. The high FA content favours the formation of N-A-S-H gel (sodium aluminosilicate hydrate) and high slag content favours the formation of C-A-S-H gel (calcium aluminosilicate hydrate) respectively. Depending on the amount of FA-slag and activator concentration used while processing blended AAMs, the reaction mechanisms favour the formation of N-(C)-A-S-H/C-(N)-A-S-H gel [19]. FA based AAMs belonging to the family of aluminosilicates resembles three-dimensional pseudo zeolitic structures connected with AlO_4 and SiO_4 units and forms Al-O-Si bonds. The charge deficit developed because the isomorphic substitution of Al^{3+} for Si^{4+} is balanced by cations (Na^+ or K^+) supplied from the alkaline activator. Previous works have also shown that Na^+ ions are in the state of $\text{Na}(\text{H}_2\text{O})_n^+$ [175], they are weakly bound to both aluminosilicate gel and water molecules. Under harsh environments such as leaching and efflorescence, the alkali ions diffuse from the aluminosilicate structure. This may result in broken or distorted Al-O-Si bonds, which may lead to weaker aluminosilicate gel. The pure slag based AAMs leads to the formation of C-A-S-H gel, which resembles a disordered tobermorite structure

[67,254]. Generally, the Tobermorite structure is layered structures and made of Si tetrahedral units bridged by oxygen atoms. The consecutive layers of tobermorite are connected by intermediate Ca ions through ionic interaction and forms $\text{SiO}_4\text{-Ca-SiO}_4$ bonds. Similar to N-A-S-H gels, some of the Si^{4+} atoms are replaced by Al^{3+} atoms and the resulting charge deficit is balanced by Na^+ or K^+ ions [255].

A substantial amount of research work has been carried to understand the behaviour of AAMs under harsh environments. However, studies related to the optimization of design parameters of AAMs and structural changes of N-A-S-H/C-A-S-H gel under leaching conditions are not explored. Also, the leaching of alkalis directly influences the outward movement of free alkalis from hardened AAMs under the interaction with water and the subsequent efflorescence formation[175]. Furthermore, leaching behaviour also plays a vital role in the immobilization of radioactive toxic wastes and heavy metals such as lead, cadmium, and chromium.[256,257].

Despite the significant advancement in the field of AAMs, there is a limited understanding of the long-term leaching behaviour of AAMs and the relationship between precursor ratios, mix design and microstructural changes. Most of the previous works primarily focused on mechanical performances and other durability factors. The main theme of this work is to understand the stability and degradation of FA-slag based AAM phases under long-term leaching. Also, the effect of slag/Calcium incorporation on porosity of AAMs, leaching of alkalis and the behaviour of N-A-S-H/N-(C)-A-S-H gel under leaching. Furthermore, understanding leaching behaviour also assists in developing a key indicator of efflorescence potential and resistance to rebar corrosion. The present study aims at designing a series of low calcium FA/slag geopolymer binder specimens with a range of 9wt.%, 7wt.% and 5wt.% Na_2O content and activated with sodium hydroxide and sodium silicate ($\text{NaOH}+\text{Na}_2\text{SiO}_3$). The concentration of leached alkalis from the binder specimens after 90 days was measured using atomic absorption spectroscopy (AAS). Microstructural changes were observed using FTIR (Fourier Transform Infrared Spectrometer) and XRD (X-ray Diffractometer). MAS-NMR (Magic Angle Spinning – Nuclear Magnetic Resonance) was used to observe the changes in ^{23}Na and ^{27}Al environments. Total porosity, dry density, and capillary absorption are some of the measured physical properties along with compressive and split tensile strength. The

leaching behaviour is correlated with precursor ratios, Na₂O content and stability of AAM binder mixes.

7.2 Materials and Methods

Precursor materials Class F flyash (according to ASTM C618 [171]) and slag (basicity coefficient $K_b = 1.005$ and hydration modulus $HM = 1.9$) were procured from Neilsen's group in Queensland, Australia. The mineralogical composition of FA and slag was determined by the X-ray fluorescence technique (Table 7-1). Fig. 7-1. Shows XRD patterns of FA and slag, the presence phases such as quartz, and mullite were identified in unreacted FA. Unreacted slag shows the presence of such as tri-calcium silicates and aragonite were observed in unreacted slag.

Table 7-1 Chemical compositions of FA and GGBFS as determined by XRF. LOI is the loss on ignition at 1000 °C.

	Weight Fraction (wt.%)								LOI
	SiO ₂	Al ₂ O ₃	CaO	MgO	K ₂ O	Na ₂ O	Fe ₂ O ₃	P ₂ O ₅	
FA	55.830	34.280	2.880	0.778	0.819	0.269	2.430	0.111	0.24
GGBFS	33.680	14.540	42.49	6.010	0.320	0.180	0.551	0.022	0.07

Laboratory grade sodium hydroxide (NaOH) was obtained from Chemsupply, Australia and D-grade sodium silicate solution (Na₂O = 14.7 wt.%, SiO₂ = 29.4 wt.% and H₂O = 52.7 wt.%) with $M_s = 2.0$ (SiO₂/Na₂O ratio) was obtained from PQ Australia. The NaOH and Na₂SiO₃ solutions were prepared by mixing them to get a desired Na₂O content with a $M_s = 1.4$ SiO₂/Na₂O ratio and cooled to room temperature before mixing with precursors. The NaOH and Na₂SiO₃ solutions were formulated to get 5wt.%, 7wt.% and 9wt.% Na₂O content.

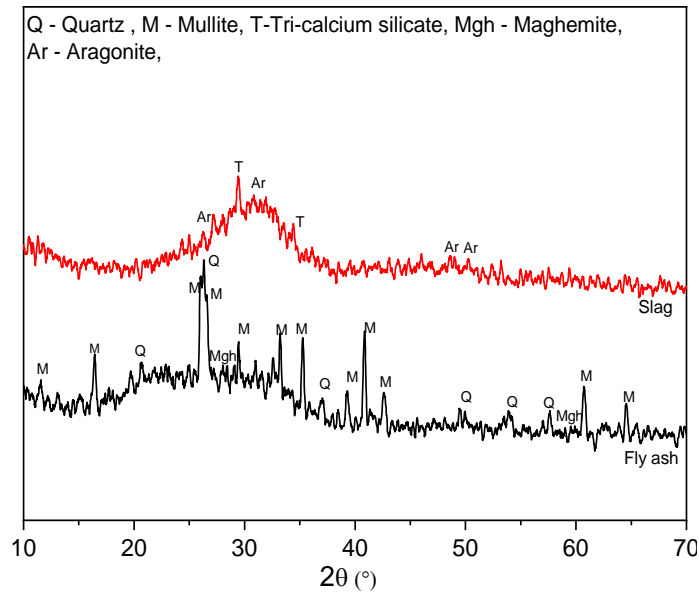


Fig. 7-1 X-ray diffractograms of FA and slag.

7.2.1 AAM binder preparation

Precursors were mixed with alkali activator solution for 5 minutes and additional was added to achieve the final water/solid (w/s) ratio of 0.35 for all specimens. The prepared pastes were poured into 30 mm × 30 mm × 30 mm cubes and Φ 23 mm × 23 mm cylindrical moulds. The prepared specimens were kept in a hermetically sealed box for 28 days of natural curing at 23 ± 2 °C. The specimens were exposed to leaching conditions for 90 days after the curing process. The final mix of proportions and details are shown in Table 7-2.

Table 7-2 Mix proportions and curing conditions of binders

Mix Id	FA (wt.%)	Slag (wt.%)	Na ₂ O (wt.%)	Al/Si	Ca/Si	Na/Al	Ca/(Si+Al)	Curing time (days)	Water/solids (w/s) ratio
9A	100	0	9	0.57	0.0	0.37	0.0	28	0.35
9B	95	5	9	0.56	0.11	0.38	0.07	28	0.35
9C	90	10	9	0.55	0.16	0.39	0.10	28	0.35
9D	70	30	9	0.52	0.36	0.44	0.25	28	0.35
7A	100	0	7	0.59	0.0	0.28	0.0	28	0.35
7B	95	5	7	0.58	0.11	0.29	0.07	28	0.35
7C	90	10	7	0.57	0.16	0.30	0.10	28	0.35
7D	70	30	7	0.54	0.38	0.35	0.25	28	0.35
5A	100	0	5	0.61	0.0	0.20	0.0	28	0.35
5B	95	5	5	0.60	0.12	0.21	0.07	28	0.35
5C	90	10	5	0.59	0.17	0.22	0.10	28	0.35
5D	70	30	5	0.56	0.40	0.25	0.25	28	0.35

7.2.2 AAM Testing and characterization

The binder specimens were analysed after 28 days of curing. Leaching tests were performed on bulk specimens, specimens were placed in the plastic box, immersed in deionised water at the ratio of 1:50 following ASTM D 3987 and ASTM E 1908-16 [172,173]. The boxes were kept at 23 ± 2 °C with a relative humidity of $\geq 90\%$. The leachate of 10 ml was collected every 30 days to measure the concentration of the Na^+ and Si^{4+} ions. At the end of 90 days, the concentration of Ca^{2+} and Al^{3+} was also measured using Shimadzu AA-7000 Atomic absorption spectrometer (AAS).

Compressive and split tensile strength on cubes and cylindrical specimens were measured after the pre-and post-leaching process. MTS universal testing machine was used to measure mechanical properties with a strain rate of 0.5 mm/min was used to measure mechanical properties, following AS1012.10 and AS1012.9:2014 [189,190]. The broken samples were taken for open porosity measurements. Samples were crushed and dried at 105 °C to attain an equilibrium weight. Later samples were kept in a vacuum desiccator with suction pressure of 90 kPa for 4 h. The specimens were kept in a hot water bath under vacuum, the surface dry and buoyant dry mass was recorded to compute open porosity values.

A water absorption test was performed on cylindrical samples. Initially, the specimens were dried at 50 °C, mass and initial dimensions were recorded. Later the specimens were partially immersed in water (5mm), the water was refilled till the constant mass of specimens was achieved and the whole test was carried in a sealed container to avoid water evaporation. The final data has been reported as the mass of water (g) absorbed per cross-sectional area (cm^2). The specimens were again dried at 105 °C until the constant mass was achieved to calculate the dry density of specimens. The final data has been reported as the ratio of the mass of dry specimens over the total volume of the specimen.

The leached specimens were crushed to measure open porosity, after drying at 105 °C to attain an equilibrium mass. Cooled samples were placed in a vacuum desiccator with suction pressure of 90 kPa for 4 h. Later specimens were immersed in a hot water bath under vacuum, the surface dry mass and buoyant mass of samples were measured for open porosity calculations.

After the curing and post leaching process, the binder specimens were crushed and dried at 60 °C to equilibrate the weight and sieved through a 75 µm sieve and dried at 60 °C to ensure the evaporation of residual water content. The powdered samples were kept in airtight plastic vials to avoid atmospheric exposure. Later microstructural analysis was performed on these samples.

The powdered binder samples were used for XRD, FTIR, and MAS NMR analysis. XRD was carried using PAN Analytical Xpert Pro with Cu K_α radiation, operated at 30mA and 40 kV, with a step size of 0.020°, 2θ range of 5 - 70° and scan time of 0.85 s/step. FTIR analyses were carried on binder specimens using Shimadzu FTIR spectrometer, with a wavelength range from 400 cm⁻¹ to 4000 cm⁻¹. JEOL (ECX400) solid-state NMR (11.7T) 400 MHz using a probe of 4 mm with a spinning speed of 10 kHz was used to measure the chemical shift of ²⁷Al (transmitter frequency = 156 MHz, scans = 3072) and ²³Na (transmitter frequency = 132 MHz, scans = 3072) nuclei. The pulse width of 6 µs and a relaxation delay of 2 s was used for all samples.

7.2.3 Simulation details

Molecular dynamics (MD) simulations were performed to leach the behaviour of Na⁺ ions from the N-A-S-H gel structure. The amorphous N-A-S-H gel structure was built by modifying the Sodalite structure [258]. The structure was built by randomly replacing Si⁴⁺ ions with Al³⁺ ions. To build a N-A-S-H structure of Al/Si = 1.0, equal number of Na⁺ ions were added to balance the charge deficit developed because of the substitution of Al³⁺ instead of Si⁴⁺. CHARMM forcefield was used to develop the potential parameters of bonds, angles and nonbonded interaction. The total potential expression of the CHARMM force field is as follows.

$$U_{potential} = \sum_{bond} [k_b(r - r_o)^2] + \sum_{angle} [k_a(\theta - \theta_o)^2] + \sum_{dihedral} [V^D[1 + \cos(n\phi + \delta)]] \\ + \sum_{van\ der\ Waals} \sum_{i \neq j} 4\epsilon_{ij} \left[\left(\frac{\sigma_{ij}}{r_{ij}} \right)^{12} - \left(\frac{\sigma_{ij}}{r_{ij}} \right)^9 \right] + \sum_{electrostatic} \sum_{i \neq j} \epsilon_{14} \frac{Cq_i q_j}{\epsilon r_{ij}}$$

NAMD [176] version 2.8 package was used to run MD simulations. Virtual Molecular Dynamics (VMD 1.9.2) [178] was used for post-process and interactive studies. Simulations were performed on Dell workstation, i9 10core/20 processors with 32 GB ram for 1ns. Fig. 7-2 and 7-3 shows the structure of sodalite and amorphous N-A-S-

H. The solvation box (Fig. 7-4) with 900 water molecules was built around the N-A-S-H structure to simulate the leaching condition. Energy minimization was carried (0 kPa and 0 K) using the conjugate gradient method. The model was brought to atmospheric temperature (300 K) in three intervals and brought to 1 bar pressure in four intervals.

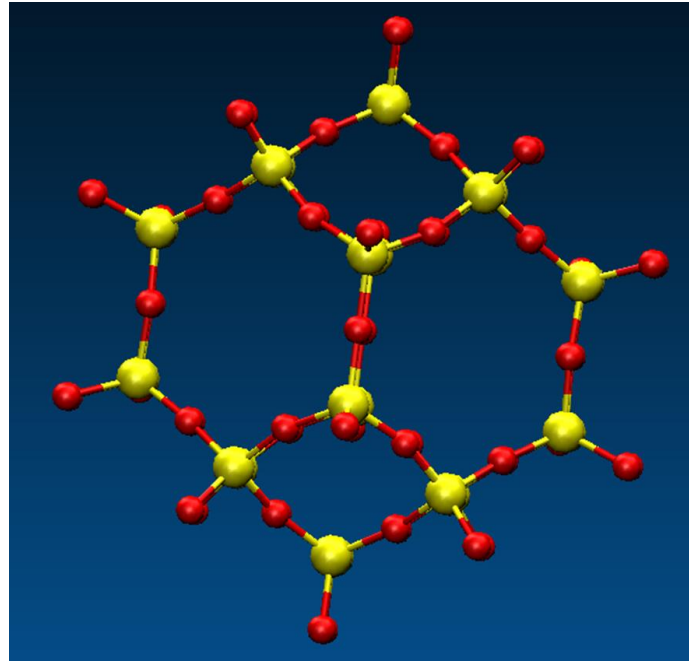


Fig. 7-2 Structure of Sodalite

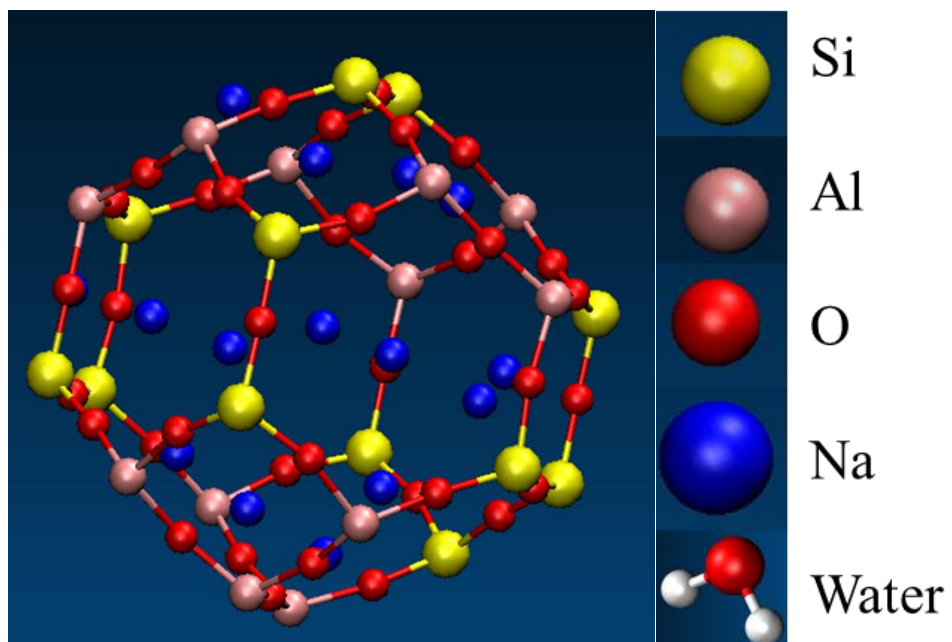


Fig. 7-3 Amorphous N-A-S-H structure

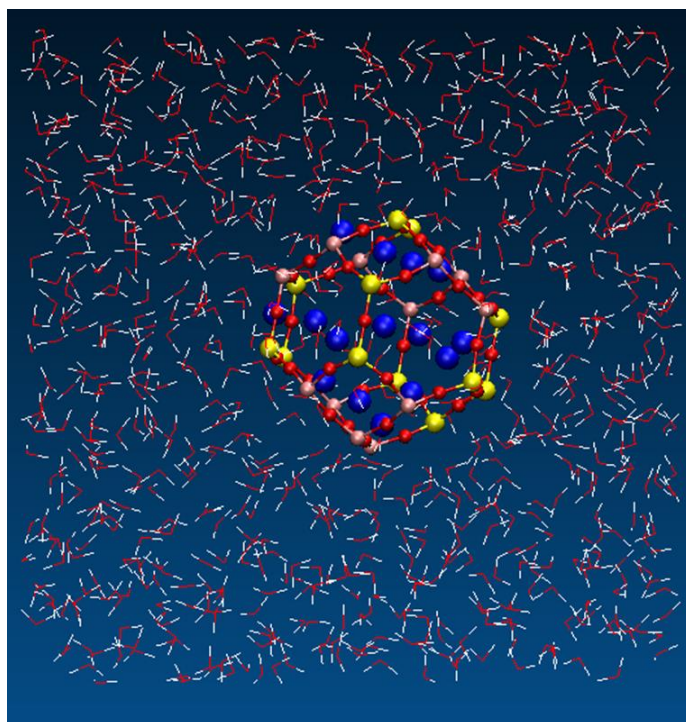


Fig. 7-4 Solvation model of N-A-S-H structure

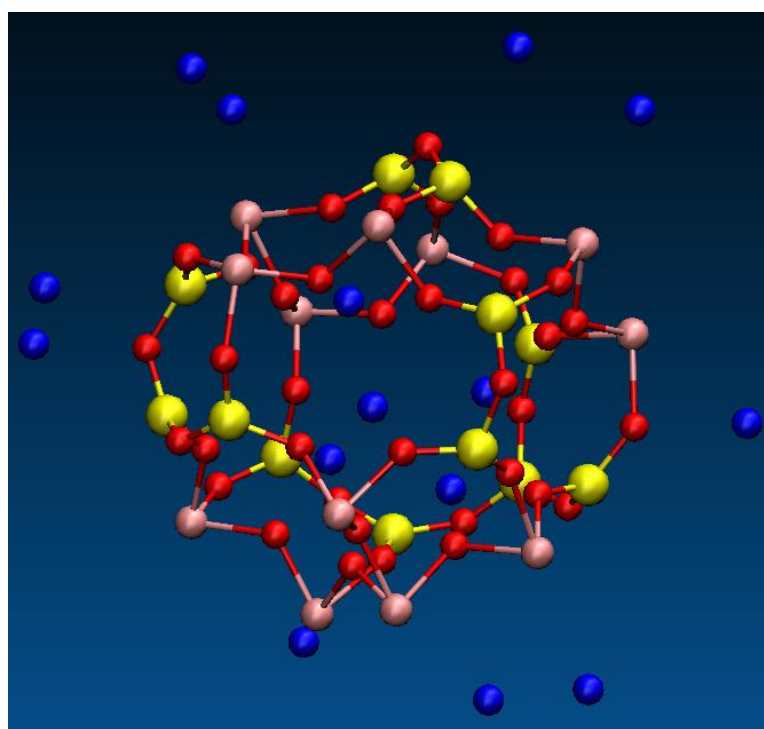


Fig. 7-5 Amorphous N-A-S-H gel structure at 300 K and 1 bar pressure

7.3 Results and discussion

7.3.1 Leaching behaviour

Fig. 7-6(a) to Fig. 7-6(c) show the concentrations of Na^+ ions in leachate after 30, 60 and 90 days. The leaching of Na^+ ions was observed to be monotonically increasing with time. However, specimens with lower Na_2O concentrations showed lower leaching potential. The presence of slag in all the systems influenced the leaching of Na from the binder system. Fig. 7-7a shows the leached fractions of Na from the binder specimens at the end of 90 days. The incorporation of slag in AAMs has significantly reduced the leaching concentration of Na ions from the binder matrix. Fig 7-6(d) to Fig. 7-6(f) shows the leaching behaviour of Si with time. There was an increase in the leached Si concentrations at the end of 60 days, attributed to the presence of unreacted soluble silica in the binder specimens. The binder systems with high soluble silica content exhibited a higher leaching potential of Si. However, at the end of 90 days, a significant reduction in the rise of Si concentration in leachate was observed. Fig. 7-7(b) shows the effect of slag content on the silica leaching behaviour at the end of 90 days. Like Na leaching, the substitution of slag up to 30wt.% significantly reduced the leaching potential of silica. Previously published studies of FA-based geopolymers showed the Na concentration in leachate about 100-150 ppm (up to 16%) within the first 24 h of leaching [175] and 17-30% after 28 days of leaching [183]. The difference in the behaviour is attributed to the change in sample size. This behaviour is attributed to the substitution of slag, the surface area of the specimens and low Na_2O contents.

The use of sodium silicates as an activator reduces the porosity in binder specimens and reduces Na leaching up to 14% compared with sodium hydroxide activated binder specimens [183]. Also, sodium silicates as an activator enhance the molecular interaction between reactive species and develop a strong framework of aluminosilicates, higher density, porosity, which would contribute towards enhancement of mechanical properties and reduction of alkali leaching[183].

The slag substitution in these systems significantly refines the pore structure in slag based AAMs and increase the tortuosity of AAMs[259]. It has also been observed that the replacement of slag in FA up to 50wt.% has decreased pore diameters from 47.1 nm to 9.1 nm and decreased the volume fraction of pores from 33% to 8% [248]. Also, C-A-S-H gels formed because of the activation of slag significantly refine the pore

structure increase the tortuosity and develops better packing density[220]. Based on the results and published research works, the slag inclusion and the use of sodium silicates significantly alter the Na and Si leaching properties. Fig. 7-8(a) shows the leaching concentrations of Al and Ca at the end of 90 days. There was a small amount of Al and Ca was observed in leachate, this could be due attributed to the leaching of unreacted Al/Ca or dissolution of Al/Ca from the binder specimens because of a longer leaching period. There is also a slight increase in the amount of Al and Ca was observed in the leachate of 5 wt.% Na₂O binder specimens. Studies have shown the leaching of a small concentration of Al (up to 1.6 ppm) from the binder matrix under acid leaching because of the dealumination of aluminosilicate gel[260].

With the increase in the leaching period researchers have observed the dissolution of portlandite and transport of calcium by diffusion in OPC systems [261,262]. Hence, there is a possibility of dealumination and decalcification of N-A-S-H and N-(C)-A-S-H gel when exposed to a longer leaching period. The FTIR, XRD and NMR discussed in subsequent sections are consistent with this observation.

Fig. 7-8(b) shows the pH profiles of selected binder specimens. The pH of all binder specimens was observed at ~10.30 within the first 30 minutes of leaching, indicating leaching of alkalis from all binder specimens. However, the pH of leachate was observed to be at 11 -11.5 after 4 - 5 days of immersion, which is attributed to the presence of sodium silicates. Studies have reported that binder specimens activated with sodium silicate as an activator exhibits lower pH compared with binder specimens without sodium silicates [183]. Also, binder specimens with higher slag contents exhibited slightly higher pH values (12 - 12.5) at the end of 30 days of leaching. Previous work has reported the inclusion of slag in FA based binder specimens initially reduced the leaching potential of alkalis, at the end of 96 h of leaching the pH was observed to be in the increasing trend between 11.5 – 12[175]. In OPC based system dissolution of calcium-based phases (~240 ppm) were observed at the end of 56 days of leaching, with the pH measurements between 12-12.5[261]. Therefore, the higher pH observed in the leachate of specimens with high slag content could be attributed to the dissolution of calcium from the binder specimens.

7.3.2 FTIR Analysis

Fig. 7-9(a) shows the FTIR spectra of binder specimens with varying slag and Na₂O contents before after 28 days of curing. The bands observed at 560-565 cm⁻¹ and 1055-1180 cm⁻¹ is assigned to octahedral aluminium present in mullite[238]. The band between 700-800 cm⁻¹ is attributed to the bending vibrations of Al-O-Si [238]. The shoulder at 870-880 cm⁻¹ is attributed to asymmetric stretching of AlO₄⁻ groups in aluminosilicate gel and the small peak at 848 cm⁻¹ is assigned to the presence of HCO₃⁻ formed because of reaction with water and CO₂ [206]. A sharp peak at 875 cm⁻¹ was observed in all binder specimens with higher slag content, which indicates the stretching of Al-O-Si bonds within the C-A-S-H structure[206]. The band between 967-1020 cm⁻¹ is attributed to the asymmetric stretching of Si-O-T (Si or Al) of geopolymer gel [19,238]. The band between 1420-1485 cm⁻¹ is assigned to asymmetric stretching of O-C-O bonds of CO₃²⁻ groups.

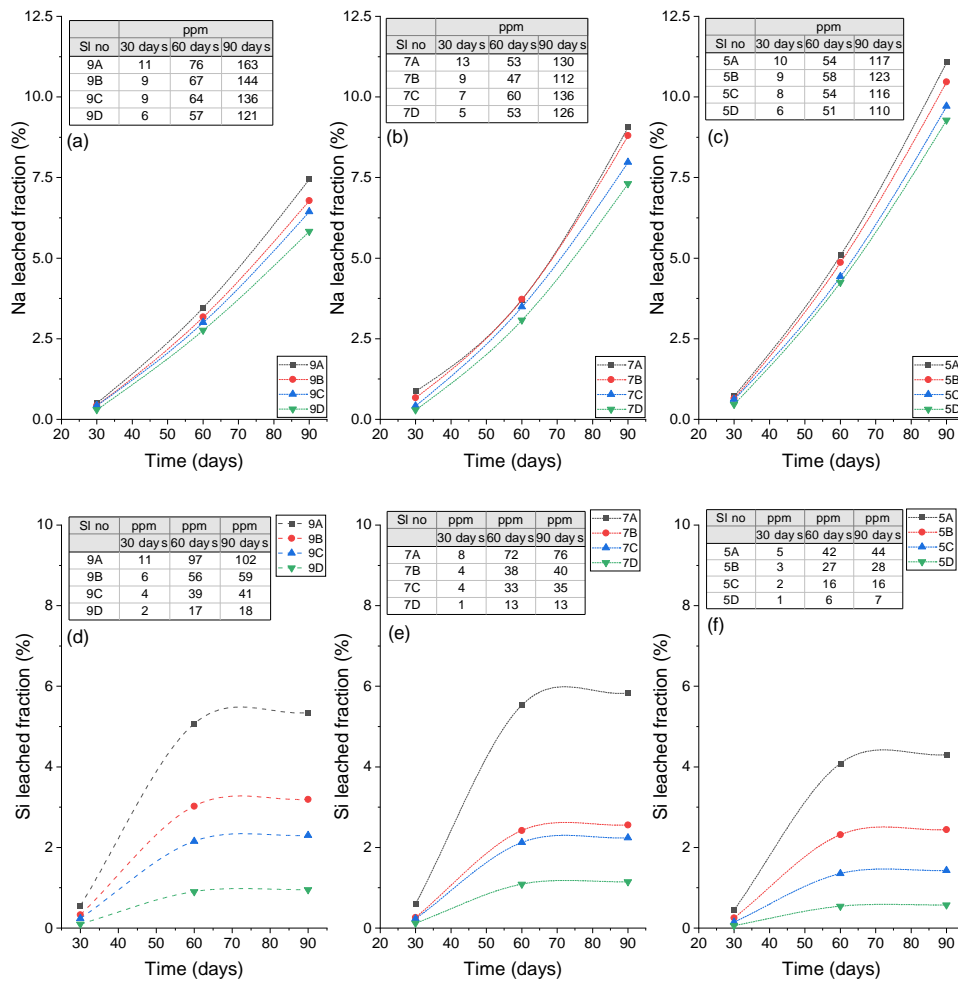


Fig. 7-6 (a-c) leached fractions of Na as a function of time and (d-f) leached fractions of Si as a function of time

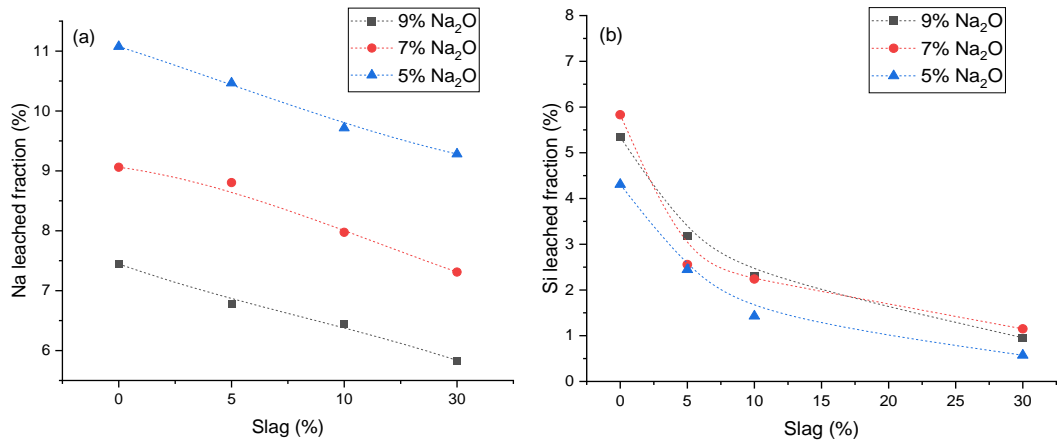


Fig. 7-7 (a) Effect of slag on leaching fractions of Na and (b) Effect of slag on leaching fractions of Si

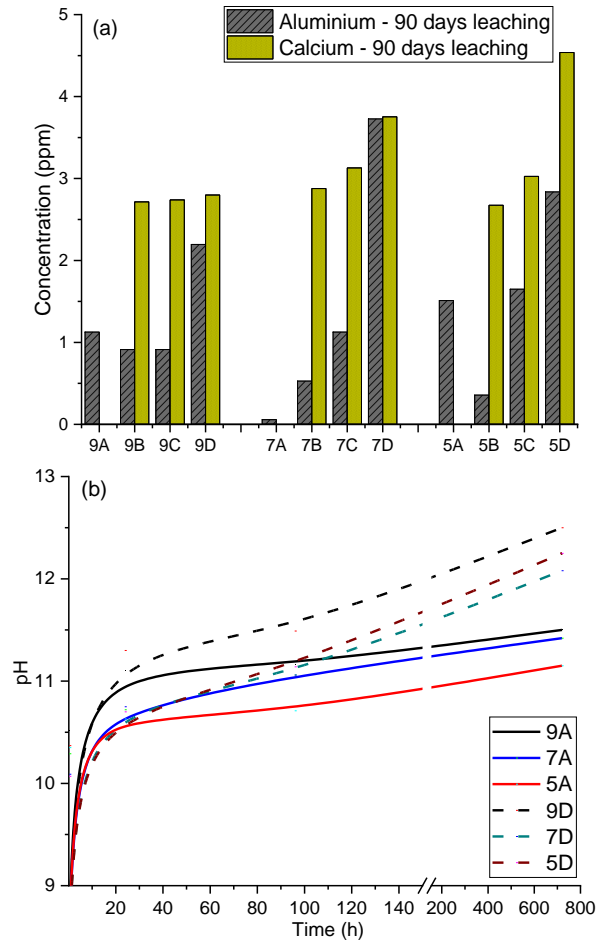


Fig. 7-8 (a) Concentrations of Ca and Al in leachate and (b) pH profiles of selected binder mixes

Fig. 7-9(b) shows the FTIR spectra of binder specimens after 90 days of leaching. A significant reduction in the intensity of the broad region between 600-1300 cm⁻¹ was

observed in all binder specimens. However, the peaks assigned to the Si-O-T stretching of geopolymer gel shifted to higher wavenumbers. Major changes were observed in the Al-O-Si bending ($700\text{-}800\text{ cm}^{-1}$) region and at asymmetric stretching of AlO_4 groups ($800\text{-}880\text{ cm}^{-1}$), indicating the dissolution of AlO_4 and SiO_4 units under leaching because of the presence of soluble silica. In FA binders activated with sodium silicates, the spectral range between $500 - 800\text{ cm}^{-1}$ is attributed to the presence of cyclic structures in different silicates and aluminosilicates, where AlO_4 is bridged to SiO_4 units via oxygen atoms [238]. Under leaching, a significant reduction in these bands indicates the dissociation of cyclic structures. The bands assigned to O-C-O stretching of CO_3^{2-} groups between $1420\text{-}1485\text{ cm}^{-1}$ almost disappeared, indicating leaching of carbonated products of binder specimen under long-term immersion. A small peak at 676 cm^{-1} was observed in 9wt.% Na_2O specimens, which is attributed to the presence of mullite[238].

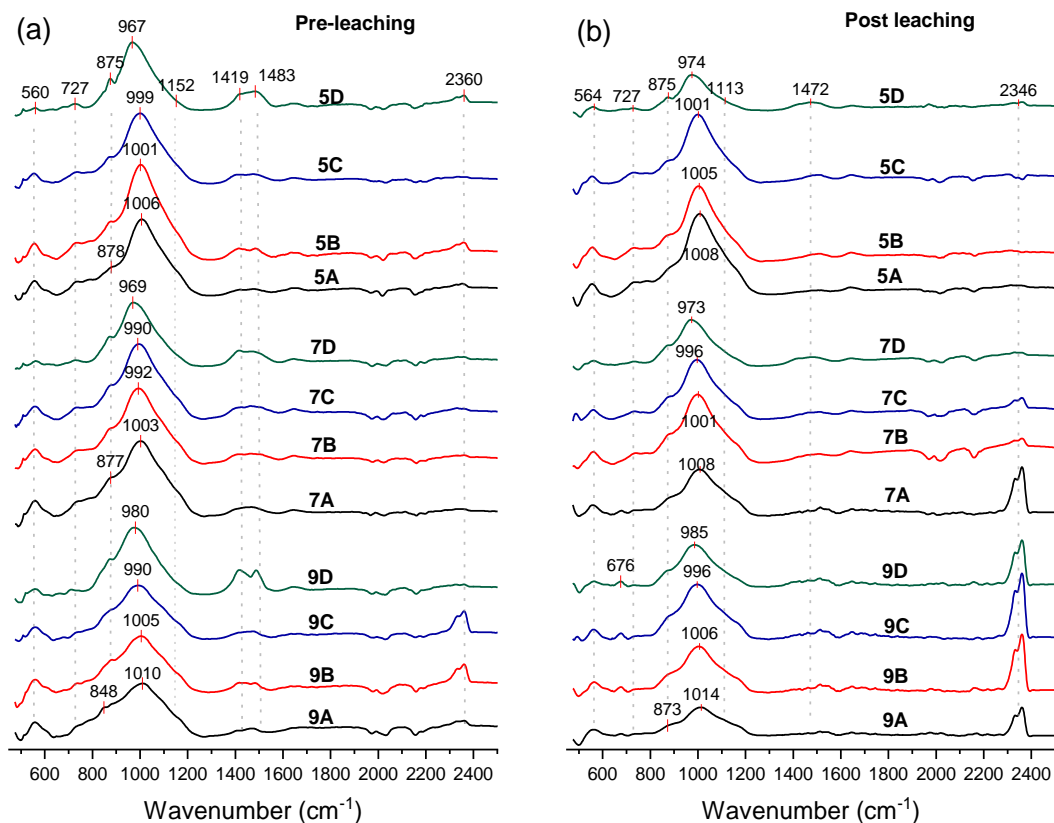


Fig. 7-9 (a) FTIR spectra of binder mixes after activation and (b) after leaching

The effect of slag on alkali-activated with 5% Na_2O content and leaching behaviour is shown in Fig. 7-10. The leaching behaviour of other binder mixes activated with 7 wt.%, 9 wt.% Na_2O and slag content up to 30 wt.% are given in supplementary

information (Appendix B). Upon activation, Si-O-T stretching of binder systems with zero slag content was observed at higher wavenumbers, which indicates the formation of crystalline aluminosilicate gel in the Q^4 environment. The wavenumbers shifted to lower frequencies with the inclusion of slag indicating the inclusion of Ca in N-A-S-H and formation of N-(C)-A-S-H gel in the system. The shape of FTIR spectra was observed to be changed with the inclusion of slag. The spectra were observed to be narrower when the slag content was increased to 5 wt.% and 10 wt.%, indicating more reactivity in these binder specimens. A shoulder between 870 cm^{-1} to 875 cm^{-1} attributed to the asymmetric stretching of AlO_4 groups in C-A-S-H gel was observed to be increasing with the inclusion of slag. The bands attributed to Al-O-Si bending between 719 cm^{-1} to 732 cm^{-1} was observed to be decreasing with the increase in slag content. The increase in calcium content decreases the availability of Al for the formation of N-A-S-H gel. The low Ca content and pH environment present in these binder specimens favours the formation of low calcium N-(C)-A-S-H gels, where N-A-S-H gel is a dominant reaction product.

After leaching the asymmetric stretching attributed to Si-O-T gel was observed at higher wavenumbers, indicating the formation of more Si-O-Si bonds. Also, the intensity of the spectra was observed to decrease by 5 wt.% and 10 wt.% slag specimens, indicating the reduction in the amount of structural gel. The major changes were observed in the region between 719 cm^{-1} to 732 cm^{-1} and in 870 cm^{-1} to 875 cm^{-1} that indicating the changes in the Al and Si environment of geopolymer gel.

The effect of Na_2O content on binder specimens before and after leaching is shown in Fig. 7-11(a) to Fig. 7-11(d). Fig. 7-11(a) shows the FTIR spectra of 0 wt.% slag with varied Na_2O content, the spectra were observed to be narrower with the decrease in the Na_2O content, because of the reduction of soluble silica content in the binder mix. Also, the Si-O-T vibrations shifted to lower wavenumbers with the decrease in Na_2O content in the binder mix.

The 5 wt.% Na_2O specimens were observed to be slightly at higher wavenumbers compared to 7 wt.% Na_2O specimens, indicating more reactivity and inclusion of more Al in this binder mix. After leaching, a significant reduction in the intensity of spectra was observed. The wavenumber shifted to higher wavenumbers in 7 wt.% and 9 wt.% Na_2O specimens indicating the formation of more silica-rich gel in these binder

specimens. However, 5 wt.% of Na₂O specimens showed a slight increase in the intensity of the spectra and no change in the wavenumber attributed to Si-O-T stretching was observed. Fig. 7-11(b) and Fig. 7-11(c) show the effect of Na₂O on 5wt.% and 10wt.% slag specimens before and after leaching. The addition of slag shifted the Si-O-T stretching wavenumber to lower wavenumbers. The binder specimens with low 7 wt.%Na₂O content shifted to lower wavenumbers compared to binder specimens with 5 wt.%Na₂O content.

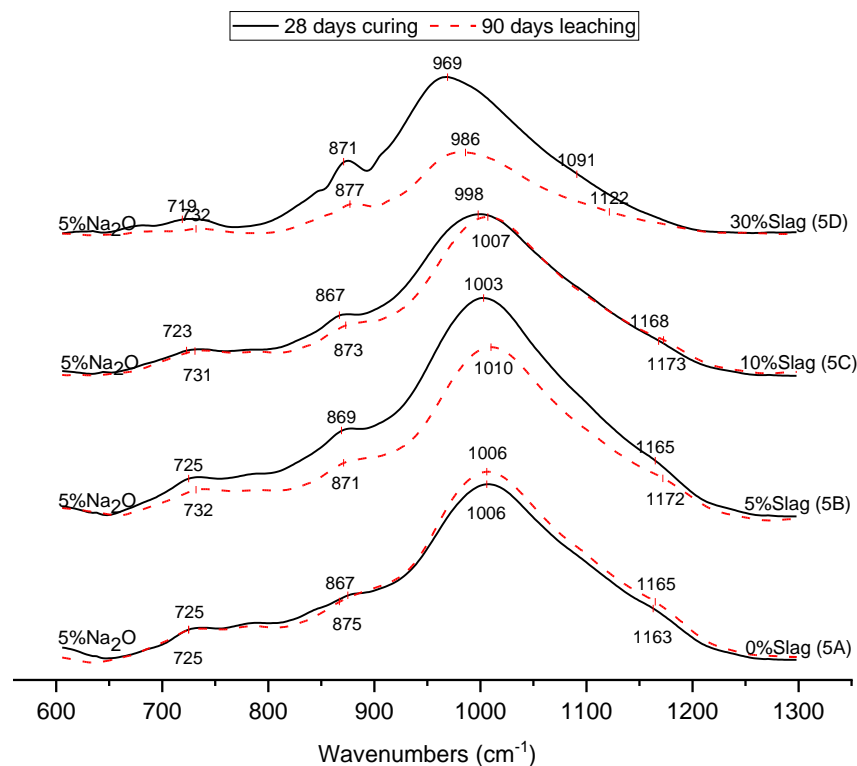


Fig. 7-10 FTIR spectra of binder mix after curing and leaching activated with 5 wt.% Na₂O and varying slag content

The bands attributed to the Al-O-Si stretching $\sim 720\text{ cm}^{-1}$ was observed to be decreasing with the increase in slag in slag content, indicating a reduction in the Al content in the binder mixes. After leaching Si-O-T stretching vibrations were observed to be shifting to a higher wavenumber because of the inclusion of more silica in Si-O-T gel. Fig. 7-11(d) shows the FTIR spectra of binder specimens with 30 wt.% slag content and varying Na₂O content. The inclusion of slag during activation shifted the Si-O-T vibration of lower wavenumbers, also the reduction in Na₂O content further shifted the wavenumbers lower wavenumbers, indicating the more inclusion of Na in N-(C)-A-S-H gel. Also, the intensity of the shoulder attributed to the AlO₄ (865 -875

cm⁻¹) groups in C-A-S-H gel was observed to be increasing with reduction Na₂O content. After leaching Si-O-T stretching wavenumbers shifted to higher wavenumbers along with a reduction in the intensity of the spectra, indicating more silica content in the geopolymer gel. Significant reduction in the intensity of bands attributed to Al-O-Si bending and asymmetric stretching of AlO₄ groups were and was observed after leaching.

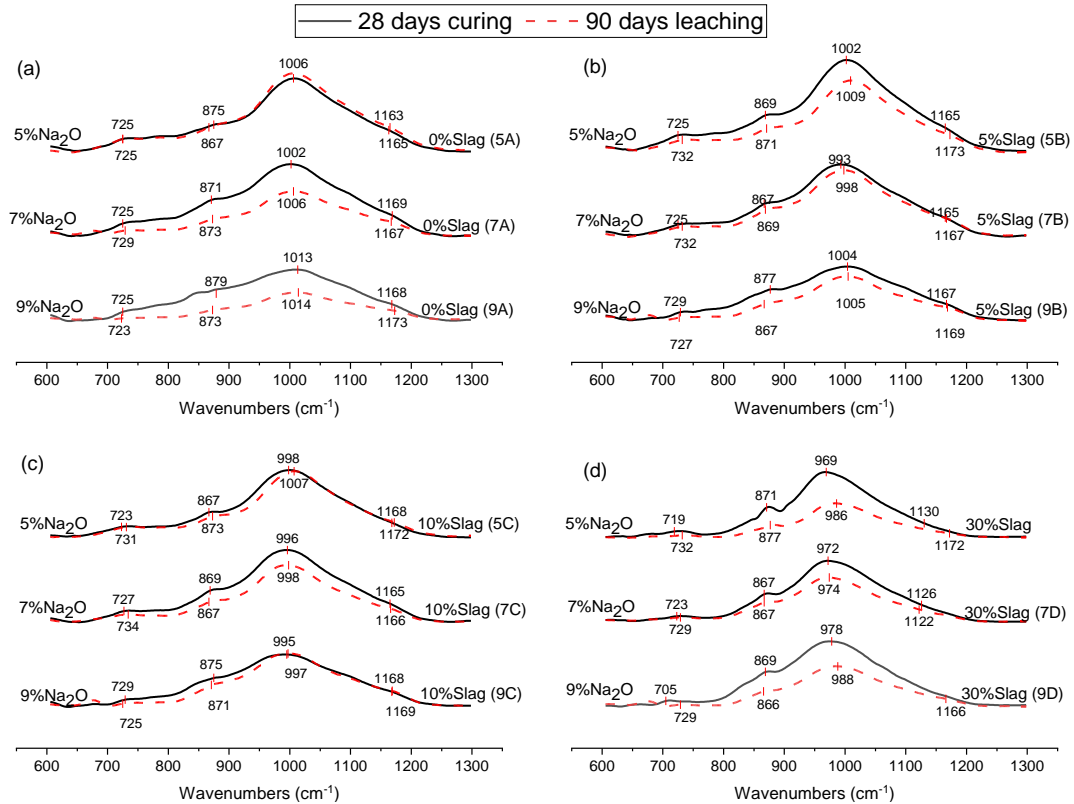


Fig. 7-11 FTIR spectra of binder mixes as a function of activator content (a) 0wt.% slag, (b) 5 wt.% slag, (c) 10 wt.% slag and (d) 30 wt.% slag

7.3.3 Nuclear magnetic resonance

The ²⁷Al and ²³Na MAS-NMR spectra unreacted precursors are shown in Fig. 7-12(a) and Fig. 7-12(b). The Fig. 7-12(a) shows the broad resonance between $\delta_{\text{obs}} = -20 - 20$ ppm in FA (centred at $\delta_{\text{obs}} = 1.9$ ppm) and $\delta_{\text{obs}} = 0 - 20$ ppm (centred at $\delta_{\text{obs}} = 14$ ppm) in slag is attributed to the resonance of octahedral environment Al[IV]. The pentahedral Al[V] was observed in FA between $\delta_{\text{obs}} = 30 - 55$ ppm. The broad signal centred at $\delta_{\text{obs}} = 67$ ppm in FA and $\delta_{\text{obs}} = 66$ ppm in slag is attributed to tetrahedral environment Al[IV] [18,236]. Fig. 7-12(b) shows the ²³Na environment in slag, shows broad signals at $\delta_{\text{obs}} = -9.5$ ppm and $\delta_{\text{obs}} = 138$ ppm. Fig. 7-13 shows the ²⁷Al environment of FA and blended precursors. The peak assigned to the Al[IV] was

observed at slightly lower values with the increase in slag content. Also, the shoulder assigned to Al[V] was observed to be disappearing, indicating the decreasing Al[V] units in these mixes. The Al[VI] peaks did not show any changes, but the intensity of these peaks was observed with increasing slag content. The precursor mix with 30 wt.% slag content showed a small shoulder at $\delta_{\text{obs}} = 11$ ppm indicating the presence of Al[VI] from slag.

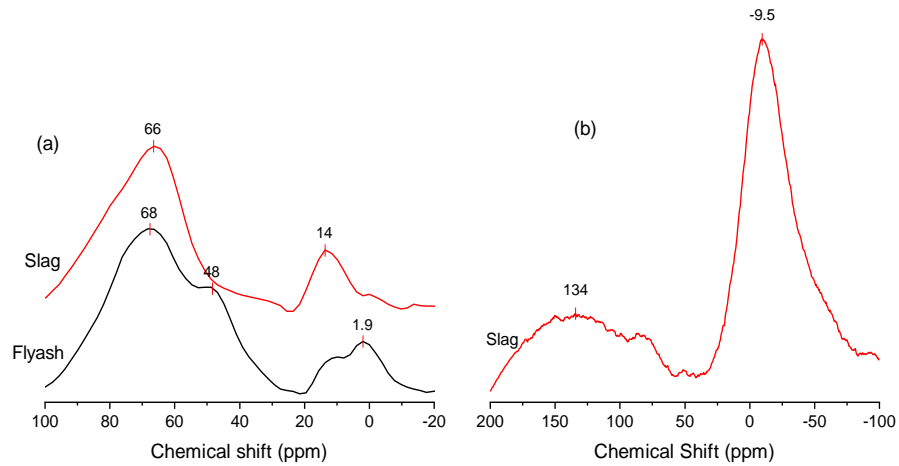


Fig. 7-12 MAS-NMR spectra of unreacted precursors: (a) ^{27}Al of FA and slag, (b) ^{23}Na of unreacted slag

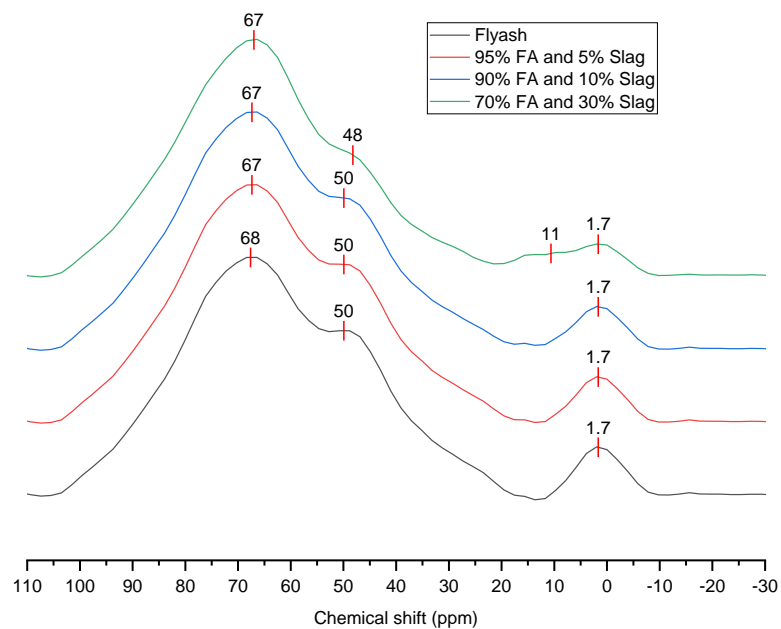


Fig. 7-13 MAS-NMR (^{27}Al) spectra of blended precursors before activation

7.3.3.1 ^{23}Na NMR

The ^{23}Na environment spectra of binder specimens after curing and leaching is shown in Fig. 7-14. Upon activation, a narrow resonance between -1 ppm to -6 ppm was observed, which indicates the Na in the 5 - 6 coordinated environment. Sodium ions neutralize the charge deficit developed by the Al in two ways. The peak observed at $\delta_{\text{obs}} = -4$ ppm is attributed to the Na^+ ions bound to Al in geopolymer gel and a small shoulder was observed at $\delta_{\text{obs}} = 0$ ppm indicates the presence of Na^+ in pore solution balancing aqueous $\text{Al}(\text{OH})_4^-$ groups [236]. ^{23}Na spectra normally move towards the lower frequencies with the increase in soluble silica content in the alkaline activators. With the increase in slag content, the spectra were observed to be broader compared with specimens zero-slag binder systems. In comparison with binder specimens with different Na_2O contents, the 9 wt.% Na_2O (9A-9D) specimens showed higher intensity of Na environment compared with 7 wt.% (7A-7D) and 5 wt.% (5A-5D) Na_2O content, indicating the higher Na-based phases in these systems. The inclusion of slag ^{23}Na NMR spectra was observed to be broader and symmetric.

After leaching a significant reduction in the intensities in the Na environment was observed in all binder mixes, especially with specimens with zero slag content (9A, 7A and 5A) showed a higher reduction in the intensity compared with the binder mixes with slag content (9B-9D, 7B-7D and 5B-5D). The ^{23}Na NMR spectra of binder specimens with 30wt.% slag showed significantly lesser changes in the intensity and shape of the spectra compared to other binders, which is consistent with the AAS results, where the reduction in the leaching potential of Na was observed with the increase in the slag content. This shows the addition of slag decreases the porosity and enhances the tortuosity of the porous network, and hence the loss of Na bearing phases could be inhibited under leaching with the increase in slag content. Also, the spectra were observed to be broader and asymmetric after the leaching process, which indicates the degradation of structural gel during the leaching process. Also, peak positions were observed to be moving towards more negative values. Studies have reported the shift of ^{23}Na spectra to lower frequencies with the rise in Si/Al ratios in aluminosilicate gel. The increase in silicate content in the geopolymer gel increases the effective Na-O distance or coordination numbers. The Na^+ ions prefer Al-O-Si sites over Si-O-Si sites because of charge deficiency [208,237]. The formation of Si-O-Si bonds or silica-rich gel in the binder mix under leaching increases the

coordination numbers of Na ions to increase the Na-O distance by reducing the interaction between Na and Al-O-Si sites. Also, molecular dynamics studies show the weakening of Si-O-Si and Al-O-Si bonds in N-A-S-H gel at an extended time of leaching. Our study shows more formation of Si-O-Si bonds because of the presence of soluble silica, the loss of Na ions might weaken the Al-O-Si bonds to initiate the leaching of Al from the binder system[219]. Therefore, leaching of Na and formation of silica-rich gel systematically shift spectra to more negative values and at the same time intensity of the spectra was observed to decrease after leaching. This was consistent with the studies with FTIR results, where Si-O-T stretching frequencies shifted to higher wavenumbers because of the formation of silica-rich gel and the intensities associated with Al-O-Si bending was observed to be decreasing under the leaching process. Also, AAS results showed the exponential increase in the leaching of sodium and the flattening trend in the leaching behaviour of soluble silica from the binder system.

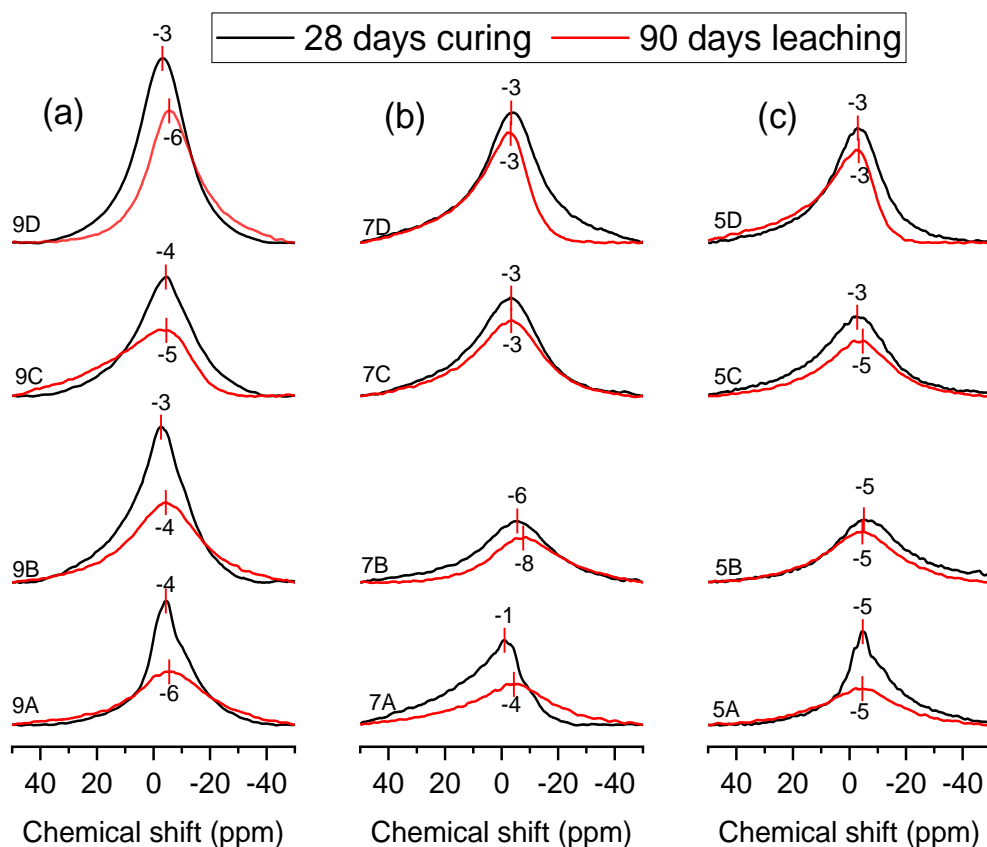


Fig. 7-14 ^{23}Na MAS-NMR spectra of binder mixes with varying slag content after curing and leaching (a) 9 wt.% Na_2O , (b) 7 wt.% Na_2O and (c) 5 wt.% Na_2O

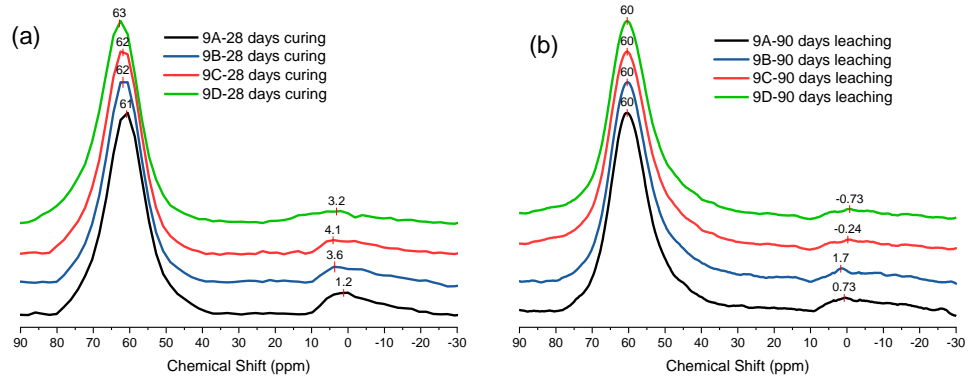


Fig. 7-15 ^{27}Al MAS-NMR spectra of binder mixes activated with 9 wt.% Na_2O and varying slag contents (a) after curing and (b) after leaching

7.3.3.2 ^{27}Al MAS-NMR

The ^{27}Al NMR of alkali-activated binders with 9wt.% Na_2O and varying slag content are shown in Fig. 7-15a. The deconvolution details of ^{23}Al spectra of different binder mixes are given in the supporting information Fig. S3, S4 and S5 (Appendix B). The broad hump observed at Al[V] and Al[VI] regions were observed to be decreasing after activation, indicating the consumption of Al content in the alkali activation reaction. A narrow intense peak spanning between $\delta_{\text{obs}} = 40 - 80$ ppm was observed in all specimens. The amorphous N-A-S-H gel with poorly crystalline Al[IV] in the tetrahedral environment was observed in all binder specimens with zero slag content at lower resonance values, centred at $\delta_{\text{obs}} = 61$ ppm (9A) [61].

The increase Ca/Si ratio and decrease in Al/Si ratios through the inclusion of slag favoured the formation of poorly crystalline N-(C)-A-S-H gel in the binder specimens. The Al[IV] peak of these binder specimens was observed at slightly higher chemical shifts, centred at $\delta_{\text{obs}} = 60 - 63$ ppm[239]. With the increase in Ca/Si ratio, a gradual shift in the resonance towards higher peak positions indicate more inclusion of Ca in N-A-S-H gel. Also, Al[V] broad region was observed to be decreasing with the increase in slag content. This is likely to be linked to the higher concentrations of Ca and reduction in Al content, indicating higher inclusion of Ca in N-(C)-A-S-H gel. A low resonance intensity associated with Al[VI] was observed to be in between $\delta_{\text{obs}} = -10 - 30$ ppm. However, the increase in slag content proportionately decreased the Al [VI] content (Table. 3), indicating the reduction in Al[VI] content and absence of other crystalline AFm phases.

Fig. 7-15b shows ^{27}Al NMR spectra of 9 wt.% Na_2O specimens with varying slag contents after 90 days of leaching. The peak of the 9A (0 wt.% slag) binder specimen was observed at lower resonance $\delta_{\text{obs}} = 60$ ppm and the spectra were observed to be slightly broader between $\delta_{\text{obs}} = 30\text{-}58$ ppm. However, in spectra of specimens with higher slag or Ca/Si content 9D, 7D and 5D, the peak positions of Al[IV] were observed at lower resonance $\delta_{\text{obs}} = 60$ ppm. This behaviour was observed in binder specimens (9A-9D, 7D and 5D). There was a broadening of NMR spectra in the region between $\delta_{\text{obs}} = 30 - 50$ ppm after leaching (Fig. 7-16a, Fig. 7-16d to Fig. 7-16f), overlapped with Al[V] region, indicating changes in Al[IV] and Al[V] environment. This could be linked to the dealumination and decalcification of N-(C)-A-S-H gel [256] because of the dissolution of Ca from the gel.

This indicates the presence of higher slag facilitate the decalcification of N-(C)-A-S-H gel. Table. 7-3 shows the peak position of all binder specimens with corresponding integral areas after the activation and leaching process. Gaussian functions with $r^2 = 0.98\text{-}99$ were used here for the deconvolution analysis. Spectra were distinguished into Al[IV], a broader region between $\delta_{\text{obs}} = 30 - 58$ ppm overlapped with Al[V] and Al[IV] regions. The deconvoluted spectra of selected binder specimens can be found in supporting information.

Fig. 7-16a to Fig. 7-16f and Table. 7-3 shows the NMR spectra of binder specimens (0 and 30 wt.% slag) with varying Na_2O (5 wt.%, 7 wt.% and 9 wt.%) contents along with deconvoluted integral areas after 28 days curing and 90 days leaching. Al[IV] resonances of 9A binder specimens observed at $\delta_{\text{obs}} = 61$ ppm, 7A and 5A binder specimens at $\delta_{\text{obs}} = 59$ ppm, this could be because of the presence of low alkali content in these mixes.

Also, a broad feature was observed in the spectra of 5A (5 wt.% Na_2O) and 7A (7 wt.% Na_2O) binder specimens between 30 – 50 ppm (Fig. 7-16b to Fig. 7-16c) after 28 days of curing, which indicates the disordered Al[IV] environment or the presence of unreacted Al[V] content within the binder specimens because of the lower alkali content. However, with the increase of slag content in these binder specimens (Fig. 7-16(d) to Fig. 7-16(f)) this broad feature was observed to be diminishing because of the reduction in Al content. After leaching, the Al [IV] resonance of 9A (Fig. 7-16(a)) shifted to lower resonance $\delta_{\text{obs}} = 60$ ppm, indicating dealumination of N-A-S-H gel in

these specimens, also the integral areas under 30 – 50 ppm region was observed to increase after leaching. However, 7A (Fig. 7-16(b)) binder specimens did not show any changes in the Al[IV] peak position and the shape of the spectra remain unchanged after leaching. But, the integral areas under Al[IV] was observed to be decreasing and 30 – 50 ppm was observed to be increasing. The Al[IV] resonance of 5A (Fig. 7-16(c)) moved to higher resonance $\delta_{\text{obs}} = 60$ ppm and spectra were observed to be narrower after leaching, indicating more inclusion of Al in the N-A-S-H gel. However, the deconvoluted areas under Al[IV] were observed to be increasing and 30 – 50 ppm was observed to be decreasing after leaching. The Al[IV] resonances of binder specimens with 30wt.% slag (9D, 7D and 5D) with varying Na₂O (5wt.%, 7wt.% and 9wt.%) content (Fig. 7-16(d) to Fig. 7-16(f) and Table. 7-3) were shifted from $\delta_{\text{obs}} = 63$ ppm (9D), $\delta_{\text{obs}} = 62$ ppm (7D and 5D) to lower resonances $\delta_{\text{obs}} = 60$ ppm at the end of leaching. Also, the region between $\delta_{\text{obs}} = 30$ -50 ppm was observed to be broader after leaching. This indicates the dealumination and decalcification in N-(C)-A-S-H gel because of the dissolution of Ca and Al because of the leaching process. The integral areas under Al[IV] resonances were observed to be decreasing significantly and integral areas under 30 – 50 ppm region were observed to be increasing after leaching. However, the peak resonances of Al[VI] shifted further to negative values and integral areas of Al[VI] was observed to be decreasing slightly after leaching.

The NMR spectra of 7B (5 wt.% slag and 7 wt.% Na₂O), 7C (10 wt.% slag and 7 wt.% Na₂O), 5B (5 wt.% slag and 5 wt.% Na₂O), and 5C (10 wt.% slag and 5 wt.% Na₂O) (Fig. 7-17(a) to Fig. 7-17(d) and Table. 7-3) binder mixes exhibited different trend compared to other binder specimens. The peak position Al[IV] (Table. 7-3) of 7B and 5B did not change after leaching. The shape of NMR spectra was observed to be slightly broader at 30 – 50 ppm regions in 5B binder specimens.

The integral areas under Al[IV] peak were observed to be increasing and area under 30 – 50 ppm was observed to be decreasing after activation. The Al[IV] peak position of 7C and 5C (Fig. 7-17(b) to Fig. 7-17(d) and Table. 7-3) moved to a higher resonance. Also, the relative integral area assigned to Al[IV] was observed to be increasing and the 30 – 50 ppm area was observed to be decreasing, this indicates the inclusion of some Al and formation of N-(C)-A-S-H gel in these binder specimens under leaching. The slight increases in the Ca/Si in these specimens affected the initial

dissolution of Al and could be favouring more inclusion of Ca in N-(C)-A-S-H gel during activation. When the specimens are exposed to leaching, the elevation of pH level of the pore solution during leaching and low porosity developed because of the addition of slag is facilitating the dissolution of unreacted Al[IV] units along with soluble silica to form N-A-S-H gel.

In NMR literature the broad region observed between $\delta_{\text{obs}} = 30 - 58$ ppm is assigned to Al[V] coordinated aluminium units, Al[IV] framework of Al and distorted non-framework of Al[IV] units of zeolites structure. The peaks of these resonances are observed at $\delta_{\text{obs}} = \sim 55$ ppm [242]. The MQ MAS NMR spectra of these studies showed large quadrupolar interactions and observed Al[IV] deviating from the diagonal [242].

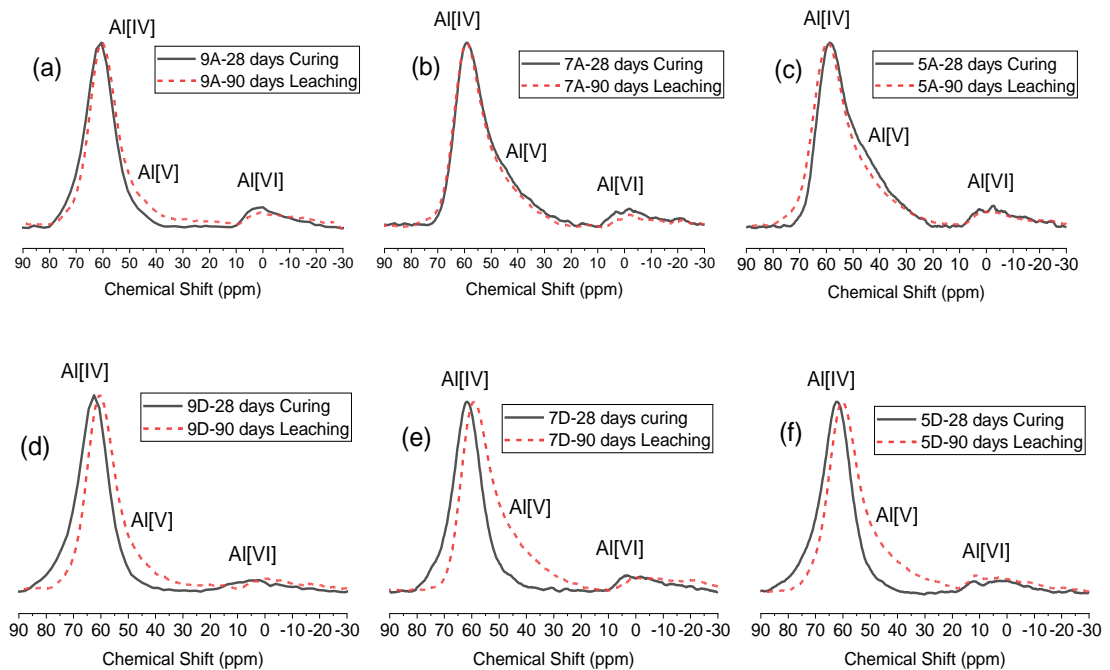


Fig. 7-16 ^{27}Al MAS-NMR spectra of (a-c) binder mix with varying Na_2O content and 0 wt.% slag content, and (d-f) binder mixes with varying Na_2O content and 30 wt.% slag content.

Also, other studies have correlated the chemical shift of different zeolites to their Al-O-Si angles (θ). According to them the ^{27}Al chemical shift at $\delta_{\text{obs}} = 62.8 - 63$ ppm indicate the presence of NaX ($\delta_{\text{obs}} = 62.8$ ppm, $\theta = 140.0^\circ$), NaY ($\delta_{\text{obs}} = 52.8$ ppm, $\theta = 140.0^\circ$) and albite zeolites ($\delta_{\text{obs}} = 63$ ppm, $\theta = 136.2^\circ$). However, the lower chemical shift values indicate the presence of mordenite ($\delta_{\text{obs}} = 59.2$ ppm, $\theta = 148.3^\circ$), gismondine ($\delta_{\text{obs}} = 56.4$ ppm, $\theta = \text{NA}$), NaA zeolite ($\delta_{\text{obs}} = 55.8$ ppm, $\theta = 148.3^\circ$)

analcime ($\delta_{\text{obs}} = 59.9$ ppm, $\theta = 144.3^\circ$), chabazite ($\delta_{\text{obs}} = 59.4$ ppm, $\theta = 145.3^\circ$), gmelinite ($\delta_{\text{obs}} = 59.9$ ppm, $\theta = 143.3^\circ$), microcline ($\delta_{\text{obs}} = 60.9$ ppm, $\theta = 141.6^\circ$) and nepheline ($\delta_{\text{obs}} = 61$ ppm, $\theta = 142^\circ$) [243]. These authors have shown the dependence of Al chemical shifts to mean Al-O-Si angle in aluminosilicate structures, it indicates that higher chemical shifts lead to lower Al-O-Si bond angles and lower chemical shifts lead to higher Al-O-Si bond angles [243]. However, our research work shows similarities to these works where a broad region in NMR spectra was observed between $\delta_{\text{obs}} = 30$ -58 ppm.

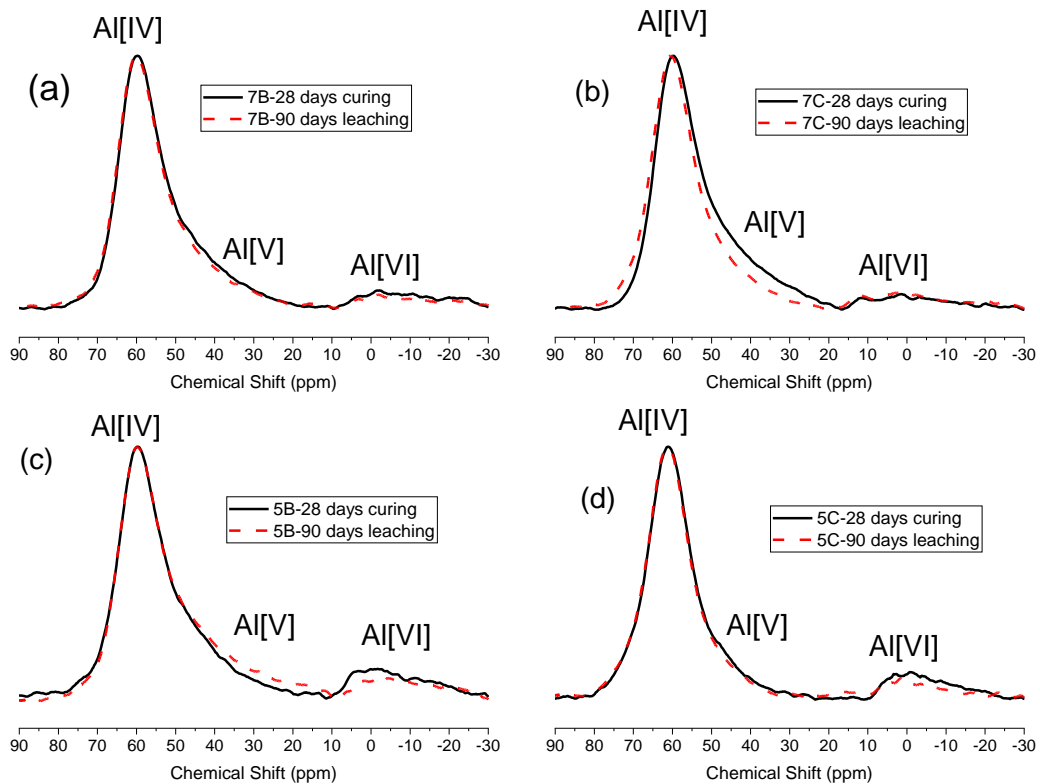


Fig. 7-17 (a-b) ^{27}Al MAS-NMR spectra of binder mixes activated with 7 wt.% Na_2O , 5 and 10 wt.% slag content. (c-d) binder mixes activated with 5 wt.% Na_2O , 5 and 10 wt.% slag content.

After activation, the peaks of this region were centred at $\delta_{\text{obs}} = 44 - 50$ ppm (Table. 7-3), after leaching these peaks were observed at higher resonances $\delta_{\text{obs}} = 49 - 58$ ppm. The jump in the chemical shift of this region and movement of Al[IV] chemical shifts to lower resonances in binder specimens with higher Ca/Si ratios indicate the changes in Al[IV] bonding environment and reducing electron density because of the increase of silica content [239] and degradation of N-(C)-A-S-H gel. The formation of silica-rich gel and leaching of Na^+ ions increases the effective Na-O distances Hence, there is a possibility of change in Al-O-Si angles or larger Al-O-Si bond angles under

leaching. It is also possible that there is the formation of more distorted Al tetrahedral gel under leaching at lower resonances, which is shifting Al[IV] to lower resonances and Al[V] to higher resonances. The Al[VI] peaks after leaching were observed to be moving towards lower ppm and a slight reduction in the integral area in this region was observed after leaching, which could be because of loss of unreacted Al[VI] under leaching.

Table 7-3 Effect of leaching on Chemical shift and areas determined through MAS-NMR

28 days curing							90 days leaching						
ID	Al[IV] (ppm)	Area (%)	30-50 (ppm)	Area (%)	Al[VI] (ppm)	Area (%)	ID	Al[IV] (ppm)	Area (%)	30-50 (ppm)	Area (%)	Al[VI] (ppm)	Area (%)
9A	61	89.40	-	0	-1	10.60	9A	60	51.95	56	40.95	-4	7.09
9B	62	91.50	-	0	-1	8.50	9B	60	52.12	54	40.21	-3	7.67
9C	62	92.70	-	0	-1	7.30	9C	60	46.72	57	50.28	-3	3.00
9D	63	92.90	-	0	4	7.10	9D	60	46.72	55	50.28	-3	3.00
7A	59	49.10	49	43.94	-4	6.96	7A	59	46.74	51	47.95	-7	5.30
7B	60	49.80	51	44.00	-8	6.00	7B	60	46.90	52	46.50	-8	6.50
7C	60	46.90	49	44.80	0.5	8.19	7C	61	48.70	55	43.09	1.4	7.95
7D	62	83.88	50	7.540	-2	8.58	7D	59	48.20	51	43.70	-9	8.10
5A	59	41.10	48	49.80	-4	9.10	5A	60	45.10	51	48.40	-4	6.55
5B	60	40.50	52	49.40	-4	10.10	5B	60	45.30	49	46.20	-7	8.40
5C	61	41.80	58	47.50	-3	10.60	5C	62	49.50	58	44.06	-1	5.90
5D	62	91.60	-	0	4	8.40	5D	60	48.20	52	43.20	4	8.40

7.3.4 Molecular Dynamics Simulations

Fig. 7-18 shows the interaction between Na ions and water molecules. The Na ions were attracted by water molecules; specifically, the oxygen atoms of water molecules attract the bound Na ions. Fig. 7-19 shows the position of bound Na ions at 0 ns, as the interaction between water Na increases the distance between N-A-S-H gel and Na ions increases. In other words, Na ions move away from the N-A-S-H gel structure, leaving behind more distorted Al-O-Si of N-A-S-H gel, which can be seen in Fig. 7-20. This behaviour was also observed in MAS-NMR results.

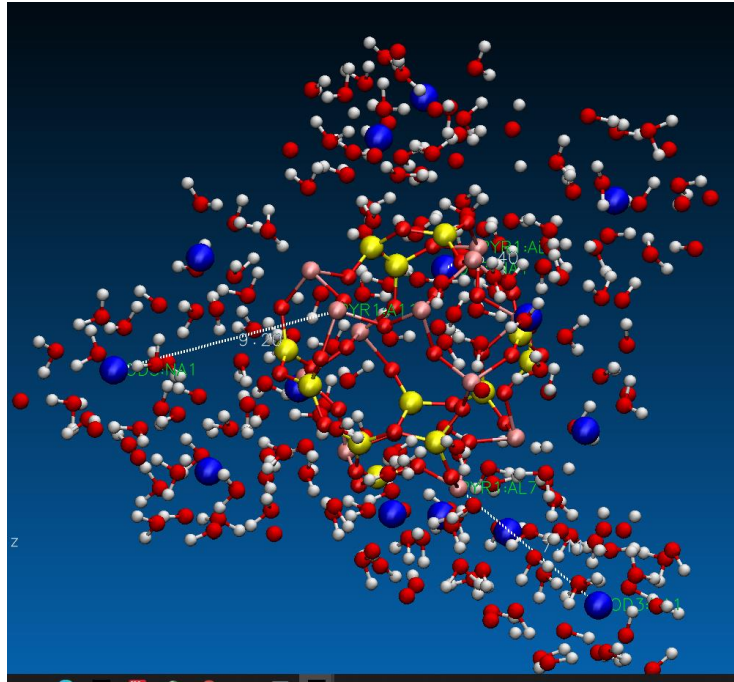


Fig. 7-18 Water clusters around Amorphous N-A-S-H gel and Na ions

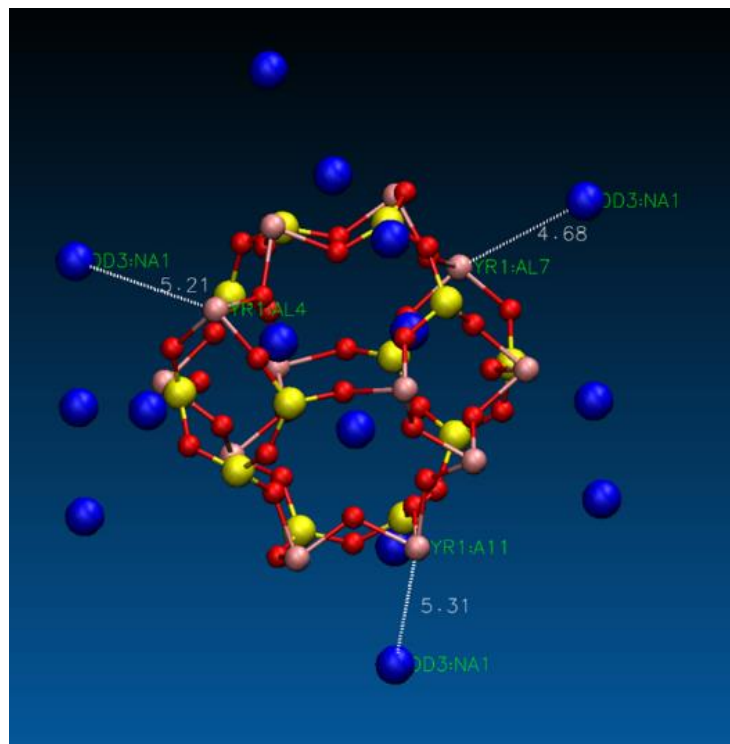


Fig. 7-19 Distance between Al atoms of N-A-S-H and Na ions at atmospheric condition

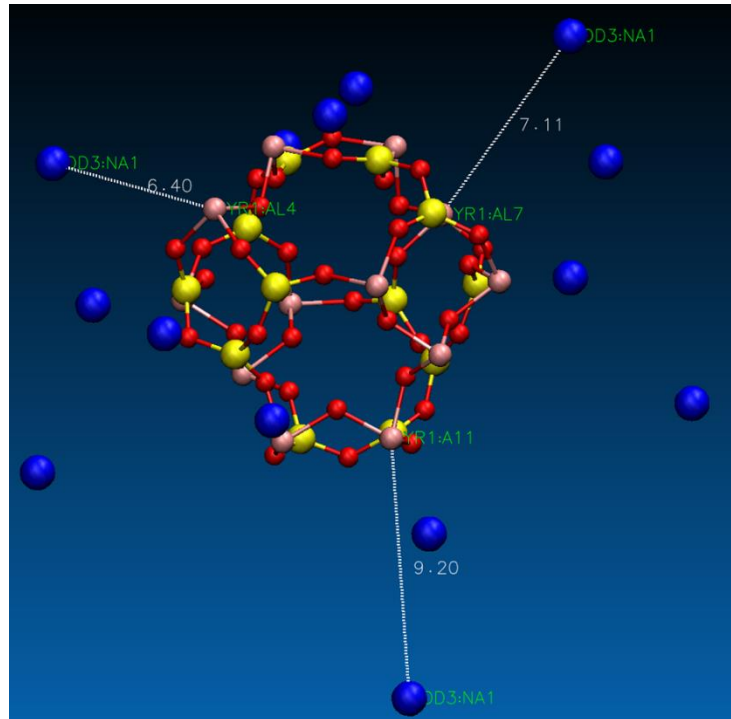


Fig. 7-20 Distance between Al atoms of N-A-S-H and Na ions at after 1ns

Fig. 7-21 shows the electrostatic interaction between AlO_4 groups of N-A-S-H structure and bound Na ions as a function time. The electrostatic interaction between any two charged bodies is a function of distance. As the Na ions leach out from the structure, the electrostatic interaction between AlO_4 groups and Na ions decreases. Conversely, the attraction between oxygen atoms of AlO_4 groups and water increases with respect to time, this is shown in Fig. 7-22. Also, the interaction between bound Na ions and water increases with time. This behaviour shows that water molecules attract the Na ions, which disturbs the ionic equilibrium of the N-A-S-H gel structure. As the Na molecules move further away from the structure, the water molecules interact with AlO_4 groups, leaving behind the distorted Al-O-Si structure.

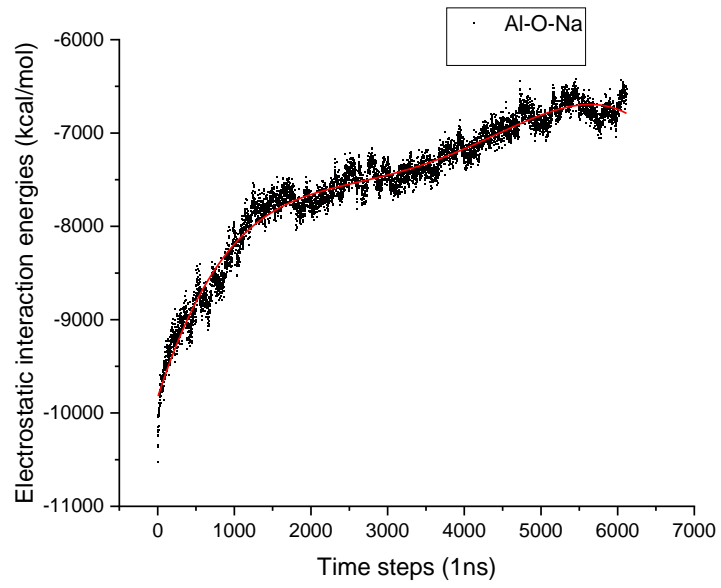


Fig. 7-21 Electrostatic interaction energies between AlO₄ and Na ions

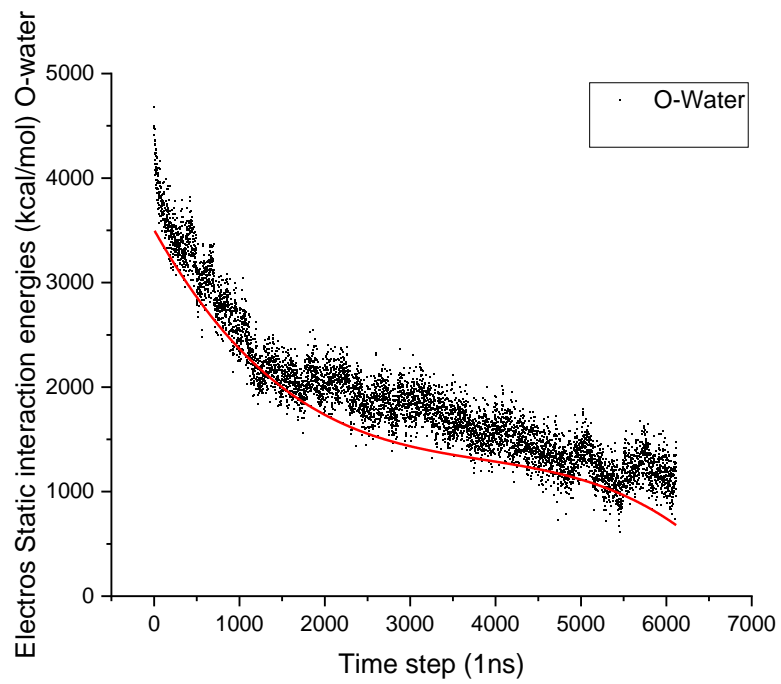


Fig. 7-22 Electrostatic interaction energies between AlO₄ and water

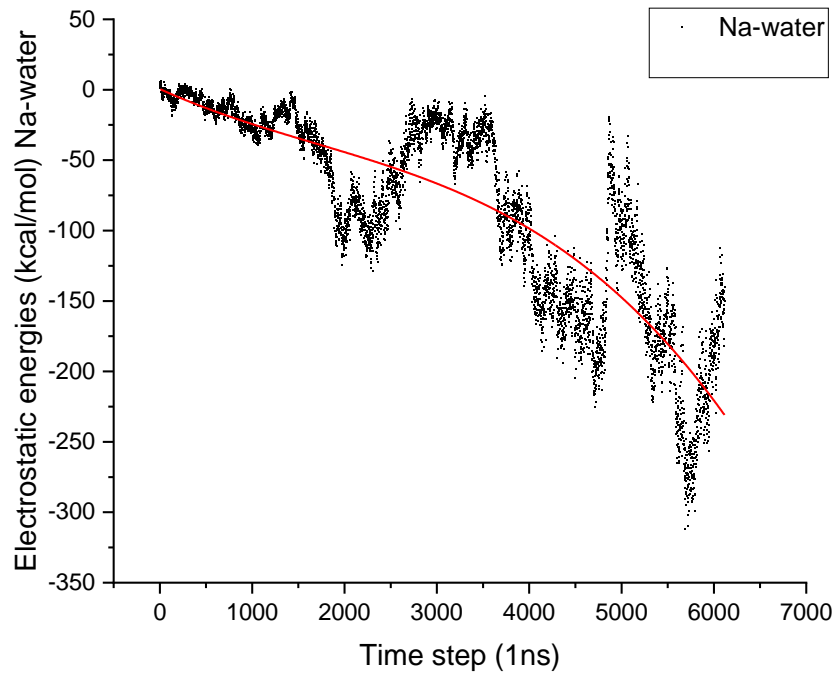


Fig. 7-23 Electrostatic interaction energies between Na and water

7.3.5 X-ray diffraction analysis

Fig. 7-24(a) to 7-24(c) shows the X-ray diffractograms of 9A, 7A and 5A specimens before and after leaching. The X-ray diffractograms of binder mixes activated with varying Na₂O and slag content are given in supporting document Fig. S5 and Fig. S6. Upon activation, a significant reduction in the amorphous hump between ($2\theta^\circ = 15^\circ - 40^\circ$) was observed at the end of 28 days during was observed, along with the formation of low-intensity peaks resembling Na-P1 (Na₆Al₆Si₁₀O₃₂, PDF# 01-074-1787) zeolites, which belongs to gismondine type of structures [19]. Usually, Na-P1 zeolites are formed at the initial stages of zeolite production under hydrothermal treatment. At later stages of the reaction, Na-P1 gradually dissolves and favours the crystallization of stable analcime zeolites[175]. The absence of Ca and the presence of sodium silicate as an activator in these binder specimens is favouring the formation of Na-P1 zeolites. After 90 days of leaching, no significant changes in XRD patterns were observed. A slight reduction in the Na-P1 zeolite reflections was observed between $2\theta^\circ = 27^\circ - 30^\circ$. This could be linked to the metastability of Na-P1 zeolites and the dissolution of soluble silica under the leaching process.

The X-ray diffractograms of binder specimens with 30 wt.% slag (9D, 7D and 5D) before and after leaching are shown in Fig. 7-24(d) to Fig. 7-24(f). Upon activation reduced intensity of amorphous hump between $2\theta = 20^\circ - 35^\circ$ was observed. An intense peak at $2\theta = \sim 29.5^\circ$ was observed in all binder specimens indicate the formation of poorly crystalline C-A-S-H ($2\text{CaSiO}_3 \cdot 3\text{H}_2\text{O}$, PDF# 00-022-0600) type gels resembling riversidite structure was observed as the main reaction product [19,58]. A minor trace of calcite was also observed in these binder specimens. Also, crystalline gismondine type of zeolites such as Na-P1 and garronites ($\text{NaCa}_{2.5}(\text{Al}_6\text{Si}_{10})\text{O}_{32} \cdot 14\text{H}_2\text{O}$, PDF # 00-059-0383) with some degree of Ca substitution was observed in diffractograms [19]. After leaching, a slight reduction in the intensity of Na-P1 zeolites and garronites was observed. However, a significant reduction in the intensity of C-A-S-H gel and decalcification was observed in all binder specimens with slag content under leaching. The reduction in the intensity of C-A-S-H gel and N-A-S-H gel was also observed in the leaching tests of alkali-activated FA and slag specimens under accelerated leaching [147].

7.3.6 Mechanical properties

The final water absorption of all binder specimens with different Na_2O and slag content are shown in Fig. 7-25(a). The water absorption values were observed to be in the range of 2.0-2.25 g/cm^2 at the end of 24h indicating the total saturation of the specimens. Regardless of the Na_2O content used in this study, the water absorption value was almost similar in all specimens. The binder specimens with lower 7 wt.% and 5 wt.% Na_2O contents showed an insignificant increase in the water absorption value compared with 9 wt.% Na_2O specimens, because of the presence of a lower amount of soluble silicates in these binders [183]. The lower quantity of slag 5 wt.% and 10 wt.% content did not significantly change the water absorption values. However, the binder specimens with 30 wt.% slag showed the lowest value of water absorption ($\sim 2.0 \text{ g}/\text{cm}^2$), indicating a reduction in the water absorption values. The trends of water absorption correlate with AAS results, where a reduction in leaching fraction of Na and Si was observed with the increase in slag and soluble silica content.

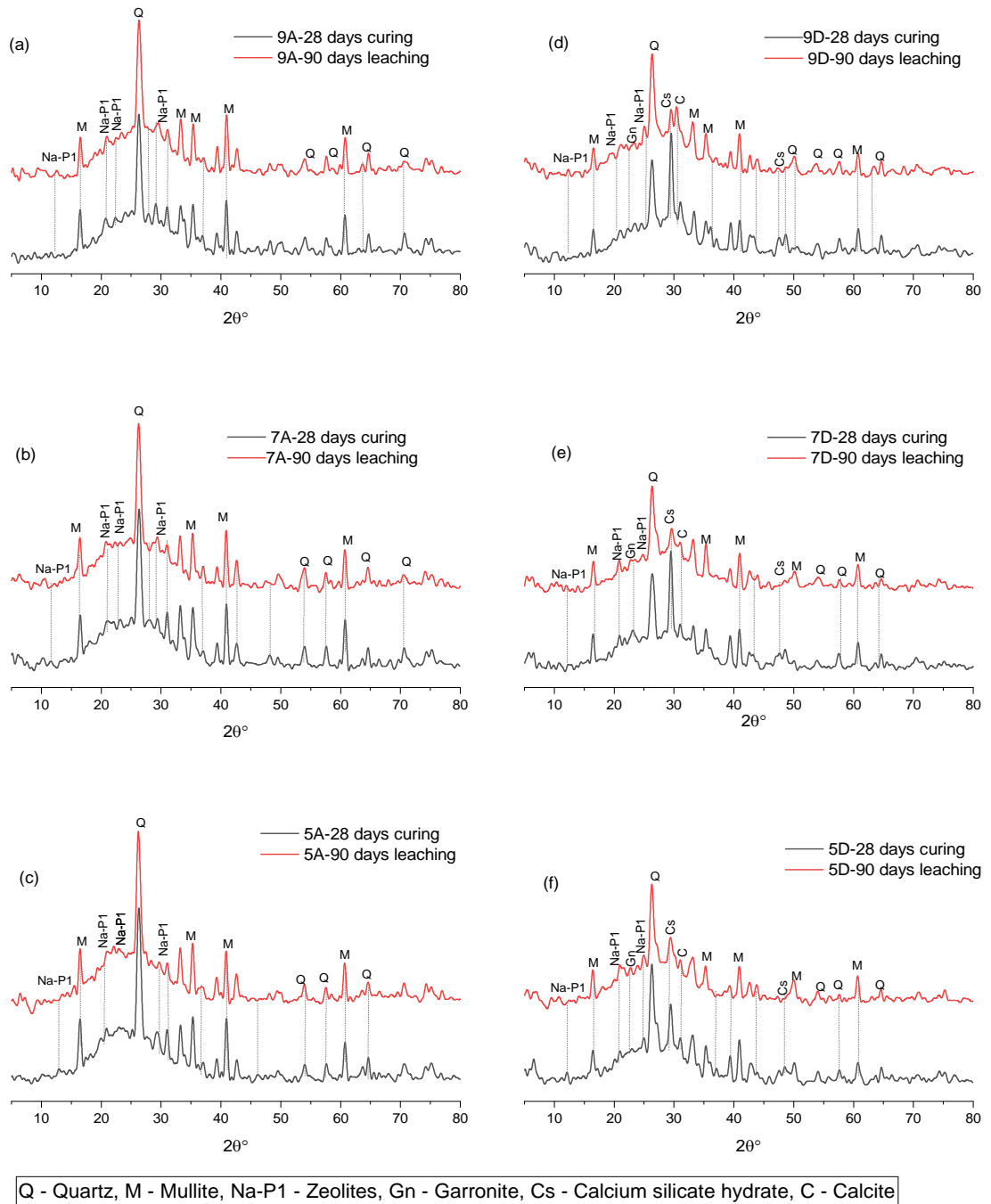


Fig. 7-24 X-ray diffractograms. (a-c) binder mixes with varying Na_2O and 0 wt.% slag content. (d-f) binder mixes with varying Na_2O and 30 wt.% slag content

The total porosity and dry density values of the binder mix after activation are shown in Fig. 7-25(b) to Fig. 7-25(c). The binder mixes with 9 wt.% Na_2O content showed lower porosity values (~29 - 35%) compared with 7 wt.% and 5 wt.% Na_2O binder specimens (~29 - 41%) because of the presence of higher soluble silica content. The higher sodium silicate content leads to the formation of smaller pores and reduces the

water permeability and porosity of binder specimens. Also, the inclusion of slag at lower quantities did not change the porosity values of binder specimens. However, the binder specimens activated 30wt.% slag showed a ~30% reduction in porosity values. This indicates the domination of C-A-S-H gel in these mixes and the beginning of the space-filling effect because of the formation of more C-A-S-H gel. The studies have reported that the binder mixes up to 25 wt.% slag content is dominated by N-A-S-H gel which does not chemically bind the water because of the lower tortuosity. The slag content >25% decrease the total porosity and increases the pore network tortuosity eventually decreasing the leaching potential of alkali ions from the binders [220]. The AAS results in this study were also consistent with this behaviour and a reduction in the leaching potential of Na and Si was observed as the slag content increased from 0-30wt.%. The dry density values reported (Fig. 7-25(c)) in this study did not show significant changes with varying Na₂O content. The binder mixes with 30wt.% slag content showed a slight increase in the dry density values.

The compressive strength of binder specimens after 28 days curing, and 90 days leaching are shown in Fig. 7-25(d). The decrease in Na₂O content reduced the compressive strength because of the low activator content in the binder mixes. The 9 wt.% Na₂O mixes showed higher compressive strength values compared to 7 wt.% and 5 wt.% Na₂O mixes. The use of a higher amount of soluble silicates leads to the development of stronger material by including more Si in the tetrahedral environment (Q⁴(1Al) and Q⁴(2Al)). The inclusion slag further enhances the compressive strength of binder mixes because of the formation of C-A-S-H gel. After 90 days of leaching, the compressive strength of binder specimens was observed to be increasing in all binder mixes, which is attributed to the formation of silica-rich gel under leaching. This behaviour is consistent with FTIR results from Si-O-T stretching vibration shifted to higher wavenumbers indicating more silica in the geopolymer gel after leaching. The ²³Na NMR results also showed a similar behaviour where chemical shifts were observed at lower resonances after leaching indicating silica-rich gel in binder specimens after leaching. The formation of silica-rich gel during leaching further increases the strength of the material under axial compression.

The split tensile strength of binder specimens after 28 days curing, and 90 days leaching are shown in Fig. 7-25(e). Regardless of Na₂O content after 28 days of curing

the split tensile strength of binder mixes varied from 1.1-3.9 MPa. After 90 days of leaching a significant reduction in the split tensile strength values were observed in several binder mixes (9A-9D, 7A, 7C-7D and 5D). This behaviour is attributed to the reduction in N-A-S-H/N-(C)-A-S-H gel after the leaching process. Also, excessive leaching of Na^+ from the aluminosilicate network leads to the breaking or weaker Al-O-Si linkage. The binder mixes with higher slag contents also showed the leaching of Ca content from the mixes. The XRD and AAS results have corroborated this behaviour. Therefore, the leaching of Na^+ and Ca^{2+} significantly changes the aluminosilicate structure, which leads to a decrease in split tensile strength.

Another explanation for this behaviour is the increase in silica content in binder specimens after leaching. Studies have reported a decrease in tensile strength of geopolymer based waterproof coatings. They have observed a reduction in tensile strength properties from ~ 3.1 – 0.5 MPa as the silicate modulus increased from 1.4-2.2 [247]. Hence, the reduction in split tensile strength is probably because of the concomitant effect of weaker Al-O-Si linkages and the formation of higher silica content in the geopolymer gel, which is enhanced the brittle behaviour of binder specimens. The binder specimens with low Na_2O (5 wt.%) and slag (5 and 10 wt.%; 5A-5C) content behaved differently, the split tensile strength in these binder mixes was observed not to be changing after leaching. The FTIR results showed the Si-O-T shift to higher wavenumbers after leaching which is attributed to Si inclusion. However, the ^{27}Al NMR results showed the inclusion of Al in these mixes under leaching. Therefore, there is a possibility of a slight increase in N-A-S-H gel with lower silica content in these specimens and contributing to the no change in split tensile strength in binder specimens after leaching.

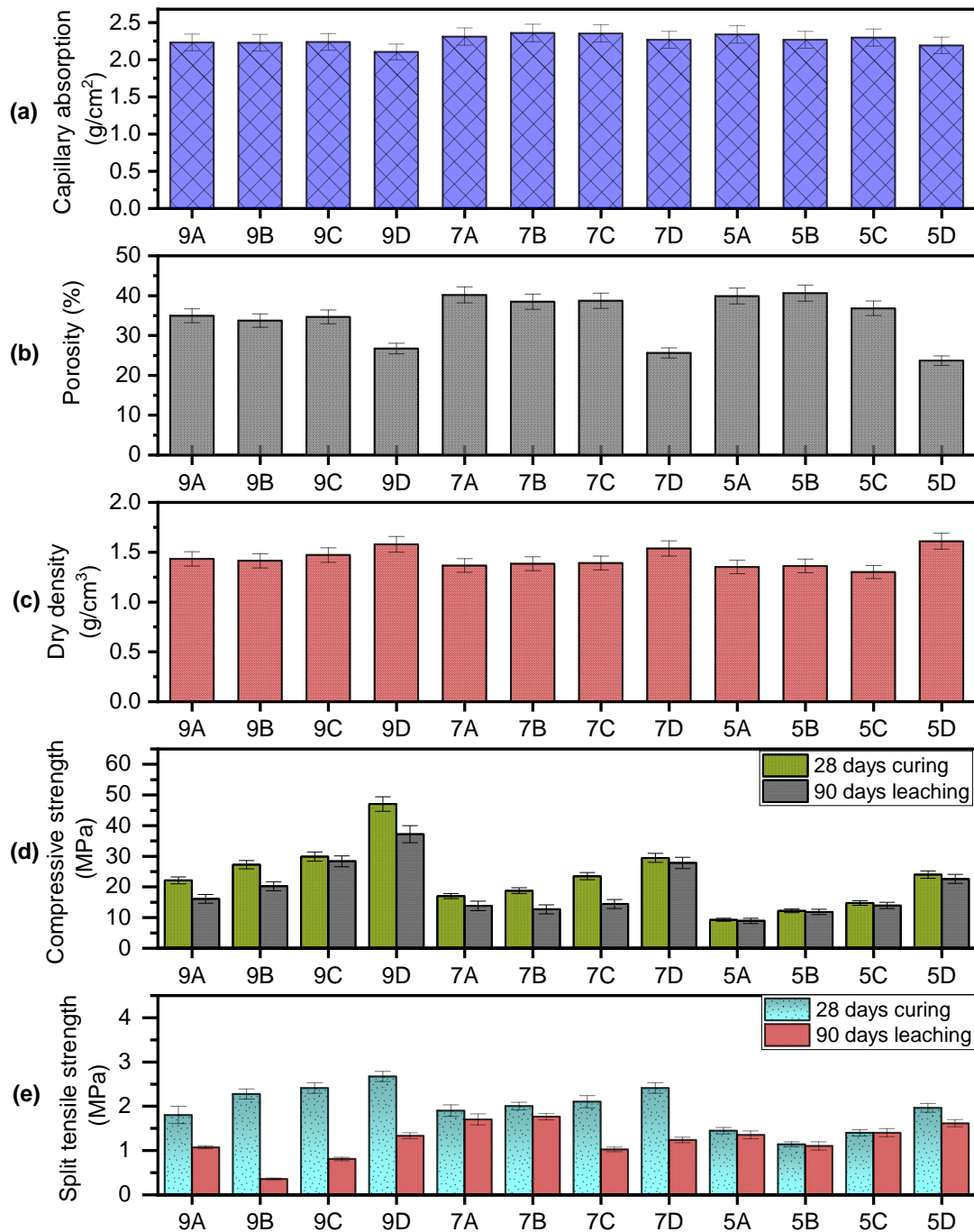


Fig. 7-25 Physical properties of binder mixes (a) Capillary absorption after curing, (b) Open porosity values after curing (c) Dry density after curing (d) Compressive strength behaviour after curing and leaching and (e) Split tensile strength behaviour after curing and leaching.

7.4 Conclusions

The effect of leaching on alkali-activated binder mixes with varying Na₂O (5, 7 and 9 wt.%) and slag (0, 5, 10 and 30 wt.%) contents were investigated in this work. The inclusion of slag in binder mixes has facilitated the formation of C-A-S-H along with

N-A-S-H gel in the binder mixes. The formation of C-A-S-H gel in binder mixes has enhanced the mechanical properties, dry density and decreased the total porosity (up to ~10%) after 28 days of curing.

The leaching of Na monotonically increased as a function of time. However, the Si leaching potential from binder mixes was significantly reduced after 60 days of leaching. The addition of slag in binder mixes led to the formation of increased tortuosity in the porous network because of the addition of slag in binder mixes. The reduction of porosity because of the inclusion of slag further decreased the leaching potential of Na and Si from binder mixes between 20-30%. However, long-term exposure to the leaching conditions has triggered the dissolution of Ca and Al from the N-A-S-H/N-(C)-A-S-H gel from the binder mixes. The leaching of Ca and Al from the binder mixes led to the degradation of binder mixes. The microstructural studies such as FTIR results showed a significant reduction in the intensity of the spectra after leaching, which indicated the degradation of aluminosilicate gels. The ^{23}Na MAS-NMR results also corroborated these observations. The ^{27}Al MAS-NMR results also showed the movement of Al[IV] chemical shifts to lower ppm, which indicates the structural changes in the Al-O-Si bonding environment of aluminosilicate gel because of the leaching of alkalis from the binder mixes.

In comparison with binder mixes activated with 9 wt.% Na_2O , the binder mixes with lower Na_2O (5 and 7 wt.%) and lower slag (5 and 10 wt.%) behaved differently under leaching. The MAS-NMR (^{23}Na and ^{27}Al) results also showed lesser movements of peaks and a slight change in the intensity of the spectra after leaching. The presence of higher alkali content and slag content in binder mixes led to significant degradation of aluminosilicate gels. MD simulations corroborated these results, where the movement of Na ions and distortions of Al-O-Si structure was observed because of the leaching of Na ions.

The compressive strength of binder mixes activated with 9wt.% Na_2O content showed a decreasing trend after leaching. However, the binder mixes activated with 5 and 7wt.% Na_2O showed an insignificant change in compressive strength after leaching. The split tensile strengths of binder mixes activated with 9wt.% Na_2O decreased up to ~50% after leaching. However, the binder mixes with lower Na_2O and slag contents showed a negligible decrement in split tensile strength values after leaching.

Overall, the binder mixes activated with lower Na₂O (5 and 7 wt.%) and lower slag (5 and 10wt.%) showed better stability and retained >90% of their structural strength after leaching. Furthermore, the leaching of C-A-S-H gel delays the leaching of N-A-S-H gel and acts as a barrier to Na bearing phases, which could significantly delay the rebar corrosion. However, further investigation is required to corroborate this behaviour.

CHAPTER 8 CONCLUSION AND FUTURE DIRECTIONS

This body of work investigated the effect of activator and slag content on phase changes of N-A-S-H and N-(C)-A-S-H gel under efflorescence and leaching conditions. Several characterization techniques were used to analyse phase formation and degradation of FA-slag based AAMs. The mechanical properties, compressive strength and split tensile were measured before and after durability testing.

8.1 Conclusions

The main conclusions and specific outcomes corresponding to the research objectives outlined in Chapter 3 are as follows:

1. The effect of mixed activators including $\text{NaOH}+\text{Na}_2\text{SiO}_3$ and Na_2CO_3 was investigated. The use of Na_2CO_3 in minor quantities increased the efflorescence formation in AAMs. The addition of slag in 10 wt.% and 30 wt.% reduced the overall porosity and efflorescence formation in binder pastes compared with pure FA AAMs. The AAM binder pastes with 0 wt.%, 5 wt.%, 10 wt.% and 30 wt.% slag activated with 9 wt.% Na_2O content showed higher efflorescence formation compared with AAM binder pastes with 0 wt.%, 5 wt.%, 10 wt.% and 30 wt.% activated slag with 5 wt.% Na_2O content. The binder pastes with 5 wt.% Na_2O content showed a negligible amount of efflorescence formation and phase degradation.
2. The MAS-NMR analysis indicated significant changes in ^{23}Na and ^{27}Al environments after efflorescence and leaching. After efflorescence, significant movement in ^{23}Na environment towards positive values and movement of ^{27}Al environment towards lower ppm values indicated the degradation of N-A-S-H and N-(C)-A-S-H gel in binder pastes activated with 9 wt.% Na_2O content with or without slag content. The inclusion of slag caused a decrease in porosity. Hence, changes in ^{23}Na and ^{27}Al environments were lower compared with pure FA binder pastes. The binder pastes with 5-30 wt.% slag, activated with 5 wt.% Na_2O content showed minor changes in the ^{23}Na environment, attributed to the lower Na_2O content and slag fraction in these binder pastes. However, the ^{27}Al environment showed changes in N-(C)-A-S-H environment, which is attributed to the natural carbonation in these conditions. With an increase in

slag content, compressive and split tensile strength increased in binder pastes after activation, attributed to the formation of N-(C)-A-S-H gel, increase in dry density and reduction in porosity of AAM binder pastes upon slag addition. After efflorescence, the mechanical properties in binder pastes activated 9 wt.% Na₂O content decreased. Specifically, the split tensile strength decreased after efflorescence, which is attributed to the development of crystallization pressure inside the binder specimens under efflorescence.

3. A significant amount of Na⁺ and Si⁴⁺ ions leached from binder pastes at the end of 90 days of leaching. With an increase in slag content, the leaching of Na⁺ and Si⁴⁺ ions decreased. The binder pastes with 30 wt.% slag showed a negligible amount of Na⁺ and Si⁴⁺ in the leachate, which indicated the inclusion of slag refined the porosity and decreased the leaching potential of alkali ions. Leaching of Ca²⁺ ions from the binder pastes with slag content indicated the leaching of Ca²⁺ from N-(C)-A-S-H gel. The leaching of Na⁺ and Si⁴⁺ from pastes led to N-A-S-H and N-(C)-A-S-H degradation, and decreased compressive and split tensile strengths. The mechanical performance of binder pastes activated with lower activator content (5wt.% and 7wt.% Na₂O) was improved compared with binder mixes with 9wt.% Na₂O content.
4. The MAS-NMR results after leaching showed significant changes in ²³Na and ²⁷Al environments. A significant reduction in the ²³Na environment was observed after leaching, indicating N-A-S-H gel degradation. The decrease in the intensity of ²³Na environment in binder pastes with slag content and 5 – 7 wt.% Na₂O content was lower compared with pure FA based-AAMs activated with 5 – 9 wt.% Na₂O contents. The ²⁷Al values moved to lower ppm values in binder pastes with slag contents indicating the N-(C)-A-S-H gel degradation under leaching. The XRD analysis also a significant reduction in the intensity of C-A-S-H gel, corroborating the N-(C)-A-S-H gel degradation under leaching.

8.2 Future directions

This study demonstrated the effect of precursor blends and the use of different activators on efflorescence and leaching of alkali-activated materials. The use of slag significantly controlled the efflorescence formation and decreased leaching potential in FA-slag based-AAMs. Also, efflorescence formation in binder pastes with low

activator content (5 – 7 wt.wt.%) was significantly lower than binder pastes with 9 wt.% Na₂O content. Further investigation is required for the development of well-informed design principles and commercial applications of AAMs in the construction industry.

The current work potentially leads to the following research directions:

- *Evaluation of efflorescence and leaching potential of AAMs activated with different activators (KOH, K₂SiO₃) and precursors such as FA-metakaolin, slag-rice husk ash:* Further investigation on the relationship between efflorescence/leaching and mechanical performance, the effect of atmospheric conditions such as relative humidity, CO₂ concentration on efflorescence, and leaching behaviour of AAMs in different solvents with varying ionic strength of mortar and concrete specimens is critical in understanding efflorescence/leaching.
- *The rheology of AAM binder pastes activated with different activators and precursors:* Since rheology defines the setting time and workability of pastes, mortars, and concrete, understanding this behaviour at a fundamental level is useful for commercial application. The effect of physical properties such as dry density and porosity of AAMs on efflorescence and leaching behaviour can be evaluated.
- *The mechanical performance of AAM based reinforced and post-tension concrete beams/columns:* Fracture, fatigue, and creep behaviour of AAMs and mechanical performance of the structural elements after different durability exposure is essential for application in the industry. Aspects of corrosion of rebars under durability exposure can be correlated with the mechanical performance of AAM.
- *The development of accurate molecular models describing phase evolution of N-A-S-H, C-A-S-H, and N-(C)-A-S-H gels:* The degradation study of N-A-S-H, C-A-S-H, and N-(C)-A-S-H atomistic level is critical in the prediction of phase degradation.

8.3 Contributions

The current body of work contributes to the field of FA/slag based AAMs in the following aspects.

- a) **Phase changes in FA and FA-Slag based AAMs under efflorescence:** The effect of slag, Na₂O content, and mixed activator concentration on N-A-S-H/N-(C)-A-S-H gel stability under efflorescence were comprehensively investigated in this work. FTIR, XRD, TGA, MAS-NMR, and X-ray Tomography were used to study phase changes in AAMs.
- b) **Phase changes in FA and FA-Slag based AAMs under leaching:** The effect of slag and Na₂O content on N-A-S-H/N-(C)-A-S-H gel stability under leaching were analysed in this work. AAS, FTIR, XRD, TGA, MAS-NMR, were used to study phase changes in AAMs.
- c) **Structural changes of N-A-S-H and N-(C)-A-S-H gels:** Structural changes in the ²³Na and ²⁷Al environments under efflorescence and leaching exposure has been investigated in this work. Significant changes in the Q⁴ environment of AAMs, indicating phase degradation under the aforementioned exposures were perceived.
- d) **Changes in compressive and split tensile strength under efflorescence and leaching:** The use of slag and higher Na₂O contents enhanced compressive and split tensile strengths. However, after efflorescence and leaching, a significant reduction in split tensile strength was observed. Thus, decrease split tensile strength is one of the key indicators of efflorescence formation.
- e) **The effect of low Na₂O (5 wt.%) on efflorescence and leaching:** AAM mixes designed with low sodium content showed significant stability under efflorescence and leaching conditions. Also, the inclusion of slag up to 30 wt.% significantly decreased the leaching of Si⁴⁺ and Na⁺ ions. However, after 90 days of leaching, significant dissolution of Ca²⁺ from the N-(C)-A-S-H gel was confirmed in AAS and XRD analysis.
- f) **Effect of porosity on efflorescence and leaching:** The use of slag significantly refined and decreased the total porosity of AAM binder mixes. The decrease in total porosity increased the phase stability in efflorescence and leaching conditions. The porosity was measured using X-ray tomography and using a method established in the literature [158].

APPENDIX A STATEMENTS OF CONTRIBUTIONS OF CO-AUTHORS

Appendix A-1: Statements of the contribution of co-authors relating to

Phase changes under efflorescence in alkali-activated materials with mixed activators, Lakshmikanth Srinivasamurthy, Venkata S. Chevali, Zuhua Zhang, and Hao Wang, *Construction and Building Materials*.

26 February 2021

To Whom It May Concern

Paper 1: Phase changes under efflorescence in alkali-activated materials with mixed activators, Lakshmikanth Srinivasamurthy, Venkata S. Chevali, Zuhua Zhang, and Hao Wang, *Construction and Building Materials*, IF – 6.141 (Published)

LS was responsible for 75% of the conceptualization, formal analysis, investigation, methodology, project administration, writing - original draft. HW and ZZ are responsible for funding acquisition, supervision, and writing - review & editing. VSC is responsible for analysis - interpretation of data and editing and proofreading.

Paper 2: The effect of fly ash/slag ratio and activator concentration on efflorescence of fly ash/slag-based alkali-activated materials, Lakshmikanth Srinivasamurthy, Zuhua Zhang, Venkata Chevali, Márlon A. Longhi, Thomas Loh, Hao Wang, *Construction and Building Materials*, IF-6.141 (Under review)

LS was responsible for 75% of the conceptualization, formal analysis, investigation, methodology, project administration, writing - original draft. HW and ZZ are responsible for funding acquisition, supervision, and writing - review & editing. VSC is responsible for analysis - interpretation of data and editing and proofreading. ML is responsible for the investigation and providing technical inputs. TL is responsible for characterization and providing technical inputs.

Paper 3: Effect of fly ash/Slag ratio and sodium content on AAMs under leaching, Lakshmikanth Srinivasamurthy, Venkata S. Chevali, Zuhua Zhang, and Hao Wang, *Journal of Building Engineering*, IF-5.1 (In submission)

LS was responsible for 75% of the conceptualization, formal analysis, investigation, methodology, project administration, writing - original draft. HW and ZZ are responsible for funding acquisition, supervision, and writing - review & editing. VSC is responsible for analysis - interpretation of data and editing and proofreading.

Paper 4: Durability behaviour of alkali-activated materials, Lakshmikanth Srinivasamurthy, Zuhua Zhang, Venkata Chevali, Hao Wang, Construction and Building Materials, IF: 6.141 (In Submission)

LS was responsible for 75% of the literature review, 75% of analysis and interpretation of the data and 100% of drafting the initial draft and final submission. HW and ZZ is responsible for the literature review and editing the draft and providing necessary technical inputs. VSC is responsible for literature review and editing drafts and providing inputs.

Undertaken with Lakshmikanth Srinivasamurthy

Student and Co-Author signatures are held at USQ.

(Co-Authors)

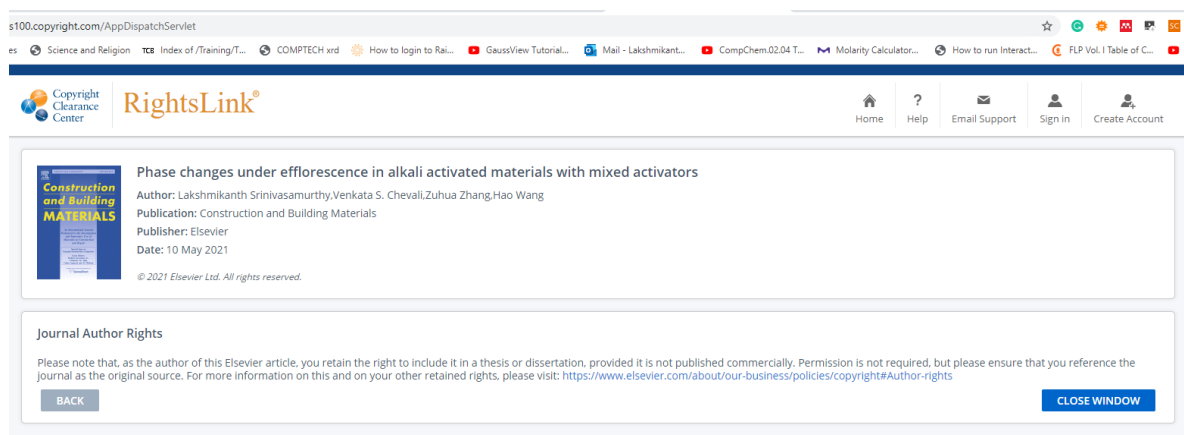
Professor Hao Wang, Zuhua Zhang, and Venkata Chevali

(First Author)

Lakshmikanth Srinivasamurthy

Appendix A-5: Copyright information relating to

Phase changes under efflorescence in alkali-activated materials with mixed activators, Lakshmikanth Srinivasamurthy, Venkata S. Chevali, Zuhua Zhang, and Hao Wang, Construction and Building Materials.



The screenshot shows a web browser window with the URL `s100.copyright.com/AppDispatchServlet`. The browser's address bar contains several tabs, including "Science and Religion", "Index of /Training/T...", "COMPTech xrd", "How to login to Rai...", "GaussView Tutorial...", "Mail - Lakshmikanth...", "CompChem.02.04 T...", "Molarity Calculator...", "How to run Interact...", and "FLP Vol. I Table of C...". The page header features the "Copyright Clearance Center" logo and the "RightsLink" logo. On the right side of the header, there are navigation links: "Home", "Help", "Email Support", "Sign In", and "Create Account".

The main content area displays the following information:

- Article Title:** Phase changes under efflorescence in alkali activated materials with mixed activators
- Author:** Lakshmikanth Srinivasamurthy, Venkata S. Chevali, Zuhua Zhang, Hao Wang
- Publication:** Construction and Building Materials
- Publisher:** Elsevier
- Date:** 10 May 2021
- Copyright:** © 2021 Elsevier Ltd. All rights reserved.

Below this information, there is a section titled "Journal Author Rights" with the following text:

Please note that, as the author of this Elsevier article, you retain the right to include it in a thesis or dissertation, provided it is not published commercially. Permission is not required, but please ensure that you reference the journal as the original source. For more information on this and on your other retained rights, please visit: <https://www.elsevier.com/about/our-business/policies/copyright#Author-rights>

At the bottom of this section, there are two buttons: "BACK" and "CLOSE WINDOW".

APPENDIX B SUPPLEMENTARY INFORMATION

Effect of microstructural changes and phase evolution on efflorescence of FA-based alkali-activated materials

Lakshmikanth Srinivasamurthy ^a, Venkata S. Chevali ^a, Zuhua Zhang ^{a, b}, and Hao Wang ^{a, *}

^aCentre for Future Materials, University of Southern Queensland, Springfield Central, QLD 4300, Australia

^bKey Laboratory for Green & Advanced Civil Engineering Materials and Application Technology of Hunan Province, College of Civil Engineering, Hunan University, Changsha 410082, China

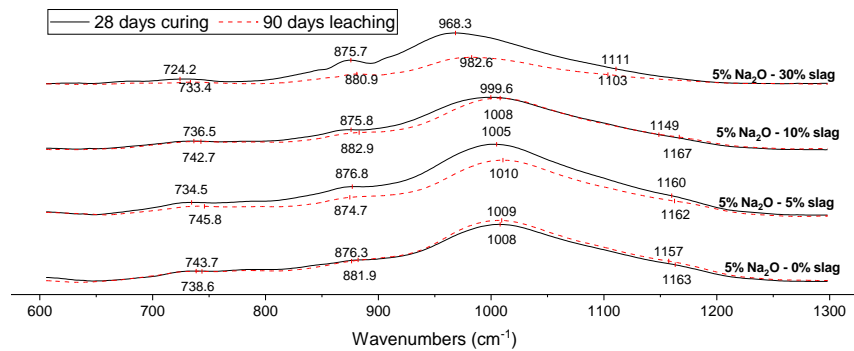


Fig. BS-1

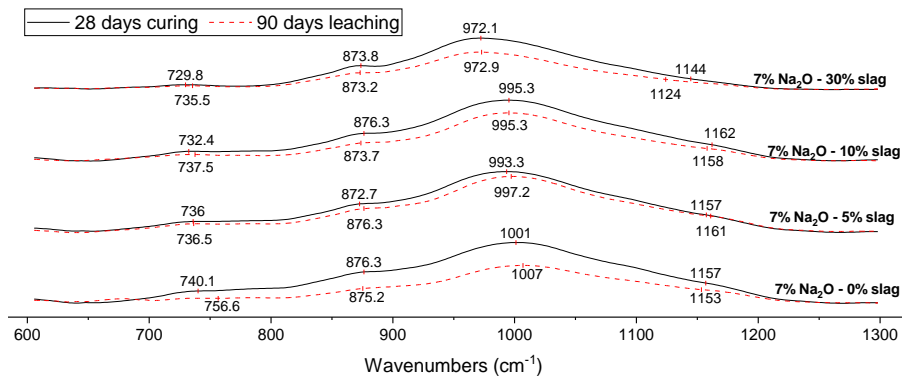


Fig. BS-2

* Corresponding Author: Hao.Wang@usq.edu.au (H. Wang). 37 Sinnathamby Boulevard, Springfield Central QLD 4300 AUSTRALIA

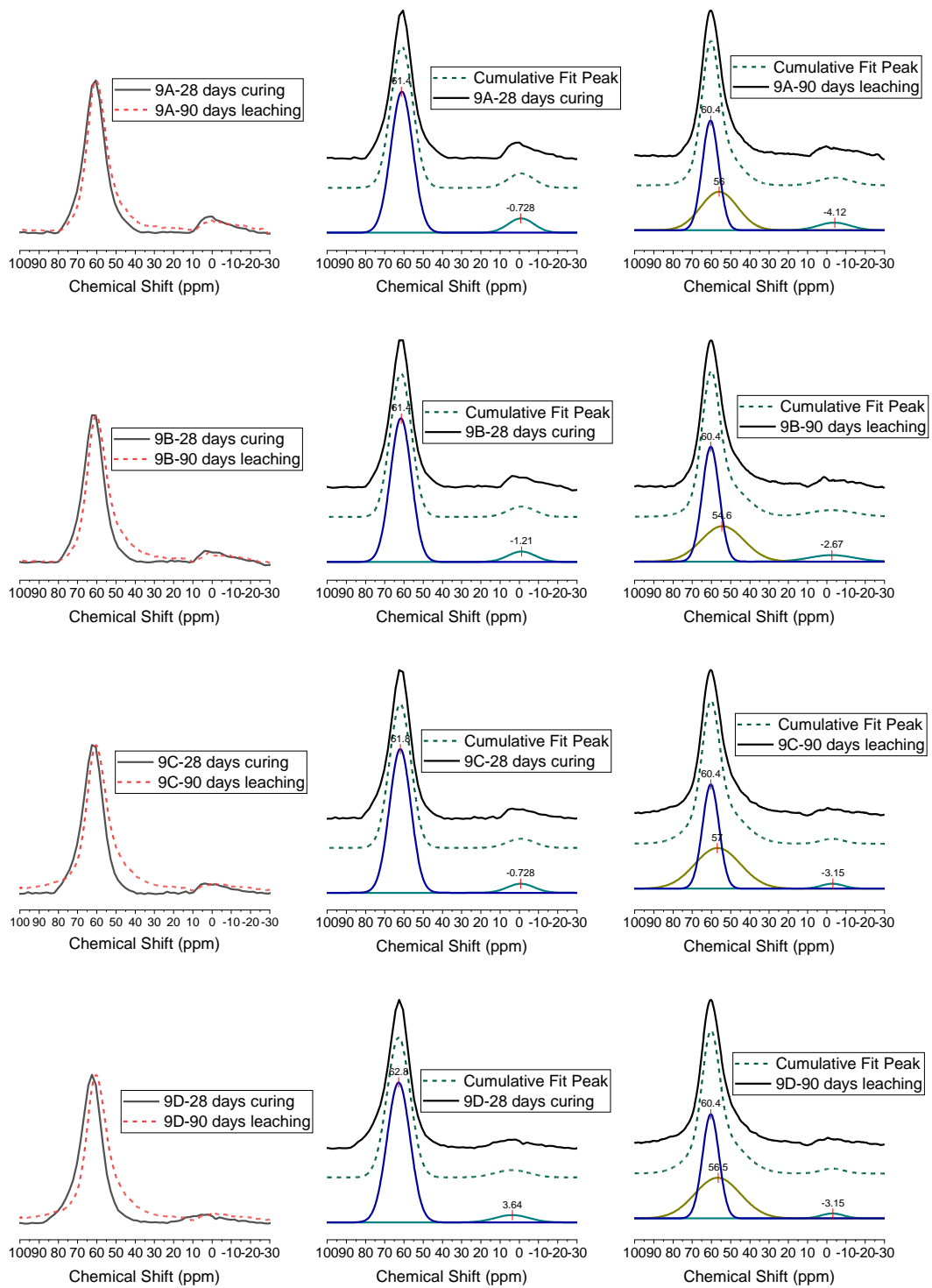


Fig. BS-3

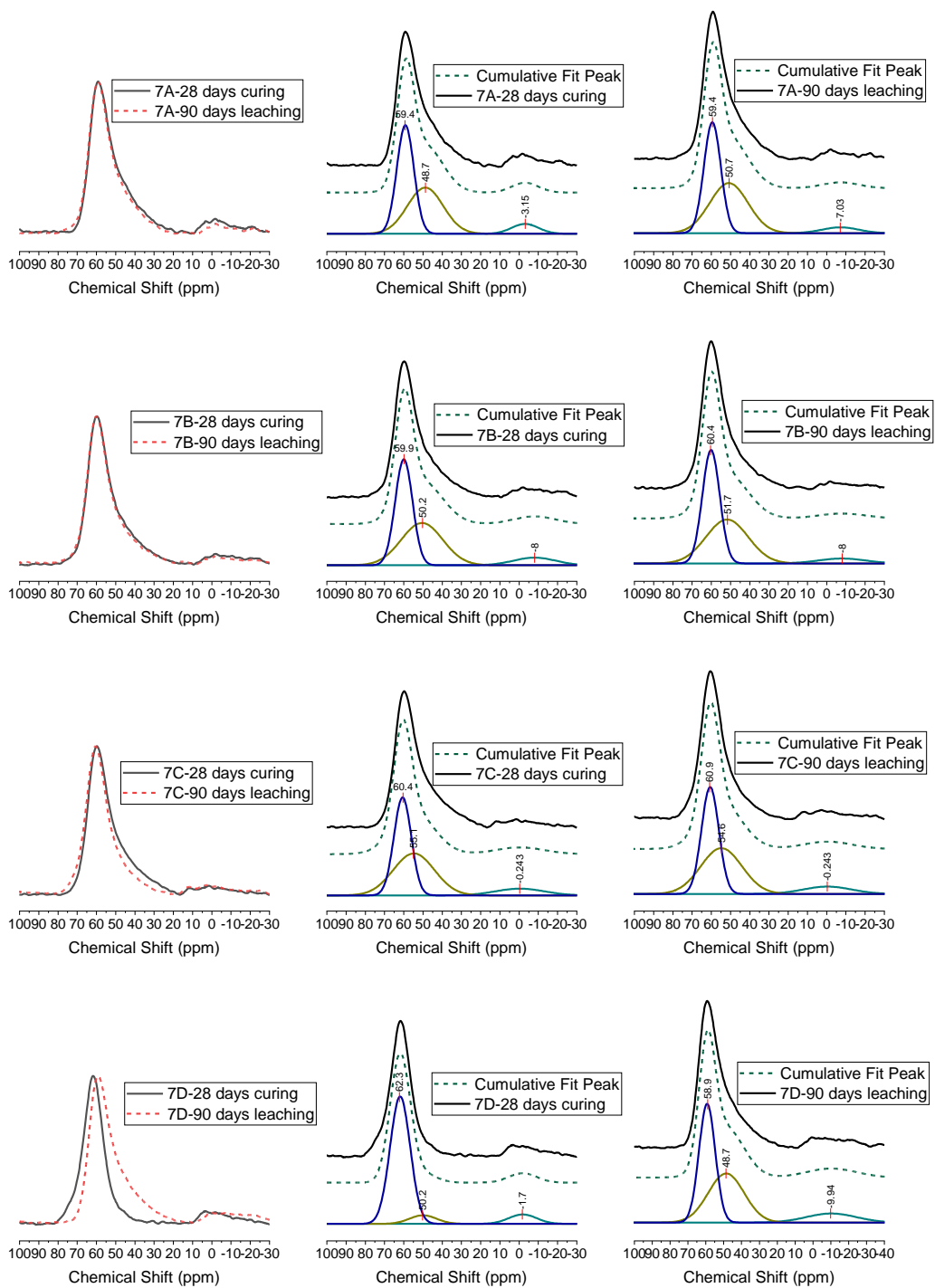


Fig. BS-4

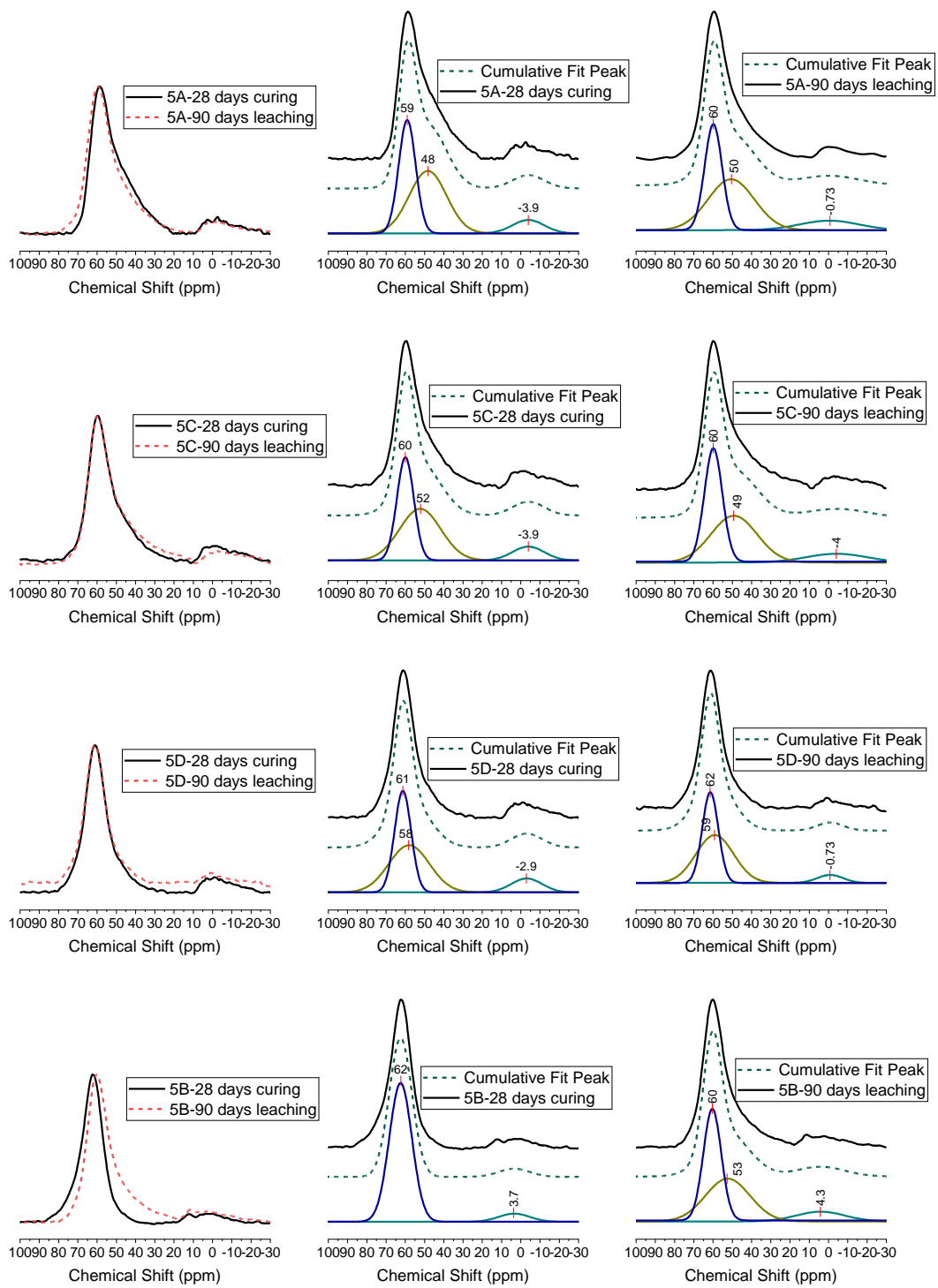


Fig. BS-5

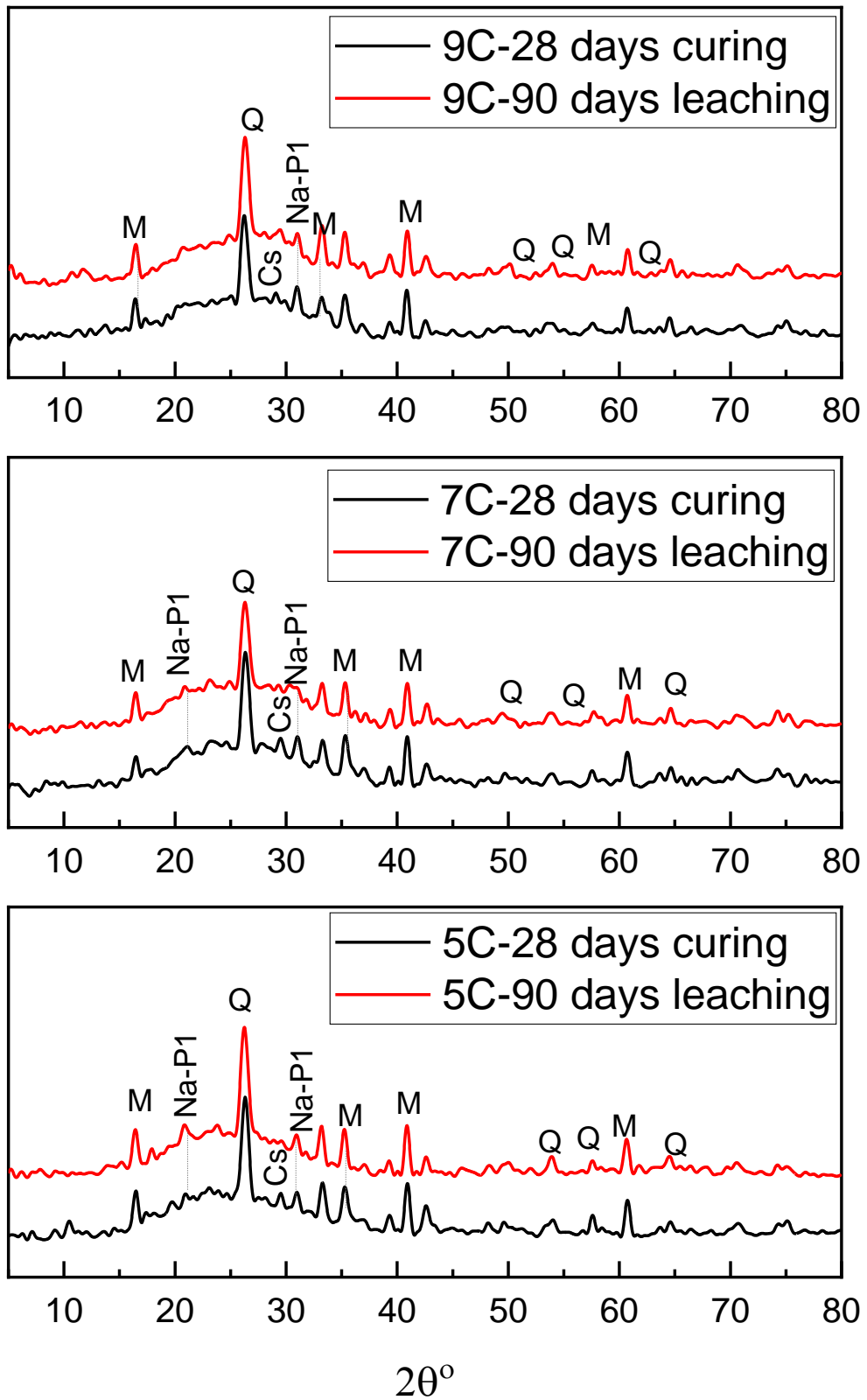


Fig. BS-6

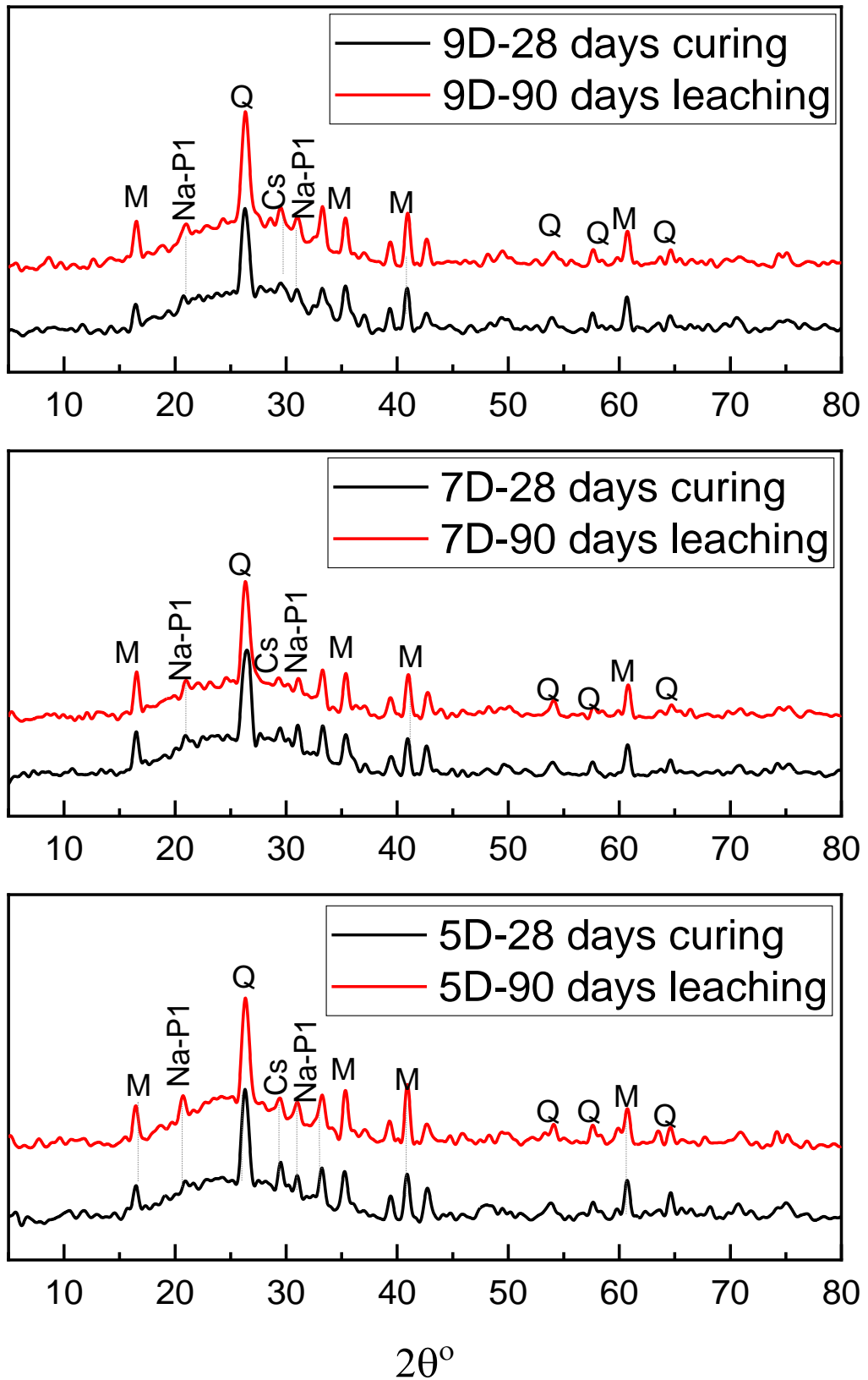


Fig. BS-7

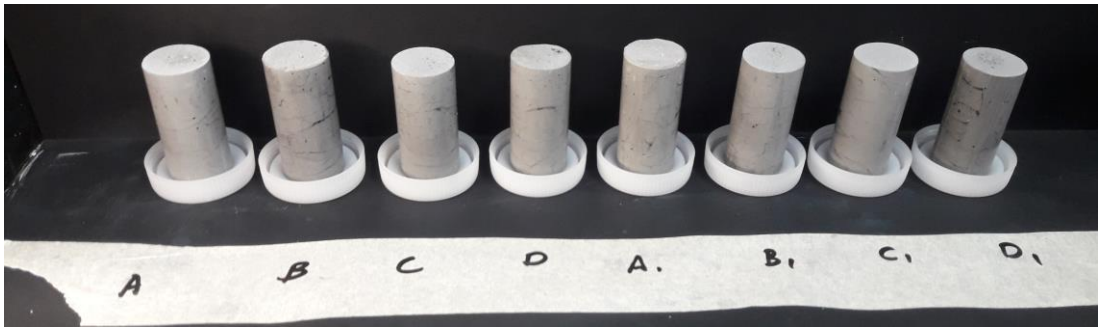


Fig. BS-8

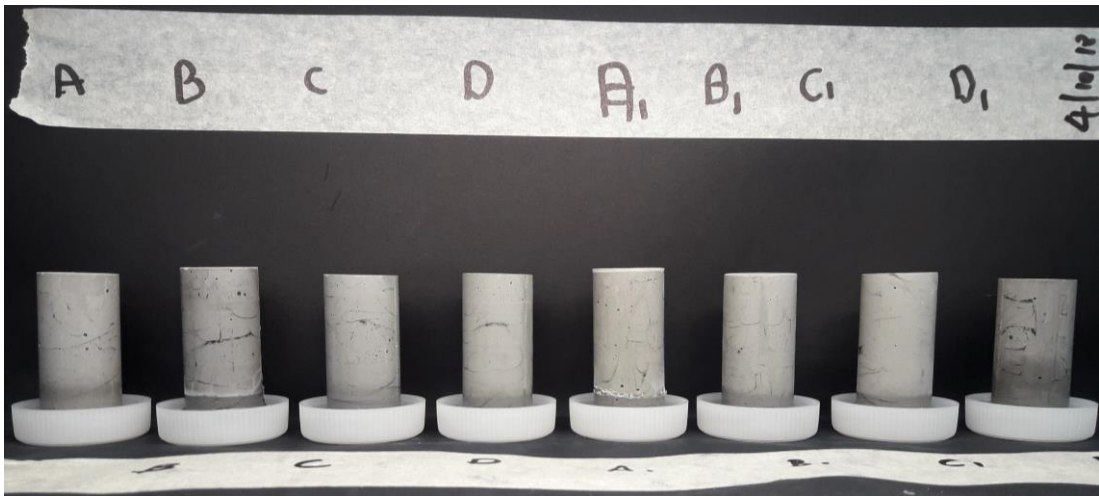


Fig. BS-9



Fig. BS-10

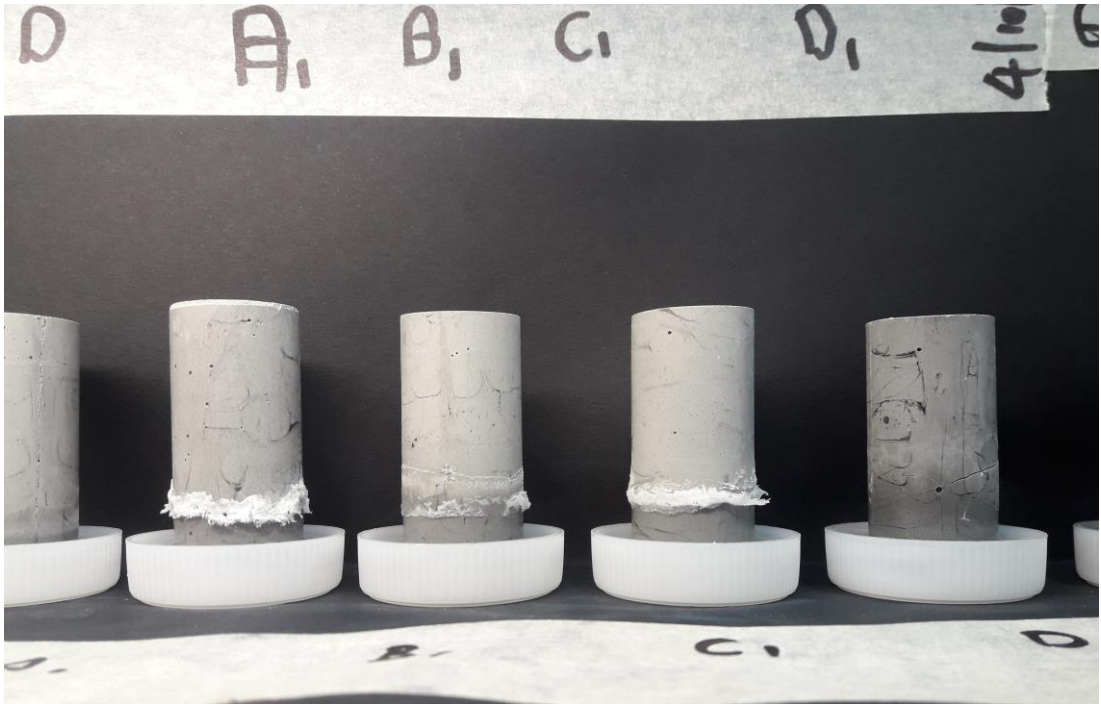


Fig. BS-11

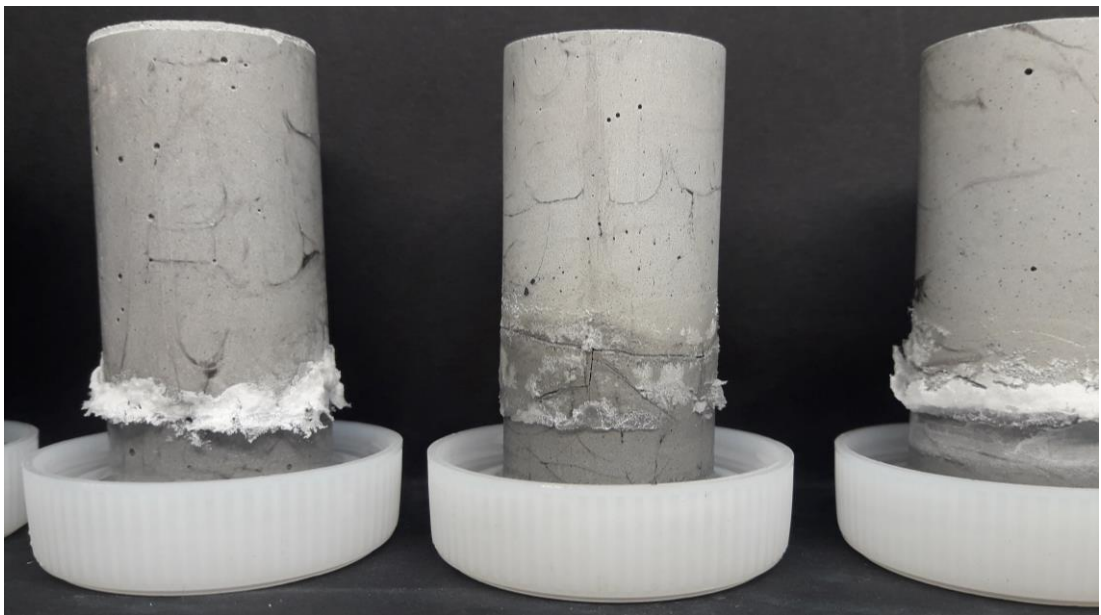


Fig. BS-12

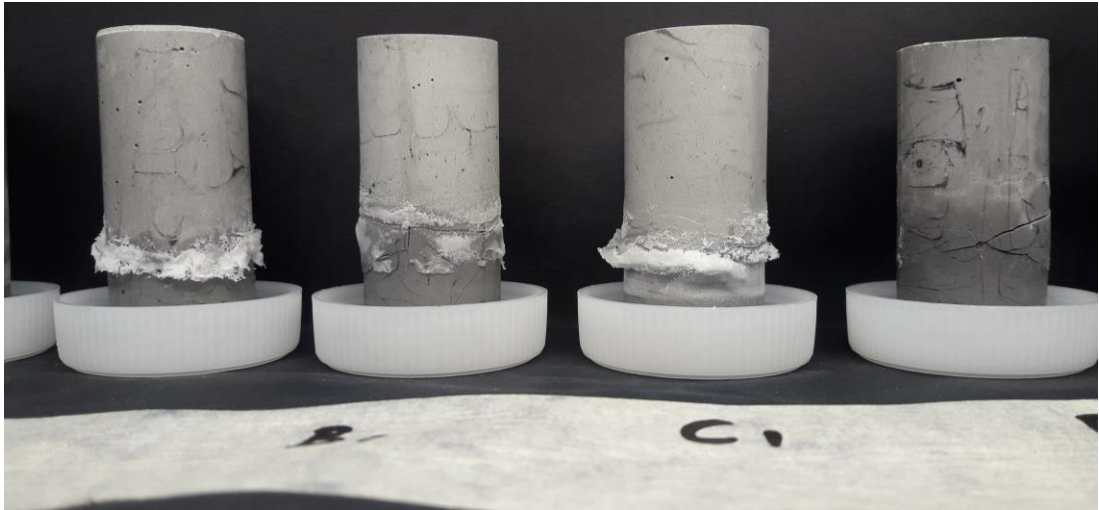


Fig. BS-13

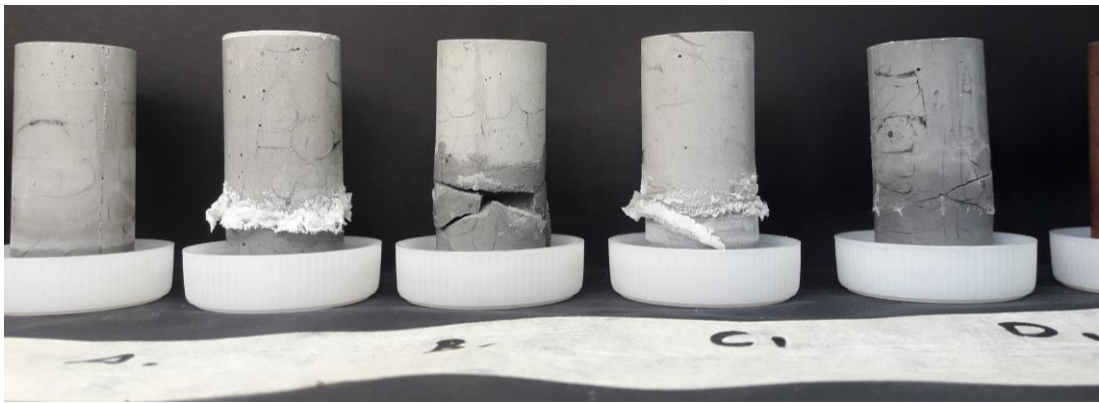


Fig. BS-14

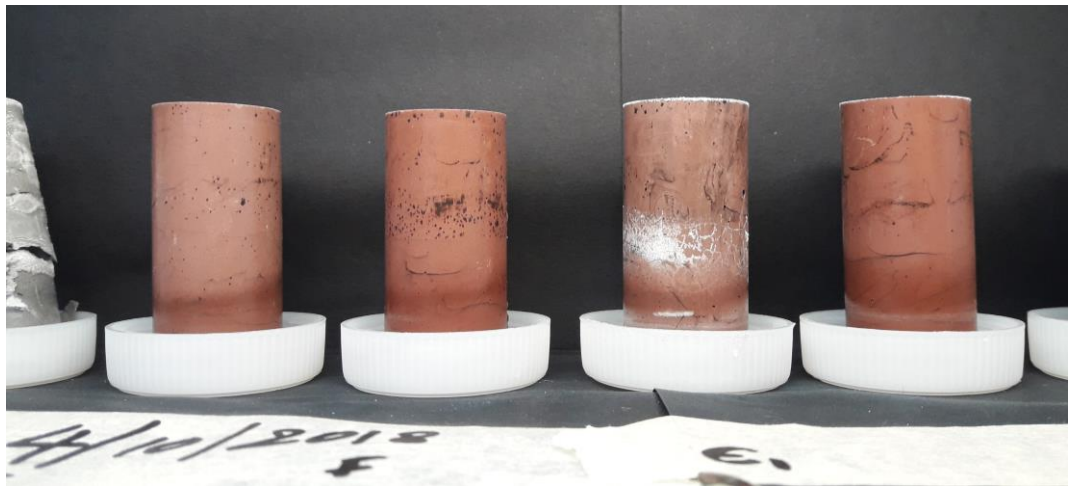


Fig. BS-15

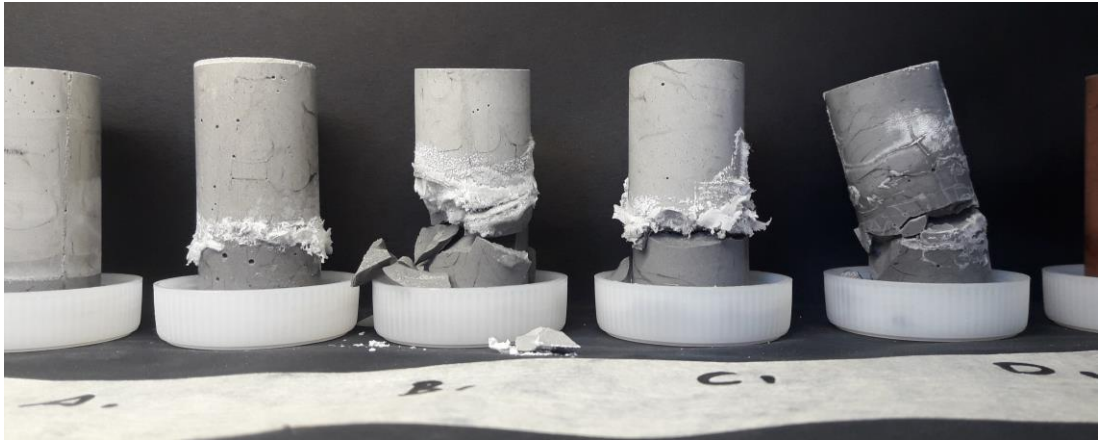


Fig. BS-16

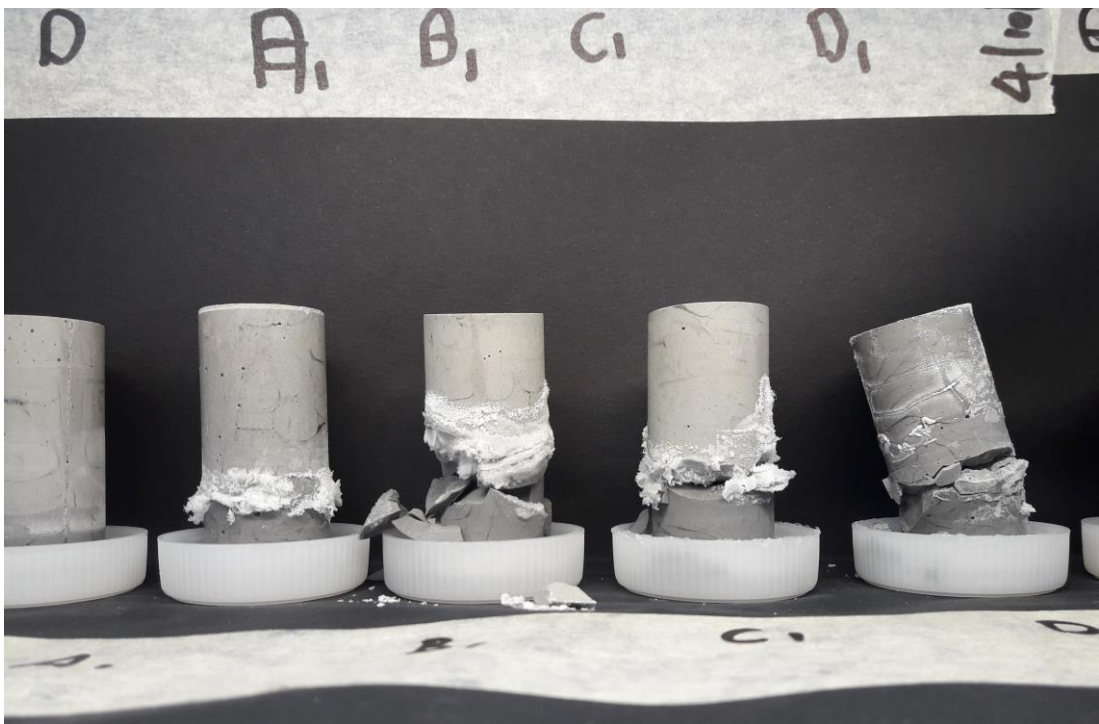


Fig. BS-17

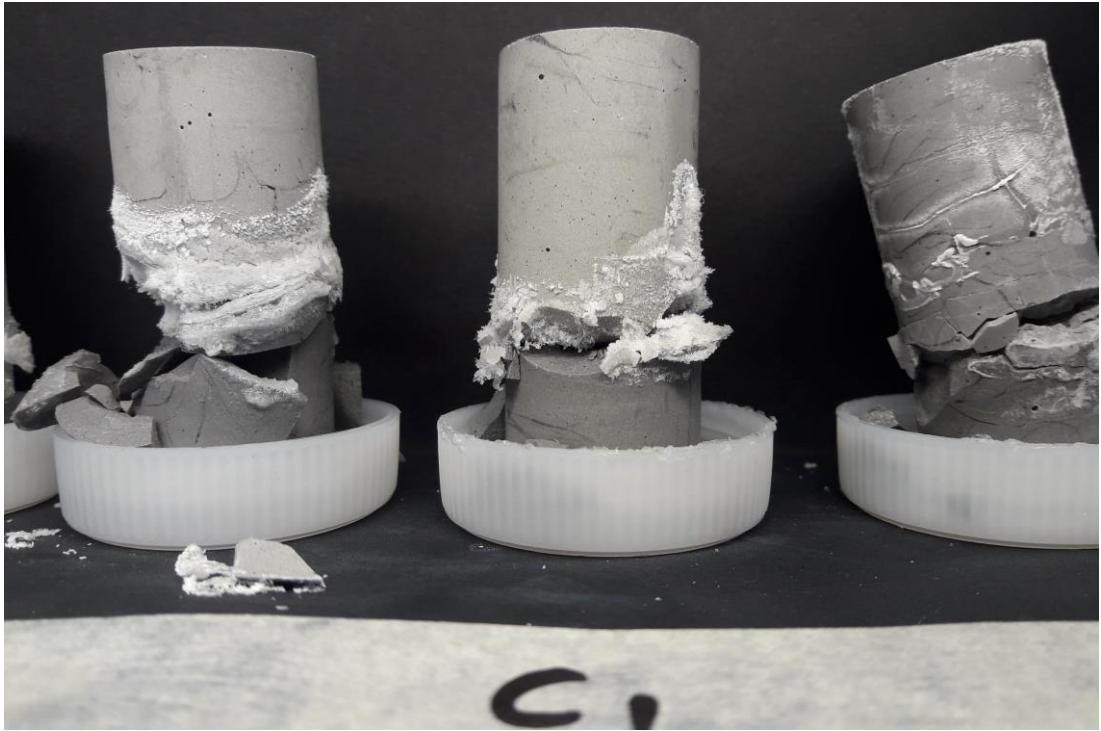


Fig. BS-18

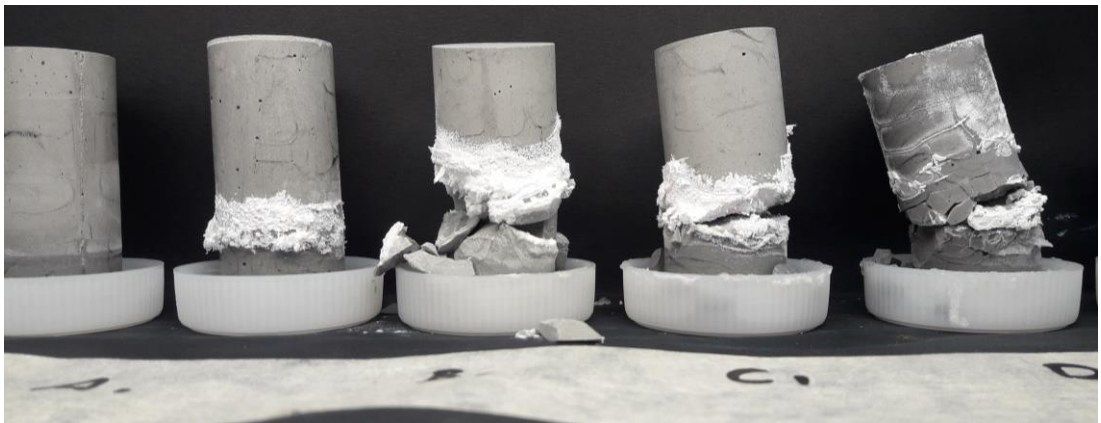


Fig. BS-19

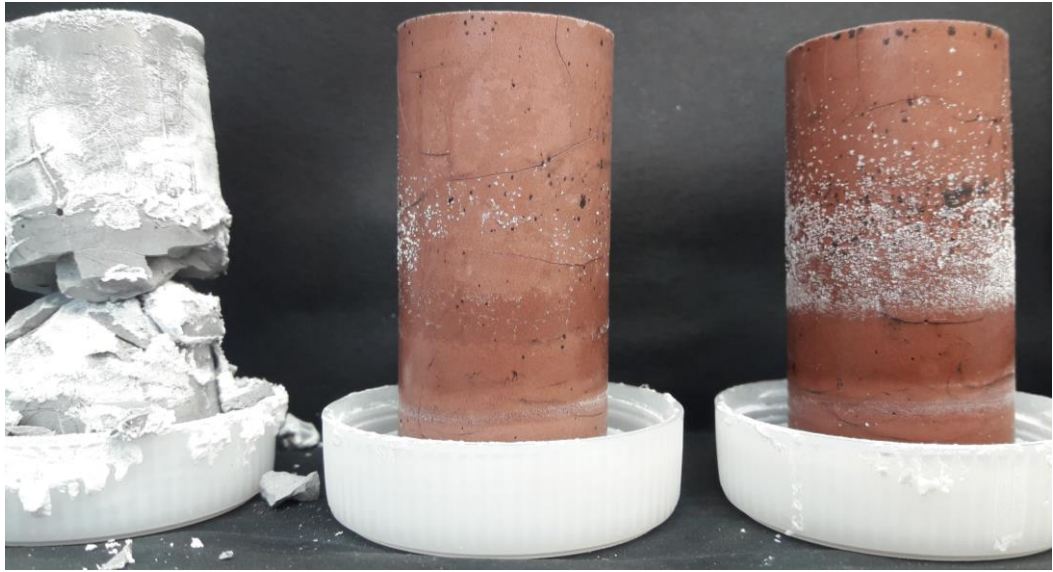


Fig. BS-20

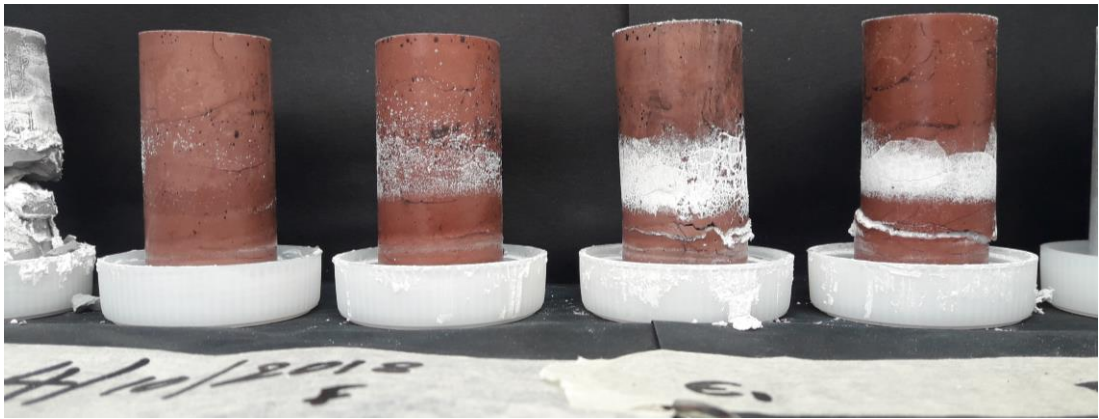


Fig. BS-21

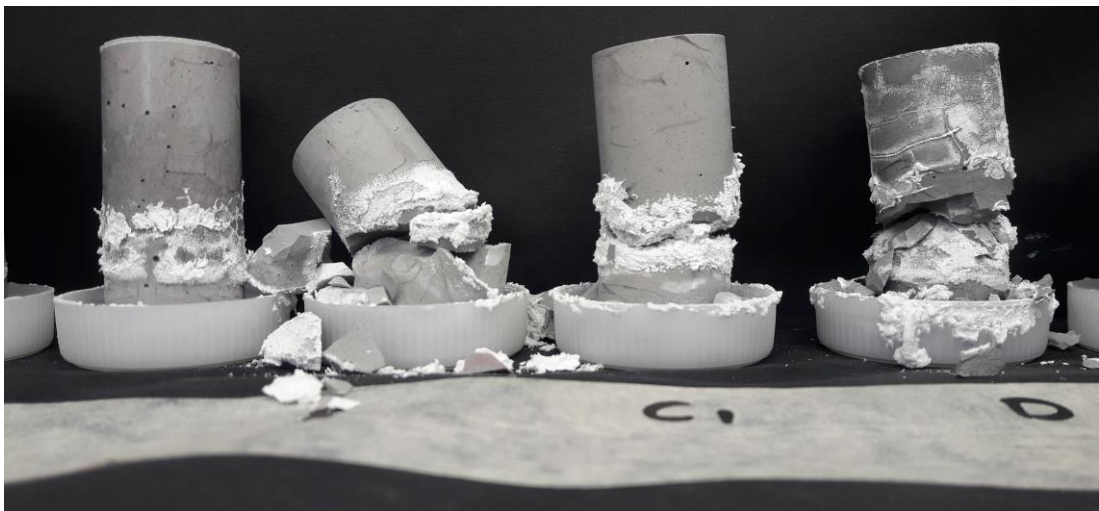


Fig. BS-22

REFERENCES

- [1] P.C. Aïtcin, Cements of yesterday and today - concrete of tomorrow, *Cem. Concr. Res.* 30 (2000) 1349–1359. doi:10.1016/S0008-8846(00)00365-3.
- [2] J.L. Provis, S.A. Bernal, Geopolymers and related alkali-activated materials, *Annu. Rev. Mater. Res.* 44 (2014) 299–327. doi:10.1146/annurev-matsci-070813-113515.
- [3] K.L. Scrivener, R.J. Kirkpatrick, Innovation in use and research on cementitious material, *Cem. Concr. Res.* 38 (2008) 128–136. doi:10.1016/j.cemconres.2007.09.025.
- [4] M.B. Ali, R. Saidur, M.S. Hossain, A review on emission analysis in cement industries, *Renew. Sustain. Energy Rev.* 15 (2011) 2252–2261. doi:10.1016/j.rser.2011.02.014.
- [5] K. Yang, J. Song, K.S.-J. of C. Production, undefined 2013, Assessment of CO₂ reduction of alkali-activated concrete _ Elsevier Enhanced Reader.pdf, Elsevier. 39 (2013) 265.
- [6] N. Ukrainczyk, T. Matusinović, Thermal properties of hydrating calcium aluminate cement pastes, *Cem. Concr. Res.* 40 (2010) 128–136. doi:10.1016/j.cemconres.2009.09.005.
- [7] M. Heikal, M.S. Morsy, M.M. Radwan, Electrical conductivity and phase composition of calcium aluminate cement containing air-cooled and water-cooled slag at 20, 40 and 60 °c, *Cem. Concr. Res.* 35 (2005) 1438–1446. doi:10.1016/j.cemconres.2004.09.027.
- [8] A.H. López, J.L.G. Calvo, J.G. Olmo, S. Petit, M.C. Alonso, Microstructural evolution of calcium aluminate cements hydration with silica fume and fly ash additions by scanning electron microscopy, and mid and near-infrared spectroscopy, *J. Am. Ceram. Soc.* 91 (2008) 1258–1265. doi:10.1111/j.1551-2916.2008.02283.x.
- [9] Y. Shen, J. Qian, J. Chai, Y. Fan, Calcium sulphoaluminate cements made with

phosphogypsum: Production issues and material properties, *Cem. Concr. Compos.* 48 (2014) 67–74. doi:10.1016/j.cemconcomp.2014.01.009.

- [10] D. Torréns-Martín, L. Fernández-Carrasco, S. Martínez-Ramírez, Hydration of calcium aluminates and calcium sulfoaluminate studied by Raman spectroscopy, *Cem. Concr. Res.* 47 (2013) 43–50. doi:10.1016/j.cemconres.2013.01.015.
- [11] P. Duan, C. Yan, W. Chen, G. Chen, Z. Shui, Influence of layered double hydroxides on carbonation resistance of concrete, *Kuei Suan Jen Hsueh Pao/Journal Chinese Ceram. Soc.* 42 (2014) 1037–1041. doi:10.7521/j.issn.0454-5648.2014.08.13.
- [12] M. García-Maté, I. Santacruz, Á.G. De La Torre, L. León-Reina, M.A.G. Aranda, Rheological and hydration characterization of calcium sulfoaluminate cement pastes, *Cem. Concr. Compos.* 34 (2012) 684–691. doi:10.1016/j.cemconcomp.2012.01.008.
- [13] M.C.G. Juenger, F. Winnefeld, J.L. Provis, J.H. Ideker, Advances in alternative cementitious binders, *Cem. Concr. Res.* 41 (2011) 1232–1243. doi:10.1016/j.cemconres.2010.11.012.
- [14] T. Grounds, D. V. Nowell, F.W. Wilburn, Resistance of supersulfated cement to strong sulfate solutions, *J. Therm. Anal. Calorim.* 72 (2003) 181–190. doi:10.1023/A:1023928021602.
- [15] S. Liu, L. Wang, Y. Gao, B. Yu, W. Tang, Influence of fineness on hydration kinetics of supersulfated cement, *Thermochim. Acta.* 605 (2015) 37–42. doi:10.1016/j.tca.2015.02.013.
- [16] A. Gruskovnjak, B. Lothenbach, F. Winnefeld, B. Münch, R. Figi, S.C. Ko, M. Adler, U. Mäder, Quantification of hydration phases in supersulfated cements: Review and new approaches, *Adv. Cem. Res.* 23 (2011) 265–275. doi:10.1680/adcr.2011.23.6.265.
- [17] C. Shi, P. V Krivenko, D. Roy, *Alkali-Activated Cements and Concretes*, Alkali-Activated Cem. Concr. (2006). doi:10.4324/9780203390672.

- [18] S.A. Bernal, J.L. Provis, B. Walkley, R. San Nicolas, J.D. Gehman, D.G. Brice, A.R. Kilcullen, P. Duxson, J.S.J. Van Deventer, Gel nanostructure in alkali-activated binders based on slag and fly ash, and effects of accelerated carbonation, *Cem. Concr. Res.* 53 (2013) 127–144. doi:10.1016/j.cemconres.2013.06.007.
- [19] I. Ismail, S.A. Bernal, J.L. Provis, R. San Nicolas, S. Hamdan, J.S.J. Van Deventer, Modification of phase evolution in alkali-activated blast furnace slag by the incorporation of fly ash, *Cem. Concr. Compos.* 45 (2014) 125–135. doi:10.1016/j.cemconcomp.2013.09.006.
- [20] K. Arbi, A. Palomo, A. Fernández-Jiménez, Alkali-activated blends of calcium aluminate cement and slag/diatomite, *Ceram. Int.* 39 (2013) 9237–9245. doi:10.1016/j.ceramint.2013.05.031.
- [21] A. Palomo, M.W. Grutzeck, M.T. Blanco, Alkali-activated fly ashes: A cement for the future, *Cem. Concr. Res.* 29 (1999) 1323–1329. doi:10.1016/S0008-8846(98)00243-9.
- [22] Á. Palomo, S. Alonso, A. Fernandez-Jiménez, I. Sobrados, J. Sanz, Alkaline activation of fly ashes: NMR study of the reaction products, *J. Am. Ceram. Soc.* 87 (2004) 1141–1145. doi:10.1111/j.1551-2916.2004.01141.x.
- [23] M. Heikal, M.Y. Nassar, G. El-Sayed, S.M. Ibrahim, Physico-chemical, mechanical, microstructure and durability characteristics of alkali activated Egyptian slag, *Constr. Build. Mater.* 69 (2014) 60–72. doi:10.1016/j.conbuildmat.2014.07.026.
- [24] S.A. Bernal, J.L. Provis, V. Rose, R. Mejía De Gutierrez, Evolution of binder structure in sodium silicate-activated slag-metakaolin blends, *Cem. Concr. Compos.* 33 (2011) 46–54. doi:10.1016/j.cemconcomp.2010.09.004.
- [25] J. Davidovits, Geopolymers - Inorganic polymeric new materials, *J. Therm. Anal.* 37 (1991) 1633–1656. doi:10.1007/BF01912193.
- [26] J. Davidovits, *Geopolymer Chemistry and Applications*, Inst. Géopolymère; Saint-Quentin, Fr. (2008).

- [27] P. Duxson, G.C. Lukey, F. Separovic, J.S.J. Van Deventer, Effect of alkali cations on aluminum incorporation in geopolymeric gels, *Ind. Eng. Chem. Res.* 44 (2005) 832–839. doi:10.1021/ie0494216.
- [28] P. Duxson, G.C. Lukey, J.S.J. van Deventer, Thermal evolution of metakaolin geopolymers: Part 1 - Physical evolution, *J. Non. Cryst. Solids.* 352 (2006) 5541–5555. doi:10.1016/j.jnoncrysol.2006.09.019.
- [29] P. Duxson, J.L. Provis, G.C. Lukey, F. Separovic, J.S.J. Van Deventer, ²⁹Si NMR study of structural ordering in aluminosilicate geopolymer gels, *Langmuir.* 21 (2005) 3028–3036. doi:10.1021/la047336x.
- [30] J.L. Provis, G.C. Lukey, J.S.J. Van Deventer, Do geopolymers actually contain nanocrystalline zeolites? a reexamination of existing results, *Chem. Mater.* 17 (2005) 3075–3085. doi:10.1021/cm050230i.
- [31] J. Davidovits, *Geopolymer Chemistry and Applications*, Second Ed. Inst. Géopolymère Saint-Quentin, Fr. (2009).
- [32] J.L. Provis, Discussion of C. Li et al., “a review: The comparison between alkali-activated slag (Si + Ca) and metakaolin (Si + Al) cements,” *Cem. Concr. Res.* 40 (2010) 1766–1767. doi:10.1016/j.cemconres.2010.08.005.
- [33] P. Duxson, A. Fernández-Jiménez, J.L. Provis, G.C. Lukey, A. Palomo, J.S.J. Van Deventer, Geopolymer technology: The current state of the art, *J. Mater. Sci.* 42 (2007) 2917–2933. doi:10.1007/s10853-006-0637-z.
- [34] K. Komnitsas, D. Zaharaki, Geopolymerisation: A review and prospects for the minerals industry, *Miner. Eng.* 20 (2007) 1261–1277. doi:10.1016/j.mineng.2007.07.011.
- [35] F. Pacheco-Torgal, J. Castro-Gomes, S. Jalali, Alkali-activated binders: A review. Part 1. Historical background, terminology, reaction mechanisms and hydration products, *Constr. Build. Mater.* 22 (2008) 1305–1314. doi:10.1016/j.conbuildmat.2007.10.015.
- [36] F. Pacheco-Torgal, J. Castro-Gomes, S. Jalali, Alkali-activated binders: A

- review. Part 2. About materials and binders manufacture, *Constr. Build. Mater.* 22 (2008) 1315–1322. doi:10.1016/j.conbuildmat.2007.03.019.
- [37] Z. Zuhua, Y. Xiao, Z. Huajun, C. Yue, Role of water in the synthesis of calcined kaolin-based geopolymer, *Appl. Clay Sci.* 43 (2009) 218–223. doi:10.1016/j.clay.2008.09.003.
- [38] C. Shi, A.F. Jiménez, A. Palomo, New cements for the 21st century: The pursuit of an alternative to Portland cement, *Cem. Concr. Res.* 41 (2011) 750–763. doi:10.1016/j.cemconres.2011.03.016.
- [39] J.S.J. Van Deventer, J.L. Provis, P. Duxson, Technical and commercial progress in the adoption of geopolymer cement, *Miner. Eng.* 29 (2012) 89–104. doi:10.1016/j.mineng.2011.09.009.
- [40] A.M. Rashad, A comprehensive overview about the influence of different admixtures and additives on the properties of alkali-activated fly ash, *Mater. Des.* 53 (2014) 1005–1025. doi:10.1016/j.matdes.2013.07.074.
- [41] J.L. Provis, Geopolymers and other alkali activated materials: Why, how, and what?, *Mater. Struct. Constr.* 47 (2014) 11–25. doi:10.1617/s11527-013-0211-5.
- [42] W.K. Part, M. Ramli, C.B. Cheah, An Overview on the Influence of Various Factors on the Properties of Geopolymer Concrete Derived From Industrial Byproducts, *Handb. Low Carbon Concr.* 77 (2017) 263–334. doi:10.1016/B978-0-12-804524-4.00011-7.
- [43] A. Palomo, P. Krivenko, I. Garcia-Lodeiro, E. Kavalerova, O. Maltseva, A. Fernández-Jiménez, A review on alkaline activation: New analytical perspectives, *Mater. Constr.* 64 (2014). doi:10.3989/mc.2014.00314.
- [44] J.L. Provis, S.A. Bernal, Geopolymers and related alkali-activated materials, *Annu. Rev. Mater. Res.* 44 (2014) 299–327. doi:10.1146/annurev-matsci-070813-113515.
- [45] V.D. Glukhovskiy, *Soil Silicates (in Russ.)*, Gosstroyizdat Kiev, Ukr. (1959).

- [46] N. Granizo, A. Palomo, A. Fernandez-Jimenez, Effect of temperature and alkaline concentration on metakaolin leaching kinetics, *Ceram. Int.* 40 (2014) 8975–8985. doi:10.1016/j.ceramint.2014.02.071.
- [47] Shao-Dong Wang.; Karen L. Scrivener, HYDRATION PRODUCTS OF ALKALI ACTIVATED SLAG CEMENT, *Cem. Concr. Res.* 25 (1995) 561–571. doi:10.1016/j.jmngm.2005.11.005.
- [48] F. Pacheco-Torgal, J. Castro-Gomes, S. Jalali, Alkali-activated binders: A review. Part 1. Historical background, terminology, reaction mechanisms and hydration products, *Constr. Build. Mater.* 22 (2008) 1305–1314. doi:10.1016/j.conbuildmat.2007.10.015.
- [49] S.A. Bernal, R.M. de Gutierrez, J.L. Provis, V. Rose, Effect of silicate modulus and metakaolin incorporation on the carbonation of alkali silicate-activated slags, *Cem. Concr. Res.* 40 (2010) 898–907. doi:10.1016/j.cemconres.2010.02.003.
- [50] S.A. Bernal, R. San Nicolas, R.J. Myers, R. Mejía De Gutiérrez, F. Puertas, J.S.J. Van Deventer, J.L. Provis, MgO content of slag controls phase evolution and structural changes induced by accelerated carbonation in alkali-activated binders, *Cem. Concr. Res.* 57 (2014) 33–43. doi:10.1016/j.cemconres.2013.12.003.
- [51] A.E. Morandau, C.E. White, Role of Magnesium-Stabilized Amorphous Calcium Carbonate in Mitigating the Extent of Carbonation in Alkali-Activated Slag, *Chem. Mater.* 27 (2015) 6625–6634. doi:10.1021/acs.chemmater.5b02382.
- [52] H.A. Khan, M.S.H. Khan, A. Castel, J. Sunarho, Deterioration of alkali-activated mortars exposed to natural aggressive sewer environment, *Constr. Build. Mater.* 186 (2018) 577–597. doi:10.1016/j.conbuildmat.2018.07.137.
- [53] C. Shi, X. Wu, M. Tang, Hydration of alkali-slag cements at 150°C, *Cem. Concr. Res.* 21 (1991) 91–100. doi:10.1016/0008-8846(91)90035-G.
- [54] S.A. Bernal, J.L. Provis, D.G. Brice, A. Kilcullen, P. Duxson, J.S.J. Van

- Deventer, Accelerated carbonation testing of alkali-activated binders significantly underestimates service life: The role of pore solution chemistry, *Cem. Concr. Res.* 42 (2012) 1317–1326. doi:10.1016/j.cemconres.2012.07.002.
- [55] S.A. Bernal, J.L. Provis, B. Walkley, R. San Nicolas, J.D. Gehman, D.G. Brice, A.R. Kilcullen, P. Duxson, J.S.J. Van Deventer, Gel nanostructure in alkali-activated binders based on slag and fly ash, and effects of accelerated carbonation, *Cem. Concr. Res.* 53 (2013) 127–144. doi:10.1016/j.cemconres.2013.06.007.
- [56] M. Ben Haha, G. Le Saout, F. Winnefeld, B. Lothenbach, Influence of activator type on hydration kinetics, hydrate assemblage and microstructural development of alkali activated blast-furnace slags, *Cem. Concr. Res.* 41 (2011) 301–310. doi:10.1016/J.CEMCONRES.2010.11.016.
- [57] M. Ben Haha, B. Lothenbach, G. Le Saout, F. Winnefeld, Influence of slag chemistry on the hydration of alkali-activated blast-furnace slag - Part II: Effect of Al₂O₃, *Cem. Concr. Res.* 42 (2012) 74–83. doi:10.1016/j.cemconres.2011.08.005.
- [58] G. Le Saout, M. Ben Haha, B. Lothenbach, G. Le Saout, F. Winnefeld, Influence of Slag Chemistry on the Hydration of Alkali-Activated Blast-Furnace Slag-Part I: Effect of MgO, (2011). doi:10.1016/j.cemconres.2011.05.002.
- [59] S.A. Bernal, J.L. Provis, V. Rose, R.M. De Gutiérrez, High-resolution X-ray diffraction and fluorescence microscopy characterization of alkali-activated slag-metakaolin binders, *J. Am. Ceram. Soc.* 96 (2013) 1951–1957. doi:10.1111/jace.12247.
- [60] M. Ben Haha, B. Lothenbach, G. Le Saout, F. Winnefeld, Influence of slag chemistry on the hydration of alkali-activated blast-furnace slag — Part I: Effect of MgO, *Cem. Concr. Res.* 41 (2011) 955–963. doi:10.1016/J.CEMCONRES.2011.05.002.

- [61] Á. Palomo, S. Alonso, A. Fernández-Jiménez, I. Sobrados, J. Sanz, Alkaline activation of fly ashes: NMR study of the reaction products, *J. Am. Ceram. Soc.* 87 (2004) 1141–1145. doi:10.1111/j.1551-2916.2004.01141.x.
- [62] Y. Ma, J. Hu, G. Ye, The effect of activating solution on the mechanical strength, reaction rate, mineralogy, and microstructure of alkali-activated fly ash, *J. Mater. Sci.* 47 (2012) 4568–4578. doi:10.1007/s10853-012-6316-3.
- [63] T. Bakharev, Thermal behaviour of geopolymers prepared using class F fly ash and elevated temperature curing, *Cem. Concr. Res.* 36 (2006) 1134–1147. doi:10.1016/j.cemconres.2006.03.022.
- [64] A. Fernández-Jiménez, A. Palomo, M. Criado, Microstructure development of alkali-activated fly ash cement: a descriptive model, *Cem. Concr. Res.* 35 (2005) 1204–1209. doi:10.1016/j.cemconres.2004.08.021.
- [65] M. Criado, A. Fernández-Jiménez, A.G. de la Torre, M.A.G. Aranda, A. Palomo, An XRD study of the effect of the $\text{SiO}_2/\text{Na}_2\text{O}$ ratio on the alkali activation of fly ash, *Cem. Concr. Res.* 37 (2007) 671–679. doi:10.1016/J.CEMCONRES.2007.01.013.
- [66] G. Kovalchuk, A. Fernández-Jiménez, A. Palomo, Alkali-activated fly ash: Effect of thermal curing conditions on mechanical and microstructural development - Part II, *Fuel.* 86 (2007) 315–322. doi:10.1016/j.fuel.2006.07.010.
- [67] A. Fernandez-Jimenez, I. García-Lodeiro, A. Palomo, Durability of alkali-activated fly ash cementitious materials, *J. Mater. Sci.* 42 (2007) 3055–3065. doi:10.1007/s10853-006-0584-8.
- [68] E. Álvarez-Ayuso, X. Querol, F. Plana, A. Alastuey, N. Moreno, M. Izquierdo, O. Font, T. Moreno, S. Diez, E. Vázquez, M. Barra, Environmental, physical and structural characterisation of geopolymer matrixes synthesised from coal (co-)combustion fly ashes, *J. Hazard. Mater.* 154 (2008) 175–183. doi:10.1016/j.jhazmat.2007.10.008.
- [69] J. Temuujin, A. van Riessen, Effect of fly ash preliminary calcination on the

- properties of geopolymer, *J. Hazard. Mater.* 164 (2009) 634–639. doi:10.1016/j.jhazmat.2008.08.065.
- [70] J. Temuujin, A. van Riessen, R. Williams, Influence of calcium compounds on the mechanical properties of fly ash geopolymer pastes, *J. Hazard. Mater.* 167 (2009) 82–88. doi:10.1016/j.jhazmat.2008.12.121.
- [71] J.E. Oh, P.J.M. Monteiro, S.S. Jun, S. Choi, S.M. Clark, The evolution of strength and crystalline phases for alkali-activated ground blast furnace slag and fly ash-based geopolymers, *Cem. Concr. Res.* 40 (2010) 189–196. doi:10.1016/J.CEMCONRES.2009.10.010.
- [72] Z. Sun, A. Vollpracht, One year geopolymerisation of sodium silicate activated fly ash and metakaolin geopolymers, *Cem. Concr. Compos.* 95 (2019) 98–110. doi:10.1016/j.cemconcomp.2018.10.014.
- [73] Z. Zhang, H. Wang, J.L. Provis, F. Bullen, A. Reid, Y. Zhu, Quantitative kinetic and structural analysis of geopolymers. Part 1. The activation of metakaolin with sodium hydroxide, *Thermochim. Acta.* 539 (2012) 23–33. doi:10.1016/J.TCA.2012.03.021.
- [74] Z. Zhang, J.L. Provis, H. Wang, F. Bullen, A. Reid, Quantitative kinetic and structural analysis of geopolymers. Part 2. Thermodynamics of sodium silicate activation of metakaolin, *Thermochim. Acta.* 565 (2013) 163–171. doi:10.1016/j.tca.2013.01.040.
- [75] R.A. Fletcher, K.J.D. MacKenzie, C.L. Nicholson, S. Shimada, The composition range of aluminosilicate geopolymers, *J. Eur. Ceram. Soc.* 25 (2005) 1471–1477. doi:10.1016/J.JEURCERAMSOC.2004.06.001.
- [76] A. Fernández-Jiménez, M. Monzó, M. Vicent, A. Barba, A. Palomo, Alkaline activation of metakaolin–fly ash mixtures: Obtain of Zeoceramics and Zeocements, *Microporous Mesoporous Mater.* 108 (2008) 41–49. doi:10.1016/J.MICROMESO.2007.03.024.
- [77] P. Duxson, G.C. Lukey, J.S.J. van Deventer, Thermal evolution of metakaolin geopolymers: Part 1 - Physical evolution, *J. Non. Cryst. Solids.* 352 (2006)

5541–5555. doi:10.1016/j.jnoncrysol.2006.09.019.

- [78] P. Duxson, G.C. Lukey, J.S.J. van Deventer, The thermal evolution of metakaolin geopolymers: Part 2 – Phase stability and structural development, *J. Non. Cryst. Solids.* 353 (2007) 2186–2200. doi:10.1016/J.JNONCRY SOL.2007.02.050.
- [79] C.K. Yip, J.S.J. Van Deventer, Microanalysis of calcium silicate hydrate gel formed within a geopolymeric binder, *J. Mater. Sci.* 38 (2003) 3851–3860. doi:10.1023/A:1025904905176.
- [80] S.A. Bernal, J.L. Provis, V. Rose, R. Mejía de Gutierrez, Evolution of binder structure in sodium silicate-activated slag-metakaolin blends, *Cem. Concr. Compos.* 33 (2011) 46–54. doi:10.1016/J.CEMCONCOMP.2010.09.004.
- [81] S.A. Bernal, J.L. Provis, V. Rose, R. Mejía De Gutierrez, Evolution of binder structure in sodium silicate-activated slag-metakaolin blends, *Cem. Concr. Compos.* 33 (2011) 46–54. doi:10.1016/j.cemconcomp.2010.09.004.
- [82] Z. Shi, C. Shi, J. Zhang, S. Wan, Z. Zhang, Z. Ou, Alkali-silica reaction in waterglass-activated slag mortars incorporating fly ash and metakaolin, *Cem. Concr. Res.* 108 (2018) 10–19. doi:10.1016/J.CEMCONRES.2018.03.002.
- [83] S. Ukritnukun, P. Koshy, A. Rawal, A. Castel, C.C. Sorrell, Predictive model of setting times and compressive strengths for low-alkali, ambient-cured, fly ash/slag-based geopolymers, *Minerals.* 10 (2020) 1–21. doi:10.3390/min10100920.
- [84] F. Puertas, A. Fernández-Jiménez, Mineralogical and microstructural characterisation of alkali-activated fly ash/slag pastes, *Cem. Concr. Compos.* 25 (2003) 287–292. doi:10.1016/S0958-9465(02)00059-8.
- [85] F.Q. Zhao, W. Ni, H.J. Wang, H.J. Liu, Activated fly ash/slag blended cement, *Resour. Conserv. Recycl.* 52 (2007) 303–313. doi:10.1016/j.resconrec.2007.04.002.
- [86] Z. Zhang, J.L. Provis, A. Reid, H. Wang, Fly ash-based geopolymers: The

- relationship between composition, pore structure and efflorescence, *Cem. Concr. Res.* 64 (2014) 30–41. doi:10.1016/j.cemconres.2014.06.004.
- [87] S.M. Park, J.G. Jang, N.K. Lee, H.K. Lee, Physicochemical properties of binder gel in alkali-activated fly ash/slag exposed to high temperatures, *Cem. Concr. Res.* 89 (2016) 72–79. doi:10.1016/j.cemconres.2016.08.004.
- [88] Z. Pan, Z. Tao, Y.F. Cao, R. Wuhler, T. Murphy, Compressive strength and microstructure of alkali-activated fly ash/slag binders at high temperature, *Cem. Concr. Compos.* 86 (2018) 9–18. doi:10.1016/j.cemconcomp.2017.09.011.
- [89] Y. Zuo, M. Nedeljković, G. Ye, Pore solution composition of alkali-activated slag/fly ash pastes, *Cem. Concr. Res.* 115 (2019) 230–250. doi:10.1016/j.cemconres.2018.10.010.
- [90] A.F. Abdalqader, F. Jin, A. Al-Tabbaa, Development of greener alkali-activated cement: Utilisation of sodium carbonate for activating slag and fly ash mixtures, *J. Clean. Prod.* 113 (2016) 66–75. doi:10.1016/j.jclepro.2015.12.010.
- [91] S.A. Bernal, J.L. Provis, R.J. Myers, R. San Nicolas, J.S.J. van Deventer, Role of carbonates in the chemical evolution of sodium carbonate-activated slag binders, *Mater. Struct. Constr.* 48 (2014) 517–529. doi:10.1617/s11527-014-0412-6.
- [92] R.S. Nicolas, J.L. Provis, S.A. Bernal, J.S.J. van Deventer, Alkali-activated slag cements produced with a blended sodium carbonate/sodium silicate activator, *Adv. Cem. Res.* 28 (2015) 1–12. doi:10.1680/adcr.15.00013.
- [93] M. Alexander, A. Bertron, N. De Belie, Performance of Cement-Based Materials in Aggressive Aqueous Environments, in: *RILEM State-of-the-Art Reports 10*, Springer, New York, 2013: p. 462.
- [94] M.G.D. Gutiérrez-Padilla, A. Bielefeldt, S. Ovtchinnikov, M. Hernandez, J. Silverstein, Biogenic sulfuric acid attack on different types of commercially produced concrete sewer pipes, *Cem. Concr. Res.* 40 (2010) 293–301. doi:10.1016/j.cemconres.2009.10.002.

- [95] Z. Baščarević, The resistance of alkali-activated cement-based binders to chemical attack. In *Handbook of Alkali-Activated Cements, Mortars and Concretes*, Woodhead Publ. Ser. Civ. Struct. Eng. No. 54; Elsevier Amsterdam, 2015; (n.d.).
- [96] S.A. Bernal, E.D. Rodríguez, R.M. de Gutiérrez, J.L. Provis, Performance of alkali-activated slag mortars exposed to acids, *J. Sustain. Cem. Mater.* 1 (2012) 138–151. doi:10.1080/21650373.2012.747235.
- [97] A. Allahverdi, F. Škvára, Sulfuric acid attack on hardened paste of geopolymer cements part 1. Mechanism of corrosion at relatively high concentrations, *Ceram. - Silikaty.* 49 (2005) 225–229.
- [98] K. Arbi, M. Nedeljković, Y. Zuo, G. Ye, A Review on the Durability of Alkali-Activated Fly Ash/Slag Systems: Advances, Issues, and Perspectives, *Ind. Eng. Chem. Res.* 55 (2016) 5439–5453. doi:10.1021/acs.iecr.6b00559.
- [99] I. Ismail, S.A. Bernal, J.L. Provis, S. Hamdan, J.S.J. Van Deventer, Microstructural changes in alkali activated fly ash/slag geopolymers with sulfate exposure, *Mater. Struct. Constr.* 46 (2013) 361–373. doi:10.1617/s11527-012-9906-2.
- [100] J. Marchand, I. Odler, J.P. Skalny, Sulfate Attack on Concrete, *Sulfate Attack Concr.* 32 (2001). doi:10.4324/9780203301623.
- [101] L. Guo, Y. Wu, F. Xu, X. Song, J. Ye, P. Duan, Z. Zhang, Sulfate resistance of hybrid fiber reinforced metakaolin geopolymer composites, *Compos. Part B Eng.* 183 (2020) 107689. doi:10.1016/j.compositesb.2019.107689.
- [102] S.A. Bernal, J.L. Provis, Durability of alkali-activated materials: Progress and perspectives, *J. Am. Ceram. Soc.* 97 (2014) 997–1008. doi:10.1111/jace.12831.
- [103] H. Zhu, S. Yang, W. Li, Z. Li, J. Fan, Z. Shen, Study of mechanical properties and durability of alkali-activated coal gangue-slag concrete, *Materials (Basel).* 13 (2020) 1–20. doi:10.3390/ma13235576.
- [104] I. Ismail, S.A. Bernal, J.L. Provis, R. San Nicolas, D.G. Brice, A.R. Kilcullen,

- S. Hamdan, J.S.J. Van Deventer, Influence of fly ash on the water and chloride permeability of alkali-activated slag mortars and concretes, *Constr. Build. Mater.* 48 (2013) 1187–1201. doi:10.1016/j.conbuildmat.2013.07.106.
- [105] H. Zhu, Z. Zhang, Y. Zhu, L. Tian, Durability of alkali-activated fly ash concrete: Chloride penetration in pastes and mortars, *Constr. Build. Mater.* 65 (2014) 51–59. doi:10.1016/j.conbuildmat.2014.04.110.
- [106] T. Yang, X. Yao, Z. Zhang, Quantification of chloride diffusion in fly ash-slag-based geopolymers by X-ray fluorescence (XRF), *Constr. Build. Mater.* 69 (2014) 109–115. doi:10.1016/j.conbuildmat.2014.07.031.
- [107] T. Bakharev, J. Sanjayan, Y.-B. Cheng, Resistance of alkali-activated slag concrete to carbonation, *Cem. Concr. Res.* 31 (2001) 1277–1283. doi:10.1016/S0008-8846(01)00574-9.
- [108] S.A. Bernal, J.L. Provis, D.G. Brice, A. Kilcullen, P. Duxson, J.S.J. Van Deventer, Accelerated carbonation testing of alkali-activated binders significantly underestimates service life: The role of pore solution chemistry, *Cem. Concr. Res.* 42 (2012) 1317–1326. doi:10.1016/j.cemconres.2012.07.002.
- [109] F. Puertas, M. Palacios, T. Vázquez, Carbonation process of alkali-activated slag mortars, *J. Mater. Sci.* 41 (2005) 3071–3082. doi:10.1007/s10853-005-1821-2.
- [110] M. Palacios, F. Puertas, Effect of carbonation on alkali-activated slag paste, *J. Am. Ceram. Soc.* 89 (2006) 3211–3221. doi:10.1111/j.1551-2916.2006.01214.x.
- [111] M. Fernández Bertos, S.J.R. Simons, C.D. Hills, P.J. Carey, A review of accelerated carbonation technology in the treatment of cement-based materials and sequestration of CO₂, *J. Hazard. Mater.* 112 (2004) 193–205. doi:10.1016/j.jhazmat.2004.04.019.
- [112] E. Rodriguez, S. Bernal, R.M. de Gutierrez, F. Puertas, Alternative concrete based on alkali-activated slag, *Mater. Construcción.* 58 (2008) 53–67.

- [113] S.A. Bernal, R.M. de Gutierrez, J.L. Provis, Engineering and durability properties of concretes based on alkali-activated granulated blast furnace slag/metakaolin blends, *Constr. Build. Mater.* 33 (2012) 99–108. doi:10.1016/j.conbuildmat.2012.01.017.
- [114] S.A. Bernal, R. San Nicolas, R.J. Myers, R. Mejía De Gutiérrez, F. Puertas, J.S.J. Van Deventer, J.L. Provis, MgO content of slag controls phase evolution and structural changes induced by accelerated carbonation in alkali-activated binders, *Cem. Concr. Res.* 57 (2014) 33–43. doi:10.1016/j.cemconres.2013.12.003.
- [115] S.A. Bernal, R. San Nicolas, J.L. Provis, R. Mejía De Gutiérrez, J.S.J. Van Deventer, Natural carbonation of aged alkali-activated slag concretes, *Mater. Struct. Constr.* 47 (2014) 693–707. doi:10.1617/s11527-013-0089-2.
- [116] B. Walkley, R. San Nicolas, M.A. Sani, S.A. Bernal, J.S.J. van Deventer, J.L. Provis, Structural evolution of synthetic alkali-activated CaO-MgO-Na₂O-Al₂O₃-SiO₂ materials is influenced by Mg content, *Cem. Concr. Res.* 99 (2017) 155–171. doi:10.1016/j.cemconres.2017.05.006.
- [117] K. Pasupathy, M. Berndt, A. Castel, J. Sanjayan, R. Pathmanathan, Carbonation of a blended slag-fly ash geopolymer concrete in field conditions after 8 years, *Constr. Build. Mater.* 125 (2016) 661–669. doi:10.1016/j.conbuildmat.2016.08.078.
- [118] P. Duan, C. Yan, W. Luo, W. Zhou, Effects of adding nano-TiO₂ on compressive strength, drying shrinkage, carbonation and microstructure of fluidized bed fly ash based geopolymer paste, *Constr. Build. Mater.* 106 (2016) 115–125. doi:10.1016/j.conbuildmat.2015.12.095.
- [119] K. Behfarnia, M. Rostami, An assessment on parameters affecting the carbonation of alkali-activated slag concrete, *J. Clean. Prod.* 157 (2017) 1–9. doi:10.1016/j.jclepro.2017.04.097.
- [120] J.G. Jang, S.M. Park, G.M. Kim, H.K. Lee, Stability of MgO-modified geopolymeric gel structure exposed to a CO₂-rich environment, *Constr. Build.*

Mater. 151 (2017) 178–185. doi:10.1016/j.conbuildmat.2017.06.088.

- [121] M. Nedeljković, B. Šavija, Y. Zuo, M. Luković, G. Ye, Effect of natural carbonation on the pore structure and elastic modulus of the alkali-activated fly ash and slag pastes, *Constr. Build. Mater.* 161 (2018) 687–704. doi:10.1016/j.conbuildmat.2017.12.005.
- [122] M. Sufian Badar, K. Kupwade-Patil, S.A. Bernal, J.L. Provis, E.N. Allouche, Corrosion of steel bars induced by accelerated carbonation in low and high calcium fly ash geopolymer concretes, *Constr. Build. Mater.* 61 (2014) 79–89. doi:10.1016/j.conbuildmat.2014.03.015.
- [123] J. DEJA, Carbonation aspects of alkali activated slag mortars and concretes, *Silic. Ind.* 67 (2002) 37–42.
- [124] S.A. Bernal, Effect of the activator dose on the compressive strength and accelerated carbonation resistance of alkali silicate-activated slag/metakaolin blended materials, *Constr. Build. Mater.* 98 (2015) 217–226. doi:10.1016/j.conbuildmat.2015.08.013.
- [125] S.A. Bernal, R.M. de Gutierrez, J.L. Provis, V. Rose, Effect of silicate modulus and metakaolin incorporation on the carbonation of alkali silicate-activated slags, *Cem. Concr. Res.* 40 (2010) 898–907. doi:10.1016/j.cemconres.2010.02.003.
- [126] J.H.M. Visser, Influence of the carbon dioxide concentration on the resistance to carbonation of concrete, *Constr. Build. Mater.* 67 (2014) 8–13. doi:10.1016/j.conbuildmat.2013.11.005.
- [127] H.Z. Cui, W.C. Tang, W. Liu, Z.J. Dong, F. Xing, Experimental study on effects of CO₂ concentrations on concrete carbonation and diffusion mechanisms, *Constr. Build. Mater.* 93 (2015) 522–527. doi:10.1016/j.conbuildmat.2015.06.007.
- [128] A. Leemann, F. Moro, Carbonation of concrete: the role of CO₂ concentration, relative humidity and CO₂ buffer capacity, *Mater. Struct.* 50 (2016). doi:10.1617/s11527-016-0917-2.

- [129] M. Cyr, R. Pouhet, Carbonation in the pore solution of metakaolin-based geopolymer, *Cem. Concr. Res.* 88 (2016) 227–235. doi:10.1016/j.cemconres.2016.05.008.
- [130] S.A. Bernal, J.L. Provis, R. Mejía de Gutiérrez, J.S.J. van Deventer, Accelerated carbonation testing of alkali-activated slag/metakaolin blended concretes: effect of exposure conditions, *Mater. Struct. Constr.* 48 (2014) 653–669. doi:10.1617/s11527-014-0289-4.
- [131] S.A. Bernal, J.L. Provis, R. Mejía de Gutiérrez, J.S.J. van Deventer, Accelerated carbonation testing of alkali-activated slag/metakaolin blended concretes: effect of exposure conditions, *Mater. Struct. Constr.* 48 (2014) 653–669. doi:10.1617/s11527-014-0289-4.
- [132] Y.F. Houst, The role of moisture in the carbonation of cementitious materials, *Int. J. Restor. Build. Monum.* 2 (1996) 49–66. http://infoscience.epfl.ch/record/29446/files/I_J_Rest_Buildg_96.pdf.
- [133] Y.F. Houst, F.H. Wittmann, Influence of porosity and water content on the diffusivity of CO₂ and O₂ through hydrated cement paste, *Cem. Concr. Res.* 24 (1994) 1165–1176. doi:10.1016/0008-8846(94)90040-X.
- [134] V.G. Papadakis, C.G. Vayenas, M.N. Fardis, Experimental investigation and mathematical modeling of the concrete carbonation problem, *Chem. Eng. Sci.* 46 (1991) 1333–1338. doi:10.1016/0009-2509(91)85060-B.
- [135] I. Galan, C. Andrade, M. Castellote, Natural and accelerated CO₂ binding kinetics in cement paste at different relative humidities, *Cem. Concr. Res.* 49 (2013) 21–28. doi:10.1016/j.cemconres.2013.03.009.
- [136] B. Lagerblad, Carbon dioxide uptake during concrete life cycle—state of the art, Swedish Cement and Concrete Research Institute, CBI, n.d.
- [137] S.A. Bernal, J.L. Provis, Durability of alkali-activated materials: Progress and perspectives, *J. Am. Ceram. Soc.* 97 (2014) 997–1008. doi:10.1111/jace.12831.
- [138] E. Dubina, L. Korat, L. Black, J. Strupi-Suput, J. Plank, Influence of water

- vapour and carbon dioxide on free lime during storage at 80 degrees C, studied by Raman spectroscopy, *Spectrochim Acta A Mol Biomol Spectrosc.* 111 (2013) 299–303. doi:10.1016/j.saa.2013.04.033.
- [139] C. Shi, Corrosion resistance of alkali-activated slag cement, *Adv. Cem. Res.* 15 (n.d.) 77–81.
- [140] M. Criado, A. Fernández-Jiménez, A. Palomo, Alkali activation of fly ash. Part III: Effect of curing conditions on reaction and its graphical description, *Fuel.* 89 (2010) 3185–3192. doi:10.1016/j.fuel.2010.03.051.
- [141] Saloni, Parveen, Y. Yan Lim, T.M. Pham, Influence of Portland cement on performance of fine rice husk ash geopolymer concrete: Strength and permeability properties, *Constr. Build. Mater.* 300 (2021) 124321. doi:10.1016/j.conbuildmat.2021.124321.
- [142] A. Noushini, A. Castel, The effect of heat-curing on transport properties of low-calcium fly ash-based geopolymer concrete, *Constr. Build. Mater.* 112 (2016) 464–477. doi:10.1016/j.conbuildmat.2016.02.210.
- [143] S.A. Materials, Stanford Advanced Materials, (n.d.). <http://www.samaterials.com>.
- [144] T. Tho-In, V. Sata, P. Chindaprasirt, C. Jaturapitakkul, Pervious high-calcium fly ash geopolymer concrete, *Constr. Build. Mater.* 30 (2012) 366–371. doi:10.1016/j.conbuildmat.2011.12.028.
- [145] Z. Sun, X. Lin, A. Vollpracht, Pervious concrete made of alkali activated slag and geopolymers, *Constr. Build. Mater.* 189 (2018) 797–803. doi:10.1016/j.conbuildmat.2018.09.067.
- [146] M.S. Seungmin Kang, Kyungnam Kim, Sol-A Bak, Properties of ion leaching of alkali-activated blast furnace slag at early hydration, *Adv. Cem. Res.* 28 (2015) 151–157. doi:10.1017/CBO9781107415324.004.
- [147] S. Park, H.N. Yoon, J. Seo, H.K. Lee, J.G. Jang, Structural evolution of binder gel in alkali-activated cements exposed to electrically accelerated leaching

- conditions, *J. Hazard. Mater.* 387 (2020) 121825. doi:10.1016/j.jhazmat.2019.121825.
- [148] M.A. Longhi, Z. Zhang, E.D. Rodríguez, A.P. Kirchheim, H. Wang, Efflorescence of alkali-activated cements (geopolymers) and the impacts on material structures: A critical analysis, *Front. Mater.* 6 (2019) 1–13. doi:10.3389/fmats.2019.00089.
- [149] A. Allahverdi, E. Najafi Kani, K.M.A. Hossain, M. Lachemi, Methods to control efflorescence in alkali-activated cement-based materials, in: F. Pacheco-Torgal Labrincha, J. A., Leonelli, C., Palomo, A., Chindaprasirt, P. (Ed.), *Handb. Alkali-Activated Cem. Mortars Concr.*, Woodhead Publishing Series in Civil and Structural Engineering, Elsevier, Amsterdam, 2015: pp. 463–483. doi:10.1533/9781782422884.3.463.
- [150] J. Chwast, J. Todorović, H. Janssen, J. Elsen, Gypsum efflorescence on clay brick masonry: Field survey and literature study, *Constr. Build. Mater.* 85 (2015) 57–64. doi:10.1016/j.conbuildmat.2015.02.094.
- [151] C. Dow, F.P. Glasser, Calcium carbonate efflorescence on Portland cement and building materials, *Cem. Concr. Res.* 33 (2003) 147–154. doi:10.1016/S0008-8846(02)00937-7.
- [152] R.R. Lloyd, J.L. Provis, J.S.J. Van Deventer, Acid resistance of inorganic polymer binders. 1. Corrosion rate, *Mater. Struct. Constr.* 45 (2012) 1–14. doi:10.1617/s11527-011-9744-7.
- [153] F. Škvára, L. Kopecký, L. Myšková, V.Í.T. Šmilauer, L. Alberovská, L. Vinšová, Aluminosilicate polymers - Influence of elevated temperatures, efflorescence, *Ceram. - Silikaty.* 53 (2009) 276–282.
- [154] F. Škvára, V. Šmilauer, P. Hlaváček, L. Kopecký, Z. Cílová, A weak alkali bond in (N, K)-A-S-H gels: Evidence from leaching and modeling, *Ceram. - Silikaty.* 56 (2012) 374–382.
- [155] X. Yao, T. Yang, Z. Zhang, Compressive strength development and shrinkage of alkali-activated fly ash–slag blends associated with efflorescence, *Mater.*

Struct. Constr. 49 (2016) 2907–2918. doi:10.1617/s11527-015-0694-3.

- [156] Z. Zhang, J.L. Provis, H. Wang, Critical thinking on efflorescence in alkali activated cement (AAC), in: D. Fernando Teng, J.-G., Torero, J. L. (Ed.), Proc. Second Int. Conf. Performance-Based Lifecycle Eng. (PLSE 2015), Brisbane, Australia, 2016: pp. 147–153. doi:10.14264/uql.2016.776.
- [157] F. Pacheco-Torgal, Z. Abdollahnejad, A.F. Camões, M. Jamshidi, Y. Ding, Durability of alkali-activated binders: A clear advantage over Portland cement or an unproven issue?, *Constr. Build. Mater.* 30 (2012) 400–405. doi:10.1016/j.conbuildmat.2011.12.017.
- [158] Z. Zhang, J.L. Provis, X. Ma, A. Reid, H. Wang, Efflorescence and subflorescence induced microstructural and mechanical evolution in fly ash-based geopolymers, *Cem. Concr. Compos.* 92 (2018) 165–177. doi:10.1016/j.cemconcomp.2018.06.010.
- [159] J.L. Provis, J.S.J. van Deventer, Alkali activated materials: State of Art Report, 2014.
- [160] C. Chen, W. Gong, W. Lutze, I.L. Pegg, J. Zhai, Kinetics of fly ash leaching in strongly alkaline solutions, *J. Mater. Sci.* 46 (2011) 590–597. doi:10.1007/s10853-010-4997-z.
- [161] C. Chen, W. Gong, W. Lutze, I.L. Pegg, Kinetics of fly ash geopolymerization, *J. Mater. Sci.* 46 (2010) 3073–3083. doi:10.1007/s10853-010-5186-9.
- [162] M.T. Anderson, N. Lu, Role of Microscopic Physicochemical Forces in Large Volumetric Strains for Clay Sediments, *J. Eng. Mech.* 127 (2001) 710–719. doi:10.1061/(asce)0733-9399(2001)127:7(710).
- [163] D.R. Katti, L. Srinivasamurthy, K.S. Katti, Molecular modeling of initiation of interlayer swelling in Na-montmorillonite expansive clay, *Can. Geotech. J.* 52 (2015). doi:10.1139/cgj-2014-0309.
- [164] H. Manzano, R.J. Pellenq, F.J. Ulm, M.J. Buehler, A.C. van Duin, Hydration of calcium oxide surface predicted by reactive force field molecular dynamics,

Langmuir. 28 (2012) 4187–4197. doi:10.1021/la204338m.

- [165] L. Liu, A. Jaramillo-Botero, W.A. Goddard 3rd, H. Sun, Development of a ReaxFF reactive force field for ettringite and study of its mechanical failure modes from reactive dynamics simulations, *J Phys Chem A*. 116 (2012) 3918–3925. doi:10.1021/jp210135j.
- [166] D. Hou, C. Hu, Z. Li, Molecular Simulation of the Ions Ultraconfined in the Nanometer-Channel of Calcium Silicate Hydrate: Hydration Mechanism, Dynamic Properties, and Influence on the Cohesive Strength, *Inorg Chem*. 56 (2017) 1881–1896. doi:10.1021/acs.inorgchem.6b02456.
- [167] L.Y. Xu, Y. Alrefaei, Y.S. Wang, J.G. Dai, Recent advances in molecular dynamics simulation of the N-A-S-H geopolymer system: modeling, structural analysis, and dynamics, *Constr. Build. Mater*. 276 (2021) 122196. doi:10.1016/j.conbuildmat.2020.122196.
- [168] M.R. Sadat, S. Bringuier, K. Muralidharan, G. Frantziskonis, L. Zhang, Atomic-scale dynamics and mechanical response of geopolymer binder under nanoindentation, *Comput. Mater. Sci*. 142 (2018) 227–236. doi:10.1016/j.commatsci.2017.10.026.
- [169] M.R. Sadat, K. Muralidharan, L. Zhang, Reactive molecular dynamics simulation of the mechanical behavior of sodium aluminosilicate geopolymer and calcium silicate hydrate composites, *Comput. Mater. Sci*. 150 (2018) 500–509. doi:10.1016/j.commatsci.2018.04.041.
- [170] V.D. Glukhovskiy, *Alkaline and Alkaline-Alkali-Earth Hydraulic Binders and Concretes* (in Russ.), Ysscha Shkola Publ. Kiev, USSR. (1979).
- [171] ASTM C618-19, Standard Specification for Coal Fly Ash and Raw or Calcined Natural Pozzolan for Use in Concrete, ASTM International, West Conshohocken, PA, 2019, www.astm.org, (n.d.).
- [172] A. Standard, ASTM D 3987, Standard Test Method for Shake Extraction of Solid Waste With Water, American Society for Testing and Materials, W. Conshohocken, PA, 1985., (1985).

- [173] A. Standard, ASTM E1908-16, Standard Guide for Sample Selection of Debris Waste from a Building Renovation or Lead Abatement Project for Toxicity Characteristic Leaching Procedure (TCLP) Testing for Leachable Lead (Pb), ASTM International, West Conshohocken, PA, 2016, (2016).
- [174] N. Li, C. Shi, Q. Wang, Z. Zhang, Z. Ou, Composition design and performance of alkali-activated cements, *Mater. Struct. Constr.* 50 (2017). doi:10.1617/s11527-017-1048-0.
- [175] Z. Zhang, J.L. Provis, A. Reid, H. Wang, Fly ash-based geopolymers: The relationship between composition, pore structure and efflorescence, *Cem. Concr. Res.* 64 (2014) 30–41. doi:10.1016/j.cemconres.2014.06.004.
- [176] J.C. Phillips, K. Schulten, A. Bhatele, C. Mei, Y. Sun, E.J. Bohm, L. V. Kale, Scalable molecular dynamics with NAMD, *Parallel Sci. Eng. Appl. Charm++ Approach.* 26 (2016) 60–76. doi:10.1201/b16251-15.
- [177] 2009. Gaussian 09, Revision E.01, Frisch, M. J.; Trucks, G. W.; Schlegel, H. B.; Scuseria, G. E.; Robb, M. A.; Cheeseman, J. R.; Scalmani, G.; Barone, V.; Mennucci, B.; Petersson, G. A.; Nakatsuji, H.; Caricato, M.; Li, X.; Hratchian, H. P.; Izmaylov, A. F.; Bl, Gaussian 09, (n.d.).
- [178] W. Humphrey, A. Dalke, K. Schulten, VMD: Visual molecular dynamics, *J. Mol. Graph.* 14 (1996) 33–38. doi:10.1016/0263-7855(96)00018-5.
- [179] P. Duxson, J.L. Provis, G.C. Lukey, J.S.J. Van Deventer, The role of inorganic polymer technology in the development of “green concrete,” *Cem. Concr. Res.* 37 (2007) 1590–1597. doi:10.1016/j.cemconres.2007.08.018.
- [180] M. Palacios, P.F.G. Banfill, F. Puertas, Rheology and setting of alkali-activated slag pastes and mortars: Effect if organic admixture, *ACI Mater. J.* 105 (2008) 140–148. doi:10.14359/19754.
- [181] Z. Luo, W. Li, Y. Gan, K. Mendu, S.P. Shah, Maximum likelihood estimation for nanoindentation on sodium aluminosilicate hydrate gel of geopolymer under different silica modulus and curing conditions, *Compos. Part B Eng.* 198 (2020) 108185. doi:https://doi.org/10.1016/j.compositesb.2020.108185.

- [182] F. Pacheco-Torgal, S. Jalali, Influence of sodium carbonate addition on the thermal reactivity of tungsten mine waste mud based binders, *Constr. Build. Mater.* 24 (2010) 56–60. doi:10.1016/J.CONBUILDMAT.2009.08.018.
- [183] M.A. Longhi, E.D. Rodríguez, B. Walkley, Z. Zhang, A.P. Kirchheim, Metakaolin-based geopolymers: Relation between formulation, physicochemical properties and efflorescence formation, *Compos. Part B Eng.* 182 (2020). doi:10.1016/j.compositesb.2019.107671.
- [184] Z. Zhang, H. Wang, J.L. Provis, Quantitative study of the reactivity of fly ash in geopolymerization by ftir, *J. Sustain. Cem. Mater.* 1 (2012) 154–166. doi:10.1080/21650373.2012.752620.
- [185] ASTM International, ASTM D7072-04(2019), Standard Practice for Evaluating Accelerated Efflorescence of Latex Coatings, (2019).
- [186] T.L. Weng, W.T. Lin, A. Cheng, Effect of metakaolin on strength and efflorescence quantity of cement-based composites, *Sci. World J.* 2013 (2013). doi:10.1155/2013/606524.
- [187] K. Ellis, R. Silvestrini, B. Varela, N. Alharbi, R. Hailstone, Modeling setting time and compressive strength in sodium carbonate activated blast furnace slag mortars using statistical mixture design, *Cem. Concr. Compos.* 74 (2016) 1–6. doi:10.1016/j.cemconcomp.2016.08.008.
- [188] T. Luukkonen, H. Sreenivasan, Z. Abdollahnejad, J. Yliniemi, A. Kantola, V.V. Telkki, P. Kinnunen, M. Illikainen, Influence of sodium silicate powder silica modulus for mechanical and chemical properties of dry-mix alkali-activated slag mortar, *Constr. Build. Mater.* 233 (2020) 117354. doi:10.1016/j.conbuildmat.2019.117354.
- [189] Standards Australia, AS1012.9:2014 Methods of testing concrete Method 9: Compressive strength tests — Concrete, mortar and grout specimens, Stand. Aust. Int. Ltd, Sydney. (2014) 1–13.
- [190] Australian Standard, AS 1012.10 Determination of indirect tensile strength of concrete cylinders (“Brazil” or splitting test), 2000 (2000).

- [191] S.A. Bernal, R. San Nicolas, J.S.J. Van Deventer, J.L. Provis, Alkali-activated slag cements produced with a blended sodium carbonate/sodium silicate activator, *Adv. Cem. Res.* 28 (2016) 262–273. doi:10.1680/jadcr.15.00013.
- [192] S. Kumar, R. Kumar, S.P. Mehrotra, Influence of granulated blast furnace slag on the reaction, structure and properties of fly ash based geopolymer, *J. Mater. Sci.* 45 (2010) 607–615. doi:10.1007/s10853-009-3934-5.
- [193] G.W. Scherer, Stress from crystallization of salt, *Cem. Concr. Res.* 34 (2004) 1613–1624. doi:10.1016/J.CEMCONRES.2003.12.034.
- [194] L. Zheng, C. Wang, W. Wang, Y. Shi, X. Gao, Immobilization of MSWI fly ash through geopolymerization: Effects of water-wash, *Waste Manag.* 31 (2011) 311–317. doi:10.1016/J.WASMAN.2010.05.015.
- [195] X. Guo, H. Shi, W.A. Dick, Compressive strength and microstructural characteristics of class C fly ash geopolymer, *Cem. Concr. Compos.* 32 (2010) 142–147. doi:10.1016/j.cemconcomp.2009.11.003.
- [196] T. Bakharev, Geopolymeric materials prepared using Class F fly ash and elevated temperature curing, *Cem. Concr. Res.* 35 (2005) 1224–1232. doi:10.1016/j.cemconres.2004.06.031.
- [197] J.S.J. van Deventer, R.S. Nicolas, I. Ismail, S.A. Bernal, D.G. Brice, J.L. Provis, Microstructure and durability of alkali-activated materials as key parameters for standardization, *J. Sustain. Cem. Mater.* 4 (2014) 116–128. doi:10.1080/21650373.2014.979265.
- [198] E.D. Rodríguez, S.A. Bernal, J.L. Provis, J. Paya, J.M. Monzo, M.V. Borrachero, Effect of nanosilica-based activators on the performance of an alkali-activated fly ash binder, *Cem. Concr. Compos.* 35 (2013) 1–11. doi:10.1016/j.cemconcomp.2012.08.025.
- [199] T. Yang, H. Zhu, Z. Zhang, Influence of fly ash on the pore structure and shrinkage characteristics of metakaolin-based geopolymer pastes and mortars, *Constr. Build. Mater.* 153 (2017) 284–293. doi:10.1016/j.conbuildmat.2017.05.067.

- [200] P. Lu, Q. Li, J. Zhai, Mineralogical characterizations and reaction path modeling of the pozzolanic reaction of fly ash-lime systems, *J. Am. Ceram. Soc.* 91 (2008) 955–964. doi:10.1111/j.1551-2916.2007.02193.x.
- [201] X. Ke, S.A. Bernal, J.L. Provis, Controlling the reaction kinetics of sodium carbonate-activated slag cements using calcined layered double hydroxides, *Cem. Concr. Res.* 81 (2016) 24–37. doi:10.1016/j.cemconres.2015.11.012.
- [202] S.A. Bernal, J.L. Provis, V. Rose, R.M. de Gutierrez, Evolution of binder structure in sodium silicate-activated slag-metakaolin blends, *Cem. Concr. Compos.* 33 (2011) 46–54. doi:10.1016/j.cemconcomp.2010.09.004.
- [203] B. Walkley, A. Kashani, M.A. Sani, T.D. Ngo, P. Mendis, Examination of alkali-activated material nanostructure during thermal treatment, *J. Mater. Sci.* 53 (2018) 9486–9503. doi:10.1007/s10853-018-2270-z.
- [204] R.J. Myers, B. Lothenbach, S.A. Bernal, J.L. Provis, Thermodynamic modelling of alkali-activated slag cements, *Appl. Geochemistry.* 61 (2015) 233–247. doi:10.1016/j.apgeochem.2015.06.006.
- [205] F. Škvára, L. Kopecký, L. Myšková, V.Í.T. Šmilauer, L. Alberovská, L. Vinšová, Aluminosilicate polymers - Influence of elevated temperatures, efflorescence, *Ceram. - Silikaty.* 53 (2009) 276–282.
- [206] B. Walkley, R. San Nicolas, M.A. Sani, G.J. Rees, J. V. Hanna, J.S.J. van Deventer, J.L. Provis, Phase evolution of C-(N)-A-S-H/N-A-S-H gel blends investigated via alkali-activation of synthetic calcium aluminosilicate precursors, *Cem. Concr. Res.* 89 (2016) 120–135. doi:10.1016/j.cemconres.2016.08.010.
- [207] M.R. Rowles, J. V. Hanna, K.J. Pike, M.E. Smith, B.H. O'Connor, ²⁹Si, ²⁷Al, ¹H and ²³Na MAS NMR study of the bonding character in aluminosilicate inorganic polymers, *Appl. Magn. Reson.* 32 (2007) 663–689. doi:10.1007/s00723-007-0043-y.
- [208] A. Fernández-Jiménez, A. Palomo, Nanostructure/microstructure of fly ash geopolymers, *Geopolymers.* (2009) 89–117.

doi:10.1533/9781845696382.1.89.

- [209] V.F.F. Barbosa, K.J.D. MacKenzie, C. Thaumaturgo, Synthesis and characterisation of materials based on inorganic polymers of alumina and silica: Sodium polysialate polymers, *Int. J. Inorg. Mater.* 2 (2000) 309–317. doi:10.1016/S1466-6049(00)00041-6.
- [210] Y. Kim, R. James Kirkpatrick, ²³Na and ¹³³Cs NMR study of cation adsorption on mineral surfaces: Local environments, dynamics, and effects of mixed cations, *Geochim. Cosmochim. Acta.* 61 (1997) 5199–5208. doi:10.1016/S0016-7037(97)00347-5.
- [211] K.S. Getvoldsen, T.E. Butt, C. House, F. Ferreira, Sustainable Development and Climate Change, *World Sustain. Ser.* 38 (2018) 445–457. doi:10.1007/978-3-319-63007-6_27.
- [212] B. Singh, G. Ishwarya, M. Gupta, S.K. Bhattacharyya, Geopolymer concrete: A review of some recent developments, *Constr. Build. Mater.* 85 (2015) 78–90. doi:10.1016/j.conbuildmat.2015.03.036.
- [213] C. Shi, A.F. Jiménez, A. Palomo, New cements for the 21st century: The pursuit of an alternative to Portland cement, *Cem. Concr. Res.* 41 (2011) 750–763. doi:10.1016/j.cemconres.2011.03.016.
- [214] P. Duxson, J.L. Provis, G.C. Lukey, S.W. Mallicoat, W.M. Kriven, J.S.J. Van Deventer, Understanding the relationship between geopolymer composition, microstructure and mechanical properties, *Colloids Surfaces A Physicochem. Eng. Asp.* 269 (2005) 47–58. doi:10.1016/j.colsurfa.2005.06.060.
- [215] A. Fernandez-Jimenez, A. Palomo, I. Sobrados, J. Sanz, The role played by the reactive alumina content in the alkaline activation of fly ashes, *Microporous Mesoporous Mater.* 91 (2006) 111–119. doi:10.1016/j.micromeso.2005.11.015.
- [216] M.R. Rowles, B.H. O'Connor, Chemical and structural microanalysis of aluminosilicate geopolymers synthesized by sodium silicate activation of metakaolinite, *J. Am. Ceram. Soc.* 92 (2009) 2354–2361. doi:10.1111/j.1551-2916.2009.03191.x.

- [217] E. Najafi Kani, A. Allahverdi, J.L. Provis, Efflorescence control in geopolymer binders based on natural pozzolan, *Cem. Concr. Compos.* 34 (2012) 25–33. doi:10.1016/J.CEMCONCOMP.2011.07.007.
- [218] M.A. Longhi, B. Walkley, E.D. Rodríguez, A.P. Kirchheim, Z. Zhang, H. Wang, New selective dissolution process to quantify reaction extent and product stability in metakaolin-based geopolymers, *Compos. Part B Eng.* 176 (2019) 107172. doi:10.1016/j.compositesb.2019.107172.
- [219] H. Wan, L. Yuan, Y. Zhang, Insight Into the Leaching of Sodium Alumino-Silicate Hydrate (N-A-S-H) Gel: A Molecular Dynamics Study, *Front. Mater.* 7 (2020) 1–11. doi:10.3389/fmats.2020.00056.
- [220] J.L. Provis, R.J. Myers, C.E. White, V. Rose, J.S.J. Van Deventer, X-ray microtomography shows pore structure and tortuosity in alkali-activated binders, *Cem. Concr. Res.* 42 (2012) 855–864. doi:10.1016/j.cemconres.2012.03.004.
- [221] J. Xie, J. Wang, R. Rao, C. Wang, C. Fang, Effects of combined usage of GGBS and fly ash on workability and mechanical properties of alkali activated geopolymer concrete with recycled aggregate, *Compos. Part B Eng.* 164 (2019) 179–190. doi:https://doi.org/10.1016/j.compositesb.2018.11.067.
- [222] I. García Lodeiro, A. Fernández-Jimenez, A. Palomo, D. Macphee, Effect on fresh C-S-H gels of the simultaneous addition of alkali and aluminium, *Cem. Concr. Res.* 40 (2010) 27–32. doi:10.1016/J.CEMCONRES.2009.08.004.
- [223] C.K. Yip, G.C. Lukey, J.S.J. Van Deventer, The coexistence of geopolymeric gel and calcium silicate hydrate at the early stage of alkaline activation, *Cem. Concr. Res.* 35 (2005) 1688–1697. doi:10.1016/j.cemconres.2004.10.042.
- [224] B. Qu, A. Martin, J.Y. Pastor, A. Palomo, A. Fernández-Jiménez, Characterisation of pre-industrial hybrid cement and effect of pre-curing temperature, *Cem. Concr. Compos.* 73 (2016) 281–288. doi:10.1016/j.cemconcomp.2016.07.019.
- [225] A. Roy, P.J. Schilling, H.C. Eaton, P.G. Malone, W.N. Brabston, L.D. Wakeley,

- Activation of Ground Blast-Furnace Slag by alkali metal and alkaline earth hydroxides, *J. Am. Ceram. Soc.* 12 (1992) 3233–3240. doi:10.1111/j.1151-2916.1992.tb04416.x.
- [226] G.W. Scherer, Theory of Drying, *J. Am. Ceram. Soc.* 73 (1990) 3–14. doi:10.1111/j.1151-2916.1990.tb05082.x.
- [227] C.A. Rees, J.L. Provis, G.C. Lukey, J.S.J. van Deventer, The mechanism of geopolymer gel formation investigated through seeded nucleation, *Colloids Surfaces A-Physicochemical Eng. Asp.* 318 (2008) 97–105. doi:10.1016/j.colsurfa.2007.12.019.
- [228] I. García-Lodeiro, A. Fernández-Jiménez, M.T. Blanco, A. Palomo, FTIR study of the sol-gel synthesis of cementitious gels: C-S-H and N-A-S-H, *J. Sol-Gel Sci. Technol.* 45 (2008) 63–72. doi:10.1007/s10971-007-1643-6.
- [229] J.W. Phair, J.S.J. Van Deventer, J.D. Smith, Mechanism of polysialation in the incorporation of zirconia into fly ash-based geopolymers, *Ind. Eng. Chem. Res.* 39 (2000) 2925–2934. doi:10.1021/ie990929w.
- [230] A. PALOMO, F. GLASSER, Chemically-bonded cementitious materials based on metakaolin, *Br. Ceram. Trans. J.* 91 (1992) 107–112.
- [231] and X.C. Ping Yu, R. James Kirkpatrick, Brent Poe, Paul F. McMillan, Structure of Calcium Silicate Hydrate (C-S-H): Near-, Mid-, and Far-Infrared Spectroscopy, *J. Am. Ceram. Soc.* 82 (1999) 742–748.
- [232] C.A. Rees, J.L. Provis, G.C. Lukey, J.S.J. Van Deventer, In situ ATR-FTIR study of the early stages of fly ash geopolymer gel formation, *Langmuir.* 23 (2007) 9076–9082. doi:10.1021/la701185g.
- [233] I. Majchrzak-Kuceba, W. Nowak, Thermal analysis of fly ash-based zeolites, *J. Therm. Anal. Calorim.* 77 (2004) 125–131. doi:10.1023/B:JTAN.0000033195.15101.4e.
- [234] C.L. Hwang, D.H. Vo, V.A. Tran, M.D. Yehualaw, Effect of high MgO content on the performance of alkali-activated fine slag under water and air curing

- conditions, *Constr. Build. Mater.* 186 (2018) 503–513. doi:10.1016/j.conbuildmat.2018.07.129.
- [235] F. Jin, K. Gu, A. Al-Tabbaa, Strength and drying shrinkage of reactive MgO modified alkali-activated slag paste, *Constr. Build. Mater.* 51 (2014) 395–404. doi:10.1016/j.conbuildmat.2013.10.081.
- [236] P. Duxson, G.C. Lukey, F. Separovic, J.S.J. Van Deventer, Effect of alkali cations on aluminum incorporation in geopolymeric gels, *Ind. Eng. Chem. Res.* 44 (2005) 832–839. doi:10.1021/ie0494216.
- [237] S.K. Lee, J.F. Stebbins, The distribution of sodium ions in aluminosilicate glasses: a high-field Na-23 MAS and 3Q MAS NMR study, *Geochim. Cosmochim. Acta.* 67 (2003) 1699–1709. doi:10.1016/S0016-7037(03)00026-7.
- [238] M. Criado, A. Fernández-Jiménez, A. Palomo, Alkali activation of fly ash: Effect of the SiO₂/Na₂O ratio: Part I: FTIR study, *Microporous Mesoporous Mater.* 106 (2007) 180–191. doi:10.1016/J.MICROMESO.2007.02.055.
- [239] X. Gao, Q.L. Yu, H.J.H. Brouwers, Apply 29Si, 27Al MAS NMR and selective dissolution in identifying the reaction degree of alkali activated slag-fly ash composites, *Ceram. Int.* 43 (2017) 12408–12419. doi:10.1016/j.ceramint.2017.06.108.
- [240] B. Walkley, J.L. Provis, Solid-state nuclear magnetic resonance spectroscopy of cements, *Mater. Today Adv.* 1 (2019) 100007. doi:10.1016/j.mtadv.2019.100007.
- [241] A. Carvalho, P. Jo, Characterization of Y zeolites dealuminated by solid-state reaction with ammonium hexafluorosilicate, *J Porous Mater.* 13 (2006) 107–114. doi:10.1007/s10934-006-7005-x.
- [242] J.A. Van Bokhoven, A.L. Roest, D.C. Koningsberger, J.T. Miller, G.H. Nachttegaal, A.P.M. Kentgens, Changes in structural and electronic properties of the zeolite framework induced by extraframework Al and Ia in H-USY and La(x)NaY: A 29 Si and 27 Al MAS NMR and 27 Al MQ MAS NMR study, *J.*

Phys. Chem. B. 104 (2000) 6743–6754. doi:10.1021/jp000147c.

- [243] E. Lippmaa, A. Samoson, M. Mägi, High-Resolution ^{27}Al NMR of Aluminosilicates, *J. Am. Chem. Soc.* 108 (1986) 1730–1735. doi:10.1021/ja00268a002.
- [244] C. Ruiz-Santaquiteria, A. Fernandez-Jimenez, J. Skibsted, A. Palomo, Clay reactivity: Production of alkali activated cements, *Appl. Clay Sci.* 73 (2013) 11–16. doi:10.1016/j.clay.2012.10.012.
- [245] P. Duxson, J.S.J. Van Deventer, 17 - Commercialization of geopolymers for construction – opportunities and obstacles, in: J.L. Provis, J.S.J.B.T.-G. van Deventer (Eds.), *Woodhead Publ. Ser. Civ. Struct. Eng.*, Woodhead Publishing, 2009: pp. 379–400. doi:https://doi.org/10.1533/9781845696382.3.379.
- [246] G. Huang, Y. Ji, L. Zhang, J. Li, Z. Hou, The influence of curing methods on the strength of MSWI bottom ash-based alkali-activated mortars: The role of leaching of OH^- and free alkali, *Constr. Build. Mater.* 186 (2018) 978–985. doi:10.1016/J.CONBUILDMAT.2018.07.224.
- [247] J. Chang, W. Li, D. Wang, Y. Zhang, Effect of silicate modulus on tensile properties and microstructure of waterproof coating based on polymer and sodium silicate-activated GGBS, *Constr. Build. Mater.* 252 (2020) 119056. doi:10.1016/j.conbuildmat.2020.119056.
- [248] T. Yang, X. Yao, Z. Zhang, Quantification of chloride diffusion in fly ash-slag-based geopolymers by X-ray fluorescence (XRF), *Constr. Build. Mater.* 69 (2014) 109–115. doi:10.1016/j.conbuildmat.2014.07.031.
- [249] J.L. Provis, Geopolymers and other alkali activated materials: Why, how, and what?, *Mater. Struct. Constr.* 47 (2014) 11–25. doi:10.1617/s11527-013-0211-5.
- [250] J.L.P.S.A.B.E.D.R. Ana Paula Kirchheim, Management and valorisation of wastes through use in producing alkali-activated cement materials, *J. Chem. Technol. Biotechnol.* 91 (2016) 2365–2388. doi:10.1002/jctb.4927.

- [251] D. Jacques, L. Wang, E. Martens, D. Mallants, Modelling chemical degradation of concrete during leaching with rain and soil water types, *Cem. Concr. Res.* 40 (2010) 1306–1313. doi:10.1016/j.cemconres.2010.02.008.
- [252] F.B. Neall, Modelling of the near-field chemistry of the SMA repository at the Wellenberg site: Application of the extended cement degradation model, *PSI Inst.* (1994) 84.
- [253] V.Í.T.Š. FRANTIŠEK ŠKVÁRA PETR HLAVÁČEK, LUBOMÍR KOPECKÝ, ZUZANA CÍLOVÁ, A WEAK ALKALI BOND IN (N, K)–A–S–H GELS - EVIDENCE FROM LEACHING AND MODELING, *Ceram. – Silikáty.* 56 (2012) 374–382.
- [254] J.L. Provis, S.A. Bernal, Geopolymers and Related Alkali-Activated Materials, *Annu. Rev. Mater. Res.* 44 (2014) 299–327. doi:10.1146/annurev-matsci-070813-113515.
- [255] F. Puertas, M. Palacios, H. Manzano, J.S. Dolado, A. Rico, J. Rodríguez, A model for the C-A-S-H gel formed in alkali-activated slag cements, *J. Eur. Ceram. Soc.* 31 (2011) 2043–2056. doi:10.1016/J.JEURCERAMSOC.2011.04.036.
- [256] S. Park, H.N. Yoon, J. Seo, H.K. Lee, J.G. Jang, Structural evolution of binder gel in alkali-activated cements exposed to electrically accelerated leaching conditions, *J. Hazard. Mater.* 387 (2020) 121825. doi:10.1016/j.jhazmat.2019.121825.
- [257] C. Shi, A. Fernández-Jiménez, Stabilization/solidification of hazardous and radioactive wastes with alkali-activated cements, *J. Hazard. Mater.* 137 (2006) 1656–1663. doi:10.1016/j.jhazmat.2006.05.008.
- [258] F. Lolli, H. Manzano, J.L. Provis, M.C. Bignozzi, E. Masoero, Atomistic Simulations of Geopolymer Models: The Impact of Disorder on Structure and Mechanics, *ACS Appl. Mater. Interfaces.* 10 (2018) 22809–22820. doi:10.1021/acsami.8b03873.
- [259] H. Zhu, Z. Zhang, Y. Zhu, L. Tian, Durability of alkali-activated fly ash

concrete: Chloride penetration in pastes and mortars, *Constr. Build. Mater.* 65 (2014) 51–59. doi:10.1016/j.conbuildmat.2014.04.110.

[260] S. Ahmari, L. Zhang, Durability and leaching behavior of mine tailings-based geopolymer bricks, *Constr. Build. Mater.* 44 (2013) 743–750. doi:10.1016/J.CONBUILDMAT.2013.03.075.

[261] K. Haga, S. Sutou, M. Hironaga, S. Tanaka, S. Nagasaki, Effects of porosity on leaching of Ca from hardened ordinary Portland cement paste, *Cem. Concr. Res.* 35 (2005) 1764–1775. doi:10.1016/j.cemconres.2004.06.034.

[262] H. Yang, Y. Che, F. Leng, Calcium leaching behavior of cementitious materials in hydrochloric acid solution, *Sci. Rep.* 8 (2018) 1–9. doi:10.1038/s41598-018-27255-x.